Bed Properties and Three-Dimensional Topography From Radar at Rutford Ice Stream, West Antarctica

Swansea University
Prifysgol Abertawe

Rebecca Schlegel

Department of Geography

Swansea University

A thesis submitted to Swansea University in fulfilment of the requirements for the Degree of

Doctor of Philosophy

29th September, 2021

Abstract

Outlet glaciers and ice streams of the Antarctic Ice Sheet provide discharge pathways, transporting >90% of the continents ice into the oceans. Elongated landforms beneath fast flowing ice streams form as a result of ice-bed interactions. Understanding their link to ice flow dynamics will better inform subglacial processes and allow these processes to be correctly implemented in predictive numerical flow models, thus improving predictions of future contributions to sea level rise. In this thesis, a section of the bed of Rutford Ice Stream (West Antarctica), containing numerous elongated subglacial landforms, was analysed using a suite of 2D and 3D radar data with repeat surveys. Bed properties vary spatially over a 100 m scale and imply the pattern of inferred basal motion in this area is more complex, and basal sliding dominated areas are more extensive, than previously assumed. Local erosion rates are high (1 m/a), indicating a mobile bed, whereas most of the bed shows no temporal change, implying stability of the basal environment. Observations of landforms shortening, and previous observations of landforms extending, highlight that landforms are a non-static part of the bed. Isolated landforms appear to consist of a more rigid sediment at their upstream end with softer sediment downstream. Some landforms contain a water body (up to 10 km length) along their crest. 3D processed data reveal a so far unseen moat (depression) around one landform. Dimensions of the upstream part of the moat are comparable to dimensions of the upstream end of the landform (<50 m height, <300 m width). Observations suggest landforms are depositional features, while the moat was likely eroded. The radar and other data analysed provide detailed landform and moat architecture, at a resolution comparable to digital elevation models of deglaciated terrain, and together with interpreted properties give a solid basis for testing existing landform formation theories.

Acknowledgements

Although the front page only contains my name, writing this thesis I have drawn so much on work, advice and knowledge of my supervisors and the whole BEAMISH team. As Phil Jackson said "the strength of a team is each individual member. The strength of each individual member is the team". I am deeply grateful to be part of such a diverse, welcoming and cooperative team.

First of all, I would like to express my sincere appreciation to my supervisory team: Tavi Murray (Swansea University), Andy Smith (BAS), Ed King (BAS), Roger Clark (Leeds University), Adam Booth (Leeds University) and Steph Cornford (Swansea University) for always having an open door. I really appreciate your constant support and advice throughout the last 4 years.

Tavi, your broad knowledge and ideas of subglacial processes is inspiring to me. Thank you for various supporting letters for grant applications, pointing out outreach and lecturing opportunities and sharing your experience of how to best pursue my career in academia. I do appreciate your honesty and that you always had a solution to challenges arising during my PhD.

Andy, you are the BEAMISH master mind and your ability to always see the bigger picture affirms you as such. I don't know which language to use, "och nie bother..." "marvolosso grazie"... Thanks for all the laughter during fieldwork. Thanks for the wobbly lines you drove during acquisition. But that might just be tit-for-tat response for times when I called DELORES a GPR or cross-cutting your way while dragging the radar system and make you jump over it. I wish I could say I am sorry...

Adam and Roger, thanks so much for welcoming me to Leeds, always offering help, going over ideas and how we could evaluate these ideas using geophysics. Thanks to you both for sharing your immense knowledge of geophysics and processing. Now, before you read this thesis Roger, let me say that I am sorry for not, in any form, including Q in this work. I hope by mentioning it in here I can tick that box. Not less important, Adam, thanks for keeping up with my slang talk for 4 years and your encouragement - PENG.

Big thanks to **Ed** for sitting down several times with me, even when on crutches, explaining the technicalities of DELORES, processing and sharing your knowledge and ideas on what the hell is going on under Rutford Ice Stream.

I would also like to extend my sincere gratitude to **Alex Brisbourne** (BAS), although not officially a supervisor, you spent a lot of time and patience going through manuscripts, ideas and problems. Although it is a shame that the biggest challenge of our field season, the question of "was it a mooli or a radish" could not have been solved so far and it might remain a mystery forever.

Data used in this thesis were collected by Ed, Alex, Andy and myself and it goes without saying that without their efforts in the field, as well as the efforts pre- and post season, none of this work would have been possible. Big thank you for a great time to all the people part of the field seasons 2017/18 and 2018/19. I still do not know how to pronounce the nedles without making it sound like nudles. It will probably still take me some time to NOT show the "water level in the hot water drill tank" when Sridhar Anandakrishnan enters a meeting.

I would like to thank the whole Glaciology group and my geography lunch group in Swansea; I miss our lunch breaks at the pond. Furthermore, I want to thank the group of Chris Clark, Maarten Krabbendam, Richard Alley, Keith Nicholls, Hugh Corr and the rest of the BEAMISH team for discussion and brainstorming.
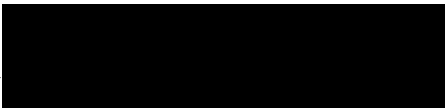
Thanks to my **family** for supporting me all these years. Mum I really hope by now you believe that I am a scientist - if not it's time for me to give up (Mama ich hoffe, dass du mit Einreichen meiner Doktorarbeit mich als Wissenschaftler ansiehst, wenn nicht, dann geb ich jetzt auf). Thanks to Alex Roesner, for your constant support and your ability to always make me laugh. Many thanks to my **friends** in Germany, UK, Canada and Norway: Sina, Nina, Anna-lena, Moni, Enya, Anna, meine Baerchen Sarah und Micha, Emma S. and Emma P., Tamsyn, Tinchen, Nellija, Alex W., Ash, Alvaro and Nadine.

Finally I want to thank my examiners Bernd Kulessa and Rob Bingham for taking the time and examining my thesis, looking forward to the feedback and discussions during the viva.

Declaration

This work has not previously been accepted in substance for any degree and is not being concurrently submitted in candidature for any degree.
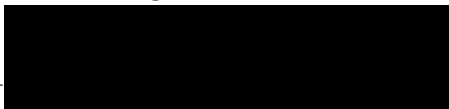
Swansea, 29.09.2021 ⎯⎯ ██████████████

This thesis is the result of my own investigations, except where otherwise stated. Where correction services have been used, the extent and nature of the correction is clearly marked in a footnote(s).

Other sources are acknowledged by footnotes giving explicit references. A bibliography is appended.

Swansea, 29.09.2021 ⎯⎯ ██████████████

I hereby give consent for my thesis, if accepted, to be available for photocopying and for inter-library loan, and for the title and summary to be made available to outside organisations.

Swansea, 29.09.2021 ⎯⎯ ██████████████

The University's ethical procedures have been followed and, where appropriate, that ethical approval has been granted.

Swansea, 29.09.2021 ⎯⎯ ██████████████

Contents

List of Figures

List of Tables

Abbreviations

3D *three dimensional*

2D *two dimensional*

AGC *Automatic gain control*

BAS *British Antarctic Survey*

BEAMISH *Bed Access, Monitoring and Ice Sheet History*

BRP *bed-reflection power*

BRP$_{est}$ *estimated* bed-reflection power

BSIS *Barents Sea Ice Sheet*

CDP *common depth point*

CMP *common mid point*

COP *cosine of phase*

CSRS-PPP *Canadian Spatial Reference System Precise Point Positioning*

DEM *digital elevation model*

DELORES *Deep Look Radio Echo Sounder*

EM *electromagnetic*

GLCM *Grey-Level Co-Occurrence Matrix*

GNSS *global navigation satellite systems*

GPS *Global Positioning System*

GPR *Ground-penetrating radar*

ILINE *inline*

IRP *internal reflection power*

InSAR *Space-borne Synthetic Aperture Radar Interferometry*

IPCC *Intergovernmental Panel on Climate Change*

LIDAR *Light Detection and Ranging*

MSGL *megascale glacial lineation*

MSGLs *megascale glacial lineations*

NMO *normal moveout*

R *reflection coefficient*

RINEX *Receiver Independent Exchange Format*

RIS *Rutford Ice Stream*

RES *Radio Echo Sounding*

RMS *root mean square*

SNR *signal-to-noise ratio*

SAR *synthetic-aperture radar*

twtt *two-way traveltime*

UTC *Coordinated Universal Time*

WAIS *West Antarctic Ice Sheet*

WEM *Wave Field Extrapolation Migration*

WGS *World Geodetic System*

XLINE *crossline*

Z *acoustic impedance*

Chapter 1

Introduction

1.1 Motivation

1.1.1 Global Sea Level and Contribution of Ice to Sea Level

The *Intergovernmental Panel on Climate Change* (IPCC) sixth assessment report predicts a global sea-level rise caused by ocean warming and glacier melting of 0.5–1 m, possibly even 2 m by 2100, depending on the emission scenario within the next years (IPCC, 2021). Sea-level rise has a significant impact on coastal areas, causing increased coastal erosion and risk of flooding (Hinkel *et al.*, 2015; Nicholls & Cazenave, 2010). Around 10% of the world's population live in low elevation coastal zones (McGranahan *et al.*, 2007). To develop successful mitigation strategies, there is an urgent need for reliable predictions of sea-level rise, and therefore predictions and understanding of ice discharge to the oceans. Figure 1.1 shows measured surface flow velocities of the Antarctic Ice Sheet, including areas of ice flowing faster than $1000\,\mathrm{m\,a^{-1}}$. Ice streams, shown as high-velocity river-like shapes, discharge 90% of ice that is lost from the Antarctic Ice Sheet to the ocean (Benn & Evans, 2011). Understanding and predicting ice stream dynamics is therefore crucial to be able to forecast sea-level rise.

1.1.2 Contribution from Marine Ice Sheets

The complete melt of the Antarctic Ice Sheet would be expected to cause a 60 m sea-level rise (Vaughan *et al.*, 2013), with approximately 3.3 m contribution by the *West Antarctic Ice Sheet* (WAIS) (Bamber *et al.*, 2009). Antarctica has
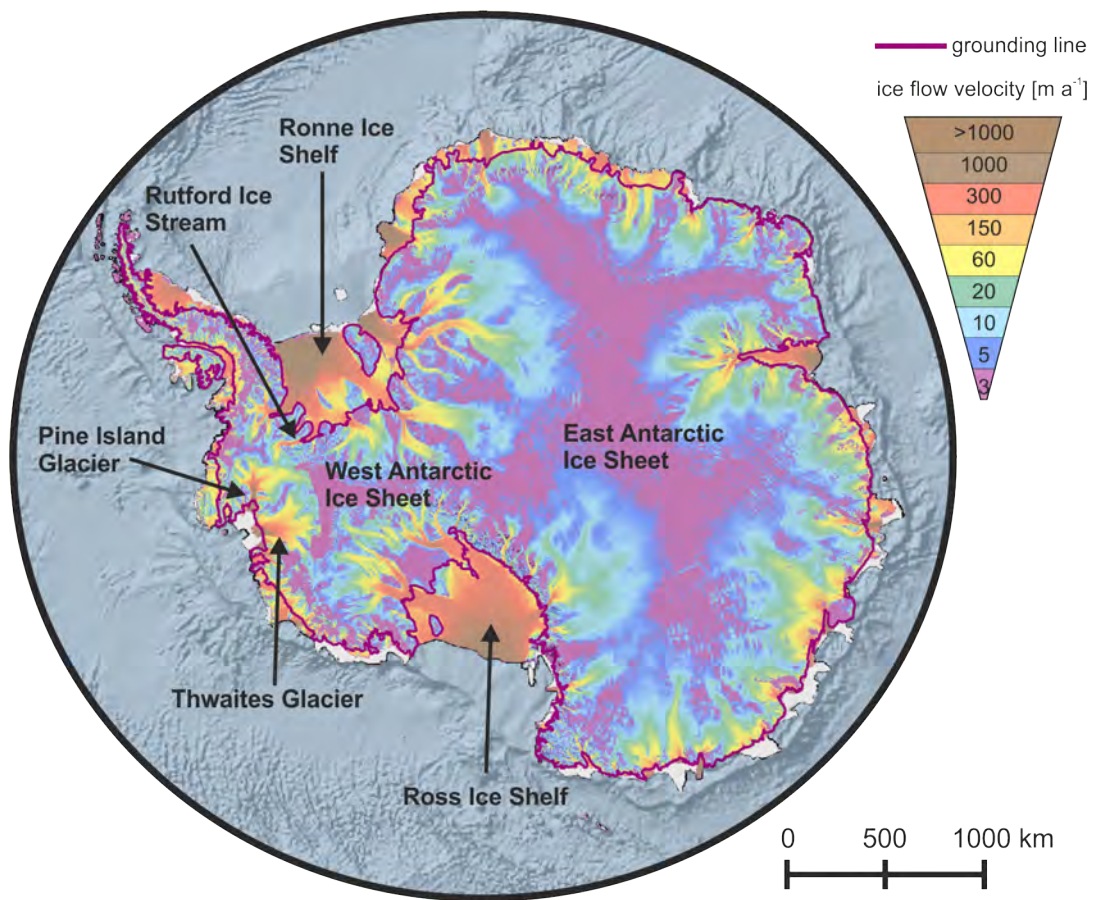
Figure 1.1: Surface flow velocity of the Antarctic Ice Sheet from Space-borne Synthetic Aperture Radar Interferometry satellite data (Rignot *et al.*, 2011). The purple line is the ASAID grounding line (Bindschadler *et al.*, 2011).

contributed 14 mm to sea-level rise since 1979, with 6.9 mm originating from the WAIS (Rignot *et al.*, 2019). Although the current contribution to global sea level by the Antarctic Ice Sheet is relatively small, the massive amount of ice stored represents a significant risk. The challenge to predicting sea-level rise is that ice discharge to the oceans is not linear over time. This applies particularly to the WAIS, which is a so-called marine ice sheet, which means that the bed beneath the ice sheet lies below sea level (Lythe & Vaughan, 2001). A retrograde slope of the bed of marine ice sheets makes the ice sheet vulnerable to atmospheric and ocean warming. This vulnerability is known as Marine Ice Sheet Instability (Hughes, 1981; Joughin & Alley, 2011; Mercer, 1978; Weertman, 1974) and can be demonstrated by the increase in ice flow velocity observed for Pine Island (12% over the past three years (Joughin *et al.*, 2021)) and Thwaites Glacier (100% since 2009 (Scambos *et al.*, 2017), for location see Figure 1.1).

Marine Ice Sheet Instability involves the inland retreat of the grounding line on a retrograde sloped bed (blue arrows Figure 1.2). Warm water circulating beneath ice shelves (red arrows) leads to enhanced basal melting at the grounding line (Joughin *et al.*, 2014). A retreat of the grounding line on a retrograde sloped bed results in thicker ice in deeper water at the grounding line. Due to the greater ice thickness, the ice flux at the retreated grounding line is greater compared to the previous grounding line position, while the accumulation in the upstream region has not changed. This imbalance results in further retreat of the grounding line (Weertman, 1974), which in turn increases the discharge of ice to the oceans (Joughin *et al.*, 2010; Shepherd *et al.*, 2004). A grounding line position at a downward slope is considered unstable, as the grounding line will be forced to migrate further downslope due to the differences in ice flux at the grounding line and the upstream accumulation. The positive feedback will stop once a stable grounding line position, such as a bedrock high, where the ice flux equals the upstream accumulation, is reached.

1.1.3 Ice Dynamics and Subglacial Landforms

The reduced resistance due to a retreated grounding line can lead to a speed-up of ice streams. However, the large-scale behaviour of ice sheets and glaciers is largely controlled by subglacial processes (Joughin *et al.*, 2009; Pollard & DeConto, 2012; Ritz *et al.*, 2015) and, therefore, the conditions at the ice-sediment interface, such as availability of water, properties of the sediment or bedrock, and the
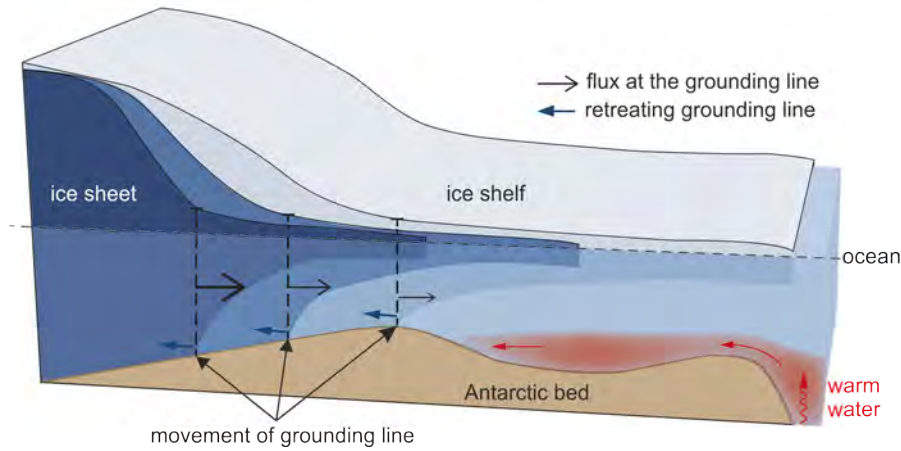
Figure 1.2: Principle of Marine Ice Sheet Instability (modified after Pattyn & Morlighem, 2020).

topography. To reliably model ice dynamics, information on the basal properties and topography, and notably their spatial and temporal variability, is needed. In deglaciated areas, the past ice flow is reconstructed using the distribution and orientation of subglacial landforms (Boulton & Clark, 1990; Greenwood & Clark, 2009a,b; Kleman & Borgström, 1996; Kleman *et al.*, 1997). Elongated subglacial landforms develop due to glacial movement and are indicative of fast-flowing ice (Clark, 1993; Stokes & Clark, 2002). Some studies even suggest a relation between their elongation ratio (ratio between length and width) and the former ice flow velocity (Chorley, 1959; Hess & Briner, 2009; Stokes & Clark, 2002). Although landforms in deglaciated areas in the marine record (mapped by bathymetry, seismics and shipboard systems) as well as in the terrestrial record (mapped by satellites and airborne systems) constitute a large record of the size and the shape of landforms, a consensus of their formation has yet to be found (Clark, 2011; Fowler, 2010; Menzies, 1979). As subglacial landforms are indicative of fast ice flow, information about their composition and geometry as well as properties of their surrounding area is needed to develop and test theories of their formation and understand the mechanisms involved with fast ice flow. However, observations in deglaciated areas can only provide a limited insight into past basal conditions as the deglaciated topography represents an integrated record of processes during deglaciation, during the retreat of the ice and possibly during periglacial cycles and processes after deglaciation (Holschuh *et al.*, 2020).

The inaccessibility of the bed of contemporary ice streams or glaciers complicates direct and in-situ measurements and observations of the subglacial envi-

ronment. Nevertheless, over the past years, the basal environment of Antarctica has been revealed by drilling through the ice and sampling the bed or using geophysical methods such as radar or seismic reflections. Sediment samples of the bed can provide absolute measurements of properties of the subglacial material (Engelhardt *et al.*, 1990; Kamb, 2001; Smith *et al.*, 2021), including sediment composition, layering or porosity, but this information only provides point measurements (spatially limited). Using geophysics (e.g., King *et al.*, 2009; Smith, 1997b), topography can be determined over large distances, but measurements of properties of the bed are relative and at lower vertical resolution compared to samples retrieved from drilling. However, maps of the subglacial topography of Antarctica are often based on sparsely spaced geophysical data, with survey lines spaced on a kilometre scale, which impedes the mapping of subglacial landforms. Only a few surveys provide information on the bed on a metre scale, which can be used to analyse subglacial landforms and bed properties (e.g., Bingham *et al.*, 2017; Holschuh *et al.*, 2020; King *et al.*, 2007, 2009, 2016). Furthermore, repeated geophysical surveys can be used to evaluate how fast the glacier bed, including landforms, is changing (Smith & Murray, 2009; Smith *et al.*, 2007). High-resolution in-situ measurements of subglacial landforms and the glacier bed open up the opportunity to (1) compare conditions under former ice sheets and conditions found under today's glacier systems (e.g., done for the Barents Sea Ice Sheet in comparison to the WAIS (Newton & Huuse, 2017)), and therefore raise expectations of a better understanding of the current changes of the WAIS (Andreassen & Winsborrow, 2009), and (2), which is the most relevant for this thesis, enable comparison with existing models of landform formation, e.g., differences in the time scale of observed landform formation with theoretical models (King *et al.*, 2009; Smith & Murray, 2009).

1.2   Research Aims and Objectives

The previous section highlighted the need for a better understanding of subglacial properties, including the formation of subglacial landforms. Connecting to this, the overall aim of this PhD thesis is to analyse the subglacial topography and properties under *Rutford Ice Stream* (RIS). RIS is a fast-flowing ($>300\,\mathrm{m\,a^{-1}}$) ice stream in West Antarctica. It has a long history of research (more than 40 years (e.g., Doake *et al.*, 1987; King *et al.*, 2016; Murray *et al.*, 2008; Smith, 1997b));

therefore, many different datasets, as well as repetitions of surveys, are available. Combining data collected in different years and data with different acquisition geometries (e.g., the area surveyed) enables the investigation of temporal and spatial variation at the bed and, therefore, of subglacial landforms.

In order to fulfil these aims, the following three research objectives have been defined:

1. **What is the spatial pattern of bed properties beneath RIS, and how does this pattern modulate ice flow?** The composition of the bed influences the mechanism of flow and can therefore influence the ice flow velocity. Spatial variations in sediment stiffness, which imply a change in ice flow mechanism as well as properties of subglacial landforms, have been identified in previous studies on RIS (e.g., King *et al.*, 2004, 2009; Murray *et al.*, 2008; Smith, 1997b; Smith *et al.*, 2007). However, properties of landforms and the bed have only been determined over a limited spatial extent. Detail, such as properties along the whole length of landforms, is missing. An area of 14.5×18 km surveyed by surface-radar data in 2016/17 is analysed to identify spatial variations in bed properties. This area contains numerous subglacial landforms, including upstream and downstream ends of landforms. Analysis of bed properties over such a wide area, but with relatively dense line spacing, will highlight detail in bed properties and properties of landform. Both can modulate flow, but can also give indications of subglacial conditions involved in the formation of landforms.

2. **How mobile or stable is the bed beneath RIS, and what are possible implications for the stability of the ice flow?** Previous studies on RIS have found substantial temporal changes of the bed conditions as well as the bed topography, whereas observation of surface flow velocity has given no indications for changes in flow dynamics (Davies *et al.*, 2018; Smith *et al.*, 2007). However, so far, the analysis of temporal changes at the bed has been limited to a small area (∼10×5 km Smith & Murray, 2009) on the bed of RIS. Using repeated radar grids with dimensions 14.5×18 km, the temporal variability of the bed are analysed. Results give indications on how fast RIS can reorganise its bed and on which spatial scale. Using this information, assumptions about the stability of the bed, and therefore implications on the future dynamics can be considered.

3. **What do the upstream and downstream ends of landforms beneath RIS look like, and what are the implications for the formation process of landforms?** Subglacial landforms, like drumlins and *megascale glacial lineations*, are understood to form during active ice flow. Numerous models describe their theoretical formation. However, most theories of landform formation are based on observations in deglaciated areas and remain untested within contemporary subglacial systems. This highlights the need for high-resolution data of in-situ conditions of subglacial landforms. Seismic and radar reflection profiles are a commonly used tool to map subglacial topography, and they represent the best existing data of in-situ subglacial conditions (Holschuh *et al.*, 2020). However, these data often contain dense sampling along the radar or seismic line, but coarse sampling perpendicular to the lines, and data interpolation is needed between lines, due to which detail perpendicular to the acquisition direction is missed. Surface-radar data acquired in 2017/18 are compliant with *three dimensional* (3D) processing. As a result of close line spacing (20 m) and 3D processing, the theoretical horizontal resolution of this dataset is 24 m along and across track. This data resolution is compliant with morphological analysis (Napieralski & Nalepa, 2010) and allows quantitative and qualitative comparison with, for example, terrestrial *Light Detection and Ranging* (LIDAR) and marine side-scan sonar data. Analysing high-resolution 3D bed topography for small-scale features possibly reveals detail of the landforms and its surrounding which will help to model their formation and link to ice dynamics.

1.3 Outline

This thesis contains 9 Chapters (including this one).

Chapter 2 provides some background on the current state of knowledge of ice stream dynamics and the mechanisms acting at the bed. Furthermore, characteristics and formation theories of drumlins, *megascale glacial lineations* (MSGLs) and moats around landforms are introduced. This is followed by a description of the study area, the *Rutford Ice Stream*. Finally, the theoretical background of the application of radar surveys in the cryosphere, including the basics of migration, are given.

Chapter 3 can be split into three parts. First, the *Deep Look Radio Echo Sounder* system used for data acquisition in this thesis is introduced. This is followed by a summary of *two dimensional* (2D) data that was acquired previous to this PhD project but is analysed in this thesis. Acquisition and processing of the 2D data have not been part of this PhD project and are therefore only briefly introduced. The third part of this chapter includes the data acquired as part of this PhD project. This includes design considerations for the survey to acquire radar data compliant with 3D migration. Finally, the 3D processing is summarised, and a description of the visualisation of a 3D dataset is given.

Chapter 4 includes the methods used to (1) determine the topography along the radar lines, (2) calculate and calibrate the reflectivity of the bed reflection along the 2D radar lines , (3) identify topographic changes in the bed topography along the 2D radar lines and (4) analyse the bed reflection in the 3D dataset using different attributes to identify small-scale features on the bed and determine bed properties.

Chapter 5, 6, 7 include the results and discussion of the following analyses: **Chapter 5:** Reflectivity analysis of the bed along the 14.5×18 km grid of 2D radar data. The calibrated bed reflection was used to make assumptions of bed properties. This includes bed properties along landforms and other features at the bed.

Chapter 6: Topographic changes identified from a repeated radar dataset. Changes are linked to bed properties identified in Chapter 5. Possible mechanisms causing these topographic changes are discussed.

Chapter 7: Results of the 3D migration and the following topography are given. By calculating different attributes of these high-resolution 3D datasets, small-scale as well as large-scale features on the bed, are identified. Implications

of these features to ice flow are discussed. Furthermore, the limitations of the application of 3D migration and radar data, in general, are discussed.

Chapter 8 includes a discussion of the major findings of this thesis and puts those in relation to the current understanding of the subglacial processes.

Chapter 9 summarises the key findings of this thesis, and suggestions for future work are given.

Each chapter apart from the current and Chapter 9, includes a summary at the end of the section to highlight the important findings and key facts of this chapter.

Chapter 2

Background

This chapter provides some background to ice stream dynamics, the study area and the principles of radar surveys. First, ice dynamics and the different types of glacier movement are introduced (Section 2.1). This includes a description of the properties of ice stream beds (Section 2.1.4) and subglacial sediment (Section 2.1.4.2). The second part of this chapter focuses on subglacial landforms, specifically drumlins, MSGLs (Section 2.2.1) and moats around landforms (Section 2.2.2). The study area and results from previous studies on RIS are introduced in Section 2.3. The final part of this chapter introduces the principle of *electromagnetic* (EM) wave propagation (Section 2.4) and the application of migration to radar data (Section 2.4.4).

2.1 Ice Dynamics

Over the past decades a lot of research has been focused on the processes of glacier motion. Glacier dynamics and flow velocity are influenced by several factors, including the glacier geometry (thickness, surface slope, width), ice properties (temperature, density, chemistry), bed properties (stiffness, temperature), hydrology (availability of water), mass balance (accumulation vs. ablation) and the environment at the terminus (land- or water-based, sea ice) (Jiskoot, 2011). The ice flow can be described as the residual of stresses acting on the ice, while the driving stress is opposed to the resistive stresses. The driving stress is generated by the weight of the ice and the surface slope. Resistive stresses arise from the strength of the bed and resistance against the flow at the ice base (basal drag), the shear margins of the ice stream (lateral drag) and spatial variations of
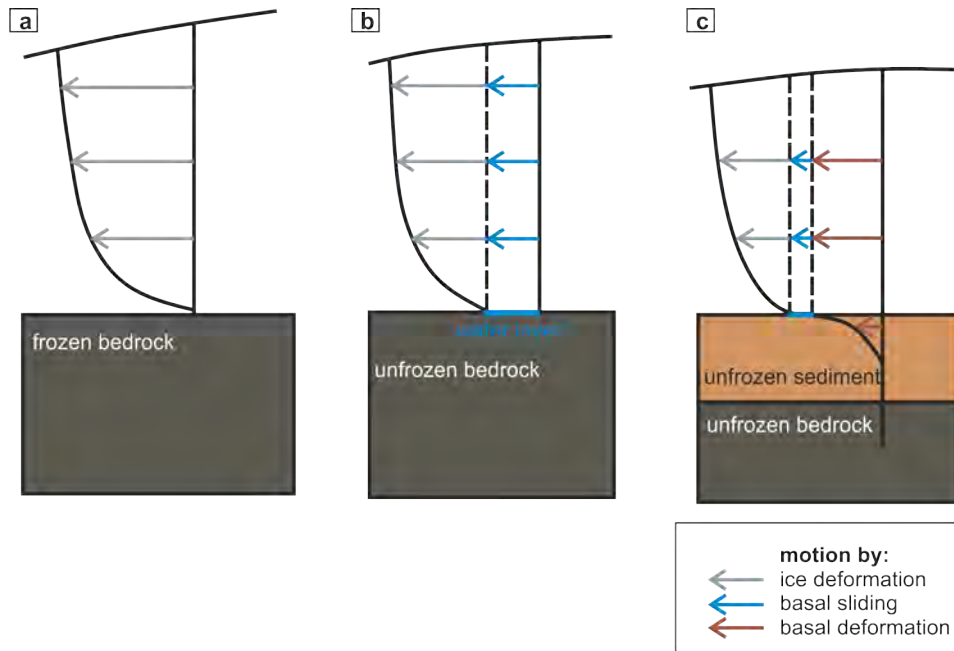
Figure 2.1: Types of glacier movement: a) ice deformation on a frozen bed, b) ice deformation and basal sliding on an unfrozen, possibly wet, bedrock, c) ice deformation, basal sliding and basal deformation on an unfrozen, soft sediment. The length of arrows indicating the contribution of different mechanisms to motion are not to scale (graph modified after Benn & Evans, 2011).

pulling and pushing within the ice influenced by ice-shelf conditions (longitudinal stresses, Benn & Evans, 2011).

Three different types of glacier movement are known (Figure 2.1; Benn & Evans, 2011; Cuffey & Paterson, 2010):

- ice deformation

- ice deformation and basal sliding

- ice deformation, basal sliding and subglacial deformation

In the following the three processes are introduced in more detail:

2.1.1 Ice Deformation

Ice can deform by fracture or creep, where the latter is considered as the more important process when ice moves over a frozen bed (Figure 2.1 a). Ice creep results from movement within or between individual ice crystals, where the crystals get displaced relative to each other, which results in a forward movement.

Ice creep is described by Glen's Flow law, where ice is described to behave as a non-linear viscous material. The contribution to ice flow is highest at the surface, with decreasing velocities with depth (Figure 2.1 a). If stresses applied are too large to be accommodated by creep, fracturing of ice takes place, which is an important process during calving events and can lead to the weakening of ice stream and ice shelf margins (Benn & Evans, 2011).

2.1.2 Basal Sliding

Basal sliding describes the slipping of ice on top of solid bedrock or a thin water layer between bedrock and ice (Figure 2.1 b), while the bed is considered to be at the pressure melting point. When glacier ice slides along a wet bed, resistance to flow arises from obstacles on the bed, such as bedrock bumps, or debris incorporated into the basal ice. Ice flow around large obstacles (>1 m (Boulton, 1972)) is assumed to be most efficient by enhanced creep, while flow around small obstacles is attributed to regelation. Enhanced creep causes the ice to deform around and possibly above the obstacle due to the high strain rates upstream of the obstacle. Regelation includes the melting of ice to pass an obstacle and subsequent freezing of this water, once the obstacle is passed. Ice movement against a local hill might lead to a high-pressure zone (Figure 2.2) in the upstream end of the hill, which could cause melt. Meltwater and possibly detached sediment particles will tend to move to the low-pressure area downstream of the hill, where sediment could be deposited or incorporated into the basal ice by refreezing. The latter would transport sediment further downstream, where it would melt out due to the heat generated from the ice moving over sediment. Either way, the relief of the hill will be eroded over time. The generated water is assumed to flow as a thin layer between the ice and the bed (Weertman, 1964). Ultimately, flow around obstacles is likely to be accommodated by a combination of creep and regelation, while the influence of either is dependent on the obstacle size.

Rapid basal sliding is attributed to the presence of water at the bed (Engelhardt & Kamb, 1997). Water between the bed and ice acts as a lubricating film and leads to de-coupling of the bed and the ice, and therefore reduced resistance to basal sliding. The speed at which the ice slides is dependent on the water pressure and, therefore the efficiency of the drainage system. Only an inefficient drainage system that enables high water pressures, such as a distributed water
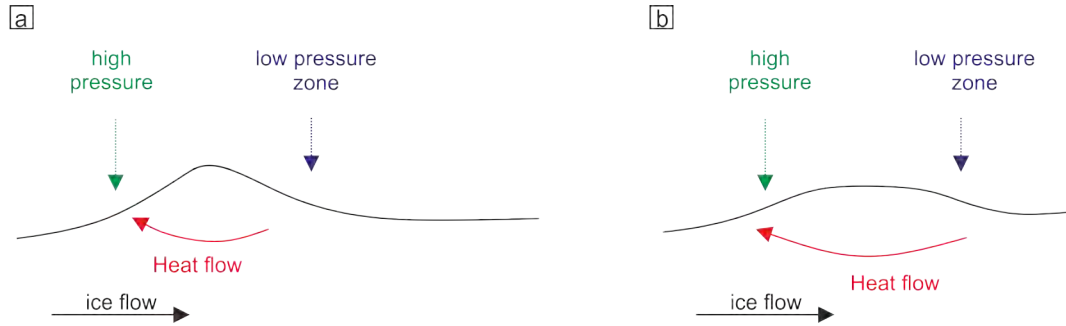
Figure 2.2: Schematic drawing of the principle of erosion of a small local hill by regelation and refreezing. Melt occurs due to an increase of pressure in the upstream end of the hill, meltwater will then move to the low-pressure zone, possibly transporting sediment. Due to low pressure in the downstream end the meltwater can refreeze, the mobilised sediment might get deposited downstream of the hill or get incorporated into the basal ice due to refreezing of meltwater (graph modified after Bennett & Glasser, 2009; Boulton, 1972).

film, will enable fast ice flow by basal sliding. An efficient drainage system, however, where water is transported in channels and canals, results in low water pressure at the bed and, therefore more resistance to ice flow. Ice streams in Antarctica are found to flow at low effective pressure, which means the ice overburden pressure (caused by the weight of the ice) is close to the water pressure at the bed, and the weight of the ice is largely balanced by the water at the base (Flowers, 2015; Fowler, 2009; Kamb, 1991; Smith *et al.*, 2021).

2.1.3 Subglacial Deformation

The fast flow of ice streams is attributed to their weak bed due to low effective pressure and the existence of soft sediment (Benn & Evans, 2011), which deforms in response to stress (Figure 2.1 c). For approximately 35 years now, the idea of sediment deformation while ice flows over a soft bed, including groundbreaking work by Alley *et al.* (1986); Blankenship *et al.* (1986, 1987); Boulton & Hindmarsh (1987), has been accepted. However, the scientific debate about the importance of the deforming bed, the thickness and the spatial distribution of these deforming beds is still ongoing. Several studies on palaeo ice streams in the marine record have shown that the uppermost sediment under former ice streams is unconsolidated (Dowdeswell *et al.*, 2004; Nygård *et al.*, 2007; Ó Cofaigh *et al.*, 2005, 2007). This unconsolidated sediment is assumed to contain a low shear strength and is therefore interpreted as a formerly deforming layer, facilitating

fast ice flow (Dowdeswell *et al.*, 2004; Ó Cofaigh *et al.*, 2005, 2007). The first evidence of basal deformation on a contemporary glacier indicated 80–90% of the basal movement to be accounted for in the upper 0.5 m (Boulton & Hindmarsh, 1987; Boulton & Jones, 1979). Several studies confirm most of the movement to be composed of basal shear in the uppermost centimetres of the bed (Engelhardt, 1998; Kamb, 2001; Truffer & Harrison, 2006). However, findings by Smith & Murray (2009) and Truffer *et al.* (1999) imply sediment deformation to occur in depth of up to 2–12 m (Smith & Murray, 2009).

2.1.4 Basal Properties of Ice Streams

Ice streams are river-like structures that channel ice from the accumulation area, the interior of an ice sheet, to the ablation area, the ocean. They are characterised by their sharply defined margins, separating fast and slow-flowing ice (Benn & Evans, 2011; Cuffey & Paterson, 2010). As introduced in the previous section, bed and ice properties have an important influence on the mechanism of ice flow (Ó Cofaigh *et al.*, 2002), where ice flow over a crystalline bedrock is dominated by basal sliding and flow over soft sediment by basal deformation. Bed properties under Antarctic Ice Streams are variable in space and time (Kamb, 2001; Piotrowski *et al.*, 2004). Spatial variation of bed properties and presumably flow mechanism were confirmed under RIS, where parts of the bed consist of soft, saturated sediment that is interpreted to be deforming, and other parts consist of stiffer material, that is, either highly consolidated sediment or poorly lithified sedimentary rock, which offers more resistance to ice flow (Smith, 1997b; Smith & Murray, 2009; Smith *et al.*, 2007).

2.1.4.1 Temporal Variation in Bed Properties

Piotrowski *et al.* (2004) argued that the stiffness of sediments can vary over time, triggered by temporal variation in water pressure. Temporal changes in sediment stiffness have been observed to occur rapidly (within a few years; Murray *et al.*, 2008; Smith, 2006; Vaughan *et al.*, 2003), whereas in other places, the basal conditions are stable over time (Davies *et al.*, 2018; Smith *et al.*, 2007). Basal water pressure is dependent on the influx and outflux of water, properties of the subglacial material, efficiency (therefore geometry) of the subglacial drainage system and the thermal state at the ice-bed interface (Benn & Evans, 2011). High water pressure is associated with a weaker coupling of sediment and ice, hence reduced
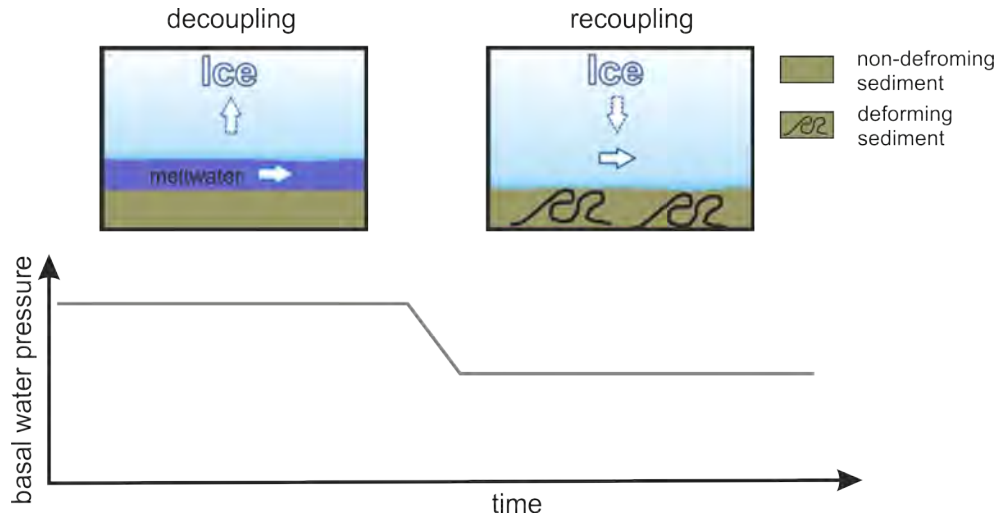
Figure 2.3: Schematic of the influence of basal water pressure on the coupling between ice and sediment (graph modified after Lesemann *et al.*, 2011).

resistance at the ice-bed interface, encouraging rapid sliding (Figure 2.3 a) and, due to the decoupling, reduced deformation (Hooke *et al.*, 1997; Iverson *et al.*, 1995). Likewise, a decrease in water pressure will couple the ice and sediment stronger by ice infiltration into the pore space and therefore enhance deformation (Figure 2.3 b). Further decrease in water pressure can lead to a consolidation of the sediment.

Studies on actively flowing ice streams indicate the presence of generally high basal water pressure, close to the ice overburden pressure, although local variations in water pressure can occur at the bed (Engelhardt & Kamb, 1997). Fluctuations of water pressure are reported to be strong over a length of $\sim$1–10 m for valley glaciers (Murray & Clarke, 1995), while pressure fluctuations caused by effects of ocean tides have been detected over a length of $\sim$100 km upstream the grounding line under West Antarctic ice streams (Anandakrishnan & Alley, 1997; Anandakrishnan *et al.*, 2003; Bindschadler, 2003).

2.1.4.2 Subglacial Sediment

Subglacial sediment, often referred to as till, has been retrieved from various places, including the forefield of glaciers (Clarke, 1987) and from beneath active glaciers and ice streams (Engelhardt *et al.*, 1990; Hooke & Iverson, 1995; Kamb, 2001; Tulaczyk *et al.*, 1998). The matrix of the retrieved sediment spans a wide range of sizes, tending to be poorly sorted. Analysed samples of soft, deforming

sediment are unconsolidated and of high porosity. The sediment is water saturated and shows a low shear strength (Blankenship *et al.*, 1987; Doake *et al.*, 2001; Kamb, 2001; Murray *et al.*, 2008; Vaughan *et al.*, 2003).

Depending on the hydraulic conductivity of the sediment the load applied to the subglacial sediment can result in consolidation and therefore reduce pore space. The reverse process is called dilation, where the sediment matrix gets rearranged, which results in an increased pore volume and therefore an increase in porosity. Shear stress is capable of causing an increase in porosity due to dilation to around 0.4 (Atre & Bentley, 1993; Boulton *et al.*, 1974; Boulton & Dent, 1974; Boulton, 1976). Most sediments have a loading history, which means that they consolidate when force is applied, but once this force is removed, the sediments do not return to their original state. By repeated cycles of loading, sediments can progressively reduce their porosity (Clarke, 2005). This leads to the occurrence of overconsolidated sediment in an environment that currently does not represent such loading stages. By analysing the sediments it is therefore possible to interpret the past overburden conditions in any area (Boulton & Dobbie, 1993; Piotrowski & Kraus, 1997; Tulaczyk *et al.*, 2001).

Rheology of Subglacial Sediment: Boulton & Hindmarsh (1987) proposed a model commonly referred to as the "Boulton-Hindmarsh model" describing the subglacial deformation, assuming weakly non-linear behaviour for the subglacial sediment. This model can account for sediment deformation over several metres of depth and is underpinned by modelling studies and interpretations of field observations (Boulton & Hindmarsh, 1987; Licciardi *et al.*, 1998). However, laboratory studies (shear studies) using collected sediment samples revealed a nearly Coulomb-plastic behaviour (Kamb, 2001; Tulaczyk *et al.*, 2000). Deformation of a Coulomb-plastic rheology is restricted to a thin layer (Tulaczyk *et al.*, 1998, 2000). Different explanations have been found for the inconsistency of the theoretical deformation depth and the deep deformation observed (Smith & Murray, 2009; Truffer *et al.*, 1999): (1) Ice keels ploughing through the sediment or (2) variations in depth of the weakness of sediment. Depending on water flow through the sediment, the depth of the weakest part of the sediment might not be located at the top (Benn & Evans, 2011; Clark *et al.*, 2003; Iverson & Iverson, 2001; Tulaczyk *et al.*, 2000).

Shear Strength of Subglacial Sediment and Significance for Ice Flow:
The low shear strength of subglacial sediments results in low basal resistance. To explain velocities observed for ice streams, the driving stress must be balanced by other stresses such as stresses acting at ice stream margins (Raymond *et al.*, 2001) or at sticky spots (MacAyeal *et al.*, 1995; Smith *et al.*, 2015). Stiff till, till free areas, outcropping bedrock and areas of basal freezing are considered to cause areas of higher basal drag, also referred to as sticky spots (Stokes *et al.*, 2007). Sliding laws are often based on the assumption that basal motion is determined by local stresses, rather than a combination of local and non-local stresses. For instance, the existence of a sticky spots will have a restraining influence on the basal motion in areas of lower drag (e.g., with no sticky spot or decoupled areas) via longitudinal and lateral stresses in the ice. Due to this, local resistance is redistributed over a larger area, therefore smoothing out variations in resistance and therefore influencing the basal motion, ultimately the ice surface speed. To fully understand influences on basal motion, it is important to get a better knowledge of spatial patterns of basal drag (e.g., from sticky spots) and incorporate a full 3D stress-strain relationship within the ice body into ice flow models (Benn & Evans, 2011).

2.2 Subglacial Landforms

Subglacial landforms are directly linked to the ice stream or glacier flow (e.g., Clark, 1993; Clark *et al.*, 2003; Spagnolo *et al.*, 2014; Stokes & Clark, 2001, 2002; Stokes *et al.*, 2013) and evolve due to the erosion, transport and deposition of sediment. These topographic changes alter the resisting force of the bed and, in turn, influence the ice stream dynamics (Alley *et al.*, 2003; Graham *et al.*, 2009; Ó Cofaigh *et al.*, 2002). Streamlined glacial lineations are indicative of rapid ice flow (Clark, 1993).

The following gives an overview of elongated streamlined landforms, specifically drumlins and MSGLs, which are the landforms studied in this thesis. Numerous theories of subglacial landform formation exist. Section 2.2.1.3 provides a brief summary of the main theories. This is followed by the description of moats, which are occasionally observed around the head of landforms (Section 2.2.2), as well as a summary of formation theories of moats (Section 2.2.2.1).

2.2.1 Elongated Streamlined Landforms

Drumlins are often described as longitudinal asymmetric features aligned in the flow direction, with wider, steeper and rounded upstream ends and a tapered more smooth downstream end (Menzies, 1979; Spagnolo *et al.*, 2010). Clark (1993), who first introduced the term *megascale glacial lineation* (MSGL), described these as extremely elongated ridges that maintain parallel conformity over several 10s km. The length of drumlins is in the order of 100 m to a few kilometres and of 10–100 km for MSGLs (Benn & Evans, 2011). Both landforms are distinguished based on their elongation ratio, which is the ratio of length to width. The elongation ratio of MSGLs is higher compared to drumlins (Spagnolo *et al.*, 2014). Clark (1993) described the tipping point between drumlins and MSGLs to be at an elongation ratio of 1:10.

2.2.1.1 Variation in Drumlin and MSGL Composition

Stokes *et al.* (2013) reported that most studies of MSGLs are restricted to a qualitative description of their shapes, and only a few studies systematically analyse their morphology (e.g., Graham *et al.*, 2009) or sedimentology and stratigraphy (e.g., Lemke, 1958; Shaw *et al.*, 2000). According to Stokes *et al.* (2011), MSGLs and drumlins are found to have a range of internal structures (Stokes *et al.*, 2011). Furthermore, Stokes *et al.* (2011) noted that variation in structure (e.g., sorted, homogeneous, surface conformable or unconformable sediments) and composition (presence of a lithology range, clast shape, size and fabric) between individual drumlins are found in the same region. This might imply a combination of formation mechanisms acting in one region or that variations in the composition reflect differences in sediments pre-existing at the bed (Stokes *et al.*, 2011).

2.2.1.2 Spatial Pattern of Drumlins and MSGLs on the Bed

Several authors have investigated subglacial landforms in deglaciated areas. These landforms change geologically as well as geomorphologically in flow direction (Ó Cofaigh *et al.*, 2002; Wellner *et al.*, 2001). The evolution of subglacial landforms along flow in deglaciated areas is described as follows. Short, irregular drumlins are found in the onset region, a region which is often characterised by crystalline basement. The acceleration of ice flow towards downstream is often accompanied

by a transition from crystalline basement to soft sediment and an increase in landform length (Ely *et al.*, 2016; Ó Cofaigh *et al.*, 2002; Wellner *et al.*, 2001). Within the area of soft sediment, MSGLs are typically observed (Ó Cofaigh *et al.*, 2002; Wellner *et al.*, 2001). Due to the overlap of length, width and elongation ratio, several authors proposed drumlins and MSGL to be part of a continuum, where MSGLs are interpreted as an attenuated variant of drumlins (Ely *et al.*, 2016; Spagnolo *et al.*, 2014; Stokes *et al.*, 2013). An increase in landform length has been attributed to increasing ice flow velocity (e.g., Briner, 2007; Hart, 1999; King *et al.*, 2009; Shaw, 1994; Stokes & Clark, 2002; Stokes *et al.*, 2013). Therefore, drumlin and MSGL formation is often combined in formation theories.

2.2.1.3   Hypothesis of MSGL and Drumlin Formation

As drumlins and MSGLs are often considered as a continuum their formation are described together. Many formation theories exists, while consensus has yet to be found. The following list includes a brief overview of selected formation theories:

- Clark (1993) described the formation due to the deformation of subglacial till around inhomogeneities on the bed. He argued that inhomogeneities in till could act as a seeding point for drumlins and MSGLs which then develop into elongated subglacial landforms. The different scale between a drumlin and a MSGL is explained by variations in ice flow velocity acting in different areas.

- Shaw *et al.* (2000, 2008) introduced the catastrophic meltwater flood hypothesis, which describes the erosion of soft beds by turbulent subglacial water flows, leaving MSGLs behind. The occurrence of outburst floods on Kamb and Bindschadler Ice Stream (Siple Coast) supports the idea of turbulent subglacial water flow beneath ice streams. Furthermore, Shaw *et al.* (2008) argued that the occurrence of crescentic scours around drumlin heads are indicative of erosion by water currents (Lowe & Anderson, 2003; Russell *et al.*, 2006; Shaw, 1988). Drumlins are assumed to act as so-called bluff obstacles against flow and crescentic scours are eroded by horseshoe vortices (Shaw *et al.*, 1996).

- Clark *et al.* (2003) and Tulaczyk *et al.* (2001) described roughness elements (keels) in the basal ice that excavate grooves into the subglacial bed. This represents a mechanism where the surrounding area is moved and MSGL are

left behind as erosional marks. Modelling confirms that keels can survive over large distances (depending on the ice flow velocity). However, this requires basal roughness to be produced in the upstream region, which could be achieved by flow convergence and or a bed that is stiffer than the ice, and therefore deforms the basal ice.

- Different theories describing bed instability exist, but initial models have struggled to produce 3D structures (Chapwanya *et al.*, 2011). Some of these models are able to produce subglacial landforms without the need for pre-existing undulations or inhomogeneities at the bed. The instability theory described by Hindmarsh (1998) is based on differences in bed velocity and non parallel flow lines across the bed which lead to differences in thickness of the bed. These undulations and thus variations in stress at the glacier bed can lead to the formation of streamlined glacial landforms like drumlins or flutes, as a result of inherent bed instability. According to this theory, drumlins and flutes without a seeding point, such as a boulder at the upstream end, can be created (Menzies & Shilts, 2002). Schoof & Clarke (2008) explain the formation of MSGLs by transverse flows in basal ice, due to non-uniform normal stresses caused by pre-existing basal topography. Schoof & Clarke (2008) found formation time-scales of 1800 years for a lineation to grow. The theory presented by Fowler & Chapwanya (2014) describes the formation by a coupled flow of ice and sediment and the fluvial sediment transport. Within this model, ribbed moraines, drumlins and MSGLs are described to be part of a continuum.

2.2.2 Moats Around Landforms

Moats around the upstream end of landforms, also called crescent (half-moon) scours, sichelwannen shaped troughs, stoss-side moats or overdeepenings are known features on palaeo ice stream beds (e.g., Graham *et al.*, 2009; Graham & Hogan, 2016; Holschuh *et al.*, 2020; Larter *et al.*, 2012, 2019; Ó Cofaigh *et al.*, 2005; Wellner *et al.*, 2006). For consistency, these features are referred to as moats in this thesis.

Moats are mostly found wrapped around the upstream end of landforms like drumlins, crags-and-tails or around bedrock bumps, where bedrock is cropped out, or sediment is thin. In some locations, these moats are found with no

indication of an associated flow obstacle (Graham & Hogan, 2016). The moats can appear in different forms, such as linear hollows or symmetrical crescent shapes, whereas the arms of the crescent in some areas transition into the grooves between landforms (Graham & Hogan, 2016; Holschuh *et al.*, 2020; Larter *et al.*, 2012, 2019; Shaw, 1994). The moats on palaeo ice stream beds show a length of 200–3000 m, a width 60–500 m and a depth of 5–>60 m (Graham & Hogan, 2016).

2.2.2.1 Hypothesis of Moat Formation

No uniform theory that explains the formation and existence of moats has been stated so far. Possible mechanisms of moat formation include erosion by meltwater (Dreimanis, 1993; Graham & Hogan, 2016; Larter *et al.*, 2019; Ó Cofaigh *et al.*, 2005), erosion by a slurry of saturated till, erosion by mobile basal ice (Graham *et al.*, 2009) or erosion by tidal washing (Ó Cofaigh *et al.*, 2005). Graham & Hogan (2016) suggested that moats are linked to the basal drainage system, evidence of which was found by moats that interconnect to form channels in Greenland and Antarctica. Furthermore, they suggest that isolated moats are possibly formed by local pressure melting at subglacial obstacles in areas of sediment covered beds. Shaw (1994) referred to moats transitioning into the groove between landforms as hairpin erosional marks. These are interpreted to form by horseshoe vortices in turbulent fluids, which is consistent with moats produced during experiments and in nature. However, Shaw *et al.* (1996) stated horseshoe vortices are not expected in flowing ice but rather in meltwater flows.

Possible water sources for the erosion of moats are high surface melt, as found during deglaciation (Graham & Hogan, 2016) or by subglacial lake drainage (Larter *et al.*, 2019). Larter *et al.* (2019) interpret the formation of moats to develop progressively over multiple glacial cycles, based on the scale of the features and the material into which the moats are eroded.

Recently, Holschuh *et al.* (2020) explained moat formation upstream of landforms beneath Thwaites Glacier by pressure variations. Pressure variations are caused by ice flow against an obstacle that redirects water around the obstacle. The lack of water upstream of the obstacle will lead to enhanced coupling of the subglacial sediment and the ice, which leads to enhanced erosion of sediment. They propose some of the till to be deposited in the downstream end of the obstacle, while the erosion of sediment possibly exposes bedrock in the moat. Once

the moat has reached a certain depth, changes in water routing will drive water into the moat (Alley *et al.*, 2021).

2.3   Rutford Ice Stream

This section introduces the study area of this thesis, *Rutford Ice Stream*. General information about ice flow velocities and the large-scale topography is followed by a summary of findings from previous studies on the basal conditions, subglacial landforms and temporal variations at the bed.

RIS is bounded by the Ellsworth Mountains to the west and Fletcher Promontory to the east (Figure 2.4 b). The catchment area comprises the eastern flank of the Ellsworth Mountains, and areas west, north and east of the Ellsworth Mountains, including Fletcher Promontory and the western slopes of Kealey Ice Rise (King, 2009). RIS is a fast-flowing ice stream (Figure 2.4 a), draining ∼49,000 km² of WAIS (≘ 2.6% of the grounded portion of WAIS (King, 2009)) into Ronne Ice Shelf (Doake *et al.*, 2001). Similar to other ice streams, the surface slope is low, inducing low basal driving stress. Together with a basal shear stress of ∼40 kPa (Smith, 1997b), this leads to an ice flow of around 377.3 m a^{-1} in the proximal area of the grounding line (Murray *et al.*, 2007). Further upstream in the onset region of RIS ice flow velocities vary between 72–108 m s^{-1} (King *et al.*, 2004). Long term observations of the ice flow using ground-based stake measurements show no evidence for any long-term changes in the flow of the RIS (Gudmundsson, 2006; Gudmundsson & Jenkins, 2009; Murray *et al.*, 2007; Vaughan *et al.*, 2008). Strong (>10%) fortnightly variations reported by Gudmundsson (2006), correspond to a spring-neap tide cycle in ice flow velocities on RIS.

In the area studied in this thesis, RIS occupies a 26 km wide and 2.2 km deep trough (Figure 2.5), which lies around 1400 m below sea level at the grounding line (King *et al.*, 2016; Smith & Murray, 2009). The ridge in the centre of the ice stream bed is flanked by two asymmetric valleys to either side of the ridge (Figure 2.5), with the western valley being deeper than the eastern valley. The ridge can be separated into two parts, the upstream and lower elevated part (∼1700 m below the geoid) and the higher downstream part (∼1500 m below the geoid).
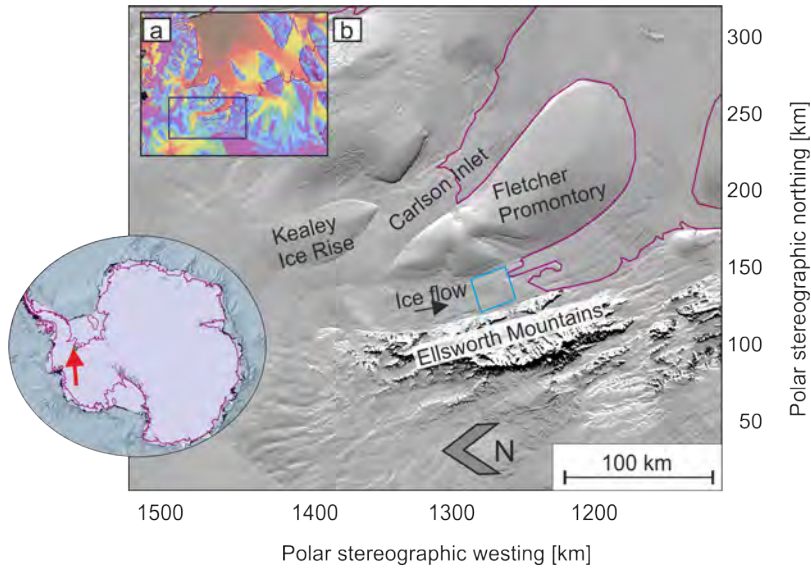
Figure 2.4: Overview map of RIS. a) Location of RIS within the Ronne Ice Shelf. The colour scheme represents surface flow velocities from InSAR satellite data (Rignot *et al.*, 2011) as shown in Figure 1.1. b) Landsat Image Mosaic of Antarctica (LIMA) of RIS and the surrounding area. The purple line is the ASAID grounding line (Bindschadler *et al.*, 2011), the cyan box bounds the area of interest in this thesis.

2.3.1 Basal conditions

2.3.1.1 Subglacial Material

Acoustic impedance of the subglacial material (Smith *et al.*, 2007; Vaughan *et al.*, 2008) as well as the low basal resistance of the RIS (King *et al.*, 2016) imply the presence of soft, water-saturated unconsolidated sediment at the bed. Due to the prolonged stability of the flow, the fast ice velocity and the low basal shear stress (Smith & Murray, 2009) the bed is assumed to be at pressure-melting point, which has been confirmed during hot-water drilling on RIS (Smith *et al.*, 2021). Observations from seismic and radar data have shown, that the sediment underneath RIS is highly mobile and has bimodal geotechnical properties (King *et al.*, 2009; Smith & Murray, 2009; Smith *et al.*, 2007). Figure 2.6 shows the composition of the bed underneath RIS as published by Smith & Murray (2009) based on seismic data. The sediment at the bed is interpreted to consist of areas of (1) deforming and (2) non-deforming [1] sediment:

---

[1]The distinction between deforming and non-deforming sediment under ice is often based on sediment porosity. According to this distinction, porous sediment, referred to as soft sediment, is assumed to accommodate ice flow by basal deformation and low porosity sediment, referred
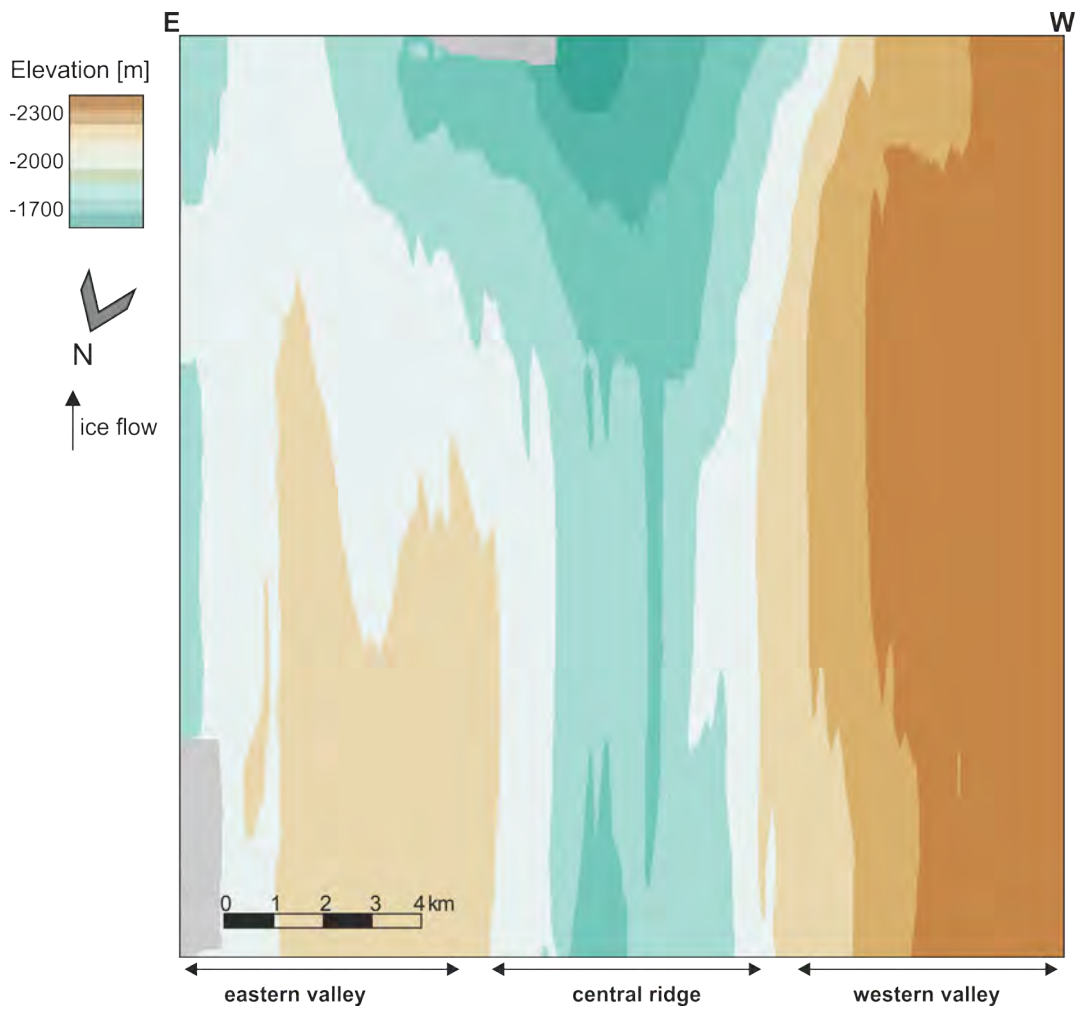
Figure 2.5: Bed elevation referenced to the WGS84 ellipsoid (King *et al.*, 2016). Location of area shown here is indicated by the blue box in Figure 2.4.
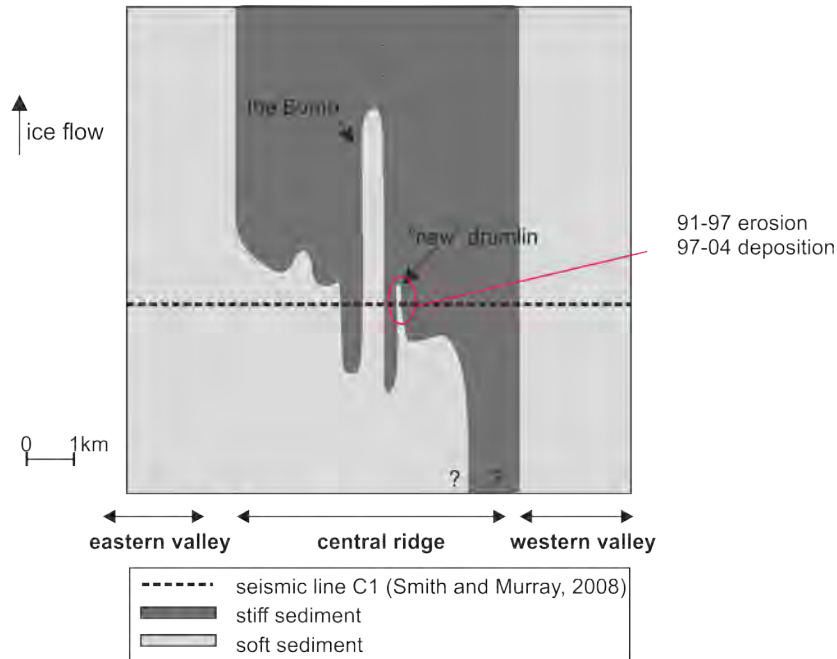
Figure 2.6: Interpretation of the composition of the bed underneath RIS as published by Smith & Murray (2009). The area marked by the red circle marks the location of observed erosion of material between 1991–1997 and the following deposition of sediment between 1997 and 2004 identified by Smith & Murray (2009) and Smith *et al.* (2007).

(1) the dilated, soft and deforming sediment (light grey) is interpreted to contain a high porosity (>0.4), low density and low shear strength (Blankenship *et al.*, 1987; King *et al.*, 2016). The dilation and deformation of the sediment are assumed to extend over a depth of several metres, triggered by the motion of the overlying ice (Smith & Murray, 2009; Smith *et al.*, 2007). Ice motion over this sediment is dominated by basal deformation.

(2) a low porosity ($\leq$ 0.3), lodged and therefore presumably stiff and non-deforming sediment. In these areas, the movement of the ice is dominated by basal sliding (King *et al.*, 2004; Smith, 1997a,b; Vaughan *et al.*, 2003, 2008).

---

to as stiff sediment, favours basal sliding (Smith, 1997a). Strictly speaking, this is not correct, as sediment deformation is dependent on many geotechnical parameters such as water content, friction angle, void ratio, shear strength, just to name a few (Craig, 2004). However, deformation measurements in subglacial sediment confirm that sediment with high porosity found under Whillans Ice Stream is deforming during ice flow (Atre & Bentley, 1993).

Following the identification of variations in bed properties, King *et al.* (2009) mapped the boundary between the soft and stiff sediment using seismic acoustic impedance and surface-radar reflectivity (Figure 2.7). The eastern and western valleys as well the upstream part of the central ridge are interpreted to consist of soft sediment. The downstream part of the central ridge is interpreted to consist of stiff sediment, the transition between both conditions appears as a sharp boundary (within 10 m). Bed roughness also maps this transition zone, where the bed changes from smooth, in the deforming bed area, to a rough bed (changes of ∼10 m high difference over a vertical distance of 40 m) in the basal sliding area (Smith & Murray, 2009). Subglacial landforms such as the Bump and the "new" drumlin (Figure 2.6) are interpreted to consist of soft sediment (Smith, 1997a,b; Smith & Murray, 2009; Smith *et al.*, 2007).

The spatial pattern of microseismicity along sticky spots supports the hypothesis of two different mechanisms (Kufner *et al.*, 2021; Smith, 2006; Smith *et al.*, 2015). More microseismicity is registered in areas consisting of stiff sediment, therefore enhanced friction, compared to the areas of soft sediment, and therefore lower friction (Anandakrishnan *et al.*, 1998; Boulton & Hindmarsh, 1987). Areas of soft sediment were described as seismologically quiet (Smith, 2006; Smith *et al.*, 2015). The observation of a weak correlation between tidally modulated surface flow velocity and microseismicity indicates that basal microseismicity is not primarily controlled by the tidal cycle (Adalgeirsdóttir *et al.*, 2008; Kufner *et al.*, 2021; Smith *et al.*, 2015). Kufner *et al.* (2021) concluded the main controls on microseismicity to be water content, topography and sediment stiffness. Furthermore, from variations in timing and spatial occurrence of microseismicity events, they interpreted three end-members of basal deformation to be responsible for the creation of event; (1) asperities within the subglacial sediment, which are built up by the glacier movement and then get destroyed once the shear stress of these asperities is overcome, which can be recorded as microseismicity, (2) ploughing of clasts while the ice moves over the bed and (3) flow oblique deformation which is linked to erosion and deposition of landforms and flow along outcropping bedrock.

2.3.1.2 Subglacial Water

In the onset region of RIS subglacial canals (<1 m depth, >1 km length, <200 m width) cut into the sedimentary bed were identified (King *et al.*, 2004). Down-
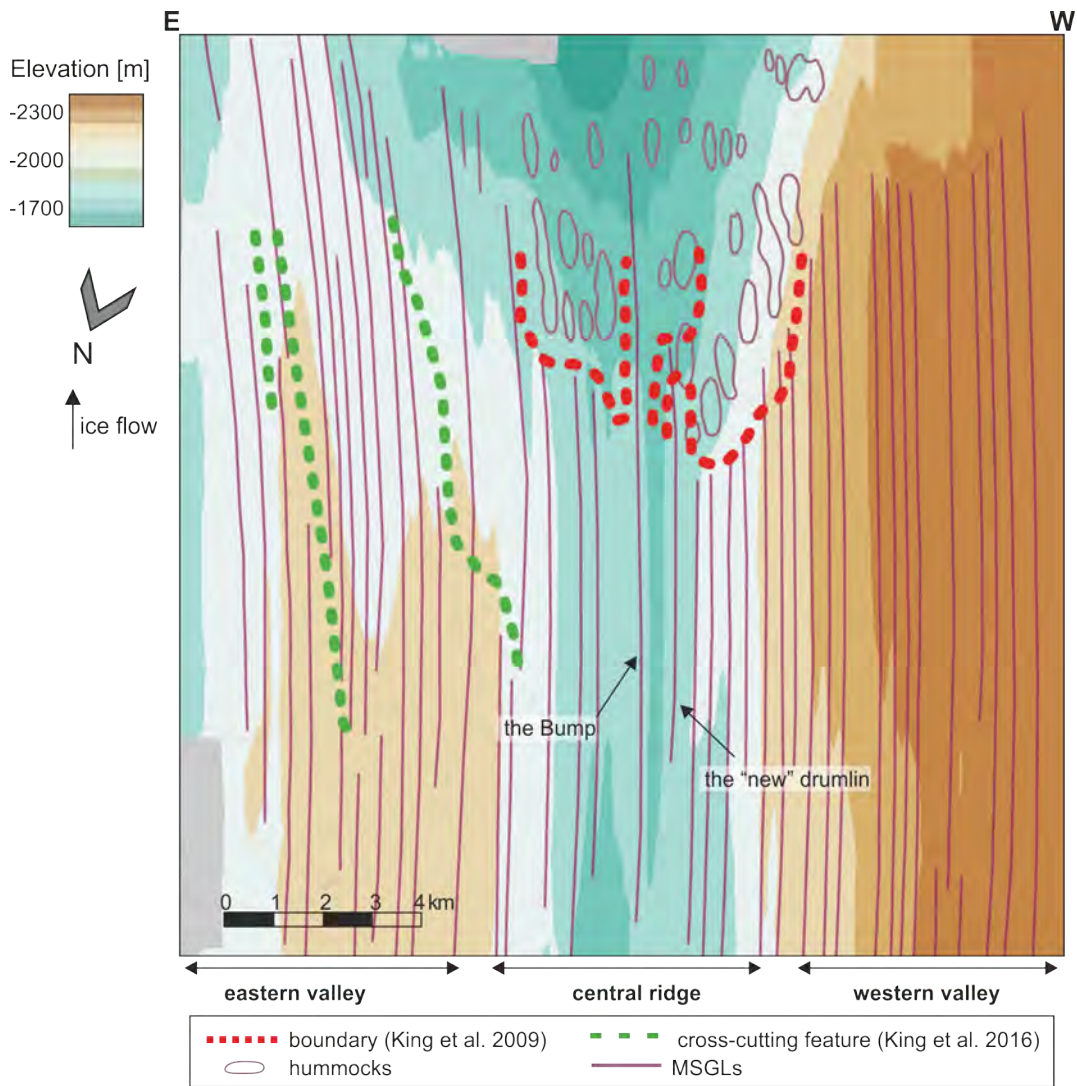
Figure 2.7: Landforms on the bed of RIS identified by King *et al.* (2016). The boundary separating soft and stiff sediment (King *et al.*, 2009) is marked by the red dashed line, features that cross-cut the topography are marked by the green dashed line.

stream, in the area of interest in this thesis, acoustic impedance is never sufficiently low to indicate the presence of liquid water. However, King *et al.* (2009) interpreted spatial variations in water content in the subglacial sediment to be linked to the sediment thickness. Furthermore, Murray *et al.* (2008) interpreted the existence of canals ($\sim$50 m width, $<$0.2 m depth, $\sim$5–10 km length) at the bed in areas of deforming sediment. They interpret areas of deforming sediment, where no water is present at the ice-sediment interface to be in intimate contact but without a distinct interface between sediment and ice.

2.3.2 Subglacial Landforms

King *et al.* (2016) developed a *digital elevation model* (DEM) including an ice thickness, bed topography and surface elevation grid with grid cell size of 10$\times$25 m that covers a 40$\times$18 km section of the fast-flowing part of the RIS. Different types of landforms have been described on the bed of RIS. The main forms described by King *et al.* (2016) included MSGL, tapering drumlins, small drumlins or hummocks and cross-cutting features (Figure 2.7). For this thesis, the landforms identified as tapering drumlins by King *et al.* (2016) are also referred to as MSGLs. King *et al.* (2016) referred to those as drumlins because they contain tapering ends and a higher vertical relief (lowest point of drumlin adjacent to highest point of drumlin). Nevertheless, the elongation ratio of these landforms supports a classification as MSGLs. Acoustic impedance surveys along and across subglacial landforms indicate that they consist of soft sediment (Smith, 1997a,b; Smith *et al.*, 2007).

In the upstream area and in the western valley MSGLs (purple lines) have a higher elongation ratio and are parallel sided (Figure 2.7). Downstream in the eastern valley MSGLs bend slightly eastwards (relative to the flow direction), and some of them are cross-cut by a feature (referred to as cross-cutting feature (green dashed line Figure 2.7)). In the downstream area of the central ridge, MSGLs terminate once the boundary (red dashed line) is reached. The area downstream of the boundary, the area of stiff sediment, lacks any significant MSGL but contains low amplitude features with small elongation ratios, referred to as hummocks (purple structures, King *et al.*, 2016).

The mean height of the landforms found in the study area is 22 m, the mean width is 267 m, and the mean separation (crest-to-crest) is $\sim$670 m. Smith & Murray (2009) pointed out that subglacial landforms in the area of stiff sediment

are shorter and shallower compared to areas of soft sediment. This is attributed to the difference in basal conditions (Engelhardt, 1998; Stokes, 2018). The minimum elongation ratio of the landforms reported for the area shown in Figure 2.7 ranges between 6–30, while further upstream, in the onset region of RIS, the elongation ratio of mounds is 1.5–4 (King *et al.*, 2007). This indicates an increase of elongation ratio towards downstream, which is consistent with interpretations of palaeo ice streams (Ó Cofaigh *et al.*, 2002, 2005; Shipp *et al.*, 1999; Wellner *et al.*, 2001).

Two subglacial landforms (locations marked in Figure 2.6 and 2.7) are described in more detail in the following:

- The Bump (named by Smith (1997b)) is up to 550 m wide and 53 m high (Smith, 1997b) and is at least 17 km long, resulting in a minimum elongation ratio of 30:1, which classifies the Bump as a MSGL (Clark, 1993; King *et al.*, 2009). The crest of the Bump has a ∼1° angle to the ice flow. It is not clear why the Bump as well as other mounds seen in this area are not aligned in the flow direction.

- The "new" drumlin was first described in Smith *et al.* (2007), and has a height of 20 m and a width of 100 m. Surface-radar data imply a length of approximately 7 km. The resulting elongation ratio classifies this landform as a MSGL.

Within this thesis, both the "new" drumlin and the Bump are referred to as MSGLs.

2.3.3 Temporal Variation at the Bed and Active Extension of a MSGL

Repeated seismic and radar surveys show that, on the one hand, in some areas the bed topography has changed within 5–10 years, even though ice flow has remained relatively stable and negligible surface lowering has been observed (Davies *et al.*, 2018). On the other hand, in other areas the bed topography seems to be constant (Smith *et al.*, 2007). Consecutive seismic surveys in the same area on RIS have been conducted in 1991, 1997 and 2004 (Figure 2.6). Between 1991 and 1997 6 m erosion of sediment was observed over a length of ∼500 m resulting in an

average erosion rate of $1 \, \mathrm{m \, a^{-1}}$ (Figure 2.6; Smith *et al.*, 2007). Following this erosion, a deposition of sediment took place over the following 7 years (1997–2004). The cessation of erosion was explained by either a lubrication of the bed or that stresses that caused the erosion have weakened. A mound (known as the "new" drumlin) was deposited in this area between 1997 and 2004. Smith *et al.* (2007) suggested the appearance of this mound in the seismic line could be due to the deposition of sediment during active formation of a drumlin, hence its naming as the "new" drumlin. However, subsequent radar surveys have demonstrated that the same feature extends significantly upstream of the repeatedly surveyed seismic line and therefore suggest the landform can be reclassified as a MSGL. This additionally opens up the question of whether the sediment "deposition" observed by Smith *et al.* (2007) represents the formation or the extension of the landform (Davies *et al.*, 2018). Within this thesis, the deposition is referred to as the latter.

2.4 Application of Radar Surveys to the Cryosphere

Ground-penetrating radar (GPR) and radar, in general, is a non-invasive geophysical technique, being highly portable and therefore suitable for imaging over large target areas. Radar surveys are well suited for application to various areas including sedimentology and geology (Davis & Annan, 1989; Grasmueck *et al.*, 2005), geotechnical engineering (Dussauge-Peisser *et al.*, 2003; Orlando, 2003), archaeology (Leucci & Negri, 2006; Neubauer *et al.*, 2002) as well as glaciology (Fukui *et al.*, 2008; Wang *et al.*, 2008). Although the instrumentation is widely portable, field effort is often governed by the complexity of the target subsurface. While simple subsurfaces can be accurately characterised using sparse radar profiles, more complex subsurface geometries require survey designs to be compliant with migration routines. Some glaciological studies use airborne radar (Ashmore & Bingham, 2014; Murray *et al.*, 2008), where several antennas are mounted on an aircraft, which enables surveying along great distances (e.g., Bedmap2 (Fretwell *et al.*, 2013) and Holschuh *et al.* (2020)). Other studies (e.g., Davies *et al.*, 2018; King *et al.*, 2009) use for instance, surface radar systems to acquire dense spaced lines, on one glacier or within one specific area. Figure 2.8 shows the surface-radar principle on ice. In this case, the system consist of two antennas, one for transmitting and one for receiving energy. During acquisition, the transmitter

antenna emits an EM wave of a certain bandwidth (depending on antenna characteristics), which propagates through the ice at a certain wave velocity. These EM waves get reflected at boundaries with different EM properties. The reflected wave can then be received by the receiver antenna. A radargram (Figure 2.8 b) represents the horizontal juxtaposition of traces therefore signals received in one position within different *two-way traveltime* (twtt). The y-axis of the radargram displays the twtt that it took the wave to travel from the transmitter back to the receiver. The x-axis shows the distance along the radar line travelled with the radar system on the surface while transmitting and receiving signals. The depth of the boundary in the subsurface can then be determined using the EM wave velocity in the corresponding medium. In the following, the EM wave propagation in different materials present in the cryosphere is introduced. This includes the EM velocities at which waves travel in typical material of the cryosphere, reflections and refractions at interfaces. Although the attenuation of energy travelling though different materials is an important factor for the propagation of EM waves, it will only be discussed very briefly here, and more details on the attenuation of energy in ice can be found in Section 4.3.1.2.2. Finally, the principle of migration is introduced.

2.4.1 Theoretical Values of EM Wave Velocity

The propagation of EM waves is described by Maxwell's equation, where the electric component is orthogonal to the magnetic. The propagation is strongly linked to the attenuation and the velocity of the waves in the medium, both of which are mainly dependent on the EM properties, therefore primarily the composition and water content of the material (Yilmaz, 2001).

The velocity v of EM waves in a material is defined as (Reynolds, 1997):

$$v = \frac{c}{\sqrt{(\epsilon_r \mu_r / 2) * ((1 + P^2) + 1)}}, \tag{2.1}$$

where c is the speed of light in a vacuum ($\sim 3 \times 10^8 \, \mathrm{m\,s^{-1}}$), ϵ_r the relative dielectric constant and μ_r the relative magnetic permeability. P is a loss factor, defined as $P = \frac{\sigma}{2\pi\epsilon f}$, where σ is the conductivity, f the frequency of the wavelet. The permittivity ϵ is defined as $\epsilon = \epsilon_r * \epsilon_0$, the latter describing the permittivity of a vacuum ($8.854 \times 10^{-12} \, \mathrm{F\,m^{-1}}$). Most materials are assumed to be non-magnetic, therefore $\mu_r = 1$. In this case, contrasts in dielectric properties are dominated by
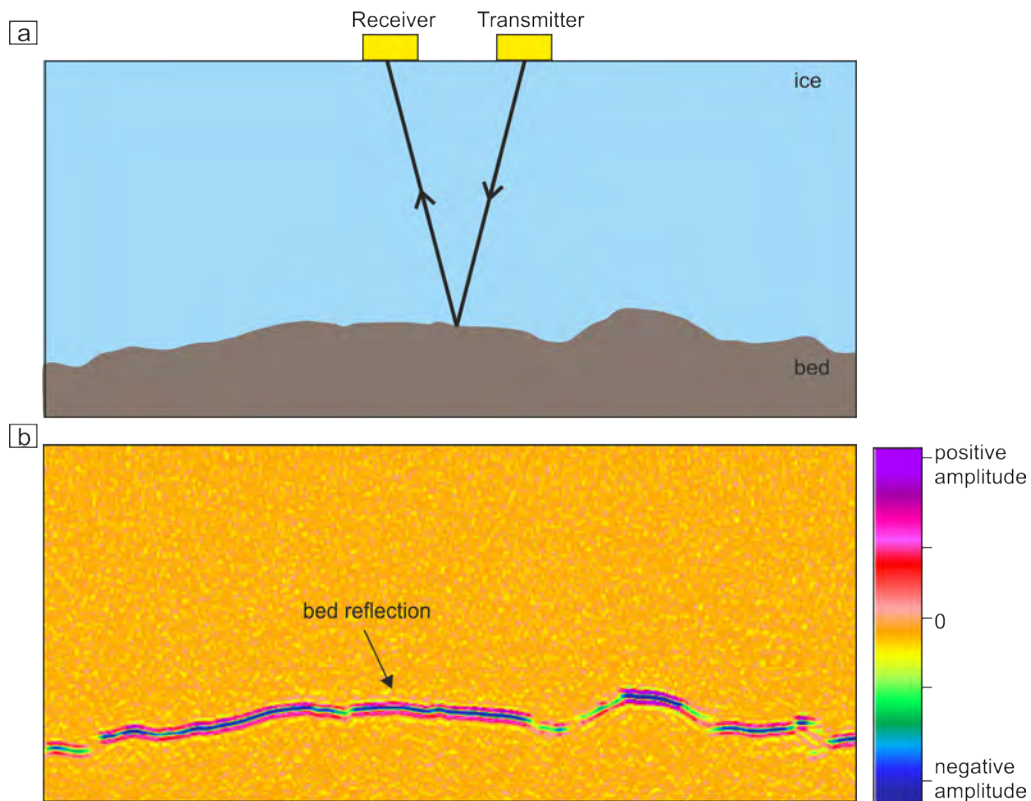
Figure 2.8: Principle of a radar survey. a) The radar system consists of a receiver and transmitter (displayed as yellow boxes). The transmitter antenna emits an EM wave which gets reflected at an interface. The reflected signal can then be recorded by the receiver antenna. The distance between transmitter and receiver compared to the ice thickness is not to scale in this image. Radar data in this thesis can be considered as zero-offset data (ice thickness >2 km, antenna separation ∼100 m (Section 3.1)). b) Radargram showing the bed reflection received from the subsurface shown in (a).

the conductivity and relative dielectric constant. Furthermore, Equation 2.1 is often simplified assuming a low loss material, therefore $P \approx 0$, resulting in the definition of the EM wave velocity as follows:

$$v = \frac{c}{\sqrt{\epsilon_r}}. \tag{2.2}$$

In the case of an ice stream, we assume the subsurface to consist of firn and ice, possibly some snow and subglacial material. Values for electromagnetic wave propagation velocity in ice are reported to vary depending on temperature, between 0.167–$0.168 \, \text{m ns}^{-1}$ (Bogodorosky *et al.*, 1985; Glen & Paren, 1975). Gascon *et al.* (2013) calculated firn velocities ranging from 0.225–$0.245 \, \text{m ns}^{-1}$ for densities from 475–$650 \, \text{kg m}^{-3}$. Eisen *et al.* (2002) compared velocities in firn from *common mid point* (CMP) measurements using different frequencies with velocities calculated from ice-core data. Velocities range from around 0.160–$0.225 \, \text{m ns}^{-1}$ for the shallow part of the firn column. Velocities in dry snow are reported to vary between 0.235–$0.237 \, \text{m ns}^{-1}$ (Heilig *et al.*, 2009). For the conversion of twtt to depth, e.g., for a bed reflection, the *root mean square* (RMS) velocity, taking into account the velocities of the individual layers (e.g., snow, firn, ice), needs to be calculated. The RMS-velocity v_{RMS} is defined as

$$v_{RMS}^2 = \frac{\sum_{i=1}^{N} v_i^2 * \Delta t_i}{\sum_{i=1}^{N} \Delta t_i}, \tag{2.3}$$

where v_i is the interval velocity and t_i is the twtt for the i-th layer (Lowrie, 2007). Within this thesis, twtt is converted to depth using a constant velocity of $0.168 \, \text{m ns}^{-1}$ (Bogodorosky *et al.*, 1985; King, 2020; Navarro & Eisen, 2009) unless otherwise stated.

2.4.2 Reflections and Refraction of EM Waves

Reflections and refractions of incident waves are caused by the contrast in EM properties between two layers. Dependent on how much the EM properties differ, the amount of EM energy reflected and refracted will change. The greater the difference, the more energy gets reflected at the interface. The proportion of energy being reflected at an interface is given by the reflection coefficient.

2.4.2.1 Reflection Coefficient

Under the assumption of waves incident at right angles to the plane reflector, the reflection coefficient can be calculated as (Reynolds, 1997):

$$R = \frac{v_u - v_l}{v_u + v_l} \tag{2.4}$$

where v_u and v_l are the EM velocity of the medium above and below the interface. Under the assumption of a low loss medium and a normal incidence reflection, the energy refracted equals 1-R and the reflection coefficient can be calculated as (Martinez & Byrnes, 2001):

$$R = \frac{\sqrt{\epsilon_{r_u}} - \sqrt{\epsilon_{r_l}}}{\sqrt{\epsilon_{r_u}} + \sqrt{\epsilon_{r_l}}} \tag{2.5}$$

where ϵ_{r_u} and ϵ_{r_l} are the relative dielectric permittivity above and below the interface, respectively. When studying the bed under a glacier or an ice stream, the upper material (therefore ϵ_{r_u}) represents ice (ϵ_{r_1}=3–4, (Martinez & Byrnes, 2001)), and the lower material (ϵ_{r_l}) represents the subglacial material. Relative dielectric permittivity values for wet sand (Figure 2.9) range from 25–30 (Davis & Annan, 1989) and for dry sand from 3–6 (Reynolds, 1997). Spatial variation in the properties above and below the interface can lead to a phase change of the reflection coefficient, and therefore, a phase change of the reflection in the radargram would be seen.
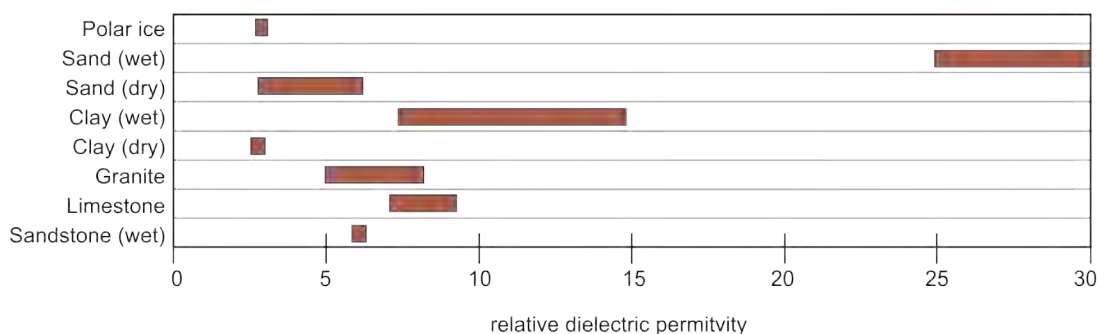
Figure 2.9: Bulk relative dielectric permittivity ϵ_r for different materials (values taken from Daniels (1996); Davis & Annan (1989); Martinez & Byrnes (2001); Reynolds (1997)).

2.4.2.2 Bulk Relative Dielectric Permittivity of Materials

The bulk relative dielectric permittivity of rocks and sediment depends on the individual relative dielectric permittivities of mineral grains and pore fluid, plus pore geometry and pore water fraction (Martinez & Byrnes, 2001), and there are different mixing models by which these elements are combined (Knoll, 1996; Martinez & Byrnes, 2001); however according to Martinez & Byrnes (2001) the most useful model for geologic materials is a volumetric model as used by Mount & Comas (2014), where the bulk relative dielectric permittivity can be calculated with varying porosity ϕ as:

$$\epsilon_r = \phi S_w \epsilon_{r(water)}^{\alpha} + (1 - \phi)\epsilon_{r(matrix)}^{\alpha} + \phi(1 - S_w)\epsilon_{r(ice)}^{\alpha}, \qquad (2.6)$$

where S_w is the fraction of water in the pore space, $\epsilon_{r(water)}$=80, $\epsilon_{r(ice)}$=3.19 ((Fujita *et al.*, 2006; Martinez & Byrnes, 2001)) and $\epsilon_{r(matrix)}$ is the relative dielectric permittivity of pore water, ice and matrix. The geometric factor α relates to the orientation of the electrical field compared to the layering of the material. Following Mount & Comas (2014) and West *et al.* (2003) α=0.5 is adopted in this thesis. The original equation is based on sediment, with a mixture of water and air in the pore space. In a subglacial environment, we assume the water-saturation to be 100%, meaning no air is present in the pore space, which is why S_w=1, therefore the last term of Equation 2.6 can be ignored. Using this mixing model proposed by Mount & Comas (2014), solely variations in porosity and different matrix compositions can be considered while neglecting effects such as mixture of minerals in the matrix, geometry of grains and pore space and grain contacts.

2.4.2.3 Angle of Reflection and Refraction

The angle at which a wave gets reflected or refracted at an interface is described by Snell's law (Figure 2.10). For a reflected wave, the angle of incidence (θ_i) equals the angle of reflection θ_{r1} (Reynolds, 1997), whereas the direction of propagation will change if energy gets refracted at an interface. The relation between incidence angle θ_i and the refraction angle θ_{r2} as well as the velocity of the upper (v_u) and lower medium (v_l) is illustrated in Figure 2.10 and can be described as:

$$\frac{\sin(\theta_i)}{\sin(\theta_{r2})} = \frac{v_u}{v_l} \qquad (2.7)$$

In the case of $v_l > v_u$ (Figure 2.10 a), the wave is refracted away from the normal to the interface, therefore $\theta_{r2} < \theta_i$ and vice versa in case $v_l < v_u$ (Figure 2.10 b).
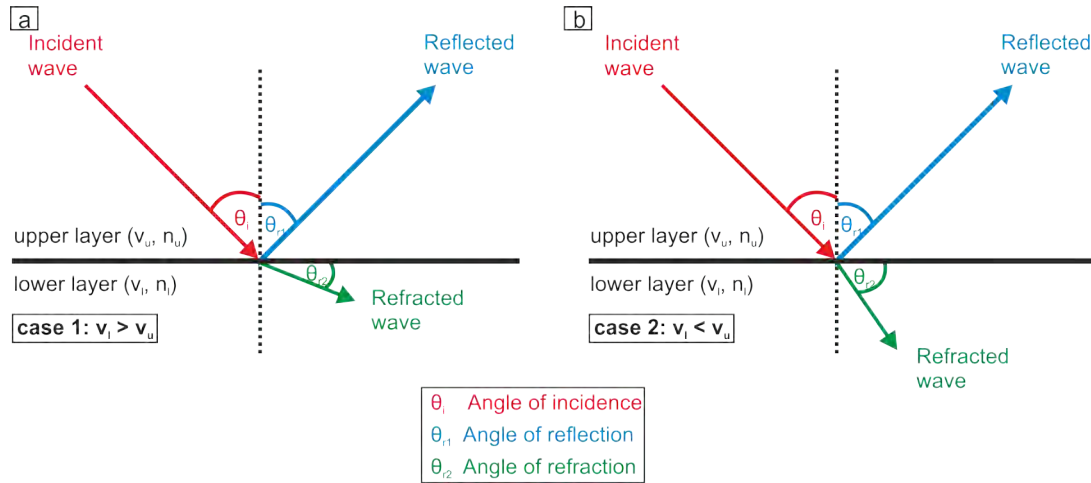
Figure 2.10: Snells law. a) Case 1 with EM velocity of the upper medium being greater than the velocity of the lower medium, b) case 2 vice versa (modified after Kearey *et al.*, 2002).

2.4.3 Energy Loss During Wave Propagation and Attenuation of EM Waves

The waves emitted by the transmitter lose energy while propagating through the medium due to various reasons. The reduction of energy transmitted is referred to as attenuation and is a combination of different factors. Some of which are listed below and are discussed in more detail in Section 4.3.1:

- reflection and refraction of energy at interfaces

- absorption (transformation of EM energy into heat), often (and within this thesis) referred to as englacial attenuation

- geometric spreading

- coupling effects between the radar antennas and the surface

- system parameters

- scattering
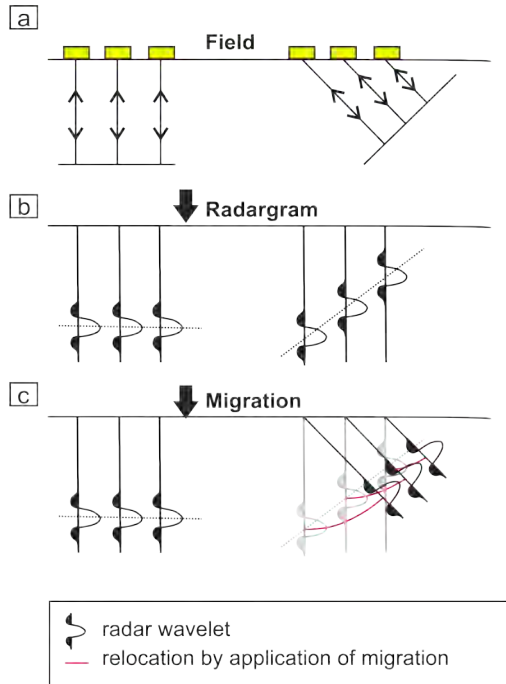
Figure 2.11: Principle of migration. a) Schematic of the subsurface and the ray path reflected at different dips, b) schematic of positioning of unmigrated radar data vertically underneath the radar system, c) relocation of signals received from dipping reflectors. The radar data are considered to be zero-offset, therefore the system is illustrated as one yellow box (graph modified after Astratti *et al.*, 2015).

The attenuation is considered as the general cause of energy loss while waves propagate. The so-called attenuation factor, which is dependent on electric, magnetic and dielectric properties of the medium as well as the frequency of the wavelet, can be used to make assumptions about the so-called skin depth, which is the depth by which the signal amplitude has decreased to 37% ($\frac{1}{e}$). For instance, the skin depth of water is $1\,\mathrm{cm}$, for wet clay $0.2\,\mathrm{m}$, whereas the skin depth is higher for dry rocks. Polar ice is often described as virtually transparent to radar waves, while water-saturated clay and seawater absorb or reflect the energy, so that no further energy can be received from underneath that material.

2.4.4 Migration

2.4.4.1 Rationale of Migration

Migration is the process of focussing energy to its true origin. The main goal of applying migration to radar data is to make the radargram look similar to the

geologic cross-section in depth along the radar line (Jones, 2014). Figure 2.11 illustrates the migration principle by comparing ray paths reflected at a plane and dipping reflector. In an unmigrated radargram (Figure 2.11 b) the reflection is assumed to be originated from directly underneath the radar system. However, although this is true for the left part of Figure 2.11, where the waves get reflected off a horizontal surface, in the right part, waves reflect at a dipping surface. The application of migration relocates the reflections of a dipping surface to their true subsurface position (red lines in Figure 2.11 c; Jones, 2014; Yilmaz, 2001). Not only are reflectors in the subsurface repositioned in the right horizontal location, but the true vertical positions are found. This can be illustrated considering a dipping surface as seen in Figure 2.12. In an unmigrated dataset, the reflection is initially located underneath the radar system (red dots). However, the energy recorded at this certain twtt could originate from any point along the semi circle (black semi circle) centred on the radar system. The reconstructed true location of the surface lies in the up-dip direction. Therefore, the horizontal and vertical location (in depth) of the surface, hence the resulting dip of the surface differs in pre- (red circles and red dashed line) and post migrated (black circles and black dashed line) data. As a result, migration steepens and shortens reflectors and moves reflectors in the up-dip direction (Kearey *et al.*, 2002; Yilmaz, 2001). In some cases, the reflection recorded might originate from locations outside the radar line. The effects of dipping reflectors have to be taken into account when planning the line length, as structures below the radar lines may not be recorded along the line, if the length is not sufficient. The same holds for the recording length (listening time). Further details on how to acquire data compliant with migration are given in Section 3.3.2.

Figure 2.12 considers only linear reflectors. Signals received from curved reflecting interfaces are more complex. Synclinal structures in the subsurface, for instance, appear as bow-ties on an unmigrated radargram. Further information can be found in Yilmaz (2001). Aside from relocating reflected energy at a dipping surface, the application of migration improves the *signal-to-noise ratio* (SNR) by focussing energy diffracted at point reflectors and faulted beds as well as collapsing the Fresnel zone, therefore focussing energy scattered over the Fresnel zone (Kearey *et al.*, 2002). In the following, different migration approaches are introduced, followed by an in depth explanation of the Kirchhoff migration, which was
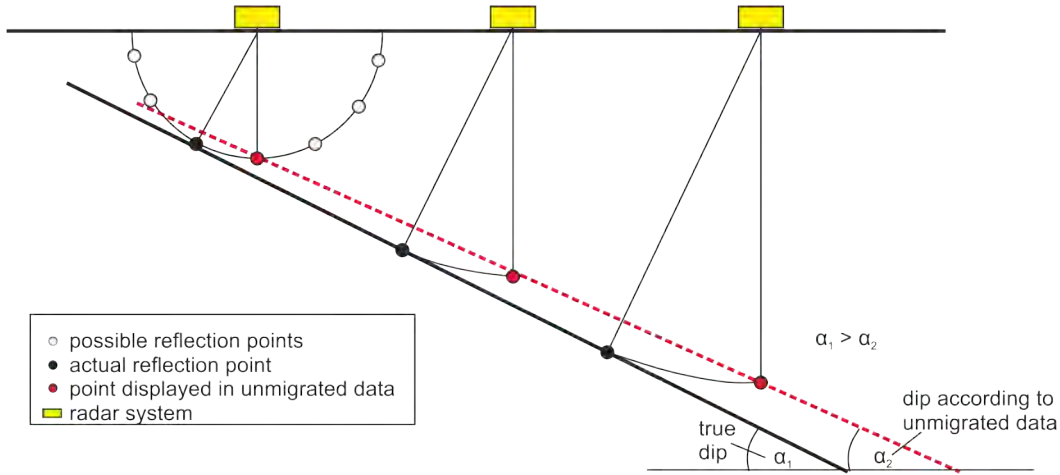
Figure 2.12: Relocation of signals received from a dipping reflector. The signal with a certain twtt can originate from anywhere along the white semicircle. Small black circles along the semi circle illustrate examples of possible positions. The red dots mark the position directly underneath the radar system (as seen in unmigrated data). The black dots mark the actual reflection position along the dipping reflector. The red dashed and black solid line represent the corresponding dip of the reflector in unmigrated and migrated data. The latter corresponds to the true dip (modified after Kearey *et al.*, 2002).

used as migration technique in this thesis. Finally, a brief introduction to 3D migration is presented.

2.4.4.2 Migration Algorithms

During the application of migration, any signal in a radargram will be treated as originating from the reflection of energy at an interface. Migration is not able to relocate energy recorded from multiple reflections, converted waves, surface waves or noise (Yilmaz, 2001). Depending on the input data and the desired outcome of the migration, different algorithms can be applied to the data. The following migration strategies are differentiated according to Yilmaz (2001)

- 2D vs. 3D migration: The difference between 2D and 3D migration are discussed in more detail in Section 2.4.4.4.

- post- vs. prestack migration: Radar data presented in this thesis, and most radar data in the cryosphere in general can be considered as zero-offset data, which means the receiver and transmitter antenna are considered to be at the same location, and the recorded energy follows raypaths that are

at normal incidence to the reflector. Comparison of the distance between the two radar antennas (for data in this thesis 110 m) and the depth of the bed reflection under an ice stream (here ≈2.2 km), validate the assumption of nearly zero-offset data. A radargram of zero-offset data is comparable to a stacked seismic section. Therefore, only poststack migration algorithms can be applied to radar data.

- time vs. depth migration: The application of time migration is appropriate as long as lateral velocity variations are moderate. If the lateral velocity gradient is significant, time migration does not produce an accurate image of the subsurface. Therefore the application of depth migration would be necessary. However, the velocity to convert data from the time domain to the depth domain is based on velocity estimations obtained from the radar data. This dependency limits the accuracy of the velocity, and therefore might have an influence on the spatial position of amplitudes. For data with low or moderate lateral velocity variations, the migration should be applied in the time domain.

According to Yilmaz (2001) the 2D/3D poststack time migration is most often used in seismic data processing. Different algorithms have been developed over time. In general, two different migration techniques are differentiated (Jones, 2014): the ray-based migration, such as Kirchhoff and Beam migration (Gray, 2004; Popov, 1982; Schneider, 1978) and the *Wave Field Extrapolation Migration* (WEM) (Hale, 1990). Kirchhoff migration is an integral solution of the wave equation, while WEM is a differential solution of the wave equation. During WEM the wavefield emitted by the transmitter and received from the receiver is calculated, at the same time the recorded wavelets are back propagated from their surface receiver position (Jones, 2014). Data presented in this thesis were processed with the Poststack Kirchhoff Time Migration technique, as lateral velocity variations in the subsurface are negligible. The following section therefore solely focuses on this technique. For a more thorough review of different migration techniques see Yilmaz (2001).

2.4.4.3   Principle of Kirchhoff Time Migration

An interface in the subsurface (black line in Figure 2.13 a) can also be considered as a sequence of points (red dots in Figure 2.13 a). Each of these points creates a
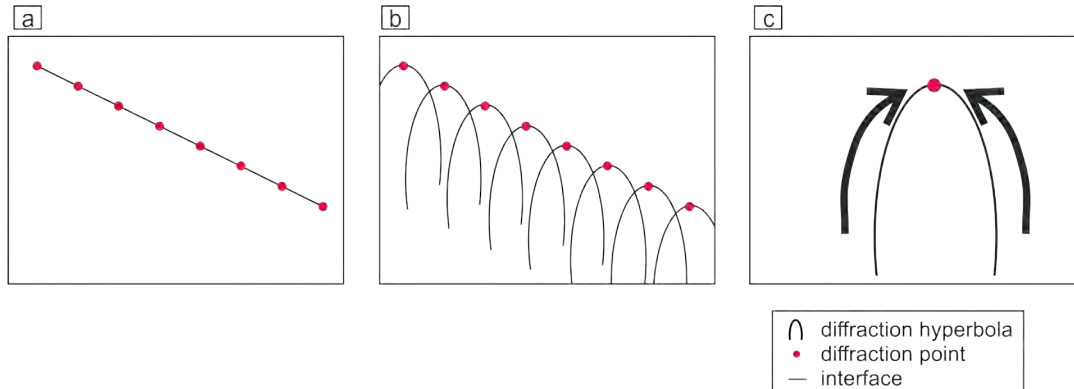
Figure 2.13: Principle of point diffractions and diffraction summation: a) An interface (black line) can be considered as a sequence of points (red dots). b) Each of these points is visible as a diffraction hyperbola in the radargram. c) Migration sums the amplitudes along the diffraction trajectory and locates the resulting amplitude on the apex of the hyperbola.

diffraction hyperbola (Figure 2.13 b) in the radargram. Kirchhoff time migration reverses this process and treats each point in the subsurface as a possible diffraction point producing a diffraction. Summation of amplitudes along the diffraction twtt trajectory reconstructs the location of the diffraction point (Figure 2.13 c). The Kirchhoff time migration is based on the Kirchhoff summation technique, which was first introduced by Schneider (1978) and is very similar to the method of diffraction summation (Yilmaz, 2001).

2.4.4.3.1 Diffraction Summation: The diffraction summation is based on the summation of amplitudes along the diffraction twtt trajectory. During the migration the algorithm searches through data in a radargram for energy that would have diffracted at any point located in the subsurface. The principle of amplitude summation is shown in Figure 2.14 and is described in the following:

a) Definition of the summation window: Migration is based on the assumption of a known RMS velocity (v_{RMS}) at any point in the subsurface. The summation window, which defines the hyperbolic twtt trajectory, can be calculated as:

$$t^2 = \tau^2 + \frac{4x^2}{v_{RMS}^2} \tag{2.8}$$

where t is the twtt, τ the output time at the apex of the hyperbola, therefore the twtt it would take a wave to travel the vertical distance between the

apex of the hyperbola to the surface on the vertical path, and x is the horizontal distance at the surface between the apex of the hyperbola and the location of the receiver (see Figure 2.14 a).

b) The apex of a hyperbolic twtt trajectory is placed at any location in the radargram (which represent a possible diffraction point).

c) Each sample (containing the amplitude) within the limits of the hyperbolic twtt trajectory is extracted.

d) All extracted amplitudes are summed up and the resulting amplitude is placed at the apex of the hyperbolic twtt trajectory.

This process is then repeated for the other positions in the radargram.

2.4.4.3.2 Diffraction Summation vs. Kirchhoff Summation: The Kirchhoff summation is a diffraction summation which incorporates the obliquity factor, effects of geometric spreading and the shaping factor of the wavelet. The obliquity factor describes the angle dependency of amplitudes, geometric spreading the distance dependency of amplitudes, both of which should be corrected for prior to the application of migration. The wavelet shaping factor involves the phase and frequency of the resulting waveform, to enable cancellation of amplitudes during summation.

2.4.4.3.3 Definition of a Migration Aperture: In theory, the diffraction hyperbola extends infinitely in time and space. However, in practice the hyperbolic twtt trajectory (therefore the summation window) needs to be spatially limited for computation time and cost reasons, but also to avoid the incorporation of low SNR data, which might be present with increasing twtt. The range of the summation window is called the migration aperture, while the aperture width describes the number of traces incorporated into the migration.

The curvature of the diffraction hyperbola is velocity dependent. Generally speaking a low-velocity diffraction hyperbola trajectory spans a narrower aperture when compared to a high-velocity diffraction hyperbola trajectory. Depending on the composition of the subsurface, the RMS velocity varies with depth, and the migration aperture is therefore time variant. A smaller aperture incorporates less data than a larger aperture in the summation process. If too small an aperture is
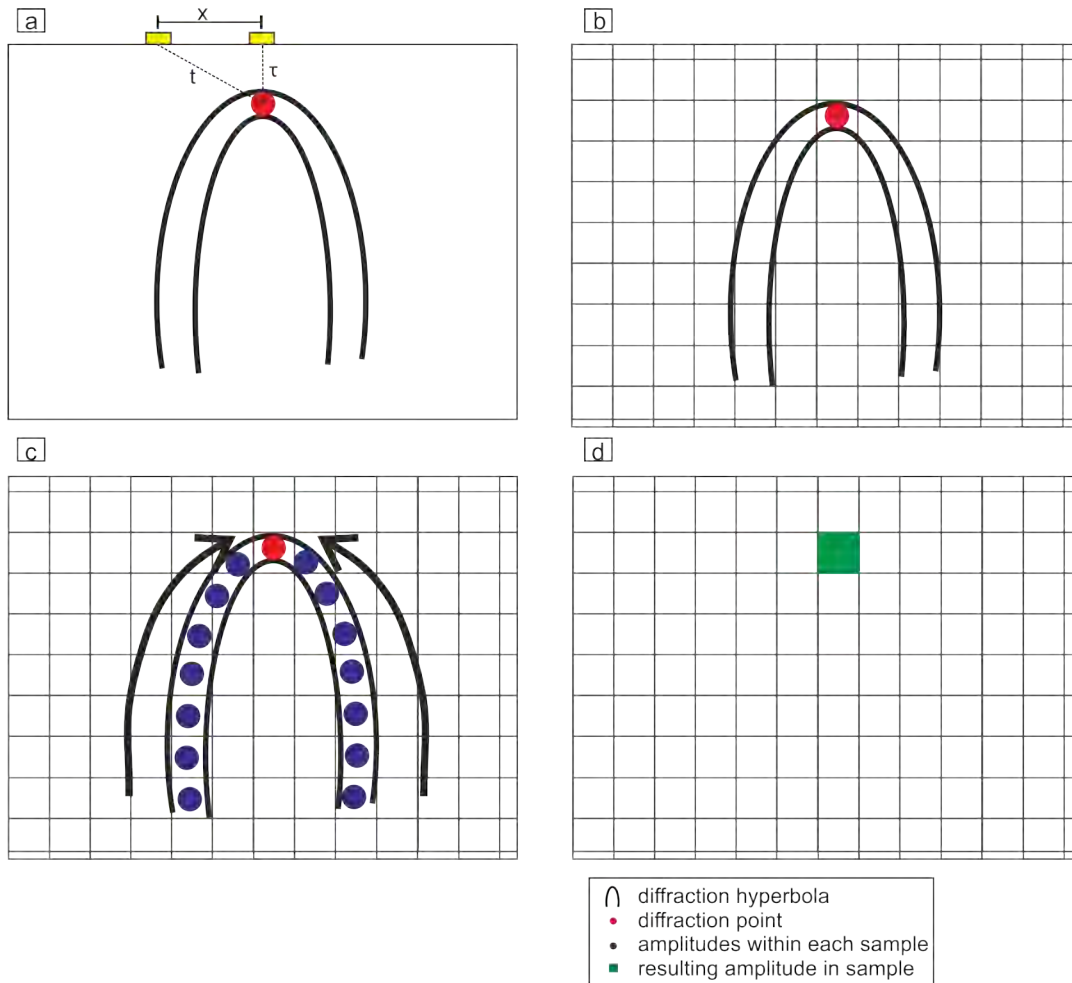
Figure 2.14: Principle of summation of amplitudes: a) Definition of the summation window, the hyperbolic twtt trajectory, b) the apex of this hyperbolic twtt trajectory is then located at any possible location in the grid, c) amplitudes within the hyperbolic twtt trajectory are extracted and summed up, d) the resulting amplitude is then the assigned to the sample, where the apex of the hyperbola was originally located.

chosen the capability of the migration to collapse diffraction hyperbolas decreases. Furthermore, choosing too narrow an aperture excludes the steeper flanks of the diffraction hyperbola originating from steeply dipping events. As a result, steep dips are not properly imaged in the migrated radargram. Important parameters for the Kirchhoff migration are the aperture used for the summation as well as the maximum dip migrated.

2.4.4.3.4 **Migration Velocity:** The accuracy of the repositioning of energy after migration is strongly dependent on the migration algorithm and the migration velocity. Under the assumption of a horizontally layered medium, the RMS velocity (see Section 2.4.1) at the apex of the hyperbola is used to calculate the hyperbolic twtt trajectory. Figure 2.15 illustrates the effect of different migration velocities on a migrated hyperbola. The migration hyperbola is collapsed (b) into a point at the apex of the hyperbola, migrating data with an adequate velocity. If the migration velocity is too low, the diffraction hyperbola is not entirely collapsed, which is known as undermigrated (Figure 2.15 c). A so-called migration frown is visible. Vice versa applies if the migration velocity is chosen too high. The diffraction hyperbola is inverted, which is known as overmigrated (Figure 2.15 d). A so-called migration smile is visible.
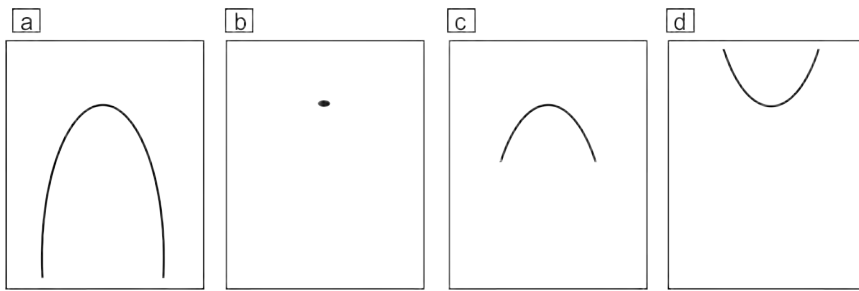
Figure 2.15: Effects of different migration velocities: a) unmigrated data, b) migrated data with correct migration velocity, c) data migrated with too low migration velocity, a migration frown appears d) data migrated with too high migration velocity, a migration smile appears (modified after Yilmaz, 2001).

2.4.4.4 **3D Migration**

Depending on the complexity of the target, the design of the survey might be motivated to acquire a series of 2D profiles, which are capable of being arranged in a 3D data cube (Grasmueck *et al.*, 2005), on which 3D migration routines can be applied. This is a known procedure in archaeological studies. 3D migration is used to focus diffracted energy back to the true origin in a 3D space. Many studies in glaciology apply 2D migration to data (e.g., Church *et al.*, 2018; Murray *et al.*, 2008; Riverman *et al.*, 2019)), which can probably be attributed to the rare acquisition of data compliant with 3D migration. The key considerations for acquiring data compliant with 3D migration are discussed in Section 3.3.2.2. Survey lines are often coarsely spaced, impeding the creation of a 3D data cube, therefore the
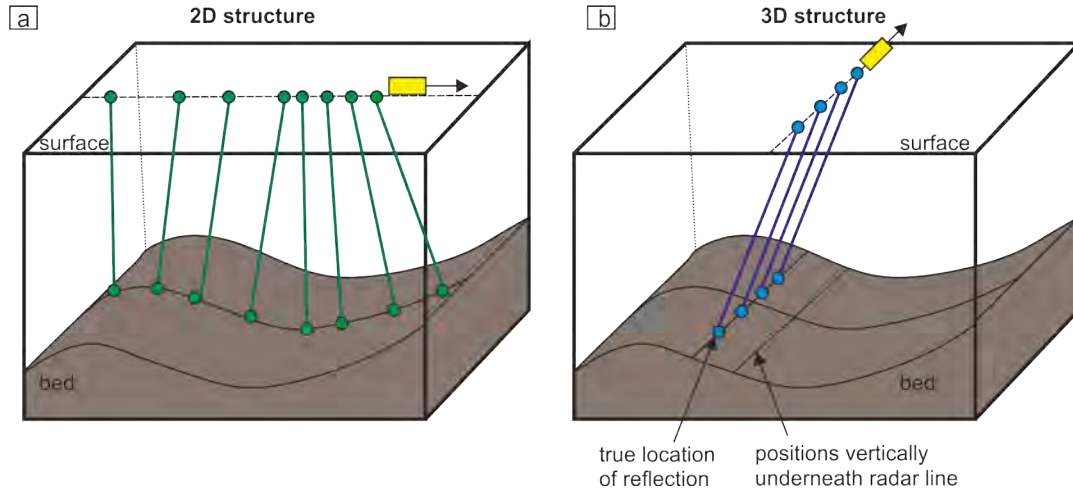
Figure 2.16: Ray path of energy reflected at an interface (e.g., glacier bed) dipping in the acquisition direction (a) and dipping in another direction to acquisition (b). If data are migrated in 2D, then only data reflected at an interface dipping in the acquisition direction can be relocated. For interfaces dipping in any other direction, than the acquisition direction the acquisition of a 3D dataset and the application of 3D migration are necessary to reconstruct the subsurface (modified after Alsadi, 2017).

application of 3D migration. Furthermore, ice stream and glacier beds are often found to be aligned in ice flow direction, representing a 2D structure (e.g., structures varying only in cross-flow direction, comparable to Figure 2.16 a). In this case a 2D migration of the data can reconstruct the topography, as long as the acquisition direction is perpendicular to the ice flow. Figure 2.16 a shows a surface dipping in acquisition direction. As the energy is received from underneath the radar line (black dashed line) the energy can be relocated to the true origin. Energy received from a reflection of a surface dipping in any other direction (Figure 2.16 b) will not originate from underneath the radar line. 2D migration would not be able to relocate the energy to the true position but position it somewhere vertically underneath the radar line. Therefore, information and detail will be lost, once the topography changes along flow, or the data acquisition is not perpendicular to ice flow. In this case, the 3D migration is crucial to reconstruct the real position of features in a 3D space. Furthermore, Grasmueck et al. (2005) highlight the importance of 3D migration on densely spaced, un-aliased data for full-resolution imaging of the subsurface with a sub-wavelength resolution. The Kirchhoff Time Migration follows the same principle in 2D and 3D, with the difference that the summation window is generated by a twtt trajectory in the shape

of a hyperboloid (3D) rather than a hyperbola (2D), performing the summation in 3D.

2.5 Summary

Ice flow is largely dependent on basal properties (Joughin *et al.*, 2009; Pollard & DeConto, 2012; Ritz *et al.*, 2015). Basal motion can occur by a combination of basal sliding and basal deformation (Benn & Evans, 2011; Cuffey & Paterson, 2010). Which of these processes dominates is dependent on basal properties, such as sediment stiffness. Basal properties are shown to vary in space and in time, with the latter attributed to temporal variation in water pressure (Piotrowski *et al.*, 2004; Smith *et al.*, 2007).

Drumlins and MSGLs are indicative of fast ice flow (Clark, 1993), and are interpreted to be a part of a continuum, while the difference in length represents an increase in ice flow velocity between areas of drumlins and areas of MSGLs. This increase in velocity towards downstream is often accompanied by a change from a crystalline basement to sedimentary bed (e.g., Ely *et al.*, 2016; King *et al.*, 2009; Spagnolo *et al.*, 2014; Stokes *et al.*, 2013).

Rutford Ice Stream, which is subject of this study, is a fast-flowing ice stream in West Antarctica (Doake *et al.*, 2001). The bed is characterised by areas of low and high porosity material, which are interpreted to be dominated by basal sliding and basal deformation, respectively (King *et al.*, 2009; Smith, 1997b; Smith *et al.*, 2007). Repeated survey lines have revealed temporal variation in bed topography and properties (Smith & Murray, 2009; Smith *et al.*, 2007). Furthermore, the bed comprises numerous MSGLs (King *et al.*, 2009), while the active extension of one of these landforms has been observed over a 7 year period (Smith *et al.*, 2007).

Finally, this chapter introduced the principles of radar surveys. Radar surveys are based on the response of EM waves to the subsurface, which are sensitive to variations in EM parameters of the material, especially the dielectric constant and electric conductivity (Davis & Annan, 1989). The recorded signal can then be used to reconstruct the topography along the interface. However, to reconstruct the true dip and depth of the interface, the application of migration to radar data is necessary. Depending on the geometry of the interface, migration should be applied in 2D or 3D (Grasmueck *et al.*, 2005).

Chapter 3

Data Summary and Field Methods

Within this chapter, the *Deep Look Radio Echo Sounder* (DELORES) radar system (Section 3.1) as well as the previously acquired data used in this thesis are introduced (Section 3.2). This is followed by a brief introduction to the aims of the field survey undertaken in 2017/18 (Section 3.3.1) as well as some theoretical constraints that were considered when planning the survey (Section 3.3.2). Following this, the data acquisition and difficulties during the acquisition, that will influence the processing of the data, are described (Section 3.3.3). Finally, a summary of the pre-processing and the migration of the data acquired in 2017/18 is given (Section 3.3.4.3).

3.1 DELORES System

Surface-based radar data (or simply radar data) described within this thesis have been acquired using the *British Antarctic Survey* (BAS)'s *Deep Look Radio Echo Sounder* (DELORES) system, a monopulse radar capable of operating in the 1–20 MHz range (King *et al.*, 2007). This is an in-house development, based on designs by the University of Washington (Gades, 1998) and St. Olaf College (Welch & Jacobel, 2003). The transmitter (Figure 3.1) comprises a Kentech pulse generator, which fires a ± 2500 V pulse at a repetition rate of 1 kHz into the antennas (King *et al.*, 2007, 2016). The antennas (identical for transmitter and receiver) consist of resistively loaded wire dipoles. The receiver antenna pair is connected to a digital oscilloscope (a chassis computer with a 250 MHz digitising
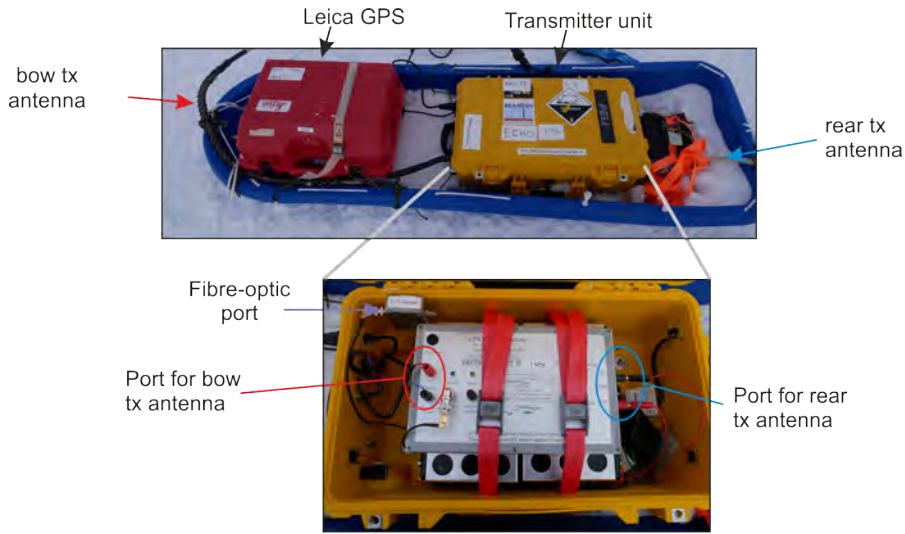
Figure 3.1: Transmitter sledge (tx = transmitter): with a GPS (red box) and the transmitter-unit (yellow box). Rear and bow transmitter antennas are plugged into the transmitter unit. To minimise the risk of the antennas getting detached due to movement, they have additionally been attached to the sledge. The batteries attached to the right side of the transmitter-box are used to run the GPS, which is attached left of the transmitter-box.

card) via a balun and an amplifier (Figure 3.2). The oscilloscope in the receiver and therefore the recording can be either trigged using a fibre optic cable or the recorded airwave arrival.

All DELORES data presented here were acquired with a half-dipole antenna length of 20 m, resulting in a centre frequency of around 3 MHz (King *et al.*, 2016). The lateral separation between the centre of the transmitter and receiver antennas is around 103 m. To achieve accurate positioning the system was equipped with a dual-frequency GPS receiver (Figure 3.3) mounted on a sledge at the mid-point between the antennas.
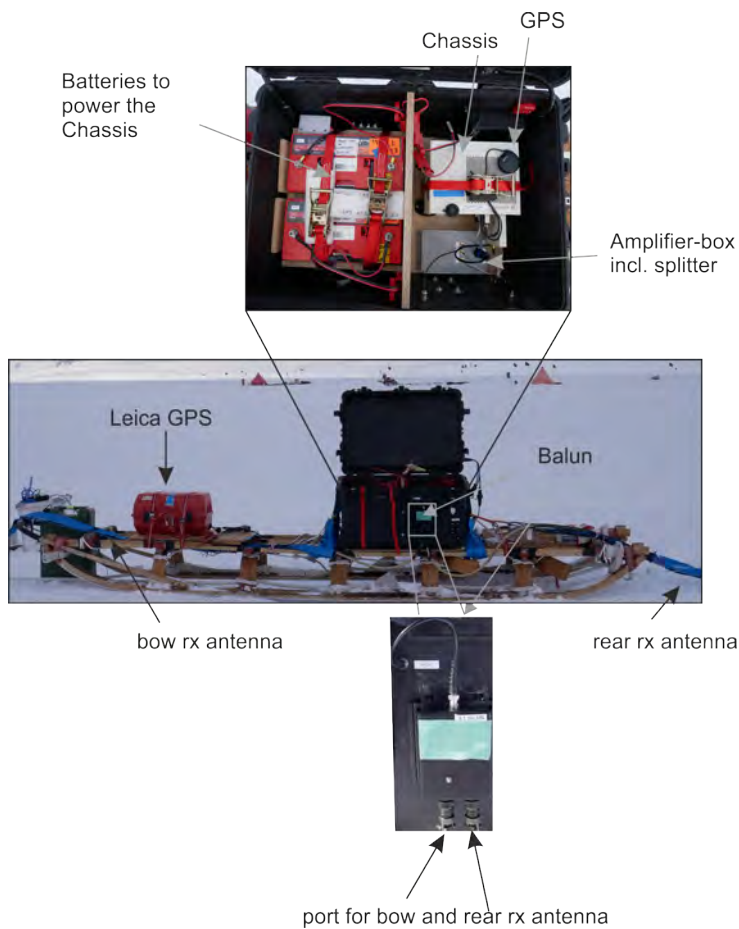
Figure 3.2: Receiver sledge (rx = receiver): the wooden sledge carries one GPS (red box) as well as the balun, splitter and chassis. The receiver-antennas are plugged into ports on the black Peli-case. To enhance stability, the antennas have also been attached to the wooden sledge.

Figure 3.3: GPS sledge including Leica GPS and solar panel, which was attached between the transmitter and receiver sledge.

3.2 Previously Acquired Data

In 2007/08 DELORES data were acquired from central RIS (location Figure 2.4) in a 40×18 km grid. Based on this dataset, a high-resolution DEM was created and published by King *et al.* (2016). In 2016/17 the upstream portion of this grid (covering an area of 14.5×18 km) was repeated, with a focus on acquiring the grid using the same geometry, so that individual lines could be compared over the 9 year time gap. Within this thesis, only the part of the data acquired in 2007/08 that was repeated in 2016/17, is considered (resulting area of interest = 14.5×18 km). Radar lines were acquired orthogonal to ice flow direction, with a line spacing of 500 m (Figure 3.4). The numbering of the radar lines within this thesis was chosen to be consistent with data acquired in 2016/17, decreasing in the flow direction, starting with line 1031 in the upstream end of the grid, and line 1001 in the downstream end of the grid (for original numbering of lines of 2007/08 data see Table 10.1 in the Appendix). Two lines were not acquired identically during the two years: line 1030 is missing in 2016/17 and line 1027 was not acquired continuously in 2007/08, while in 2016/17 line 1027 was not acquired along the same location but 250 m upstream and downstream of the original track. As far as possible, and to ensure comparability between successive surveys, the DELORES system was kept largely unchanged, but small exceptions are noted in Table 3.1. In 2007/08 1000 signals and in 2016/17 256 signals were stacked to form one recorded trace in the oscilloscope buffer in order to improve the SNR. In both surveys the radar equipment was towed behind a snowmobile travelling at around $12 \, \text{km} \, \text{h}^{-1}$, resulting in a trace recorded over a distance of 3 m for data acquired in 2007/08 and 1 m for data acquired in 2016/17. This introduces a small amount of lateral smear into the recording, but this is small compared to the radar wavelength (∼56 m).

Table 3.1: Differences in system set-up during field survey in 2007/08 and 2016/17.

	2007/08	**2016/17**
trigger	fibre optic	airwave
GPS units mounted on	receiver	midpoint between receiver & transmitter
number of signals stacked	1000	256
resulting sampling along track [m]	3	1
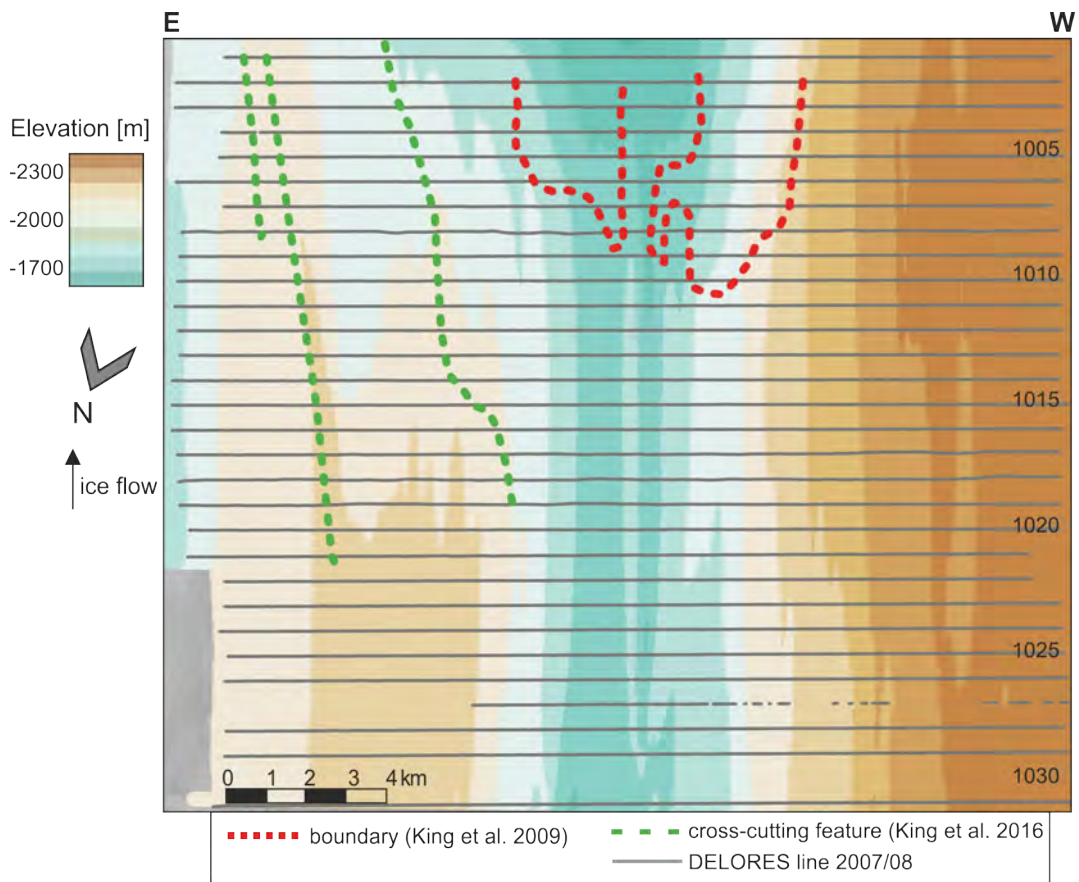
Figure 3.4: Bed elevation referenced to the WGS84 ellipsoid in the study area with geometry of field season 2007/08 (grey lines). Numbers on the right side represent the line numbering.

3.2.1 Processing of Previously Acquired Data

Radar datasets were processed by Ed King (BAS) for the 2007/08 dataset and Alex Brisbourne (BAS) for the 2016/17 dataset, both using using ReflexW (Sandmeier Scientific Software). The processing flow between the two datasets is similar (Figure 3.5), including geometry assignment, removal of the airwave and pre-trigger samples, bandpass filter, stacking as well as 2D filters to improve the SNR and amplitude correction to compensate for geometric spreading. However, some of the parameters chosen for the sampling interval and bandpass filters differ between the two datasets. The final processing step in both datasets is the migration of the signal to focus diffracted energy and reposition any energy arriving at non-vertical incidence at its correct subsurface location. For this, a finite-difference (FD) migration was chosen, with a migration velocity of $0.168\,\mathrm{m\,ns^{-1}}$ and a centre frequency of $3\,\mathrm{MHz}$ (Figure 3.6).

The main difference between the two datasets is the time sampling interval and along track sampling. However, this only affects results in Chapter 6, where these datasets are compared.

Both datasets were acquired perpendicular to ice flow, therefore the spatial sampling perpendicular to ice flow is higher (1 or $3\,\mathrm{m}$, respectively), compared to in flow direction, where lines are $500\,\mathrm{m}$ apart. The vertical resolution along track after migration is often considered to be equal to one quarter of the wavelength (Lindsey, 1989), in this case, $14\,\mathrm{m}$ (velocity in ice $0.168\,\mathrm{m\,ns^{-1}}$ and centre frequency of $3\,\mathrm{MHz}$). Spatial correlation of traces along one line is very high in both datasets (as seen in the radargram in Figure 4.2). King *et al.* (2016) described the data acquired in 2007/08 and converted to bed elevation to have a vertical precision of $\pm3\,\mathrm{m}$ (uncertainty accounting for variations in wave velocity, GPS positioning and limiting factors of the system). Considering the similarity of the two systems and the improvement of technology within 9 years (e.g. digitiser card of the chassis has been replaced) the precision of the data acquired in 2016/17 can be assumed to be similar, possibly even improved over time. The time sampling of both datasets was chosen to be well within the range of precision stated by King *et al.* (2016) (8 and $10\,\mathrm{ns}$, therefore, 0.6 and $0.8\,\mathrm{m}$, respectively).
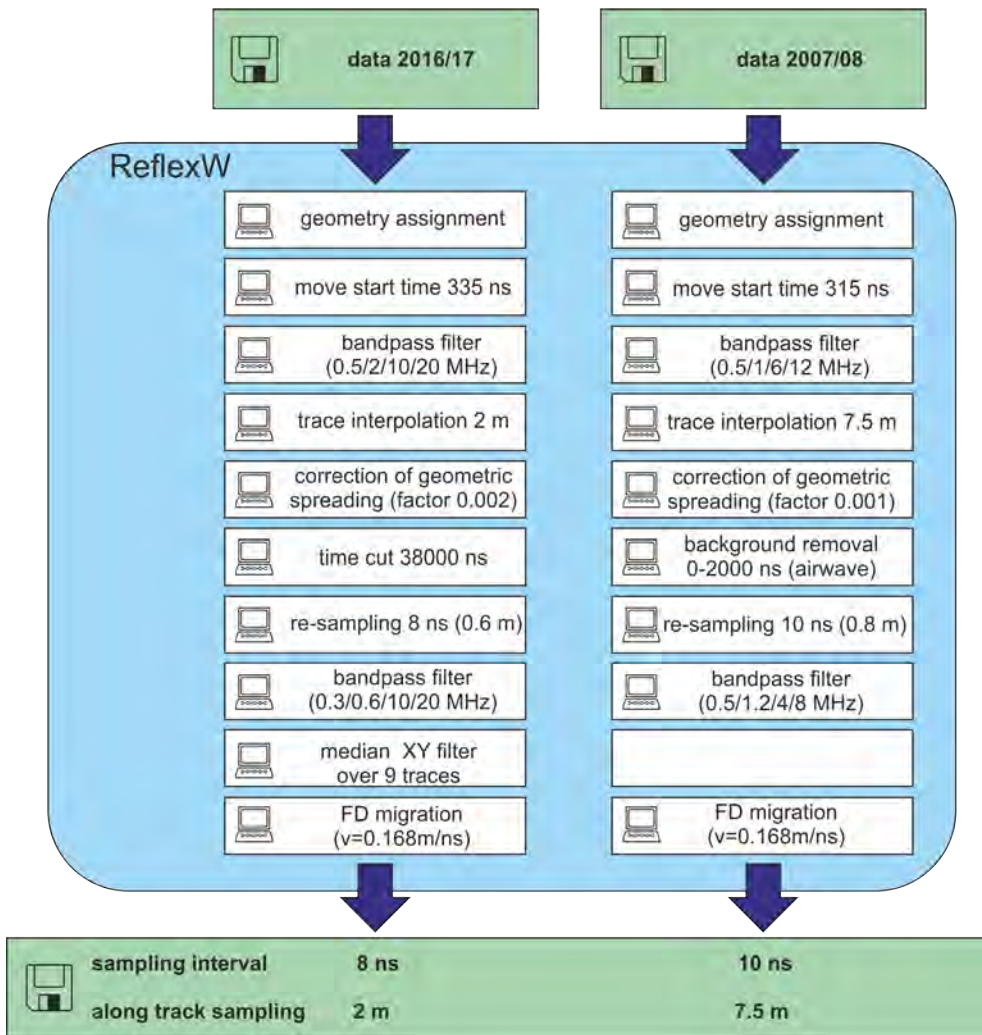
Figure 3.5: Processing flow applied to previously acquired data. Due to the time gap (9 years) between the processing of data, the processing between the two datasets does slightly differ. However, differences are limited to sampling intervals and the frequencies chosen for the bandpass filters.
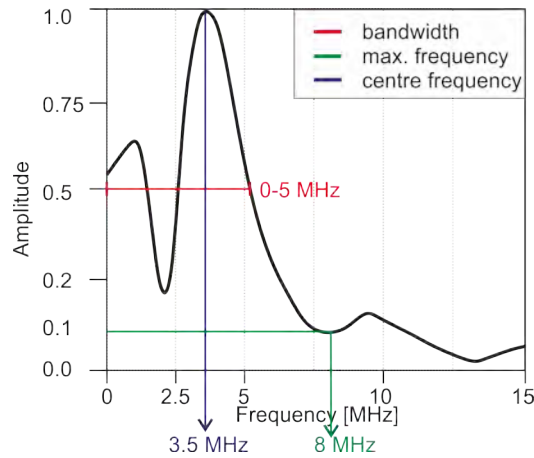
Figure 3.6: Amplitude spectrum of to previously acquired data (unprocessed). Bandwidth is defined following Simm & Bacon (2014) as the frequency range above half the maximum amplitude. Following this the bandwidth is 0–5 MHz, with a spectral notch at around 2 MHz. The received amplitude falls to 10% of its maximum at 8 MHz, and that is taken to be the maximum frequency.

3.3 Field Survey in 2017/18

The following describes the areas on the bed of RIS surveyed in season 2017/18 (Section 3.3.1) as well as considerations of survey design (Section 3.3.2). Following this, data acquisition (Section 3.3.3) and processing (Section 3.3.4) are described. Finally, the 3D dataset is briefly introduced (Section 3.3.5).

3.3.1 Area of Interest and Motivation

Figure 3.7 shows the detailed bed topography of the RIS, with the locations of the three grids acquired during season 2017/18 overlain in blue. The aim of this new survey was to map bed topography as accurately as possible, to be able to image bed shapes as well as get information on other processes occurring at the bed of the RIS. To enhance the resolution of the data compared to previous seasons, a denser spacing between the lines was used to be able to apply 3D processing (specifically 3D migration) as well as possibly *synthetic-aperture radar* (SAR) processing (not part of this thesis).

The locations for the three grids were chosen with the following motivations:

grid 1 includes the area of an upstream end of a MSGL (so-called Bump) on the central lower ridge. The upstream end of the Bump represents the steepest and most abrupt feature on the bed of the RIS. Previously acquired
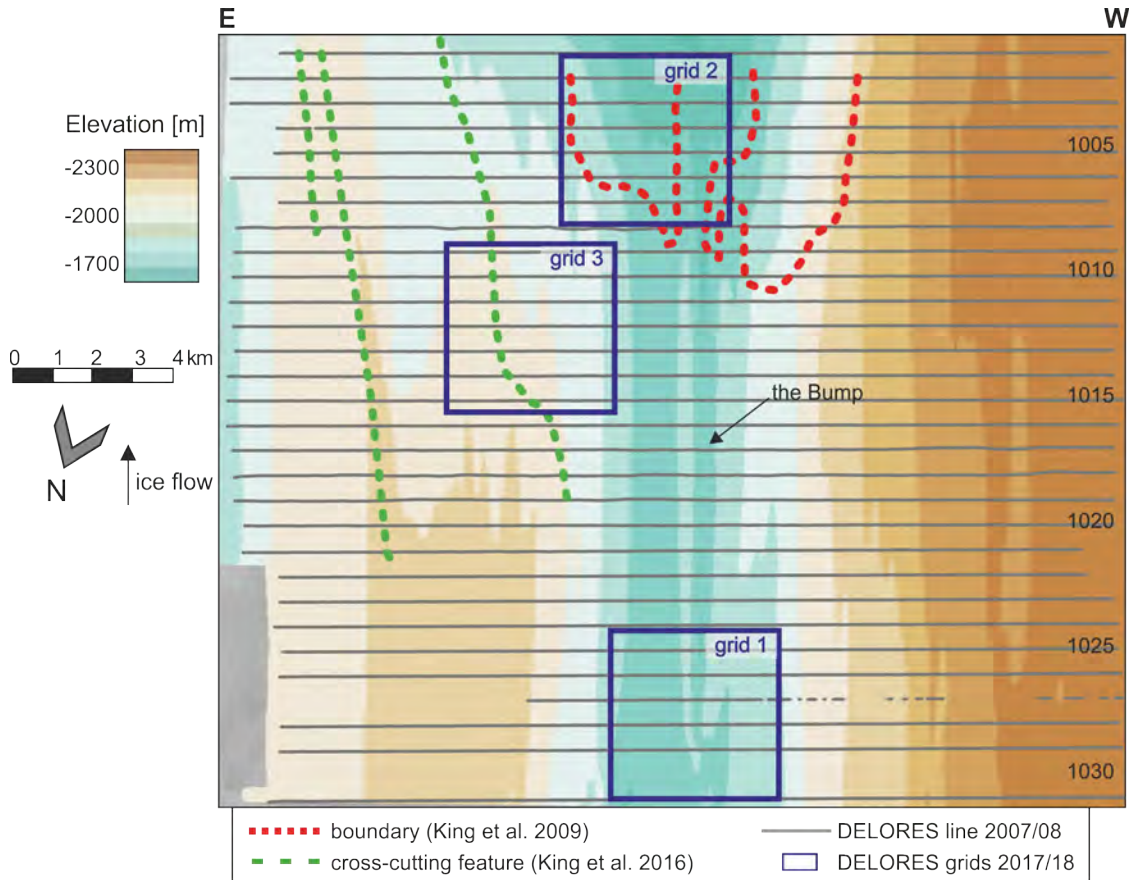
Figure 3.7: Bed topography (King *et al.*, 2016) in the study area with lines acquired in 2007/08 marked in grey and extent of grids acquired in 2017/18 marked in blue.

data suggest a depression at the upstream end of the Bump. More detailed geometry of the upstream end of landforms could give indications for mechanisms involved in their formation.

grid 2 was initially centred around the planned drilling sites of season 2018/19 (Smith *et al.*, 2021). However, due to proximity of depots and the camp sites during the field season to this grid, the location was shifted further downstream, still containing both drilling locations. The sediment in this area is interpreted to change from soft (presumably deforming) to harder (presumably non-deforming) sediment along flow. Data acquired in this grid could be used to map the course of the boundary with high accuracy and to investigate spatial changes in bed properties.

grid 3 [2] includes the downstream and upstream end of MSGL along the flow as well as some cross-cutting features. Looking at the ends and the zone between the MSGL could indicate whether these are two individual structures or if it initially used to be one structure that has been interrupted by the cross-cutting feature. Comparing the ends could give an indication of how MSGL form and of the origin of the cross-cutting feature. Radar reflectivity could be used to investigate a possible link to water, therefore if these cross-cutting features are possibly formed by water.

3.3.2 Design Considerations in the Acquisition of 3D Radar Data

RIS has been stated to be a prime location for mapping glacial bedforms in present-day conditions as well as for investigation their formation and evolution (Smith & Murray, 2009). So far, radar data on the RIS were acquired with resolution comparable to marine swath bathymetry data ($\sim$500 m cross-line spacing, King *et al.*, 2009), and a high degree of interpolation was necessary between the survey lines. To overcome this high degree of interpolation the survey for season 2017/18 was designed to acquire data compliant with 3D migration and therefore increase the horizontal resolution within the area investigated. Theoretical requirements for data to be compliant with 3D processing are described in the following section. Another aspect that influenced the field survey design was the aim to acquire data compliant with 3D processing including the phase information, so-called SAR-processing. The implementation of the phase into the processing and background on that are not discussed within this thesis, but are important to keep in mind to understand why the survey was planned and undertaken as described in the following.

3.3.2.1 Time Sampling and Record Length

The minimum time sampling requirement to prevent frequency aliasing is defined by Nyquist (1928) and requires the sampling frequency of the analogue-to-digital converter to be at least double the maximum frequency (8 MHz, see Figure 3.6)

---

[2]Due to time constraints and the difficulties arising from the pandemic happening in 2020 and onwards, it was not possible to process and analyse this grid as part of this thesis. It is therefore not be discussed further, but is available for analysis in a future study.

in the dataset. A sampling frequency of 16 MHz (or 20 MHz allowing for an anti-alias filter of the analogue-to-digital system) is the minimum requirement and would sample the wavelet every 62.5 ns. The sampling frequency during the field season was chosen to be 250 MHz. The much higher sampling frequency was chosen in the event that other processing techniques that might be applied to the data in the future (including the SAR processing) might require a denser time sampling of the wavelet. Furthermore, no negative effect of such a high sampling frequency on the overall data quality was expected.

For radar data, the theoretical time resolution is determined by a quarter of the dominant wavelength ($\lambda/4$, Sheriff & Geldart, 1995; Yilmaz, 2001) of the unaliased emitted pulse. The calculated resolution on ice (velocity of $0.168 \, \mathrm{m\,ns^{-1}}$) is 12 m assuming a dominant frequency of 3.5 MHz (Figure 3.9). Higher frequencies would result in higher resolution, but signal attenuation is also more rapid for higher frequency wavelets. As such, this resolution limit is considered reasonable for wavelets likely to remain detectable after the 4.4 km round-trip between the glacier surface and its bed.

Record length: With data volume in mind, the record length for the DELORES system was chosen to be 40,000 ns post-trigger. This includes the reflection at the bed at 2.2 km depth, which would be recorded at a twtt of around 26,000 ns (assuming a velocity in ice of $0.168 \, \mathrm{m\,ns^{-1}}$), as well as possible subglacial signals.

3.3.2.2   Spatial Sampling

The Fresnel zone diameter is a measure for horizontal resolution; two reflection points within this zone are considered as indistinguishable. The radius of the first Fresnel zone for unmigrated and normal incidence as well as zero-offset data is defined as:

$$r = \frac{v}{2}\sqrt{\frac{t}{F}}, \qquad (3.1)$$

where v is the velocity of the wave in the subsurface and F the dominant frequency of the wavelet (Yilmaz, 2001). Theoretically, the Fresnel zone can be reduced to one quarter of the wavelength using migration (Lindsey, 1989). Energy arriving from all points within that zone, within a time interval of half the dominant period, interferes constructively to some extent. However, the improvement of resolution is only observed in the direction in which migration is applied (Figure 3.8). 2D migration applied to profiles would only improve resolution in the acquisition direction (Figure 3.8 b). For the Fresnel zones to be reduced in all directions, a 3D acquisition and migration scheme is required (Figure 3.8 c). Assuming a constant wave velocity in ice of $0.168\,\mathrm{m\,ns^{-1}}$ (Navarro & Eisen, 2009), dominant frequency of $3.5\,\mathrm{MHz}$ (Figure 3.9) and twtt of 26,000 ns ($\sim$deepest bed reflection recorded), the radius of the Fresnel zone is $228\,\mathrm{m}$. The application of migration would reduce the radius to $12\,\mathrm{m}$. Therefore, two points on the bed can be distinguished if they are separated by a minimum of $24\,\mathrm{m}$ (post-migration).
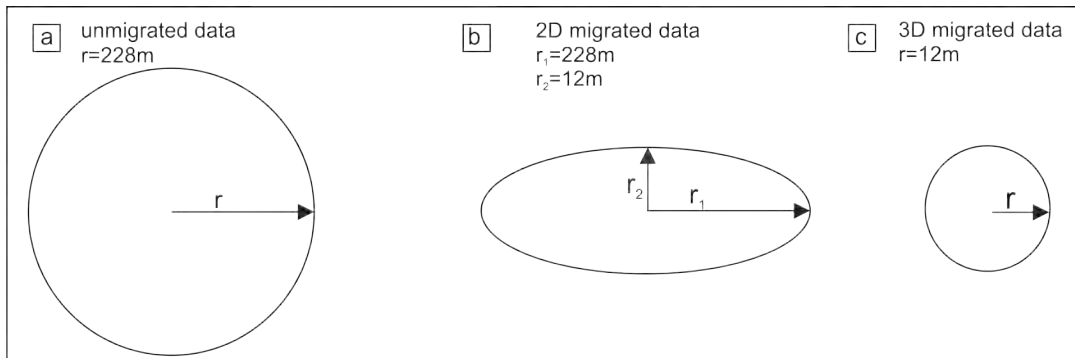
Figure 3.8: Size of Fresnel zone, (a) pre-migration, (b) after 2D migration and (c) after 3D migration. The Fresnel zone is only reduced in the acquisition direction when applying 2D migration (r_2), whereas the radius perpendicular to acquisition stays as in non-migrated data (r_1). Numbers included for the different radius are calculated for the survey in 2017/18.
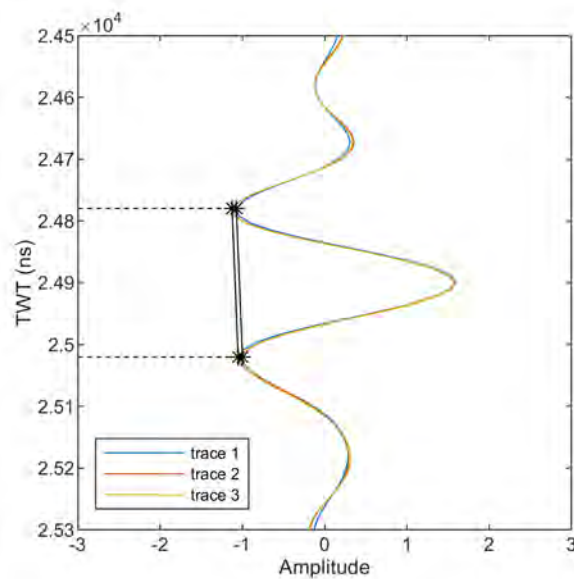
Figure 3.9: Examples of the wavelet of the bed reflection recorded at 3 different positions. The dominant period is 280 ns (dominant frequency 3.5 MHz).

Line spacing: Radar data were acquired perpendicular to the ice flow direction, towing the radar behind the snowmobile. Not all data acquired along the snowmobile track can be used for analysis: turns in the radar track have to be excluded (Figure 3.10). The line spacing is equal to the crossline sampling and describes how far the parallel lines acquired are apart. The along track sampling or inline sampling is determined by settings of the pulse repetition frequency, the number of signals stacked to one recording in the oscilloscope and the driving speed of the snowmobile towing the equipment. The definition of a sufficient
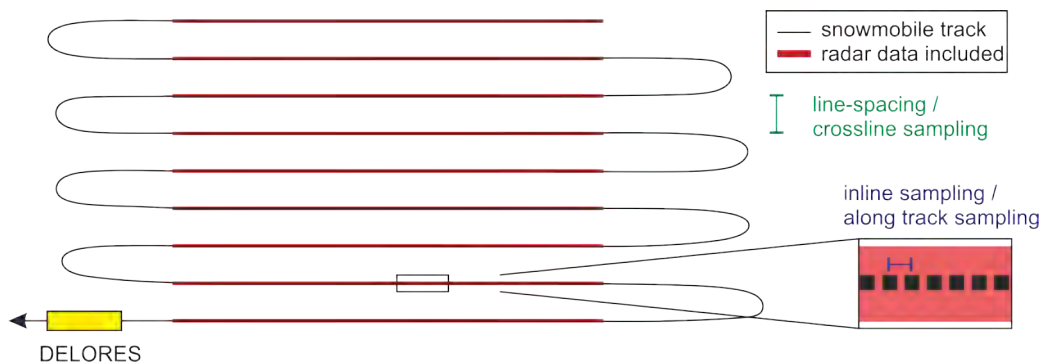
Figure 3.10: Schematic drawing illustrating the inline and crossline-sampling of the DELORES surveys.

inline and crossline sampling (Figure 3.10) is crucial for a 3D dataset, since a too coarse a sample increment could lead to spatial aliasing of data and, therefore problems with representing apparent dips in the dataset. The spatial sampling interval Δx_{max} to sample the wavefield sufficiently and avoid spatial aliasing can be calculated following Grasmueck *et al.* (2005)

$$\Delta x_{max} \leq \frac{v}{4\, f_{max}\, \sin(\beta_{max})}, \tag{3.2}$$

where f_{max} is the maximum frequency and β_{max} the maximum dip angle of the wave front. The bandwidth of the antenna is more than just the central frequency (Figure 3.6). The maximum observed frequency, which is potentially associated with energy coming from the bed reflection is around 8 MHz. The definition of β_{max} is not trivial, as it not only involves the dips of the target surface but the dips of the diffraction wavefront at which the signal arrives at the surface. If the tails of steeply dipping hyperbolas are sampled insufficiently, the energy can not be focussed back to its true origin.

Figure 3.11 shows model results using Equation 3.2 for different dips (x-axes), assuming a maximum frequency of 3.5 MHz (blue line) and 8 MHz (red line). The maximum line spacing decreases with increasing dip angle. A maximum dip of 90° requires a spacing of 12 m and 5 m or less, at 3.5 MHz or 8 MHz, respectively. Maximum dip angles of 20° would be unaliased according to this criterion using a spatial sampling interval of maximum 35 m and 15 m at 3.5 MHz and 8 MHz, respectively. For 10° a maximum spacing of 70 m and 30 m would be required, at 3.5 MHz or 8 MHz, respectively. Figure 3.12 shows a dip map of the bed topography on the basis of 500 m line spacing data (the previously acquired data) of the bed of RIS. Steepest dips are around 25° but most of the area shows dips less 15°. Given these considerations, the line spacing or crossline sampling for the 2017/18 field campaign was chosen to be 20 m. Assuming the dominant frequency of the bed reflection to be around 3.5 MHz this would allow reflection from a surface dipping up to 36° to be sufficiently sampled. This sampling is also compatible with imaging diffraction hyperbola tails dipping up to 36° (after this the curvature might be too steep to be sampled sufficiently). The sampling along the line is determined by the pulse repetition rate of the transmitter, which is 1 kHz. To increase SNR, 256 signals were stacked before recording a trace, resulting in ~4 traces per second. Increasing and decreasing of the stacked signals was considered, although by decreasing the numbers of signals stacked, the SNR
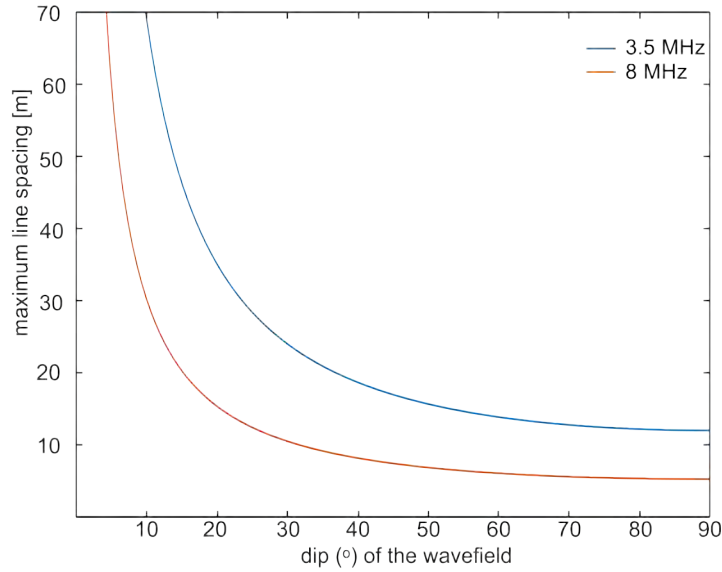
Figure 3.11: Model results for maximum allowed line spacing for different dip angle along a diffraction and reflection tail for a wavefield with frequency of 3.5 MHz (blue line) and 8 MHz (red line) and a propagation velocity of $0.168\,\mathrm{m\,s^{-1}}$. A dip of 0° represents a horizontal surface.

would decrease. Stacking more signals would have required a slower driving speed, to ensure that spatial variations in the signal were not smoothed out and the signal did not get smeared over more than 2 m. However, due to time limitations during the field season it was not possible to acquire data with a slower driving speed. Therefore, 256 signals were stacked into one trace, while driving at a speed of around $11\,\mathrm{km\,h^{-1}}$ which resulted in a trace recording every second and roughly a recording every metre. This oversampling of the data in track direction was also chosen considering the possibility of other processing in the future that might require very dense spaced data.

Horizontal grid extent: When planning the exact location of the survey lines, the location and extent of the migration aperture had to be taken into account, to ensure that signals from steeply dipping bed topography are recorded within the extent of the lines. Ignoring the effects of firn densification on the ray path, energy reflected off a 25° dipping surface would reach the surface at a lateral distance of 1065 m (considering an ice thickness of 2200 m and a firn layer thickness of 70 m, Figure 3.13). To ensure reflections from either side of the Bump could be recorded within the grid extent, the upstream end of the Bump was put into the centre of grid 1. Similarly, for the other grids, the centre of the grid and the survey lines were planned to be above the features of greatest interest.
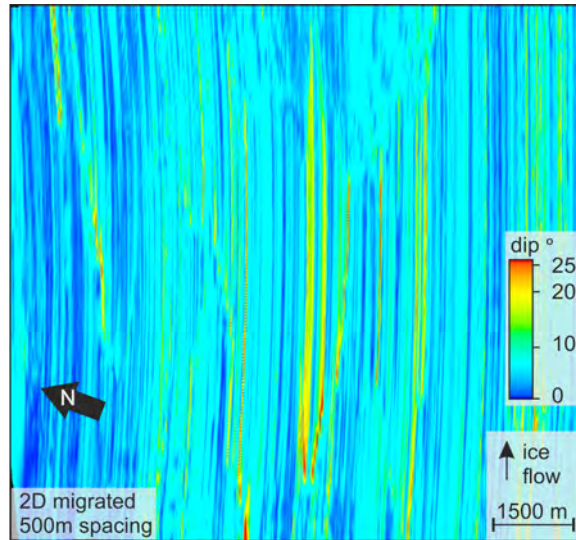
Figure 3.12: Plan view of the bed of the RIS, colour-coding presenting dip angles along the surface created from interpolated picks on the dataset acquired in 2016/17 (500 m spacing). Most of the area shows dips less than 15°, whereas the flanks of landforms, especially the Bump, show dips up to 25°.
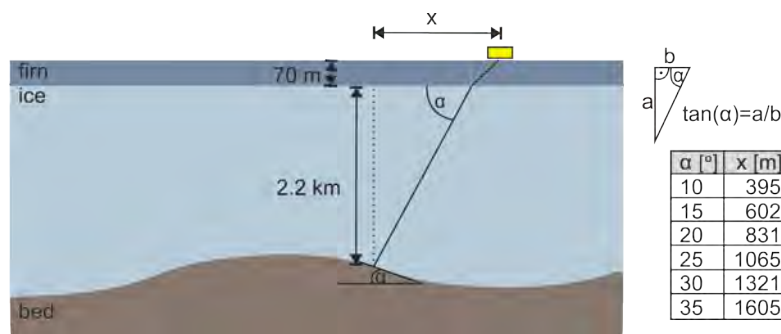
Figure 3.13: Schematic drawing of the consideration of horizontal extent to receive reflections from an dipping surface, solely considering one single firn layer of 70 m thickness (following Snell's law, Section 2.4), with no variations in properties within this layer, therefore neglecting effects of densification on the ray path. Velocity in firn is chosen to be $0.2\,\mathrm{m\,ns^{-1}}$, in ice $0.168\,\mathrm{m\,ns^{-1}}$. The table on the right gives resulting extents for different surface dip angles.

3.3.3 Data Acquisition

Data were acquired between 22nd December 2017 and 4th of February 2018 by Andy Smith (BAS) and myself. A detailed timetable of the field season can be found in the Appendix Figure 10.1. Within each grid, 151 parallel lines were recorded with line spacing of 20 m and line length of 3 km, resulting in $3 \times 3 \, \text{km}^2$ grids. In total more than 1500 km of data were acquired (excluding acquired data while transiting into next starting position) over a period of 26 days. The parameters chosen for the data acquisition are shown in Table 3.2. The acquisition described here results in a dataset compliant with 3D sampling, with a narrow (2D) azimuth coverage. The 3D sampling and limitation in azimuth is consistent with most 3D marine surveys.

Table 3.2: Acquisition parameters season 2017/18.

Stack	256
Pre-trigger samples	100
Post-trigger samples	10000
sampling interval	4 ns
centre frequency	3.5 MHz
Air-wave trigger level	-0.16 V

During data acquisition, the location of the start of the line as well as the end was marked by two flags, which were pushed into the snow. The snowmobile was stopped at the end and the start of the lines to mark these positions in the GPS data. To achieve accurate positioning of the system, a dual-frequency GPS receiver was mounted on the front of the transmitter and receiver sledge and additionally on a sledge at the mid-point between the antennas. The GPS receivers logged data every 1 s recorded in a *Receiver Independent Exchange Format* (RINEX) data format. The receiver and transmitter, including the GPS unit were towed behind a snowmobile, as shown in Figure 3.14.

3.3.3.1 Different Systems Used During Acquisition

During the acquisition of the three grids different parts of the DELORES system needed to be replaced. The different systems used are explained below:

system I was used in the beginning of the field season and also tested at Rothera Research Station. It consisted of new (never used before) antennas, the chassis II, the GPS sledge (used for the whole field season) and the transmitter-

sledge (used for the whole field season). For some reason this system stopped working on the 5th of January. System I was used for lines 1-130 in grid 3.

system II mostly consisted of the same set-up as system I, but the amplifier was replaced and the chassis III was used. System II was used for lines 130-151 in grid 3 and lines 1-20 in grid 2.

system III transmitter sledge, GPS sledge, amplifier and the balun of system I were used. Antennas got replaced by the ones used during 2016/17 field season, to allow comparison of the two seasons. System III was used for all lines in grid 1 and lines 21-151 in grid 2.

A schematic drawing of the set-up of system III can be seen in Figure 3.14. Photographs of the different parts of the system can be seen in Figure 3.1–3.3. During data acquisition, differences in the frequency content as well as the SNR
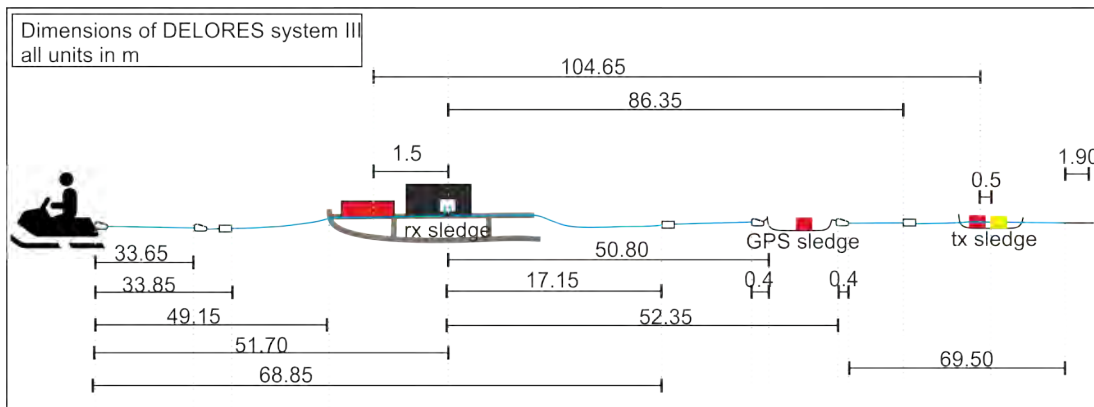
Figure 3.14: Schematic drawing of the set-up of DELORES system III with measured distances between different elements of the system. tx = transmitter, rx = receiver.

were identified between data acquired using the different systems. A brief comparison is given in the following:

3.3.3.2 Signal Difference Between Systems Visible During Fieldwork

The amplitude spectrum (Figure 3.15) of data acquired using different systems differed; however the spectrum of data of individual systems did not vary over time. The frequency content for system I and system II shows some small difference in the amplitude. Comparing system II to system III shows more significant

changes. Frequencies in the data acquired with system III between 2.2–8.3 MHz show a significantly higher amplitude compared to the other systems.
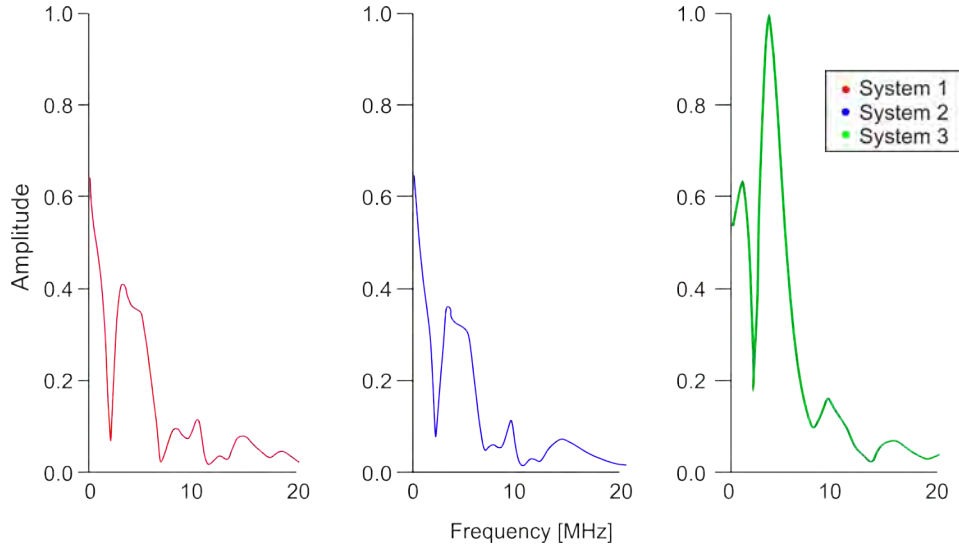
Figure 3.15: Comparisons of the amplitude spectra of the three different DELORES systems used in season 2017/18. The spectra are calculated over the whole record.

Furthermore, some of the amplitudes in the time domain of system I and II appear to be clipped (around 400 ns twtt in Figure 3.16), which can not be seen in the data of system III. However, this only relates to the arrival of the airwave, and not the arrival of internal or the bed reflections. Moreover, a shift in airwave arrival can be observed (Figure 3.16). The first break of the airwave in system I appear at 319 ns, for system II at 347 ns (∼28 ns (2.3 m) difference) and for system III at 331 ns (∼16 ns (1.3 m) compared to system II). These shifts in airwave arrival are most likely linked to the described changes in the amplitude spectrum (and therefore triggering of the recording). All of these differences are corrected for during processing of the data (Section 3.3.4.1).
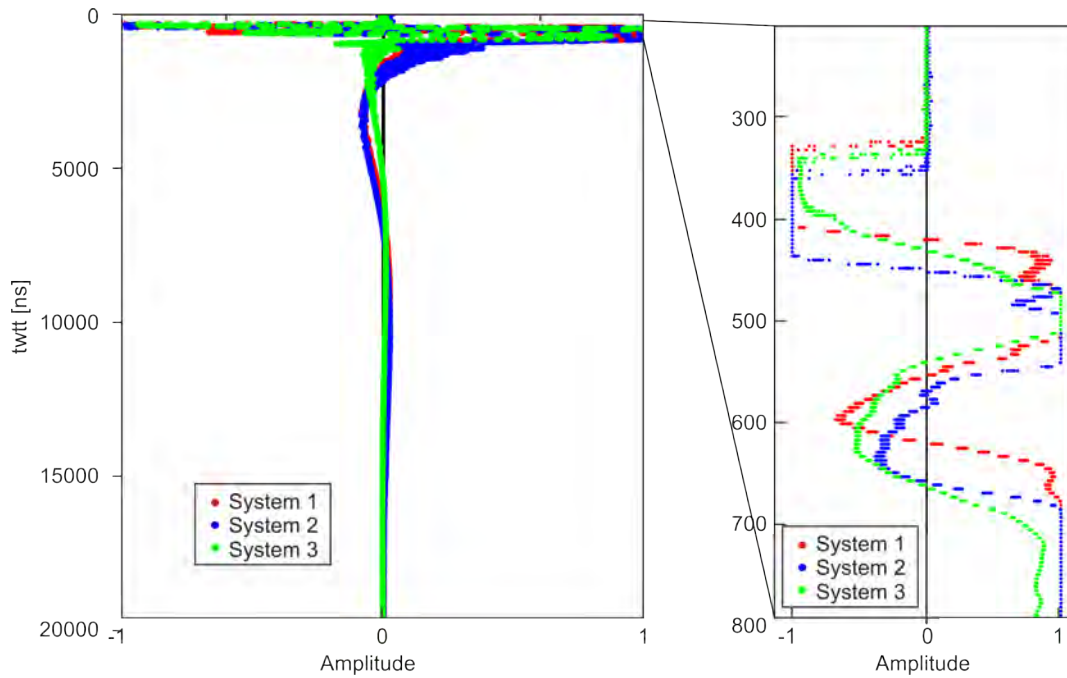
Figure 3.16: Amplitude of the signal over twtt of the three different DELORES systems used in season 2017/18.

3.3.4   Processing of 2017/18 Data

3.3.4.1   Preparation of Data - Geometry Assignment

Figure 3.17 illustrates the steps applied to the data acquired in 2017/18 for geometry assignment. This procedure was based on a routine applied to most DELORES data including the 2016/17 data introduced before in Section 3.2. During data acquisition the chassis computer stored the voltage of the received signal as a 14-bit representation in a CSV file called "Events.CSV" (Figure 3.17 right column). This file includes a timestamp for each recorded trace, the amplitudes of each sample in each trace and GPS positions (acquired approximately every second by the single frequency GPS antenna, mounted on the chassis). Dual-frequency receivers on transmitter, receiver and midpoint sledge were set up to store positions every second. For GPS position assignment, data from GPS receivers on the transmitter and receiver sledge were used. The aim of the steps described below was to convert the DELORES data into a format that could be read by ReflexW (Sandmeier Scientific Software), with corresponding headers for each trace.

step I: Using a Matlab routine (based on the "optdelcsvread3" function) developed by BAS the "Events.CSV" file was converted into a file including only the unamplified amplitudes (data not part of this thesis) and a file including only the amplified amplitudes, used in all the described analyses.

step II: To ensure accurate GPS positioning, the dual-frequency GPS data were processed using the *Canadian Spatial Reference System Precise Point Positioning* (CSRS-PPP) online application for *global navigation satellite systems* (GNSS) data post-processing.

step III: Following this, GPS data were corrected for effects of drifting clocks. These effects and the identification of these effects within the data have been described in detail in Section 10.2 in the Appendix.

step IV: The assignment of GPS positions to the recorded traces took place on the base of time stamp synchronization (using the "travdis2(out)" function). The chassis, as part of the recording system, is a computer with an internal clock. The positions of the dual-frequency GPS receivers were assigned to the radar traces, according to the time at which GPS positions (based on
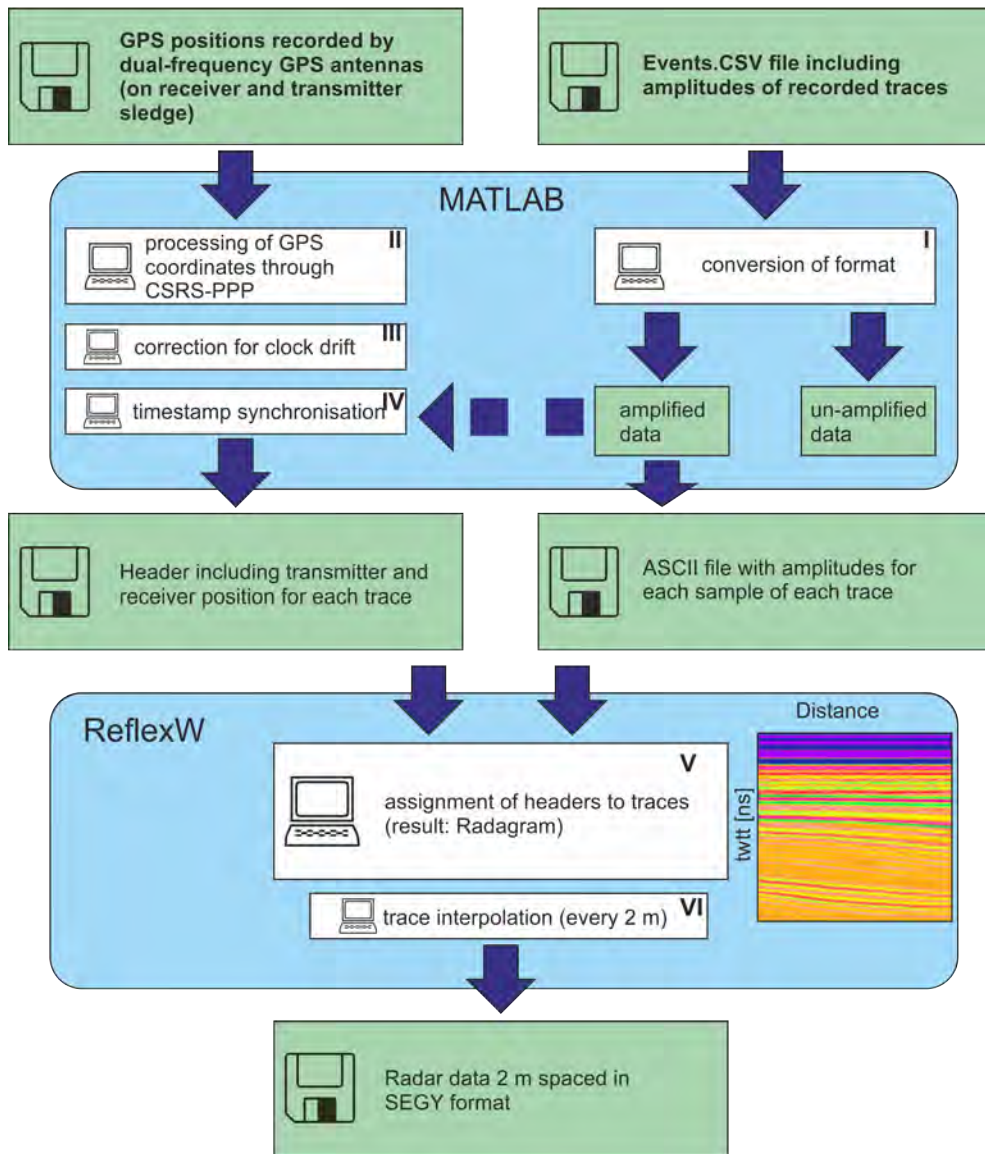
Figure 3.17: Flow chart of processes applied to assign GPS positions to the traces and convert data into SEGY format.

Coordinated Universal Time (UTC) time) and radar traces (based on the computer time) were recorded. The acquisition settings resulted in four radar trace recordings approximately every second (see Section 3.3.2.2). Dual-frequency GPS positions (of the receiver and transmitter sledge) were recorded every second and interpolated in between to get positions for every trace recorded.

step V: The export from Matlab at this stage consisted of an ASCII file including the amplitude information and a trace header file. These files were then imported into ReflexW (Sandmeier Scientific Software), where the corresponding headers (including positions of the receiver and transmitter) were assigned to each trace. The resulting CMP positions (between the transmitter and receiver sledge) were calculated within ReflexW.

step VI: Amplitude information within the traces was interpolated to achieve a trace spacing of 2 m. The main reason for the application of this step at this stage was to decrease the amount of traces and therefore memory required for data within one grid. Finally, the data (trace spacing of 2 m, vertical sampling of 4 ns) was exported into a SEGY format.

3.3.4.2 Interpolation of Data Into a Regularised Grid

For the application of 3D migration, data needs to be organised in a regularised grid with a constant trace interval for each line. The final dataset for grid 1 and grid 2 each consisted of 151 lines (in the following termed (151) inlines; see Figure 3.10) and 1501 traces per line (in the following termed (1501) crosslines). Furthermore, data should ideally have been acquired with one system, to ensure consistency throughout the dataset. Figure 3.18 illustrates the processing steps taken to interpolate the data into a regularised geometry of 151 inlines and 1501 crosslines. As mentioned in Section 3.3.3.1 data within one grid were partly acquired using different systems. A slight change in frequency content of the recorded airwave was observed between data acquired with different systems (Section 3.3.3.2). The change in frequency content of the airwave led to a delayed triggering of the recording as the trigger level was not adopted during acquisition. This can be seen as the airwaves of the different systems arrive at different twtt (Section 3.3.3.2). However, the distance between the receiver and transmitter did not change, therefore, this delay can be corrected for by applying a time shift to
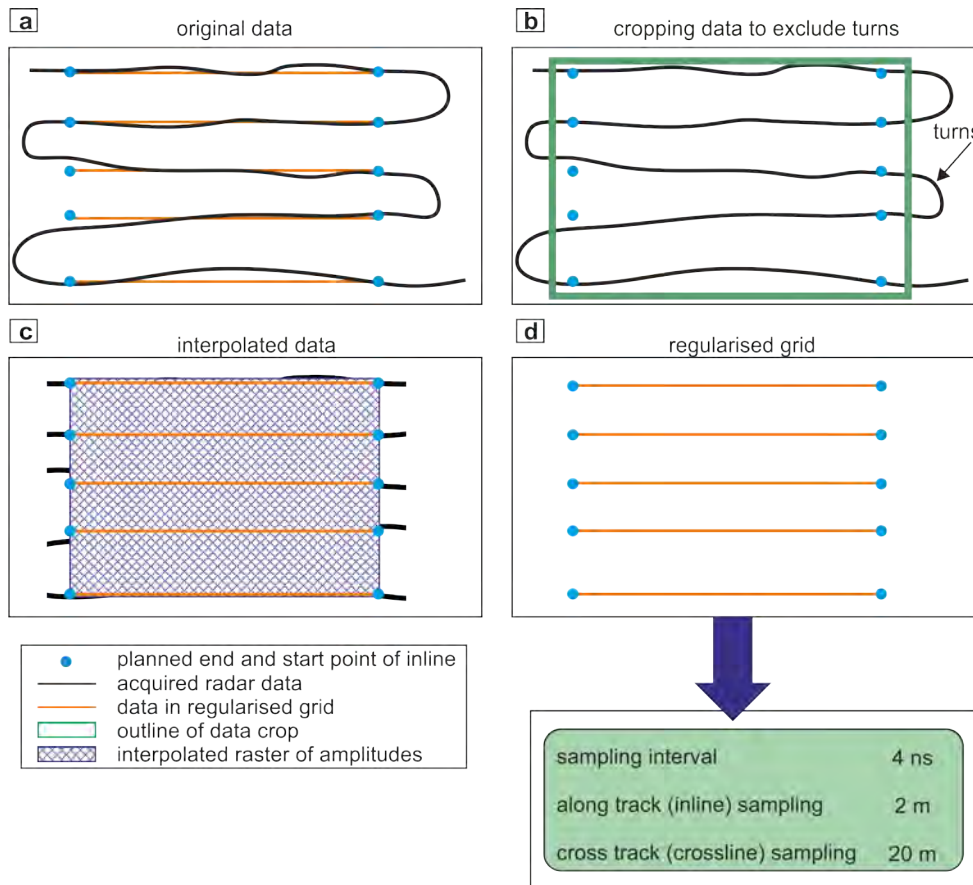
Figure 3.18: Regularisation of acquired radar data to convert data into a geometry compliant with 3D migration. First, the CMP positions in the regularised grid (blue dots represent the start and end of the orange lines) have to be defined (a). Following this, the acquired data were cropped to exclude turns (b). Resulting data were then interpolated over the extent of the regularised grid (c), from which amplitudes for the positions within the regularised grid were extracted (d). Geometry of lines is not to scale.

synchronise the airwave arrivals in all datasets to the same twtt. Furthermore, no delay in airwave arrival has been observed for data acquired using consistently one system. The coupling between the antennas and the snow surface are assumed to be constant throughout the surveys and no further correction are applied. Once the arrivals of the airwave were shifted, all data within one grid were combined into a data volume. Black lines in Figure 3.18 a illustrate the acquired radar tracks within parts of a grid. Blue dots display the start and end points of the inlines (orange line) in the regularised grid. Sampling along these lines is 2 m, while the 151 parallel lines are spaced 20 m apart. Although during data acquisition best attempts were made to acquire the lines as straight and on track as

possible, the acquired lines differ from the planned straight lines in places by up to 12 m horizontal distance.

The acquired dataset contained data acquired during the turns at the end of lines. Since the distance between the receiver and transmitter may have changed during the turns (Figure 3.18 b), these data were excluded from the volume. Following this, the amplitudes within the cropped dataset were interpolated over the extent of the regularised grid using the Matlab function "scatteredInterpolant" (Figure 3.18 c). During this step, the data were divided into time slices (according to the sampling rate, i.e., first sample in each trace is part of times slice number 1). The amplitudes within each time slice were then interpolated and using the coordinates of the points within the regularised grid (orange line) the corresponding amplitudes for each of these positions were extracted (Figure 3.18 d). Finally, a SEGY file including data in the regularised grid (coordinates and amplitudes) was exported and used for further processing. The exported dataset includes 151 inlines with a line sampling of 2 m, crossline sampling of 20 m and a time sampling interval of 4 ns.

3.3.4.3   Pre-Processing and Migration of 3D Data

The final processing flow applied to the grid in SeisSpace/ProMAX (LGC-Halliburton Software) is shown in Figure 3.19. Processing prior to migration included geometry assignment, bandpass filtering to improve the SNR, correction for geometric spreading and a bottom mute. The bottom mute was implemented into the processing to reduce noise at the end of the recording, induced by the application of filters. A topographic (static) correction has not been applied to the data, because surface topography in the 3×3 km grid is almost flat. Following the bottom mute a Poststack Kirchhoff 3D Time Migration routine is applied. Parameter testing applied to design the final migration aperture is described in the Section 10.3 in the Appendix. Migrated data arranged in a 3D cube were then further used in Petrel (Schlumberger Software) to analyse the data using different attributes (see Section 4.5).
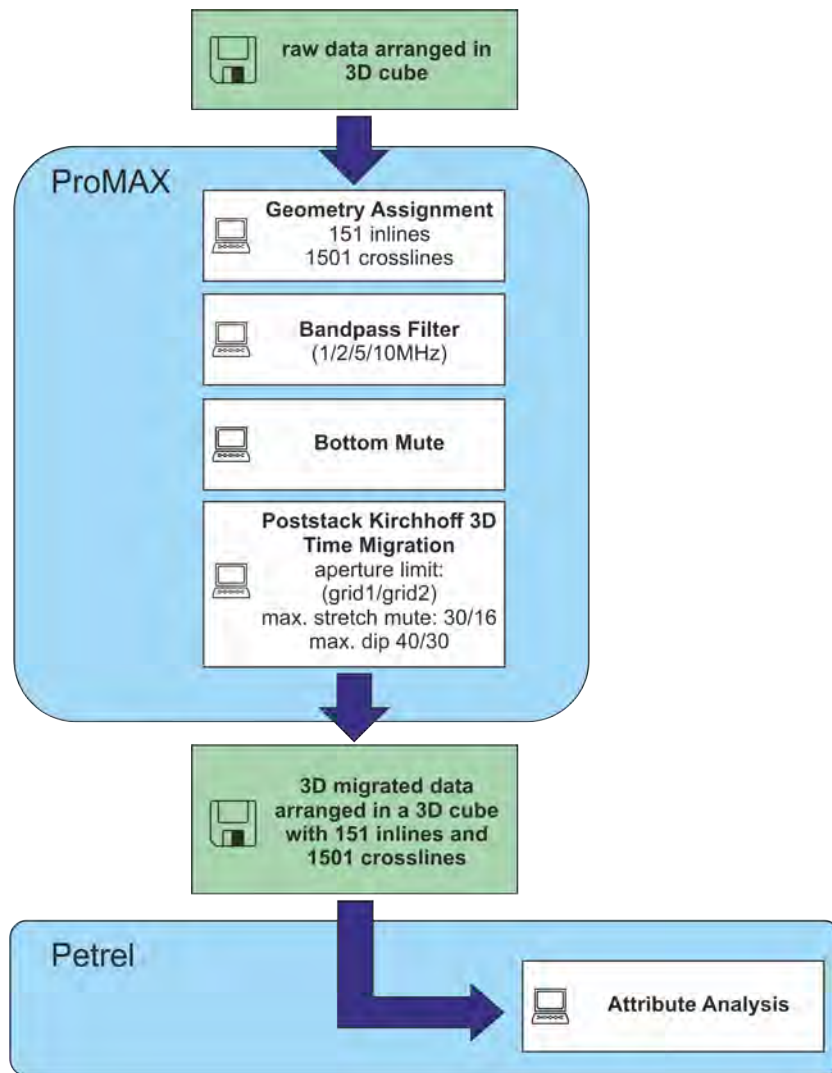
Figure 3.19: Processing flow applied to grid 1 and 2 in SeisSpace/ProMAX (LGC-Halliburton Software). The migrated 3D cube was then imported into Petrel (Schlumberger Software) for attribute analysis described in Section 4.5.

3.3.5   Description of 3D Migrated Data

If 3D processing of data is not possible a 3D cube can be created from a series of 2D lines, while solely for the application in Petrel, data in the 3D cube do not require to be in a regularised grid with identical numbers of traces per line, and/or perfectly straight lines. However, consistent trace numbers and regular trace positions are required for implementing 3D migration in SeisSpace/ProMAX. Figure 3.20 and 3.21 show data of grid 2 in 3D cubes with several in- and crosslines visible. As shown in Figure 3.19, an inline consists of 1501 traces, while 151 traces form a crossline. This is the case for grid 1 and grid 2. Inline 1 was located at the downstream end of the grids, with increasing line numbering towards upstream. The crossline numbering is chosen to increase from east to west (left to right when looking in flow direction). The twtt of the bed reflection was picked in Petrel, as described in more detail in Section 4.2. These picks can then be interpolated onto a 3D surface (see yellow arrow in Figure 3.20 and 3.21). Surfaces shown in this thesis contain a cell size of 20×65 m, while the cells are rotated ($110°$) to be aligned in flow direction, unless otherwise stated. As data are arranged as a 3D cube not only data along in- and crosslines can be extracted but time slices or random lines, with any orientation can be extracted to view data. Random lines were used for the analysis of reflections along landforms as the crosslines as defined in the 3D cube are not perfectly aligned with landforms (see crossline 1141 in Figure 3.21).

Figure 3.22 shows the radargram along inline 76. Signals in the upper 1000 ns originate from the arrival of the direct wave. Traceable englacial reflections are visible until a twtt of $\sim$15000 ns. The area between 15000 ns and the bed reflection appears chaotic and no continuously traceable englacial reflections are visible. The bed reflection at $\sim$25000 ns is visible due to its high amplitude ($\sim$0.2 V). No continuous or traceable signal can be seen beneath the bed reflection. The origin of arrivals visible above the bed reflection has been analysed in Section 10.4 in the Appendix. Following this analysis, these arrivals are interpreted to originate from migration artefacts. None of the signals in the area immediately above the bed reflection represent a true englacial reflection and were therefore categorised as noise.
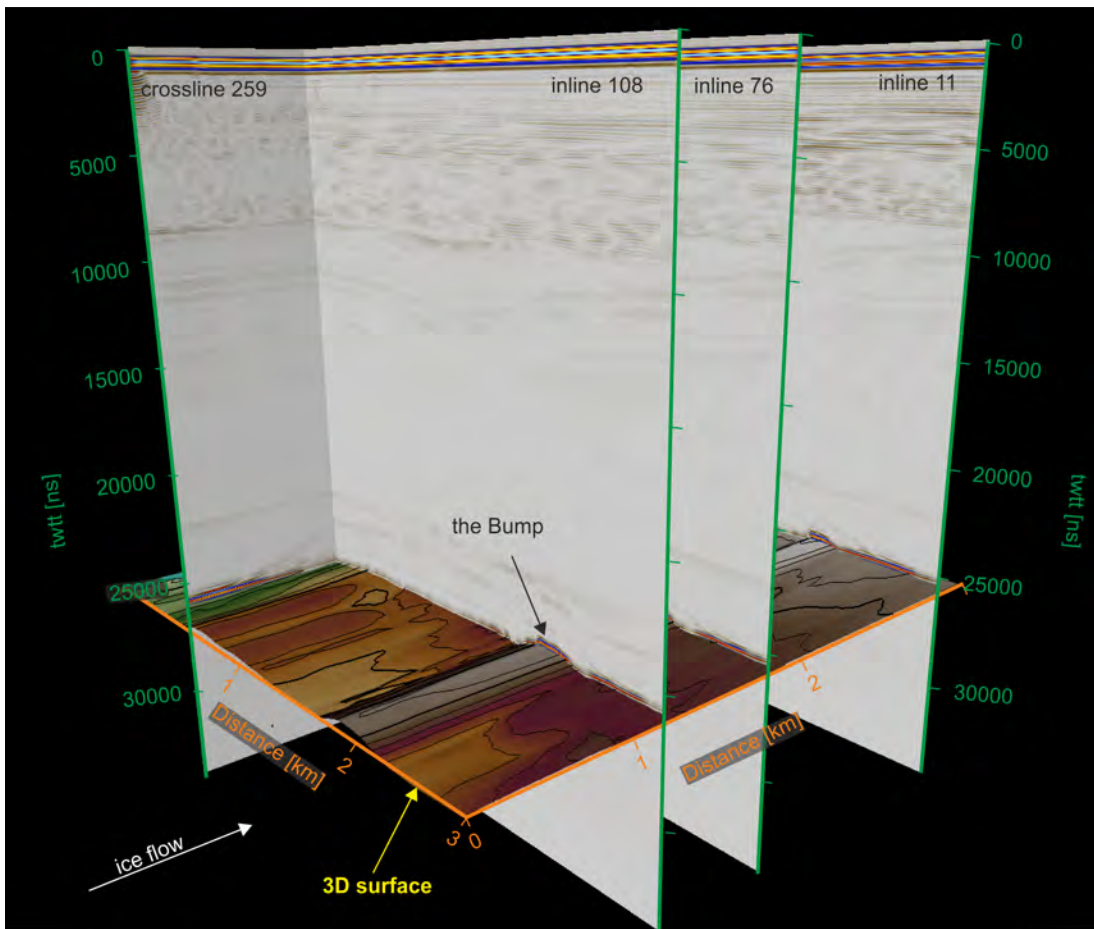
Figure 3.20: 3D cube of data in grid 2 with inline 11, 76 and 108 and crossline 259 visible. Lines of the migrated volume show the reflection of the bed. Picks of the twtt of this reflection are interpolated onto a 3D surface (yellow arrow).
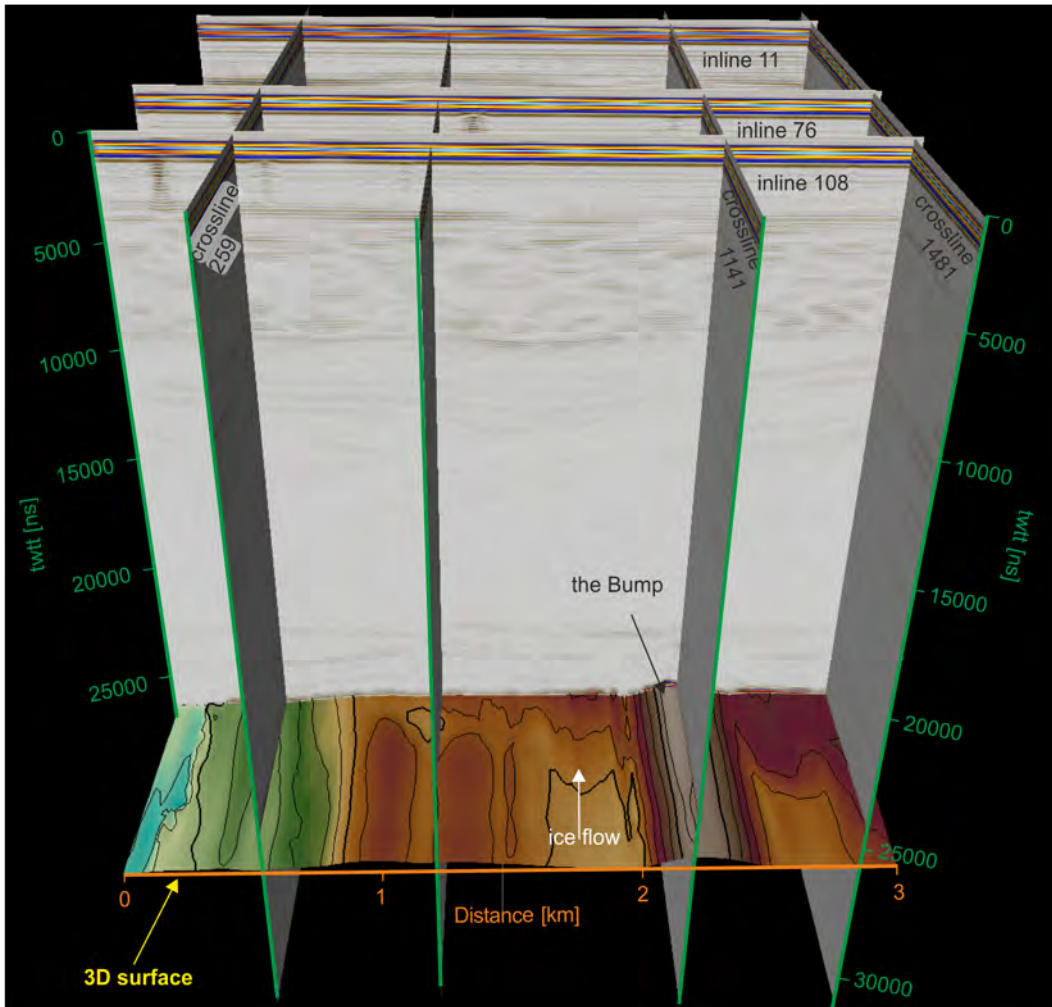
Figure 3.21: 3D cube of data in grid 2 with inline 11, 76 and 108 and crossline 259 visible. Lines of the migrated volume show the reflection of the bed. Picks of the twtt of this reflection are interpolated onto a 3D surface (yellow arrow).
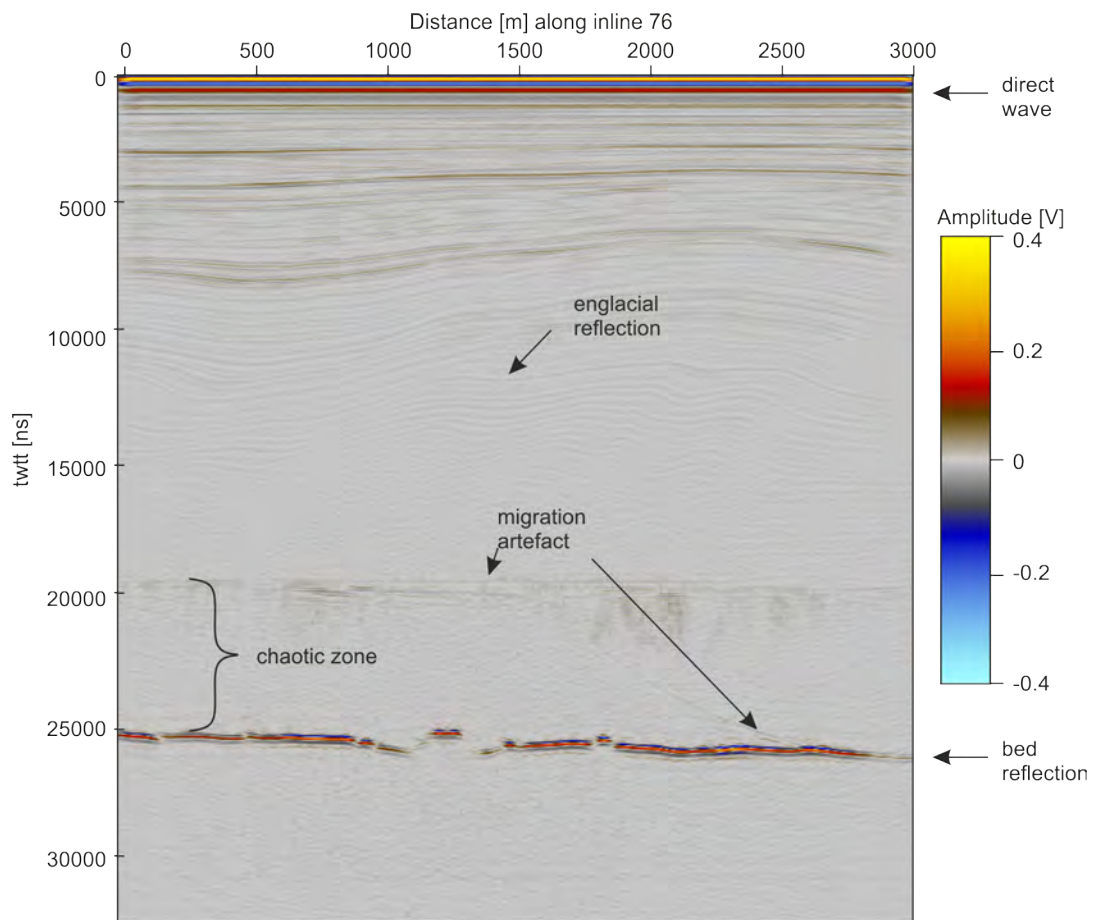
Figure 3.22: Inline 76 of grid 1 displaying the amplitude of the data. The signal of the arrival of the direct wave, englacial as well as the bed reflection and artefacts are marked. Furthermore, an area referred to as chaotic zone is highlighted.

3.3.5.1 Limitation of the Processing and 3D Migration Applied

The theoretical resolution of a 3D migrated dataset has already been introduced in Section 3.3.2. During preparation of the data and assignment of the geometry to the traces the inline trace spacing was set to 2 m, which included the interpolation of amplitudes recorded for the individual traces to be interpolated. For most areas, this meant an increase of trace spacing from around 1 m (resulting from driving speed, pulse repetition and stacking, Section 3.3.2) to 2 m. This interpolation did induce some degree of smearing of signals. Further smearing was possibly introduced to the data, when amplitudes were interpolated to create a regularised grid (Section 3.3.4.2). However, this smearing over 2 m is most likely negligible considering the theoretical horizontal resolution of 24 m and the inaccuracies introduced due to the mis-locations of data (Section 10.2).

3.4 Summary

As part of this thesis, three datasets acquired with the DELORES system were analysed. Two (acquired in 2007/08 and 2016/17) of the datasets cover a 14.5×18 km part of the main trunk of the RIS. This was also the location of several studies in the past, analysing the basal properties and the basal microseismicity (e.g., Kufner *et al.*, 2021; Murray *et al.*, 2008; Smith, 1997a,b, 2006; Smith *et al.*, 2015). The third dataset consists of two 3×3 km grids, which lie in the area of the bigger grid acquired in 2016/17. The smaller grids consist of denser line spacing and focus on areas of special interest, such as the boundary and the upstream end of the Bump. The processing that was applied to either of these datasets, as well as requirements to acquired data in a set-up, that is compliant with 3D migration was introduced. Finally, as the plan view on the glacier bed is probably the most common way to illustrate the subglacial environment, the visualisation of the bed topography as a 3D surface in a 3D cube was introduced, and migration artefacts introduced to the 3D dataset during processing were highlighted.

Chapter 4

Methods: Analysis of 2D and 3D Data

This chapter, presents the analysis of the different datasets. First, a brief motivation for studying the bed properties, subglacial landforms as well as temporal changes is given. This is followed by an introduction to how the bed reflection on all datasets was picked and how the picked twtt were converted to depth (Section 4.2). Following this, reflectivity analysis of data acquired in 2016/17 is described (Section 4.3). Section 4.4 includes the analysis of data acquired in 2007/08 and 2016/17 for temporal changes in topography. Finally, the analysis of surface-radar data using different attributes is described (Section 4.5).

4.1   Motivation

Subglacial processes and properties are known to determine the large-scale behaviour of glaciers and ice sheets (Clarke, 2005). Such properties include the presence of water at the glacier bed, thickness of the water layer, basal roughness and electrical conductivity of basal materials (Copland & Sharp, 2001). The presence of water can lead to reduced basal friction and therefore enhanced sliding or support till deformation and therefore accelerate glacier flow (Blankenship et al., 1987; Siegert et al., 2018). The possible influence of water on ice dynamics can be illustrated using the example of Kamb Ice Stream (formerly Ice Stream C; Catania et al. (2006) and Luthra et al. (2017)). Kamb Ice Stream experienced a shut-down, which was attributed to a range of mechanisms, including loss of lubricating water, and drag from a sticky spot (a topographic high composed of

consolidated sediment or sedimentary rock, enforcing a high basal resistance to ice flow; Luthra *et al.*, 2017).

Subglacial Landforms

Ice flow of palaeo ice streams can be analysed by mapping landforms in the deglaciated area. Subglacial landforms such as MSGLs and drumlins are generated by processes at the ice-bed interface and are a key component of the subglacial environment. Several models describe the theoretical formation of these landforms, but consensus has yet to be achieved. Although many landforms were observed in the deglaciated terrain and in the marine record (Dowdeswell *et al.*, 2016; Ely *et al.*, 2016; Spagnolo *et al.*, 2014), only few studies so far reveal in-situ observations of topography and properties of landforms beneath actively flowing ice (Clyne *et al.*, 2020; King *et al.*, 2007; Riverman *et al.*, 2019; Smith, 1997a; Smith *et al.*, 2007). However, topography of glacial landforms in deglaciated areas might be affected by processes during glacier retreat, interglacial periods and/or weathering (Benn & Evans, 2011; Holschuh *et al.*, 2020), which are not linked to the formation processes. Therefore, detailed knowledge of in-situ subglacial conditions and topography as well as the ice flow in such environments is crucial to constrain information about processes involved in landform formation and evaluate existing models.

Subglacial Properties

Conditions at the bed including subglacial landforms can be studied by analysing signals reflected at the ice-bed interface. The distribution of cold- and warm-based glacier ice (Copland & Sharp, 2001), frozen and wet beds (Bentley *et al.*, 1998; Gades *et al.*, 2000) and subglacial lakes, canals or channels (King *et al.*, 2004, 2007; Murray *et al.*, 2008; Siegert & Ridley, 1998) was studied previously in various places using the radar reflectivity. Following this approach, King *et al.* (2009) attributed spatial variation in radar reflectivity (DELORES data) acquired in 2007/08 on RIS to spatial variation in water-saturation of the sediment and the possible presence of free water. Although most commonly used, the reflectivity of arrivals is only one of many attributes that can be used to identify spatial variations in subglacial material. Initially, Chopra & Marfurt (2005) defined (seismic) attributes as a quantitative measure of characteristics of interest, but attribute analysis can also be used to describe characteristics of radar data. Radar attributes are influenced by the medium through which the signal travels and the interface from which the signal is reflected. Therefore, structural attributes are a

useful tool to analyse the topography and identify structural details in the topography. However, the calculation of most attributes requires data to be arranged in a 3D cube, which is why extensive attribute analysis in glaciology is rare.

Temporal Variation in Bed Topography

Bed properties and topography do not only vary spatially but also over time. Temporal changes in subglacial topography may lead to variations in subglacial conditions and, therefore possibly have an important control on glacier dynamics (Meier & Post, 1987; Motyka *et al.*, 2006; Post & Motyka, 1995). Such changes in bed topography were observed before for RIS by repeated seismic surveys. Parts of the bed are found to be highly mobile, with erosion and deposition occurring over a time scale of ∼5–10 years, while other regions showed no signs of geomorphological changes over time (Smith & Murray, 2009; Smith *et al.*, 2007). The availability of repeated radar surveys (2007/08 and 2016/17), allowed the investigation of the data for temporal changes in topography over a wide area.
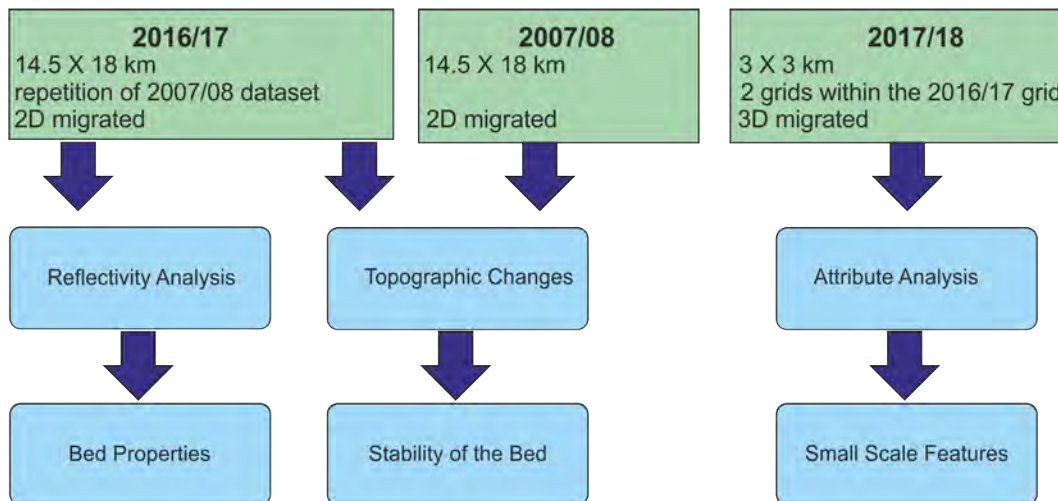
Figure 4.1: Schematic illustrating which dataset were used for which type of analysis.

Figure 4.1 is a schematic to give an overview on which dataset was used for which analysis. In the following, the pick of the bed reflection to determine the bed topography for all three datasets is introduced (Section 4.2). Bed properties and properties of subglacial landforms under RIS were analysed using the spatial pattern of reflectivity of the 2016/17 dataset (Section 4.3), results and interpretation of which are described in Chapter 5. Section 4.4 includes the analysis of

temporal changes in topography between data acquired in 2007/08 and 2016/17. Identified changes in topography are described and interpreted in Chapter 6. The analysis of different attributes in the 3D grids acquired in 2017/18 is described in Section 4.5, results and interpretation thereof are presented in Chapter 7.

4.2 Determination of Bed Topography

An example of a processed radargram acquired in 2007/08 can be seen in Figure 4.2. The bed reflection ($\sim$2200 m depth) in most parts is clearly identifiable. The upper part of the radargram shows englacial reflections to a depth of $\sim$1000 m below the surface. A zone with no visible englacial reflections can be seen above the bed reflection ($\sim$1000–2000 m depth).
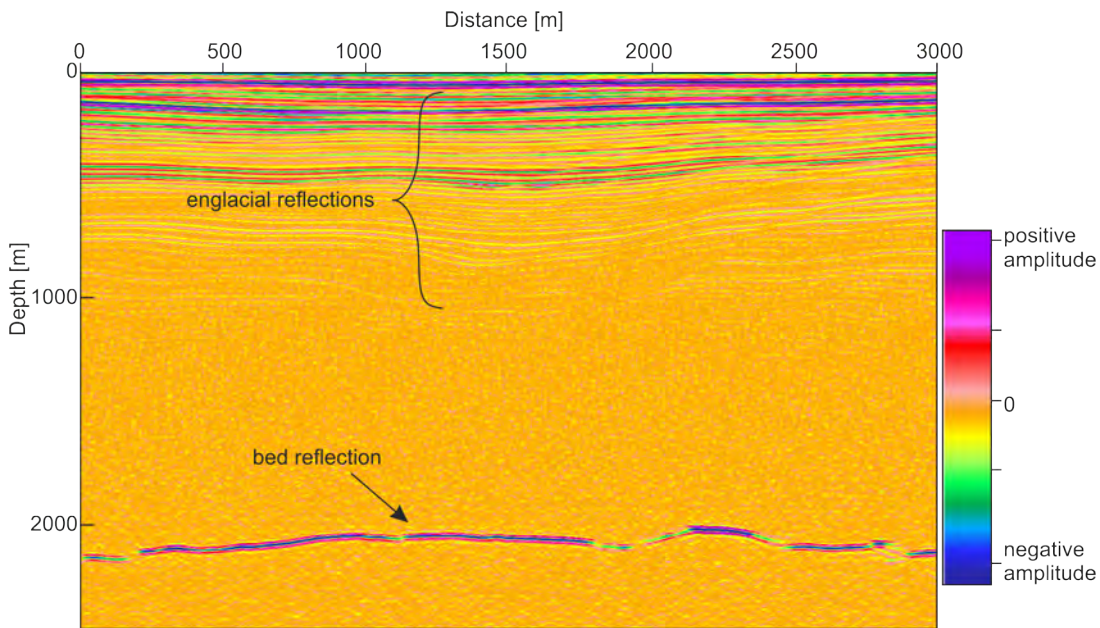
Figure 4.2: Radargram of line 1022 acquired in 2007/08, with englacial reflections and bed reflection labelled.

The bed reflection and the airwave in all datasets were picked on the maximum of the up-going part of the Ricker wavelet (Figure 3.9). By picking both waves in the same location, a possible inaccuracy from picking this location, compared to another location of the wavelet, is compensated. Furthermore, inaccuracies of this picking location are negligible compared to errors from system effects. The twtt of the bed reflection in the 2007/08 and 2016/17 dataset was determined at all trace locations using the phase follower (semi-automated) in ReflexW (Sandmeier

Scientific Software). The bed reflection of data acquired in 2017/18 was picked using a 3D seeded picking algorithm (semi-automated) in Petrel (Schlumberger Software). The application of the semi-automated picking routine was followed by a manual correction of the pick in areas of low SNR and discontinuous bed reflection (e.g. in areas of steep topography).

The resulting picks of twtt were converted to depth, assuming a constant EM wave velocity of $0.168 \, \text{m} \, \text{ns}^{-1}$ (Bogodorosky *et al.*, 1985; Navarro & Eisen, 2009). In the following, the bed elevation is referenced to the WGS84 ellipsoid, whereas depth is referenced to the ice thickness, therefore depth below surface.

4.3 Reflectivity Analysis

Within this section, the calculation of the reflectivity of the bed in data acquired in 2016/17 (Section 3.2) is described. The first part of this section focuses on the calculation of received power and how this power should be corrected for different effects to retrieve the power reflected at the bed (Section 4.3.1). The second part then focuses on the calibration of the reflectivity, calculated for the bed, to be able to link variations in reflectivity to variations in absolute bed properties. A major difference between the data presented here and in other studies is that in most airborne surveys, the amplitude can be calibrated using the reflection of an ice shelf, where properties on either side of the interface (ice and water) are assumed to be known, and therefore reflectivity can be used to describe material properties. However, as for many surface-based surveys, this was not possible here. To be able to assign absolute bed properties to reflectivity, a novel approach to calibrate the reflected power and therefore assign bed properties to the variations in reflectivity is introduced (Section 4.3.2).

For the evaluation of results of the reflectivity, the hydraulic head under RIS was calculated and introduced in Section 4.3.3. To avoid confusion between the different radar data used in the following, the DELORES data are referred to as surface-radar data.

4.3.1 Calculation of BRP From DELORES Data

The amplitude of the received signal was recorded and saved as the 14-bit representative of the voltage. Therefore, amplitudes range between ± 8192, which is equivalent to $\pm 1 \, \text{V}$. To transform these values to Volts, the amplitudes were

divided by 8192 prior to the analysis described in the following. The amplitudes and, therefore reflectivity within this thesis were calculated in Volts (V)[3]. The received power P within a certain time window t_2–t_1 can be calculated following Gades *et al.* (2000):

$$P \equiv \frac{1}{2(t_2 - t_1 + 1)} \sum_{i=t_1}^{t_2} A_i^2, \qquad (4.1)$$

where A_i are the amplitudes. The time window for the bed reflection was chosen to be twice the interval between the maximum and the minimum values of the wavelet, corresponding to the reciprocal of the dominant frequency of the wavelet (Figure 3.9). In this thesis, a time window of 280 ns was chosen. This window is assumed to encompass the power that was reflected at the bed.

The amplitude of the received power is dependent on geometric losses, attenuation within the ice column (influences by ice thickness, temperature, chemistry, layer stratigraphy and presence of crevasses) and the physical properties at the ice-bed interface (roughness, material, topography, water presence and content and water chemistry) as well as system effects (coupling to the surface, antenna frequencies and gains). By correcting the received power for these effects, the reflectivity solely influenced by conditions at the bed can be determined. For data presented here, the coupling between the antennas and the surface as well as system parameters are assumed to be constant over the time of data acquisition. The effects of ice thickness variation (englacial attenuation and geometric spreading) and roughness of the bed contribute the biggest uncertainties when analysing the received power from the bed and are discussed in detail in the following.

4.3.1.1 Effects of Roughness

Scattering of reflected radar energy occurs over a wider range of angles on rough surfaces compared to smooth surfaces. Therefore, the amplitude of nadir-reflected bed echos decreases with increasing bed roughness (Ulaby *et al.*, 1982). MacGregor *et al.* (2013) modelled the effects of basal roughness on the received radar signals and therefore on the reflectivity using the Kirchhoff theory (Ogilvy & Merklinger, 1991). They found, consistent with previous studies, a reflectivity decrease with increasing roughness. The reflectivity decrease at a fixed bed

---

[3]Several studies have presented reflectivity in Volts (Catania *et al.*, 2003; Copland & Sharp, 2001; Gades *et al.*, 2000), while others have presented reflectivity in decibels (dB). The amplitudes A_i in linear units V can be converted to the amplitude a_i the logarithmic unit dB using: $a_i = 20 * \log(A_i/V_{in})$, where V_{in} represents the input voltage (in this case 1 V).

roughness is dependent on the radar wavelength, therefore the wave frequency. Modelling results from MacGregor *et al.* (2013) shown in Figure 4.3 suggest that the reflectivity decrease for a large englacial radar wavelength, which is consistent with the wavelength of the surface-radar data in this thesis (3.5 MHz centre frequency), is small when compared to reflectivity decrease of a higher centre frequency like 150 MHz.
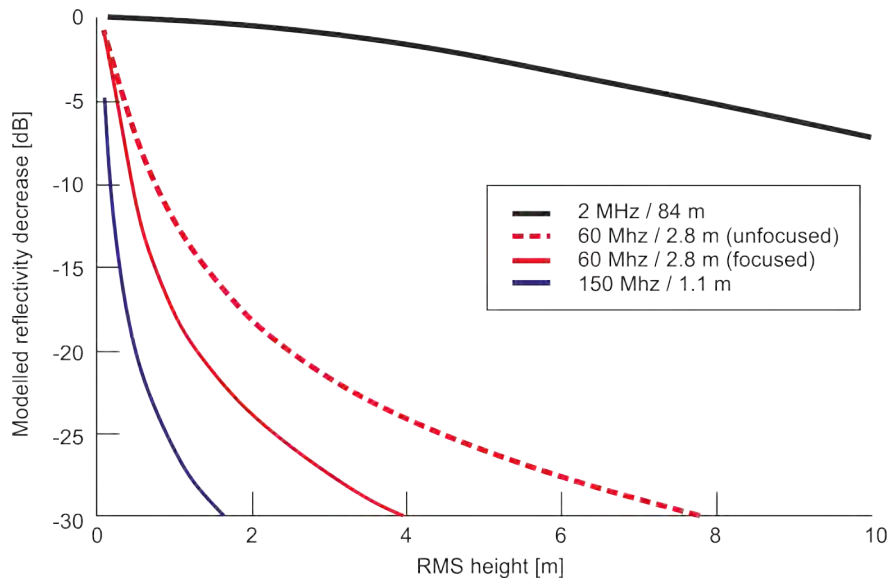
Figure 4.3: Modelling results from MacGregor *et al.* (2013): Frequency dependence of reflectivity decrease due to surface roughness for different englacial wavelength (graph modified after MacGregor *et al.*, 2013).

However, the roughness of the bed of RIS has not been quantified in previous studies. Here the topography recorded in airborne-radar data (Murray *et al.*, 2008, see Section 4.3.2.1.1) has been analysed to evaluate the short wavelength roughness of the bed. The much finer resolution of the airborne-radar data ($\lambda/4$ = 0.25 m) compared to the surface-radar data ($\lambda/4$ = 24 m) allows an estimation of roughness. The roughness on ice stream beds is expected to be much higher perpendicular to the ice flow, when compared to the ice flow direction (Bingham & Siegert, 2009; Cooper *et al.*, 2019; Falcini *et al.*, 2018; Rippin *et al.*, 2014). Airborne-radar data have only been acquired perpendicular to the ice flow (similar to the surface-radar data), therefore giving an indication for the maximum roughness. Figure 4.4 a shows the basal topography (black) from airborne-radar data and the topography with short wavelength features filtered out using a window size of 24 m (orange). This window size is consistent with the reduced Fresnel

zone after migration of the surface-radar data. The de-trended topography using a window size consistent with the reduced Fresnel zone after migration (orange) is shown in Figure 4.4 b. The maximum residual topography for the 24 m window is below 0.4 m.

Following Cooper *et al.* (2019) and MacGregor *et al.* (2013) the roughness can be described by the RMS height of the topography within a certain window:

$$RMS_{height} = (\frac{1}{n-1} \sum_{i=1}^{n} (z(x_i) - z_{detrend})^2)^{1/2}, \tag{4.2}$$

where n is the number of samples in the window, $z(x_i)$ the height of the bed and $z_{detrend}$ the height of the de-trended bed within a window. Calculated RMS_{height} is shown in Figure 4.4 c. The highest RMS_{height} along the entire airborne-radar profile using the 24 m window size is below 0.4 m. For 2 MHz radar waves, a decrease in reflectivity of less than 0.2 dB (<0.03% decrease in amplitude [V]) was modelled for RMS-height of around 0.4 m (Figure 4.3, MacGregor *et al.*, 2013), hence for this study the effect of roughness on the power P received from the bed was therefore assumed to be negligible.
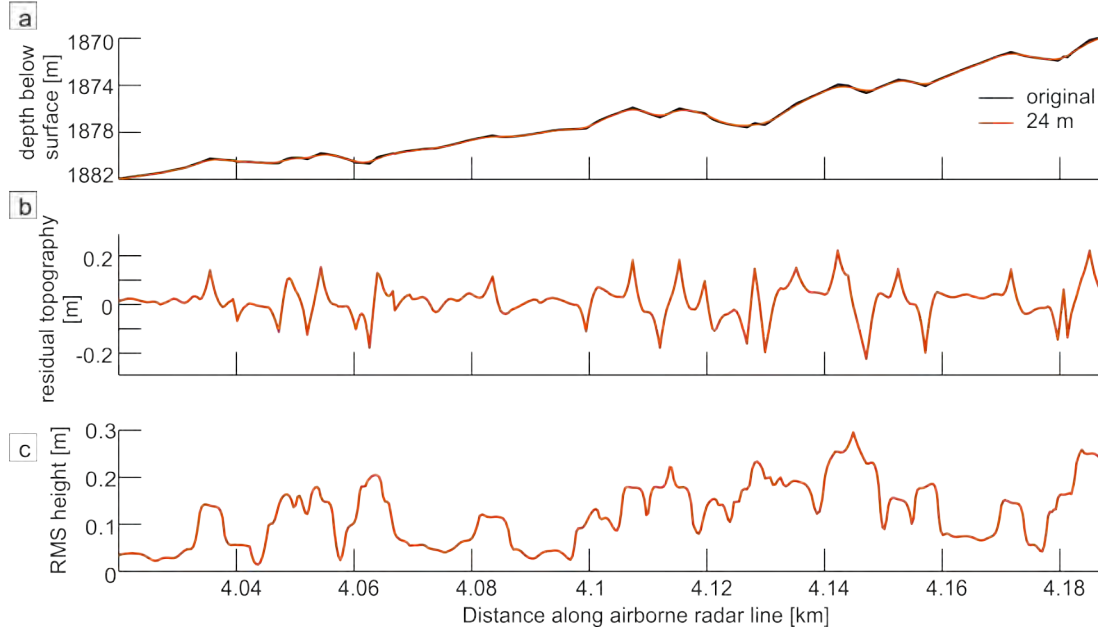
Figure 4.4: Topography along parts of the airborne-radar line R2 (Murray *et al.*, 2008). a) Topography as acquired (black) and smoothed topography using a 24 m window. b) Residual de-trended topography, when subtracting the original and smoothed topography. c) RMS-height of the residual de-trended bed topography.

4.3.1.2 Geometric Spreading and Englacial Attenuation

4.3.1.2.1 Geometric Spreading: In a homogeneous medium, the energy density decays proportional to the square of the wavefront radius. The wave amplitude is proportional to the square root of energy density, and it, therefore, decays as $1/r$. Data acquired in 2016/17 have already been corrected for geometric spreading prior to migration as part of the processing described in Section 3.2.1.

4.3.1.2.2 Englacial Attenuation: By far the biggest challenge is to constrain the englacial attenuation. Englacial attenuation is a function of ice temperature and chemical composition (Jacobel *et al.*, 2009; MacGregor *et al.*, 2007). The accuracy of correcting for englacial attenuation using uniform attenuation rates, and the applicability of such for small study areas is the subject of much debate. On the one hand, Matsuoka (2011) demonstrated that the attenuation rate could vary significantly over distances of 120 km. He suggested to calculate attenuation rates using estimates of ice temperature and chemistry. However, for RIS no data are available for constraining information about variations in chemistry or the temperature of the ice on the scale of this study (14.5×18 km). On the other hand, Ashmore & Bingham (2014) recommended the usage of a uniform englacial attenuation to be appropriate for small region, with unchanging englacial properties. Schroeder *et al.* (2016) found that using segments of the data to analyse effects of attenuation can improve the spatial resolution but, at the expense of resolution; they further suggested that segments should consist of data with sufficient topographic relief.

Although modelling of spatial variations in englacial attenuation was not possible for RIS, the *internal reflection power* (IRP), as a measure for energy absorbed by the ice can be calculated. Variations in power received from within the ice column, either for the whole ice column or for individual englacial reflectors can be analysed to investigate whether changes in received power are caused by changes in the power transmitted through the ice or changes of the bed properties. Variations in IRP could, for instance, be caused by variations in ice conditions like crevasses at the surface (Gades *et al.*, 2000). Murray *et al.* (2008) calculated the IRP for the whole ice column along their airborne-radar profiles acquired over RIS, and found that values do not vary significantly along the airborne-radar tracks, which strengthened the assumption that received power is mainly influenced by the properties at the bed and a uniform correction can be
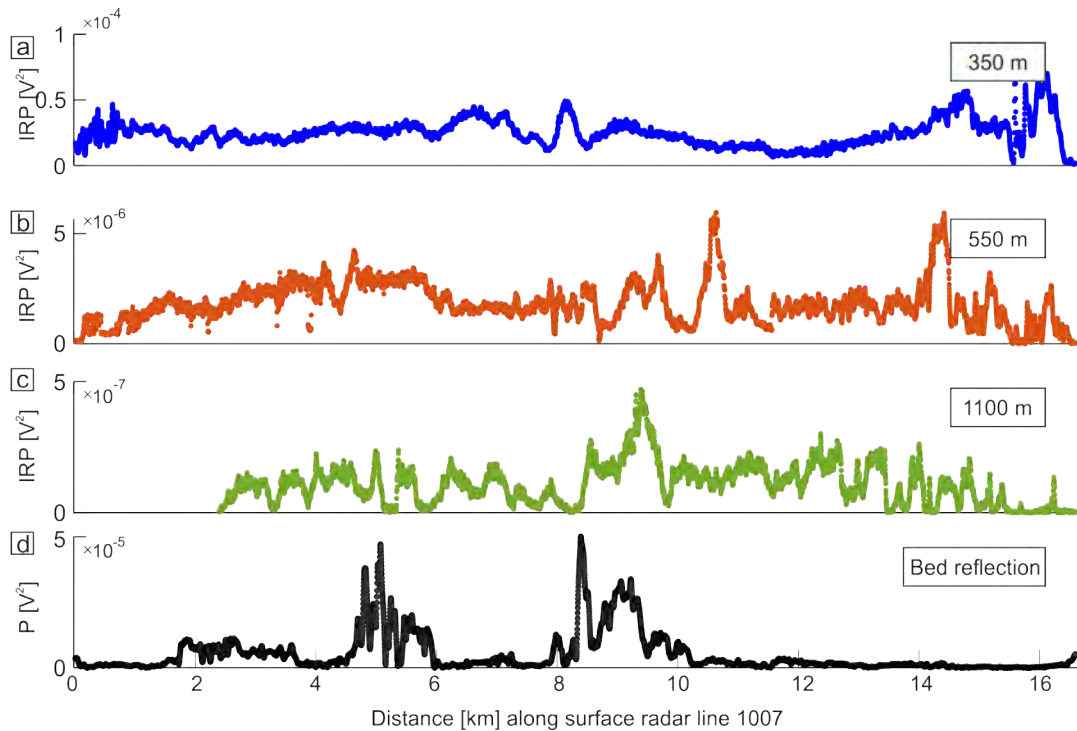
Figure 4.5: IRP of internal layers in line 1007 in approximately a) 350 m, b) 550 m, c) 1100 m depth. d) received power P calculated for the bed reflection.

applied to the data acquired on RIS. Within this thesis, the IRP is calculated using Equation 4.1, first along a choice of englacial reflections (Figure 4.5, using a 280 ns window size) and second for the whole ice column (Figure 4.6, window size 21600 ns). No visual correlation between peaks in IRP and troughs in received power can be seen comparing individual englacial reflectors and the bed reflection. Furthermore, no correlation between the peaks and troughs can be seen between the IRP calculated for the whole ice column and received power. An increase in IRP (calculated for the whole ice column) can be seen in the western part of the line (towards the Ellsworth Mountains), when compared to the eastern part (towards the Fletcher Promontory, Figure 4.6). However, the magnitude of change is smaller when compared to the magnitude of change seen for received power.

4.3.1.3 Correction for Effects of Varying Ice Thickness

Losses due to englacial attenuation (as well as geometric spreading) should be a smoothed function of the ice thickness (Gades *et al.*, 2000). Therefore, an exponential decay function (coloured lines in Figure 4.7 and 4.8) is fitted to the
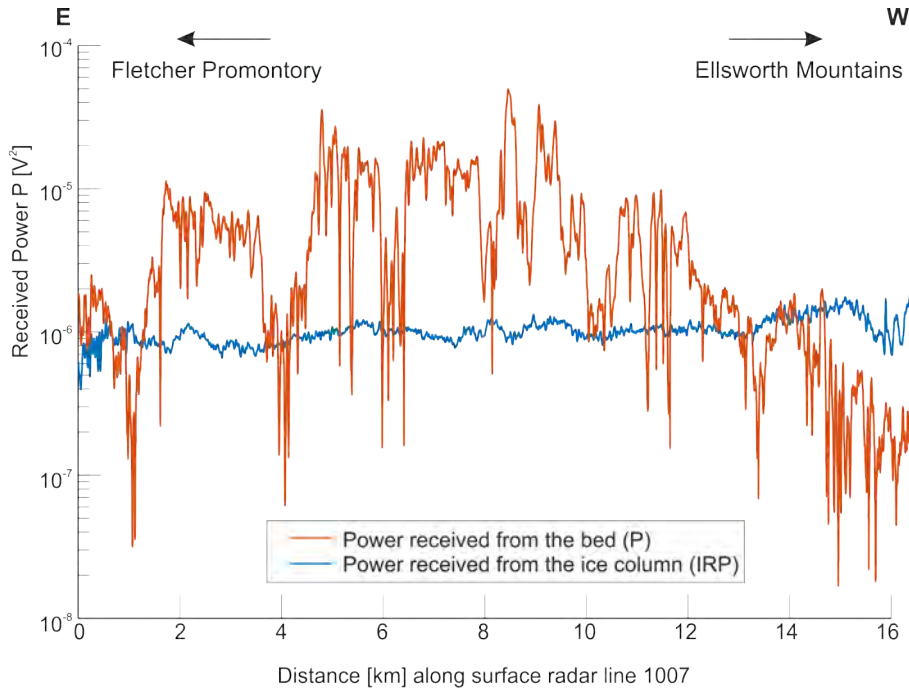
Figure 4.6: IRP calculated for the whole ice column (window size 21600 ns) and reflected power P from the bed of data acquired along line 1007.

received power vs. twtt-pairs (blue dots). This fitted function, called *estimated bed-reflection power* (BRP$_{est}$) describes the variation in receiver power, solely due to variations in ice thickness (Gades *et al.*, 2000). Ideally, this BRP$_{est}$ is calculated analysing englacial attenuation within an area of relatively homogeneous ice and bed properties but varying ice thickness. The final *bed-reflection power* (BRP) is calculated by dividing the received power P by BRP$_{est}$. To account for variations in englacial attenuation over the study area as well as known changes in bed properties, the BRP$_{est}$ was analysed for 5 different areas:

1. Based on a fit to all data (14.5×18 km). Values for the calculation of BRP$_{est}$ were chosen to be $a = 226.7$ and $b = -0.0006591$, red line Figure 4.7 a and 4.8 a,

2. Based on a fit to data in the upstream part of RIS (lines 1016–1030 (7×18 km)). The bed properties in this area were assumed not to change. Values for the calculation of BRP$_{est}$ were chosen to be $a = 318.5$ and $b = -0.0006715$, yellow line Figure 4.7 a,

3. Based on a fit to data in the downstream part (1001–1015 (7×18 km)) of the study area (around transition zone). Bed properties in the downstream

part of this area are known to change from soft to stiff till (Smith & Murray, 2009). Values for the calculation of BRP_{est} were chosen to be $a = 559$ and $b = -0.000695$, blue line Figure 4.7 a,

4. Based on a fit to data on the western half of the RIS (towards the Ellsworth Mountains (14.5×9 km)). Values for the calculation of BRP_{est} were chosen to be $a = 66.74$ and $b = -0.000598$, blue line Figure 4.7 a,

5. Based on a fit to data on the eastern half of the RIS (towards the Fletcher Promontory (14.5×9 km)). Values for the calculation of BRP_{est} were chosen to be $a = 2.595$ and $b = -0.0004883$, green line Figure 4.7 a.
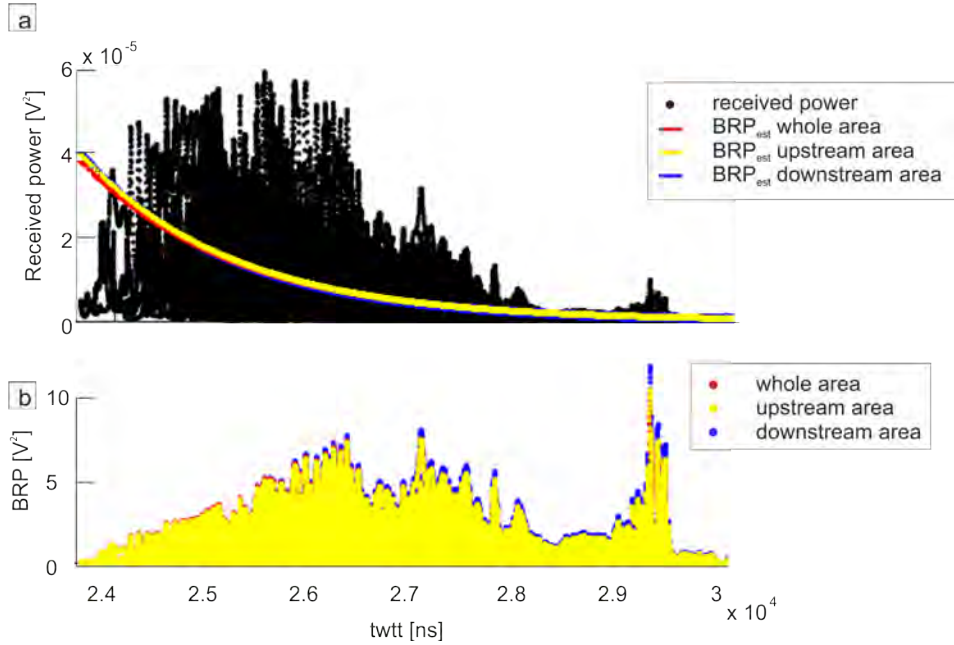
Figure 4.7: Received power from the bed and BRP. a) received power P (black) from recorded amplitudes in 2016/17 over the whole study area. The BRP_{est} for different twtt for correction of attenuation according to different datasets is shown by the red (whole study area), yellow (upstream area) and blue (downstream area) line. b) BRP in 2016 corrected for englacial attenuation using the different BRP_{est} functions as shown in a.

The difference between the BRP corrected using only the upstream or downstream part of the study area (yellow and blue dots in Figure 4.7 b) is small, when compared to differences seen between the data in the western and eastern part of the study area. The BRP used in the following was corrected for englacial attenuation using BRP_{est} calculated based on the whole dataset. However, to
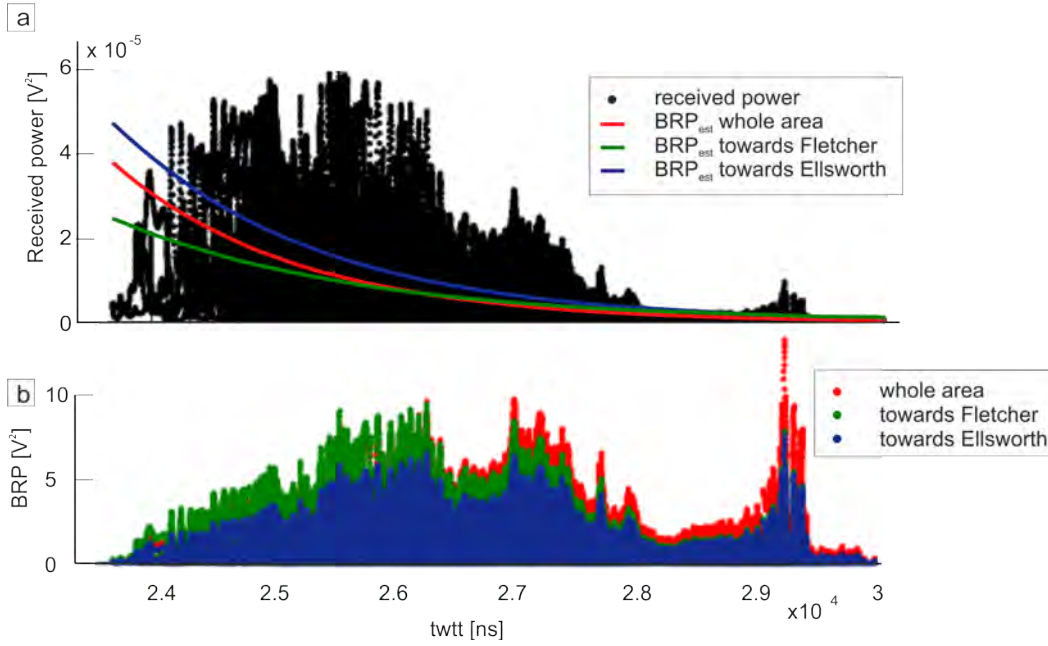
Figure 4.8: Received power from the bed and BRP. a) received power P (black) from recorded amplitudes in 2016/17 over the whole study area. The BRP_{est} for different twtt for correction of attenuation according to different datasets is shown by the red (whole study area), green (towards Fletcher Promontory) and blue (towards Ellsworth Mountains) line. b) BRP in 2016 corrected for englacial attenuation using the different BRP_{est} functions as shown in a.

account for uncertainties in englacial correction error bars accounting for the variations described before are introduced. These error bars are only shown in figures, where data are shown over a large distance, therefore great topographic relief, where the application of a different attenuation correction would change the BRP and, therefore reflectivity pattern. When describing the reflectivity of a local area, no error bars were included as they do not add value to the relative description.

4.3.1.4 Resulting BRP and Reflectivity

The BRP, as defined before, is a measure of the power reflected at the bed, corrected for ice thickness variation (Chu *et al.*, 2016a; Jacobel *et al.*, 2010) and is proportional to the square of the reflection coefficient R, which can be used to infer bed properties. In the following, the term reflectivity is termed $\sqrt{\text{BRP}}$ and is measured in Volts. However, it is important to note that the estimates of reflectivity that are obtained here are not absolute but instead are relative

indicators of reflection strength.

4.3.2 Calibration of the Reflectivity

If the amplitude recorded during surveys can be calibrated, absolute values of reflectivity and therefore bulk relative permittivity could be calculated for sub-glacial material (e.g., Murray *et al.*, 2008). However, the surface-radar survey in 2016/17 did not include acquisition of data on an ice shelf. Calibration of surface-radar amplitudes using the reflection of an ice shelf as a control reflection point (where the dielectric contrast is known, such as at the ice-water interface at the base of an ice shelf) is therefore not possible. Instead a different approach to calibrate the reflectivity was taken in this study. Under the assumption of known properties (bulk relative permittivity) of the bed (and the ice) in at least one location (the so-called reference area) the reflection coefficient in this location can be calculated as introduced in Equation 2.5. This reflection coefficient calculated for the reference area can then be used to calibrate the reflectivity calculated along the entire surface-radar dataset, as changes in the reflectivity are proportional to changes in the reflection coefficient. Assuming the ice properties to be uniform over the whole area (as already assumed for the correction of attenuation effects), the bulk relative permittivity of subglacial material can be calculated for every other point along the surface-radar line. Using the mixing model (Equation 2.6) by Mount & Comas (2014), bulk relative permittivity can be calculated for a range of properties of the matrix, the water in the pore space and porosity. Keeping the limitations of this mixing model in mind (e.g. neglecting effects such as mixture of minerals in the matrix, geometry of grains and pore space, effect of grain contacts), changes in reflectivity can be linked to changes in porosity. Variations of the reflection coefficient for different porosities and different matrix materials can be seen Figure 4.9.

Assuming the relative permittivity of the matrix material as well as the water in the pore space to not change, changes in reflectivity were linked to changes in porosity, therefore changes in water content within the sediment. In the following, the bed properties inferred from previous studies, which are then used to identify a suitable reference area, are described. This is followed by the description of the parameters assigned to the reference area. These parameters are then used to calculate porosities along the whole surface-radar line.
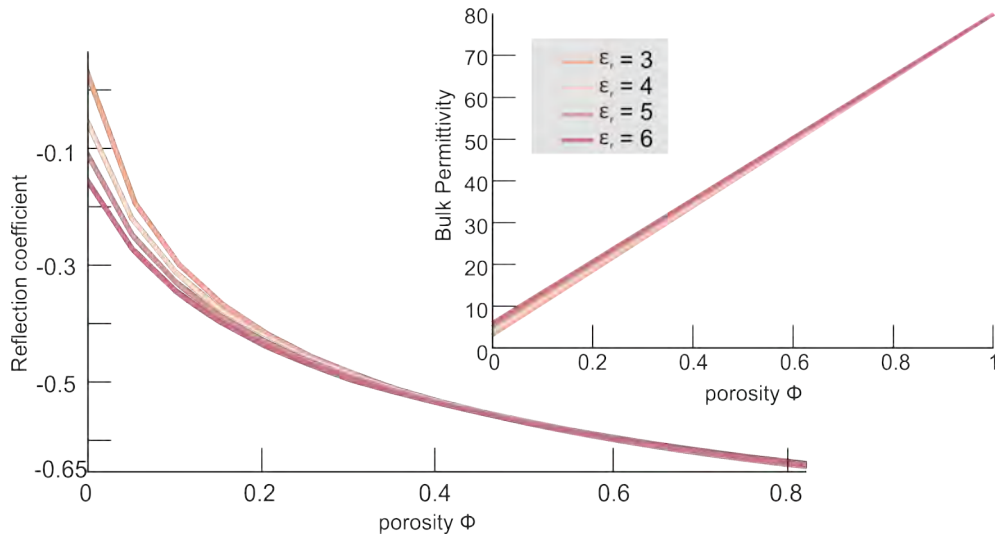
Figure 4.9: Variation of reflection coefficient with porosity according to Equation 2.5 and variations in relative bulk permittivity according to Equation 2.6, for fully-saturated sediment, with different matrix permittivities, overlain by ice. Values for relative permittivity for the matrix material $\epsilon_{r(matrix)}$ are taken from Daniels (1996); Davis & Annan (1989) and Martinez & Byrnes (2001).

4.3.2.1 Published Data on RIS and Interpretation of Bed Properties Thereof

Data used for the definition of a reference area and the properties thereof consist of airborne-radar and seismic acoustic impedance data acquired in 2004/05 on RIS. The airborne-radar and seismic data have been described and interpreted in Murray *et al.* (2008); Smith & Murray (2009) and Smith *et al.* (2007), and are only briefly summarised in the following. Results and some interpretations of airborne-radar and seismic data can be seen in Figure 4.10. Both lines coincide with surface-radar line 1007 (Figure 3.4), although the seismic and airborne-radar lines are shorter than the surface-radar line.

4.3.2.1.1 Airborne-Radar Data: Several lines of airborne-radar data (PASIN, 150 MHz centre frequency) were acquired in 2004/05, although only results and interpretation of line R2 of Murray *et al.* (2008) are part of this thesis, as this is the only line that coincides with both seismic and surface-radar profiles. The airborne-radar amplitude of the bed reflection was calibrated using the reflection of the floating part of Carlson Inlet (Figure 2.4), where electrical properties on either side of the basal reflection can be assumed (Murray *et al.*, 2008). Fifty
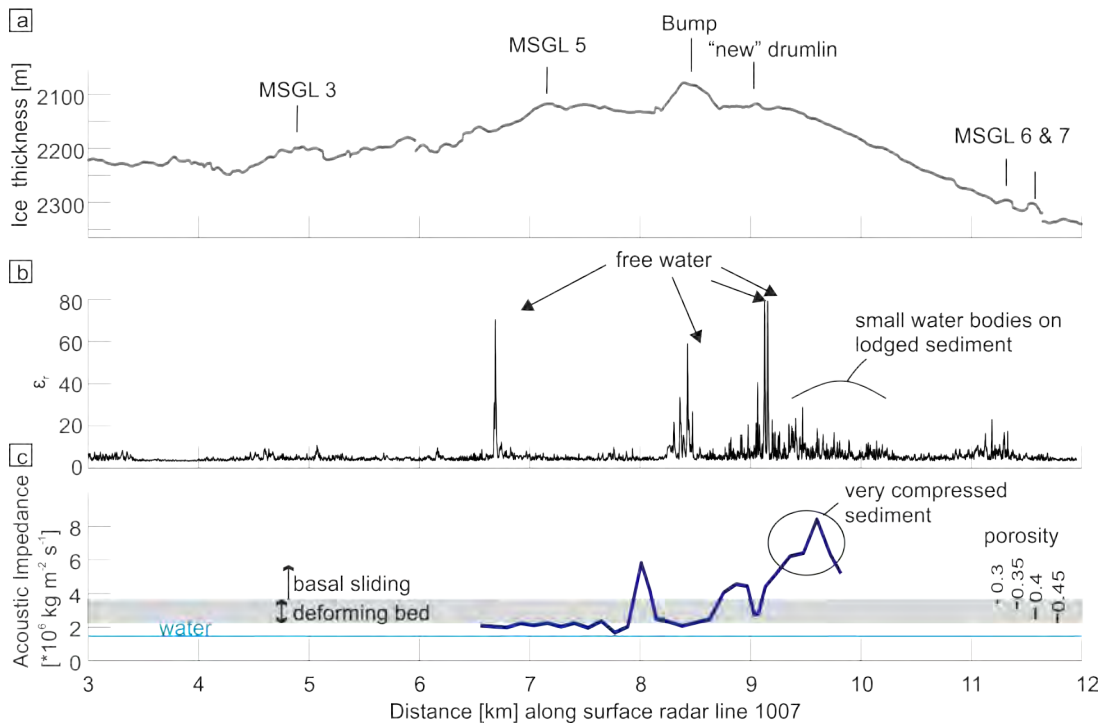
Figure 4.10: Results from previous studies on bulk relative permittivity and acoustic impedance of the bed of RIS. a) Topography of the bed with annotation of some landforms, b) bulk relative permittivity from airborne radar (Murray *et al.*, 2008) and c) acoustic impedance with ranges of porosity (Smith & Murray, 2009; Smith *et al.*, 2007). The grey filled box show values of 2.2–$3.8 \times 10^6 \, \mathrm{kg \, m^{-2} \, s^{-1}}$, corresponding to soft, deformable sediment. The cyan line shows acoustic impedance of water.

traces were integrated and recorded every 40 cm along track, following which the data were smoothed using a 20-trace running mean. The theoretical vertical resolution of this dataset is 0.28 m (quarter of the wavelength λ in ice ($\lambda = 150$ Hz / 0.168 m ns^{-1})).

The interpretation of airborne-radar data in Murray *et al.* (2008) included four spots of high bulk relative permittivity, interpreted as water at the ice-bed interface (relative permittivity=80), at 6.8, 8.5, 9.1 and 9.4 km (Figure 4.10). Two of these points are located on the crest of landforms (Bump and "new" drumlin). Scattering of values of airborne-radar permittivity in areas where the bed is assumed to consist of lodged sediment has been interpreted to originate from numerous small water bodies or cavities at the ice bed interface. No such scattering was found for the area assumed to consist of deforming sediment, which, together with results of waveform analysis, led to the interpretation that the sediment and ice are in direct contact.

Issues With the Airborne-Data: Although the airborne-radar data were calibrated, the absolute values of bulk relative permittivity calculated for parts of the bed, where no water appears to be present, are erroneous. In these areas, most values of bulk relative permittivity are below 10 or even below 5. Bulk relative permittivity (well) above 10 can be explained by wet sediment (e.g. ϵ_r=20–30 for wet sediment (Davis & Annan, 1989)), while bulk relative permittivity between 10–20 could be a sediment with porosity of 0.2. Bulk relative permittivity below 10 implies a significant amount of ice in the pore space, a crystalline bedrock (e.g., granite ϵ_r=4–6 (Davis & Annan, 1989)) or very compressed sediment. According to the absolute values of bulk relative permittivity calculated and published in Murray *et al.* (2008), most of the bed consists of very compressed sediment, sediment with partly frozen pore space or crystalline bedrock. However, from seismic acoustic impedance measurements, it is clear that this is not the case, which imply that the airborne-radar data were erroneously calibrated. A correction for this error is necessary to be able to consider the bulk relative permittivity calculated along the whole line of airborne-radar data. However, applying this correction and identifying where exactly the airborne-radar data were erroneous was not within the scope of this thesis. As the amplitude of the airborne-radar data has been calibrated using the reflection of an ice-water interface at an ice shelf, the bulk relative permittivity calculated for this area as well as other areas interpreted as water was assumed to be correct. Within this thesis, only values

of high bulk relative permittivity (indicating water) within the data by Murray *et al.* (2008) were considered.

4.3.2.1.2 Seismic Impedance: A seismic reflection profile (Smith & Murray, 2009; Smith *et al.*, 2007) with a length of 3.6 km and midpoint spacing of 5 m was acquired in 2004/05, two weeks prior to the airborne-radar data. The dominant frequency of the seismic dataset is ∼150 Hz. Acoustic impedance (the product of seismic velocity and density) of subglacial material along the profile was calculated following Smith (1997b): The reflection coefficient of the ice-bed interface was calibrated using the first multiple of the bed reflection. Data initially published in Smith & Murray (2009) and Smith *et al.* (2007) were erroneously corrected for attenuation. This was corrected by Andy Smith (BAS) within the data presented here by using the approach for correction of englacial attenuation proposed by Holland & Anandakrishnan (2009). Based on this calibration and assumed impedance for the ice overlying the bed, the acoustic impedance of the bed material was calculated. Acoustic impedance can be used to differentiate between non-deforming and deforming sediment (Atre & Bentley, 1993; Smith, 1997a), but it is important to be mindful that it can only be used to differentiate between different gross rock types. Sediment porosities are often assigned to acoustic impedance on the basis of data from Whillans Ice Stream (Atre & Bentley, 1993, 1994; Blankenship *et al.*, 1987). In these studies, wide-angle seismic reflection measurements and sediment samples from the bed of Whillans Ice Stream were used to link porosity and acoustic impedance. Acoustic impedance of more than $3.85{\times}10^6$ kg m^{-2} s^{-1} is associated with lodged (non-deforming) sediment and a porosity of $\leq$0.3 (Atre & Bentley, 1993; Muto *et al.*, 2019). Acoustic impedance values associated with soft, water-saturated sediment that is deformable (porosity = 0.3–0.5) vary between 2.3–3.8$\times10^6$ kg m^{-2} s^{-1}. Corresponding ranges of till porosity to acoustic impedance presented in Figure 4.10 c were taken from Atre & Bentley (1993). The acoustic impedance of water is around $1.49{\times}10^6$ kg m^{-2} s^{-1} (cyan line in Figure 4.10). The maximum error in the acoustic impedance for RIS using this approach is determined to be $\pm0.5{\times}10^6$ kg m^{-2} s^{-1} (Smith, 1997b).

Acoustic impedance calculated for the bed of RIS suggests the region between 6.5–7.9 km (Figure 4.10 c) consists of sediment with high porosity (>0.45). The high impedance at 8 km implies a more compacted sediment compared to the surrounding area. The Bump (8.3 km) and "new" drumlin (9 km) show values

of impedance within the range of deforming sediment (i.e. porosity >0.3). The only area where acoustic impedance implies a very compressed sediment (porosity <0.3), possibly poorly lithified rock, is between 9.5–10 km.

4.3.2.1.3 Different Sensitivities of Seismic and Radar Waves: The availability of airborne-radar as well as surface-radar and reflection seismic data enables a detailed study of basal processes at different resolutions could broaden the potential for understanding the subglacial conditions. Nevertheless, comparisons of results obtained by seismic and radar wave propagation are not straightforward. The main influences on radar wave propagation are density, conductivity, crystal orientation fabric and temperature (liquid water content), whereas the main influences on seismic waves are elastic moduli, density, crystal orientation fabric and temperature of the medium. In general, acoustic impedance should decrease with increasing porosity since water typically softens a material, while radar reflectivity would increase (due to increasing water content and the stronger dielectric contrast with the overlying ice). Furthermore, a direct comparison between acoustic impedance and radar reflectivity is not trivial, as impedance describes properties of a layer, while reflectivity is a property of the boundary of two layers. Within this thesis, the properties of the upper layer, which represents ice, are assumed not to be changing, therefore changes in the surface-radar reflectivity are a proxy for changes in bulk relative permittivity of the underlying material and, therefore the electromagnetic impedance. However, as the surface-radar reflectivity is not calibrated, no absolute values of electromagnetic impedance can be calculated. Acoustic impedance is high for sedimentary rock (3–$11 \times 10^6 \, \mathrm{kg \, m^{-2} \, s^{-1}}$ (Gardner *et al.*, 1974)) or crystalline rock ($>16 \times 10^6 \, \mathrm{kg \, m^{-2} \, s^{-1}}$ (Salisbury *et al.*, 2003)) and will result in a stronger seismic reflection, where the theoretical radar reflectivity shows only little difference between a sand of low porosity (R= 0.01– -0.11, $\epsilon_{r(matrix)}$= 3–5) and a sandstone (R= -0.11– -0.27 , $\epsilon_{r(wetsandstone)}$= 5–10), or a granite (R= -0.19, $\epsilon_{r(wetgranite)}$= 7). This relationship is reversed when a water layer of sufficient thickness is present. The acoustic impedance of water is low ($\sim 1.49 \times 10^6 \, \mathrm{kg \, m^{-2} \, s^{-1}}$), whereas the sensitivity of radar waves to water (R=-0.68 ($\epsilon_{r(water)}$= 80)) is much higher when compared to seismics. Due to the sensitivity of radar waves to the occurrence of water, radar surveys are often used to investigate water distribution and water content at the bed as well as water inclusion in ice (Navarro *et al.*, 2005).

Owing to the attenuation through electrical conductivity of subglacial till, radar seldom gives reliable information about the subglacial environment, whereas seismic waves can penetrate more reliably beyond the ice-bed interface and reveal properties of subglacial material, like seismic velocities (Navarro *et al.*, 2005; Pakiser & Black, 1957) or deformability of the material (Atre & Bentley, 1993; Smith, 1997b). Despite the challenges of combining seismic and radar data, previous studies by Bingham *et al.* (2010); Endres *et al.* (2009) and Ghose & Slob (2006) demonstrate the capability of combining seismic and radar data to obtain information about topography and material properties such as water content in soils and ice.

4.3.2.2 The Choice of the Location of the Reference Area

Material properties inferred using changes in reflectivity compared to a reference area of known properties are obviously highly dependent on the reliability of the properties chosen for the reference area. Therefore, the reference area was located along surface-radar line 1007, where the airborne-radar and the seismic lines coincide. Furthermore, this is the approximate location of a 2018/19 drilling campaign (Smith *et al.*, 2021) from which samples of the bed material were retrieved. The samples from this campaign have not been analysed, hence were not available for this thesis, but represent prospects for further validation of the results presented here in the future. Generally speaking, the acoustic impedance would be expected to decrease with increasing porosity, while the surface-radar reflectivity would increase with increasing pore space due to increasing water content. However, no empirical relation to convert acoustic impedance to radar reflectivity exists. Figure 4.11 shows values of reflectivity calculated along the line of acoustic impedance. Much more data are available for surface-radar reflectivity (every 2 m) compared to acoustic impedance (∼every 117 m). The orange marked values of reflectivity are the nearest neighbour to locations of acoustic impedance data. Values of reflectivity and acoustic impedance marked in orange were cross-correlated as shown in Figure 4.12. The correlation is not linear, but the poorly constrained trend is regressional (see value describing the slope). This regressional trend shows that there is a correlation between both variables, but due to this non-linear relation between acoustic impedance and radar reflectivity, the surface-radar data could not be calibrated using the whole length of the seismic profile. Therefore, the reference area was limited to an area where
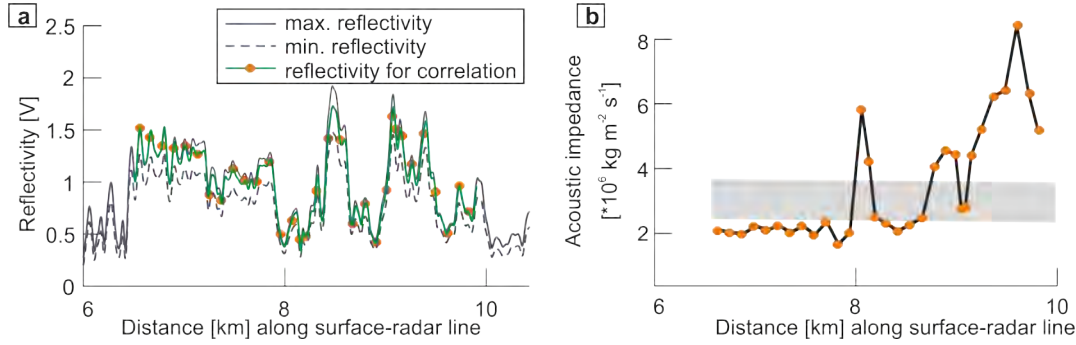
Figure 4.11: Surface-radar reflectivity compared to seismic acoustic impedance: a) Surface-radar reflectivity along line 1007. The green line represents the reflectivity corrected for attenuation calculated based on BRP_{est} for the whole study area. The maximum and minimum reflectivity correspond to the uncertainty in reflectivity arising from uncertainty of correction for englacial attenuation. b) Acoustic impedance along line C1-04 as shown in Figure 4.10. Orange dots correspond to the nearest neighbour between the location for calculated acoustic impedance and reflectivity.

seismic and radar waves are expected to react similarly to bed properties (Section 4.3.2.1.3). The reference area was therefore limited to an area where the bed neither consists of consolidated sediment or bedrock, nor where liquid water is expected to be present. Concerning the first, this rules out most of the seismic line between 8.5–10 km. The latter concerns the crest of landforms, where the presence of liquid water was interpreted from airborne-radar data (Murray et al., 2008). Hence, the area where the surface-radar and seismic waves are expected to react similarly is between 6.3–7.7 km. This portion of surface-radar line 1007 is now referred to as the reference area.

4.3.2.3 Bed Properties Assigned to the Reference Area

Values of acoustic impedance vary between 1.66–$2.35 \times 10^6 \, \mathrm{kg \, m^{-2} \, s^{-1}}$ in the reference area, implying soft sediment. To account for uncertainties arising from the analysis of acoustic impedance, a porosity of 0.4–0.5 was assigned to the reference area. There is no further information on the properties (relative permittivity) of the matrix material available. Therefore a range of relative permittivity of 3–6, representing the range of values found for dry sand (Figure 2.9) were assigned to the matrix material of the reference area. The pore space of the sediment is assumed to be fully saturated by water, therefore a relative permittivity of 80 was assigned to the pore space. The resulting bulk permittivity (of a water-saturated
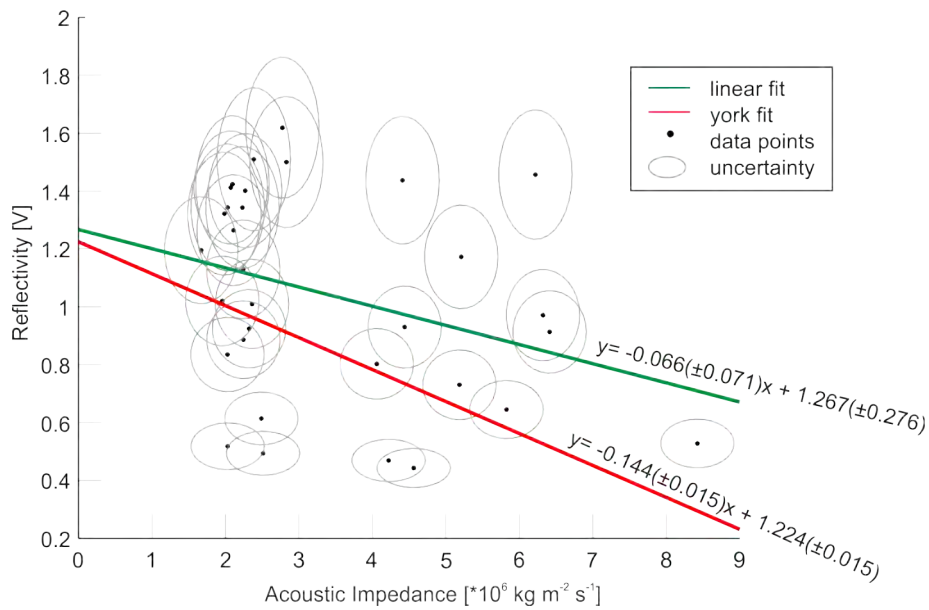
Figure 4.12: Cross-correlation of acoustic impedance and surface-radar reflectivity. Black dots represent the values, while the ellipsoids around the dots represent their corresponding uncertainties. The dashed green trend line is a simple linear fit (least-squares) approach, where the abscissa (acoustic impedance) and ordinate (reflectivity) values are assumed to be known perfectly (no uncertainty taken into account). A more representative linear trend (solid red line) was calculated following the method of York *et al.* (2004), where uncertainties in both acoustic impedance and reflectivity values are taken into account, including their variability from point-to-point. For values of reflectivity and acoustic impedance used for this correlation see Figure 4.11 orange dots.

sediment) in the reference area ranges between 21–32 (Figure 4.9). This range of material properties was assigned to all reflectivity values calculated for the reference area, including the uncertainties arising from the correction of englacial attenuation (see Table 4.1). Using the relative changes in reflectivity, compared to the reference area, values of porosity can now be inferred along the whole dataset using Equation 2.5 and Equation 2.6.

Table 4.1: Properties assigned to the reference area, including the range of reflectivity within the reference area.

	Reference area
Reflectivity [V]	0.86–1.67
porosity	0.4–0.5
permittivity of matrix material	3–6
bulk permittivity	21–32

Using the approach described above, areas of high reflectivity will result in areas of higher porosity, therefore high water content, compared to areas of lower reflectivity. As part of the analysis of this chapter, regions of high water content are compared to the hydraulic head in Section 5.1.4. Therefore, the calculation of the hydraulic head is introduced in the following.

4.3.3 Hydraulic Head

Laminar water flow within a porous medium can be described by Darcy's law, where water flux is described by the hydraulic conductivity, hydraulic head, flow length and the flow cross-sectional area. Therefore, the water flow within a porous sediment depends on the hydraulic head as well as the hydraulic conductivity. Hydraulic conductivity depends on the intrinsic permeability of the material, the degree of saturation, density, viscosity of the fluid (Craig, 2004). The hydraulic head, under the assumption of negligible effective pressure (Diez *et al.*, 2019; Livingstone *et al.*, 2013) is given by

$$\Phi_{head} = h - (1 - \frac{\rho_{ice}}{\rho_{water}})H, \tag{4.3}$$

where h is the ice surface elevation, H the ice thickness, $\rho_{ice} = 910\,\mathrm{kg\,m^{-3}}$ and $\rho_{water} = 1000\,\mathrm{kg\,m^{-3}}$ (Diez *et al.*, 2019), respectively the density of ice and water.

In many studies a simplified approach to calculate water flow is applied (Copland & Sharp, 2001; Livingstone *et al.*, 2013; Wright *et al.*, 2016), where storage

and flow of water underneath ice is determined by the hydraulic potential, which is defined by the hydraulic head with a scaling factor of the Earth gravitation. Therefore, the hydraulic head can be used to infer possible water flow paths and accumulation of water. Water is assumed to accumulate in minimas of the hydraulic head and flows along the steepest gradient (Livingstone *et al.*, 2013). Due to the difference in density between water and ice ($\rho_{water} = 910\,\mathrm{kg\,m^{-3}}$ and $\rho_{ice} = 1000\,\mathrm{kg\,m^{-3}}$), the ice-surface gradient is known to be $\sim$10-times more important than the bed gradient (Kamb, 2001). For the calculation of the hydraulic head, the surface elevation and ice thickness data presented by King *et al.* (2016) were used. The accuracy of the ice thickness is assumed to be $\pm 3\,\mathrm{m}$, while the surface elevation in the WGS84 ellipsoid might contain errors of 10–20 m.

4.4 Temporal Changes in Bed Topography

Surface-radar lines acquired in 2007/08 were repeated using a comparable system setup in 2016/17 (Section 3.2). The repeated radar lines were acquired perpendicular to the ice flow and cover an area of 14.5×18 km (Figure 3.4). Section 4.4.1 describes the detection of topographic changes along the surface-radar lines. Detected topographic changes are described and discussed in Chapter 6.

4.4.1 Detection of Topographic Changes

Temporal changes in bed topography were identified calculating the difference in the picked twtt of the bed reflection (Section 4.2) between surface-radar data acquired in 2007/08 and 2016/17 (Figure 3.4 and Section 3.2). As described in Section 3.2 the spatial sampling of the two datasets differs. To overcome this, the nearest neighbour in the 2016/17 data to each trace location in 2007/08 data was identified. Differences in twtt were then calculated using only those selected data.

4.4.1.1 Threshold for the Identification of Topographic Changes

To limit the number of possible changes, thresholds were implemented: topographic differences at the bed were only considered significant if height changes of at least 3 m were calculated over a distance of at least 30 m along the radar line (4 traces in the 2007/08 dataset). The lower boundary on the spatial extent

of the topographic differences roughly equals the theoretical horizontal resolution of the data (24 m), furthermore, a value spanning several traces, was necessary to compensate for "jumps" in the picked twtt of the bed reflection due to spatial variations in SNR. The vertical limit was chosen based on considerations of the relative accuracy when comparing the two datasets. The peaks of the recorded wavelet of the bed reflection in both datasets are identifiable within ±2 samples (i.e. ±16 and 20 ns twtt, respectively), which equals an ice thickness of 1.3 and 1.67 m, respectively. Therefore the accuracy of vertical differences between the two datasets was chosen to be around 3 m.

Each difference in twtt identified as described was then validated by comparing the radargram of both datasets, to ensure a high confidence in the pick of the bed reflection. Following this, englacial reflections above and around observed topographic changes were examined to ensure a change in bed topography is not caused by surface or englacial conditions during acquisition. Moreover, the adjacent lines upstream and downstream of each identified topographic change were examined to ensure changes affecting several lines were noticed even if only changes identified in one line fell within the threshold.

Following the thresholds, topographic changes are defined as an increase or decrease in topography of at least 3 m height and over a distance of at least 30 m (Figure 4.13).
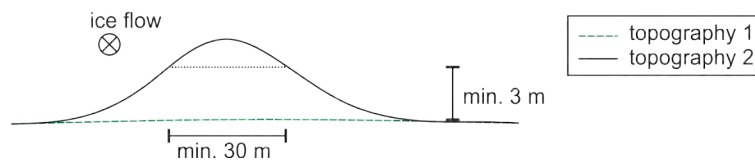
Figure 4.13: Schematic illustration the minimum requirement for a topographic change to be detected.

4.5 Attribute Analysis

Two 3D radar grids acquired in 2017/18 (Section 3.3.3) were 3D processed including 3D migration (Section 3.3.4). Each radar grid covers an area of 3×3 km, imaging complex features, such as the upstream end of the Bump (grid 1) and the downstream end of landforms and parts of the boundary (grid 2). The following describes the calculation of attributes of this radar data to enhance visibility of the bed topography.

4.5.1 Overview Attributes

Attributes, like dip, frequency, phase or amplitude, are characteristics that can be measured, calculated or implied from reflection data (Chopra & Marfurt, 2005), whether seismic or radar. The calculation of attributes for the analysis and interpretation provides quantitative and visual information of features such as complex geometries, small-scale structures and irregularities and sub-resolution properties, which could otherwise be overlooked, and therefore enhance the efficiency and accuracy of the interpretation (Zhao et al., 2016). The calculation of attributes is based on mathematical relationships of physical properties and the geometry of the subsurface (Mohebian et al., 2018). While being a commonly used tool when analysing seismic data, attribute analysis has been taken up increasingly in recent years to interpret radar data (Forte et al., 2012; McClymont et al., 2008; Zhao et al., 2013, 2015, 2016), yet is still not a standard procedure, especially in glaciology.

Within this thesis, attribute analysis of radar data was used to emphasise variations in (englacial) attenuation, lateral variations and discontinuities on the bed of the RIS by highlighting contrasts in EM (physical) properties. Attributes were calculated for the 3D migrated data of grid 1 and 2 acquired in 2017/18 in Petrel (Schlumberger Software). The following provides a brief overview of attributes used and relevant for this thesis. Taner (2001) described two categories of attributes: geometrical and physical. Geometrical attributes can be described by dip, azimuth and curvature, while physical properties are directly related to wave propagation, lithology and other parameters.

4.5.2 Geometric Attributes

Within this thesis, the analysis of geometrical attributes was limited to the bed reflection, therefore interpreted surface.

4.5.2.1 Dip and Dip Azimuth

The attributes dip and dip azimuth (an analogue to strike) are often used to highlight changes in topography. Both show deviations of a surface from a horizontal plane. The dip describes the angle of a surface to the horizontal by comparing the depth of neighbouring points (Figure 4.14). A difference in depth, respectively in surface topography, creates a dip (0–90°). The dip azimuth describes
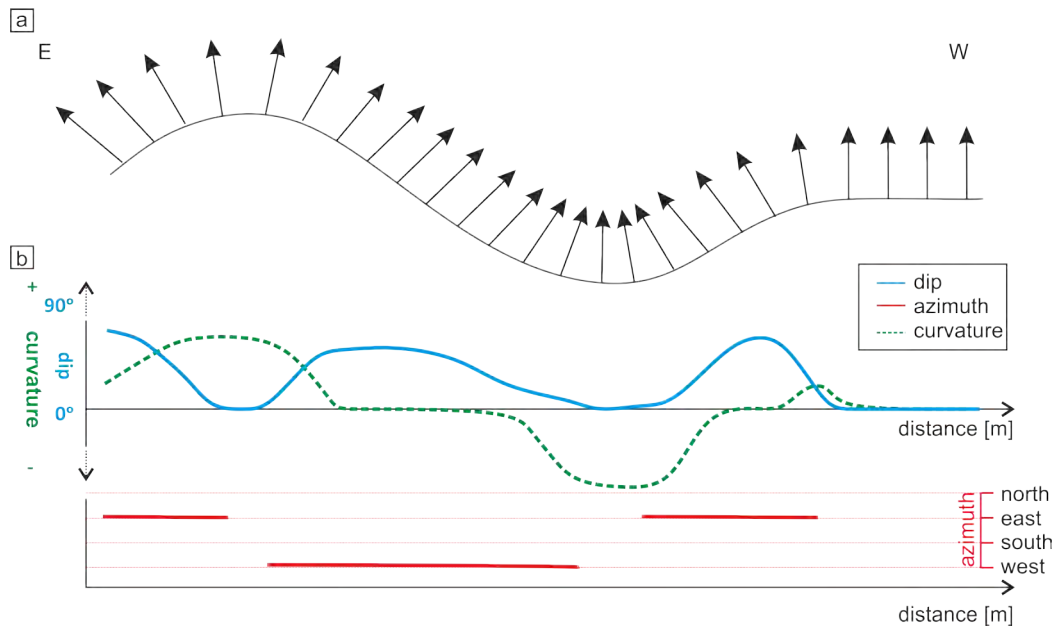
Figure 4.14: Dip, azimuth and curvature of a 2D surface. a) Topography of the surface, black arrows represent vectors which are normal to the surface. b) Values of curvature (green), dip (blue) and azimuth (red). Areas where the vectors in a) are parallel have a curvature of zero, areas with diverging vectors have a positive curvature (convex), converging vectors have a negative curvature (concave). The values given for the dip are only for illustrative reasons and were not constrained by any calculation. Values of the azimuth are given, assuming that the topography is shown from east to west, therefore only dips towards the east and west can be detected (graph modified after Roberts, 2001).

the direction (0–360°) towards which a surface is dipping (e.g. relative to north) independent of the dip angle of the surface. Within this thesis, dip azimuth is referred to as azimuth.

4.5.2.2 Curvature

Curvature describes the shape of a surface, quantifying the deviation from a planar surface. The more deformed or bent a surface, the higher the curvature. A trough is described as concave (negative curvature), and a crest of a hill is described as convex (positive curvature). The differences between dip, azimuth and curvature are shown in Figure 4.14. A completely planar (flat) surface will have 0° dip and zero curvature. However, a surface might be flat (not bent) but dipping at a certain degree towards a certain direction.
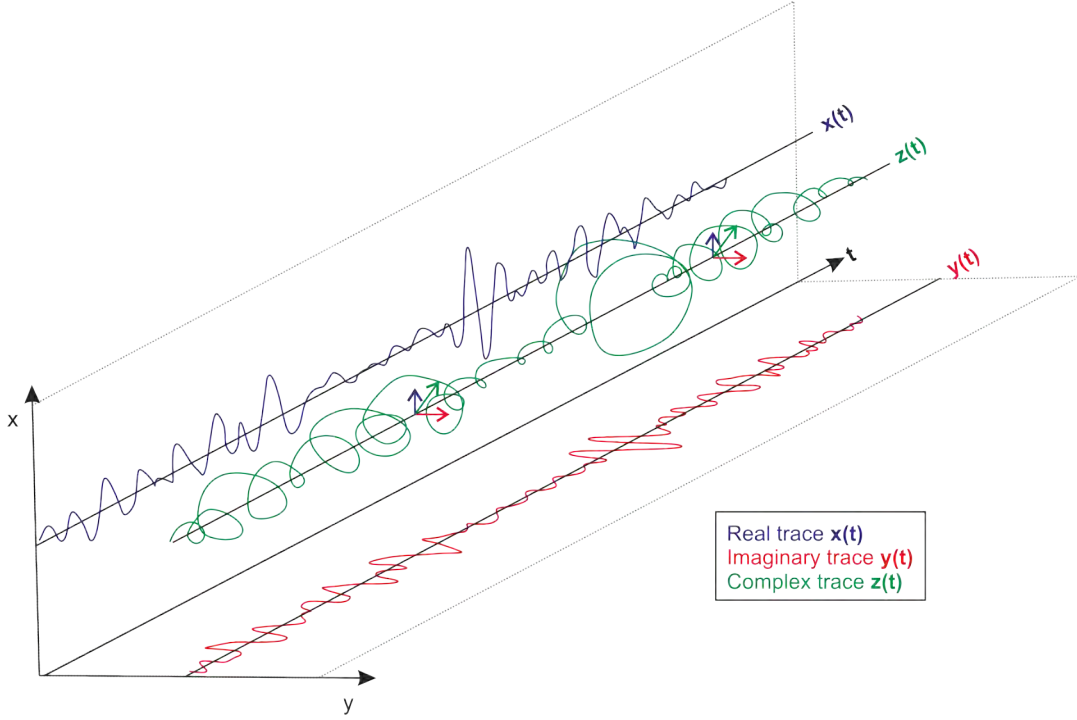
Figure 4.15: Illustration of the complex seismic trace. A complex trace consists of a real part $x(t)$, which is considered as a conventional trace, and an imaginary part $y(t)$ (graph modified after Taner *et al.*, 1979).

4.5.3 Physical Attributes

Figure 4.15 shows a 3D display of a complex trace $z(t)$, with the real trace $x(t)$ and the imaginary trace $y(t)$. The complex trace, which is a helical function centred around the time axis t, is the result of adding the vector of $x(t)$ and $y(t)$ (Taner *et al.*, 1979). The projection of the complex trace onto the real plane (x) is the real trace and the projection onto the imaginary plane (y) is the Hilbert transform of the real trace. The complex trace enables the calculation of seismic attributes, starting with the amplitude and the phase (Figure 4.16). The length of vector $A(t)$ at any point along the time axis is the amplitude of the complex trace. The phase $\phi(t)$ of the complex trace is described by the orientation of the vector $A(t)$ compared to the real plan. The mathematical calculation of the instantaneous amplitude and phase is given as

$$A(t) = \sqrt{x^2(t) + y^2(t)} \tag{4.4}$$

$$\phi(t) = \arctan(\frac{y(t)}{x(t)}). \tag{4.5}$$

Figure 4.16 illustrates the relation between the phase $\phi(t)$, the amplitude $A(t)$.
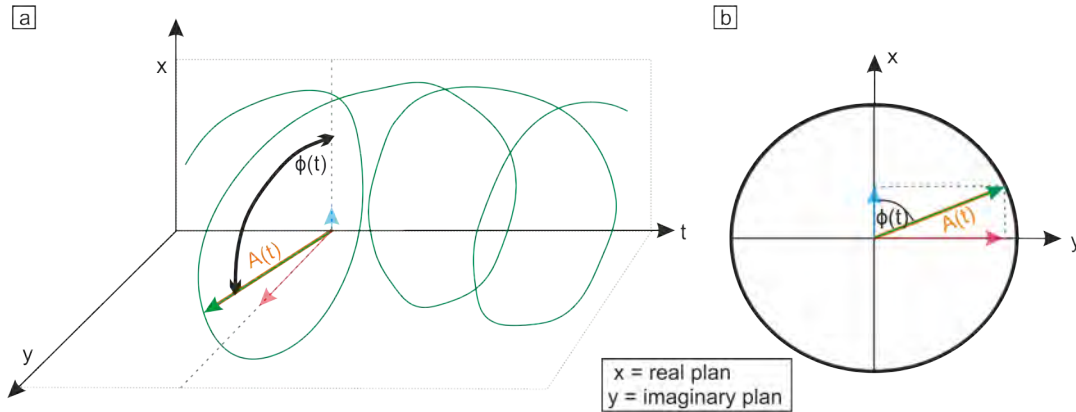
Figure 4.16: Illustration of the complex seismic trace. a) 3D view comparable to Figure 4.15. b) 2D illustration of the phase and amplitude of the complex trace. The time axis is orientated into the page. The length of the vector $A(t)$ is the amplitude of the signal at a time t. The angle $\phi(t)$ between the vector $A(t)$ to the vertical (x-plane) is the phase of the signal (modified after Taner *et al.*, 1979).

The phase and the amplitude are the two fundamental attributes, from which many other attributes can be calculated. Interpretation of the subsurface can be enhanced when using amplitude as well as phase information. Figure 4.17 illustrates the effect of variation in amplitude (a), phase (b) and frequency (c) on a wavelet. The amplitude describes the signal strength. Amplitude related attributes highlight areas characterised by changes in energy of the reflected signal, which can be used to analyse variations of physical properties of the material. The phase can be described as the position in time that the wavelet crosses the x-axis. A phase shift is therefore a shift of the wavelet in time (Figure 4.17 b). The phase can emphasise lateral discontinuities, superposition of several responses (e.g. tuning effects) as well as patchy scattering zones. The frequency is an approximation of the first time-derivative of the phase and describes the number of cycles in a wavelet within one second (Taner *et al.*, 1979). The analysis of the dominant frequency represents the reciprocal of the time between the trough to trough or peak to peak of the wavelet (Simm & Bacon, 2014). Variations in frequency content can indicate changes in layer thickness and/or lithology (e.g. water content) as well as chaotic reflection zones (Forte *et al.*, 2012; Zhao *et al.*, 2013).

Physical attributes can be calculated for in- and crosslines (2D lines or 3D cube), time slices or individual reflections (e.g. bed reflection). Within these, two
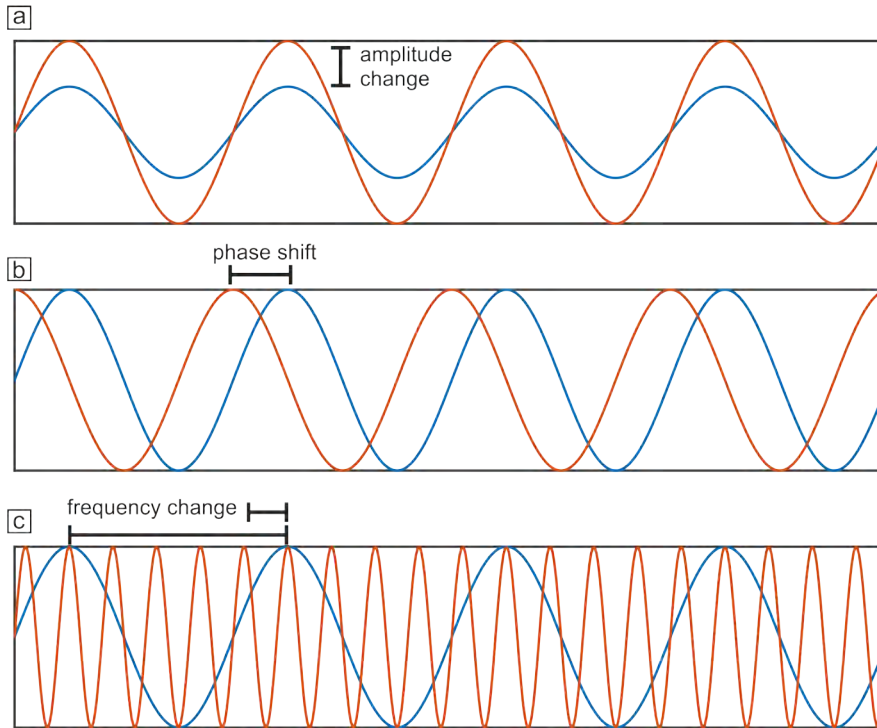
Figure 4.17: Illustration of the wavelet components; the amplitude (a), phase (b) and frequency(c).

domains (instantaneous and wavelet) are differentiated; instantaneous attributes are calculated for each sample (each instant), therefore representing characteristics along the time and space axis or along horizons. Wavelet attributes are calculated over the whole wavelet, representing characteristics of the wavelet itself.

4.5.3.1   Attributes Based on Amplitude

The amplitude of reflections is a very commonly used attribute when analysing radar data in glaciology, as it can highlight variations in the thermal state (within the ice or at the base) (Copland & Sharp, 2001), help to detect englacial layers (Delf *et al.*, 2020) or debris incorporated into the basal ice (Zhao *et al.*, 2016). Spatial changes in material properties can cause changes in amplitude of the reflected signal as the reflectivity mainly results from EM impedance contrasts. Abrupt changes in lithology or layer thickness can cause a high contrast in reflectivity (Taner *et al.*, 1979), therefore spatial discontinuities within the amplitude of the reflection. The two amplitude-based attributes used in this thesis are envelope and *Grey-Level Co-Occurrence Matrix* (GLCM).

4.5.3.1.1 Envelope The amplitude of the envelope is synonymous with the reflectivity or reflection strength and has been defined previously in Section 4.3.1. The envelope is always positive and is dependent on the amplitude, but insensitive to the phase of the wavelet (Forte *et al.*, 2012).

4.5.3.1.2 Entropy Within the GLCM The GLCM (Chopra & Marfurt, 2005) represents the amplitude value of a reference pixel's compared to neighbouring pixels. The matrix describes the differences of a pixel's brightness compared to its surroundings. The entropy of the matrix describes the local disorder within the matrix, where high entropy values represent similar values in the matrix (and low disorder) (Forte *et al.*, 2012).

4.5.3.2 Attributes Based on Phase

The phase of the wavelet is independent of the amplitude and displays events in equal strength, regardless of their reflectivity, which may simplify picking of reflections in some areas. When solely analysing the data using the amplitude, changes in the thermal state, which cause variations in amplitude, might be interpreted as discontinuities in the reflection itself. Therefore, analysing the attributes which are independent of the amplitude in these areas is crucial to identify the source for variations in reflectivity. For instance, Zhao *et al.* (2016) identified spatial variations in reflectivity in their radar record. Analysis of the instantaneous phase revealed that the reflection is continuous within the area of varying reflectivity. They interpret this as indicating an area of frozen material; these variations in thermal state are therefore interpreted as the origin for the observed spatial variations in reflectivity. The phase based attributes used here area the *cosine of phase*, dominant frequency and the coherency of wavelets.

4.5.3.2.1 *cosine of phase* (COP) The additional benefit of using the COP compared to the phase is the lack of a discontinuity at $\pm 180°$ (Forte *et al.*, 2012).

4.5.3.2.2 Dominant Frequency Variation in the thickness of sequences of layers changes the interference response and, therefore the apparent dominant frequency of the wavelet. Taner *et al.* (1979) described jumps in frequency and a reversal of the frequency to be the result of very closely located reflectors. Furthermore, variations in frequency content can give indications of changes in attenuation, hence electrical properties of the medium (Forte *et al.*, 2012).

4.5.3.2.3 Coherency Numerous attributes exist to describe the coherency of signals taking different parameters into account (Forte *et al.*, 2012). The principle of any coherency attribute is the detection of two or more similar traces. Results vary between 1 (completely identical) and 0 (completely dissimilar).

An algorithm independent of the amplitude describing the coherence of the signal is the variance or edge method. It can be used to highlight (sharp) lateral phase variations (Luo *et al.*, 1996; Marfurt *et al.*, 2002). A high variance ($\sim$1) represents a low coherency of signals, while a low variance ($\sim$0) represents a high coherency of signals within a certain window.

Table 4.2 gives an overview of values used for the calculation of the attributes in grid 1 and 2:

Table 4.2: Values used fro calculation of different attributes.

Attribute	Parameters for calculation of attributes / window size for the Hilbert transform
Cosine of Phase	33 samples (132 ns)
Dominant Frequency	250 samples (1000 ns)
Envelope	250 samples (1000 ns)
GLCM	Entropy Amplitude limit 0-0.036 V Lateral radius 4 Vertical radius 10 samples (40 ns)
Variance	Inline range 10 (20 m) Crossline range 1 (20 m) Vertical smoothing 70 samples (280 ns)

4.6 Summary

Data analysis in this thesis can be divided into three parts, first the analysis of the reflectivity of the bed, which can give indications of bed properties, including water at the ice-bed interface, second the analysis of temporal variability of bed topography and third the analysis of attributes of the bed reflection other than the reflectivity, such as dip, azimuth, frequency content etc. The reflectivity analysis (Section 4.3) of the bed reflection includes the calibration of the amplitude of the radar system using a novel approach introduced in Section 4.3.2. As a result of this calibration, sediment porosities and water content at the bed

can be approximated from the reflectivity. The analysis of temporal changes in topography involves a comparison of the topography of repeated radar lines with a time gap of 9 years (Section 4.4). Finally, the analysis of different attributes (Section 4.5) can help to highlight small-scale features on the bed by not only considering the amplitude information but also the phase and derivations of the phase.

Chapter 5

Reflectivity Analysis

The main aim of calculating the reflectivity in this thesis is to analyse spatial variation in bed properties and water availability. Water content in sediment, and therefore the porosity of sediment (assuming fully-water saturated sediment) has a strong influence on the reflectivity. High porosity, therefore water content, will result in higher reflectivity, compared to low water content, and therefore lower porosity. In the following results of the reflectivity analysis of data acquired in 2016/17 (Section 3.2) covering an area of 14.5×18 km (Figure 3.4) are described. The first part of the results focuses on the spatial pattern of reflectivity on the bed of RIS, including the reflectivity around cross-cutting features (Section 5.1.1) and along and around landforms (Section 5.1.2). Following this, the pattern of high reflectivity on the bed is compared to the hydraulic head calculated for the bed in Section 5.1.4. To be able to quantitatively link reflectivity and sediment porosity, a novel approach for the calibration of the radar amplitude was introduced in the methods in Section 4.3.2. The spatial pattern of resulting porosity is described in Section 5.2. This includes the correlation of locations of high reflectivity, and therefore high porosity material and the locations of water identified in previous studies (Section 5.2.1). The description of the results is followed by the discussion of these results in Section 5.3.

5.1 Results - Spatial Pattern in Reflectivity

Calculated reflectivity for the bed of RIS is shown in Figure 5.1 in plan view. Yellow (>1.75 V) and dark blue (1.5–1.75 V) areas represent high reflectivity, decreasing as the blue gets lighter to white (0–0.6 V) representing low reflectivity. The spatial variation in reflectivity (Figure 5.1) shows a preferred orientation in
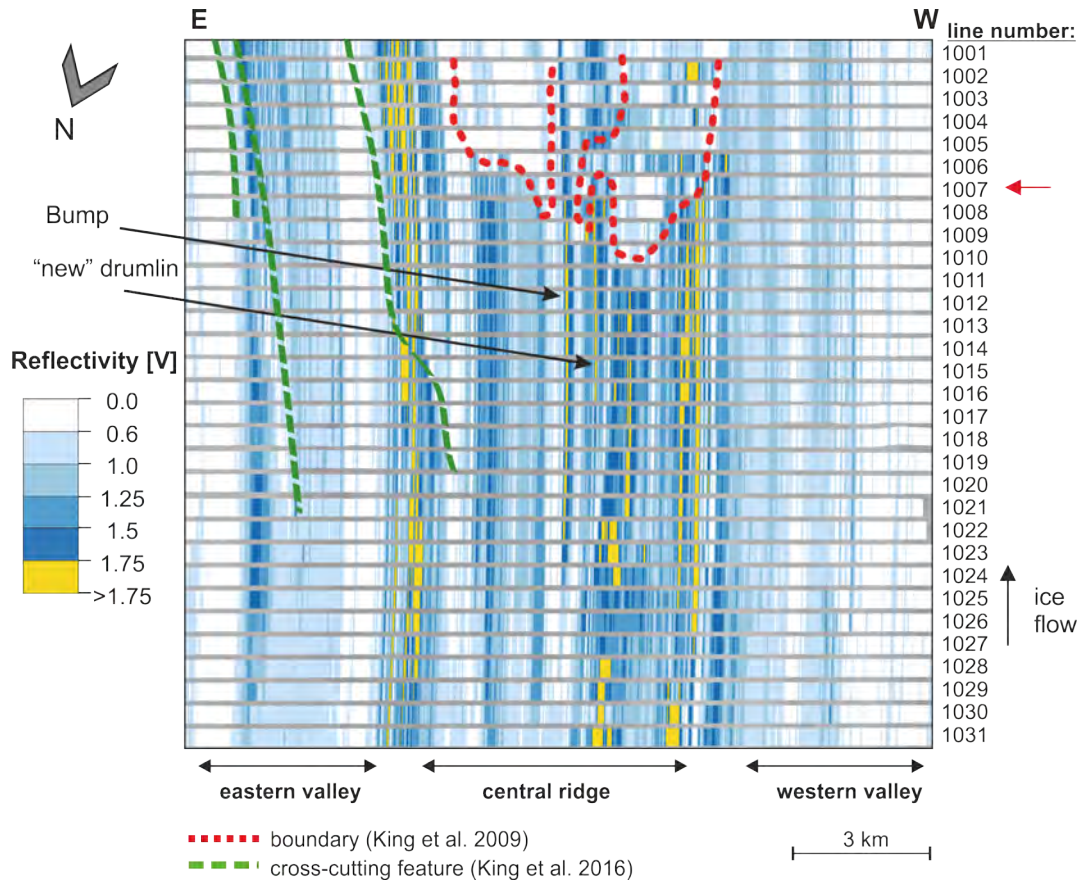
Figure 5.1: Reflectivity corrected for ice thickness variations in plan view. Data were acquired perpendicular to ice flow. Ice flow direction is from bottom to top. The green dashed line shows the interpretation of the location of cross-cutting features, the red dashed line shows the interpretation of the boundary by King *et al.* (2009), for comparison with the topography see Figure 2.7.

the flow direction in the area of deforming bed (upstream of boundary, mean reflectivity: 0.9 V). High reflectivity (>1.5 V) is aligned in thin bands in the ice flow direction. These reflectivity patterns are consistent over lengths of 14 km or possibly even exceeding the dimensions of the acquired grid. The reflectivity is very low (white and light blue colour, <0.75 V) in the area of basal sliding (downstream of boundary, mean reflectivity: 0.7 V). The valleys show low reflectivity as

well as bands of high reflectivity aligned in flow direction. Higher absolute values of reflectivity (maximum reflectivity: 3 V) are received in the eastern valley when compared to the western valley (maximum reflectivity: 1.5 V). Both valleys seem to contain large areas of low reflectivity. Phase inversion of the bed reflection has not been observed. In the following the reflectivity received around a cross-cutting feature in the eastern valley, on and around landforms as well as around the boundary is described.

5.1.1 Cross-Cutting Feature in the Eastern Valley

Previous studies (King *et al.*, 2016) have identified cross-cutting features in the eastern valley of the bed of RIS (Figure 5.1). In total, three cross-cutting features were identified, two long ones (9.5 & 10.5 km) and a shorter one (3 km). The shorter feature lies in an area of low reflectivity ($\sim$0–0.75 V). The downstream parts of the two long features are located in an area of low reflectivity ($\sim$0–0.75 V), but further upstream they seem to be cross-cut trough areas of high reflectivity (up to 2 V).

Figure 5.2 shows the topography (a) around the eastern cross-cutting feature (location of the feature indicated by the green dashed line), and values of reflectivity (b) over an area of 7.5×5 km along flow. The orientation of the cross-cutting feature is approximately 6° to the ice flow direction. The feature is located within an area of high reflectivity, with lower values of reflectivity towards the east when compared to the west. A clear trend of the reflectivity following the orientation of the cross-cutting feature can not be seen.

5.1.2 Reflectivity of and Around Landforms

Most landforms on the bed of RIS have previously been identified as MSGLs (King *et al.*, 2009, 2016). Figure 5.3 shows the topography and reflectivity along line 1013, with numbering of some MSGLs. Some of the MSGLs show a high reflectivity on their crest (e.g. MSGL 1, 2, 4, 5, 6, 8, Bump and "new" drumlin), but others do not show higher reflectivity compared to the surrounding area (e.g. parts of MSGL 3, 7, 9). In the following, the reflectivity of four different landforms is described in more detail.
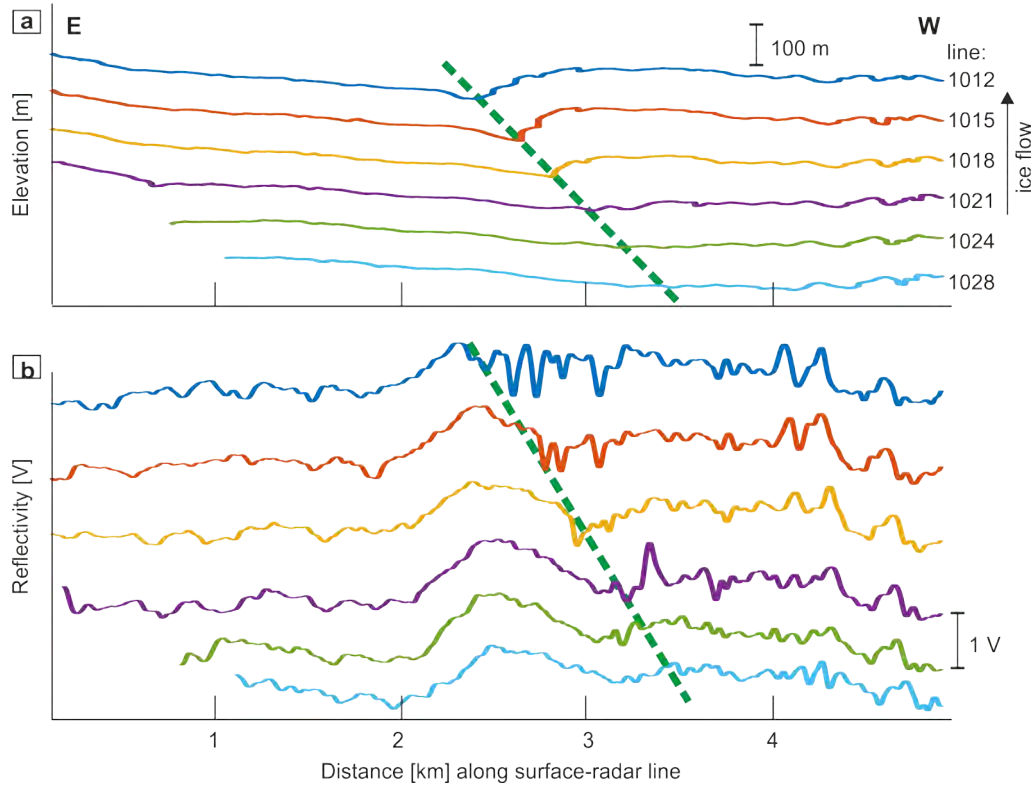
Figure 5.2: Eastern valley of the bed, line 1012–1028. a) Elevation of the bed and b) reflectivity of the bed reflection. The cross-cutting feature (green dashed line) can be identified by the topographic drop in the centre of the lines, advancing towards the east in downstream direction. The x-axes in graphs a & b are the same.

5.1.2.1 MSGL 6 and 7

Two neighbouring long elongated landforms were identified over several adjacent lines just at the edge of the central ridge towards the western valley of the bed of RIS, upstream of line 1006 (Figure 5.1, 5.4 and 5.5). The height of both landforms is around 15 m (e.g. in line 1012) and the width around 150 m. The width of the trough between the landforms ($\sim$100 m) remains the same over several lines. The landforms are not visible in data downstream of line 1006, roughly in the area of the boundary. The landforms appear in all lines acquired further upstream of line 1006; the upstream end can therefore not be detected. A topographic step at the western flank of MSGL 7 (see arrow on Figure 5.4) is visible in lines 1006 and 1007. Further downstream this step appears to cross-cut the topography (see green arrow in Figure 5.5).

Contrary to the reflectivity pattern described in the eastern valley (Sec-
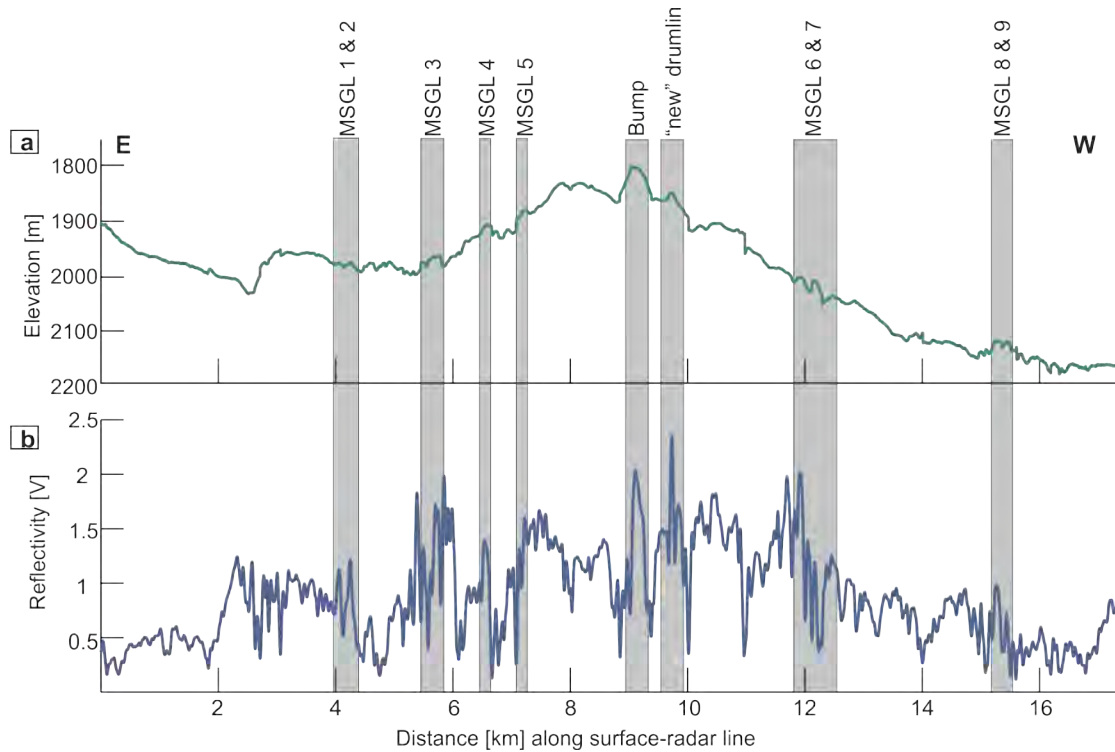
Figure 5.3: Bed elevation and reflectivity along line 1013: a) Elevation of the bed and b) reflectivity of the bed reflection. Landforms are numbered and marked by grey boxes.

tion 5.1.1), here reflectivity values in the west are lower when compared to the east. Both landforms, as well as the trough, are associated with a local peak in reflectivity, wherein the reflectivity of MSGL 6 and the trough are higher than MSGL 7 (Figure 5.4). Around 2 km downstream of the downstream end of these landforms (Figure 5.5, line 1002), within the area of basal sliding, an area of high reflectivity (>2.5 V) within an area of otherwise low reflectivity can be seen (Figure 5.5). Topographically this high reflectivity is located on a small plateau on a westwards dipping slope.

5.1.2.2 The Bump

The topography of the Bump, can be seen in Figure 5.6 a. The colour coding of the circles is chosen to represent the reflectivity. Highest reflectivity can be found on the crest of the Bump (b), as well as on the small depression west of it. The flanks of the Bump show low reflectivity. The spatial development of reflectivity along the crest of the Bump (in flow direction) show values comparable to the
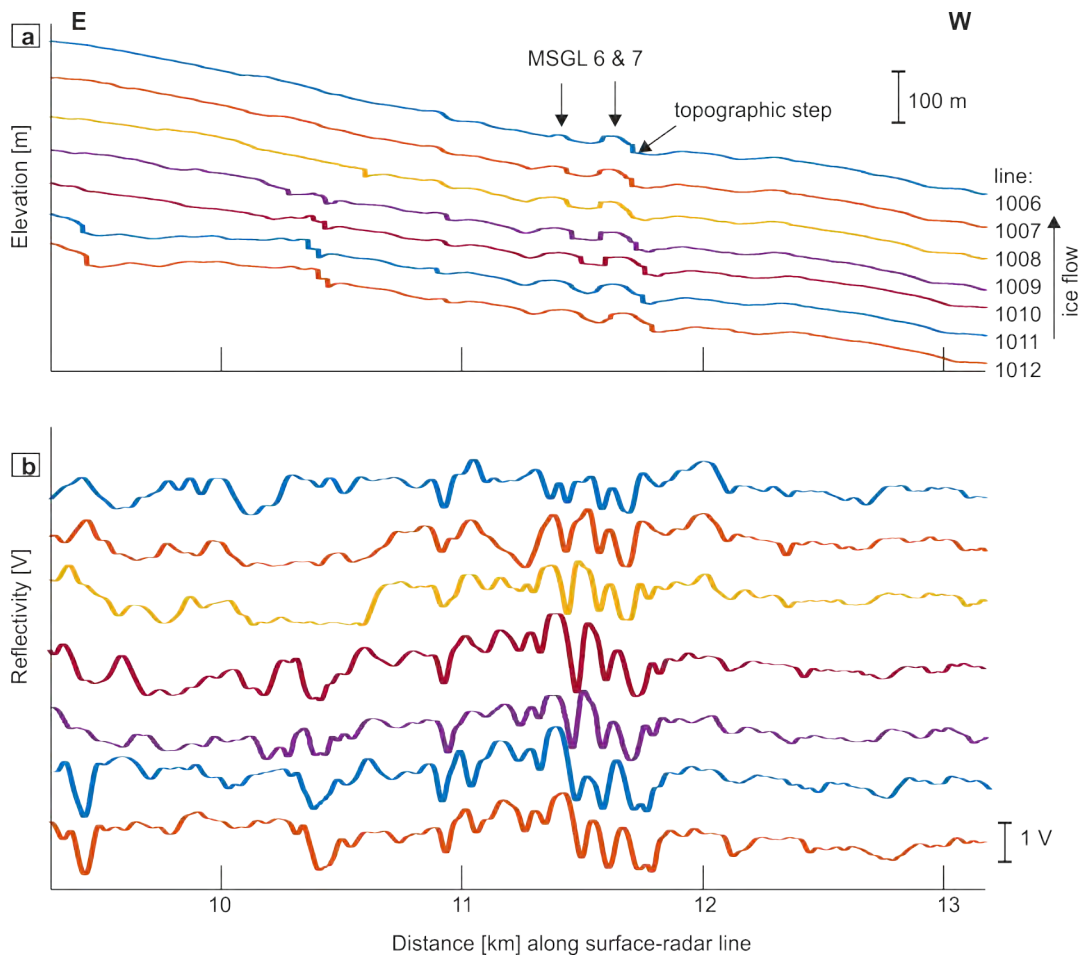
Figure 5.4: Edge of the central ridge and the western valley of the RIS, upstream of the boundary. a) Elevation of the bed and b) reflectivity. X-axes in graphs a & b are the same.

surrounding area in the location of the upstream end (∼1 V), while reflectivity increases ∼2 km further downstream, to a value of ∼1.8 V (Figure 5.6 (c)). No further trend in reflectivity can be seen downstream of this point.

5.1.2.3 The "New" Drumlin

The highest value in reflectivity, was found on the crest of the "new" drumlin (Figure 5.7 a and b), while the flanks show low reflectivity. The reflectivity along flow shows a similar pattern to the Bump, with low reflectivity around the upstream end of the "new" drumlin, increasing further downstream (>2 V). The values decrease again once the boundary (line 1007) is reached (Figure 5.7 c).
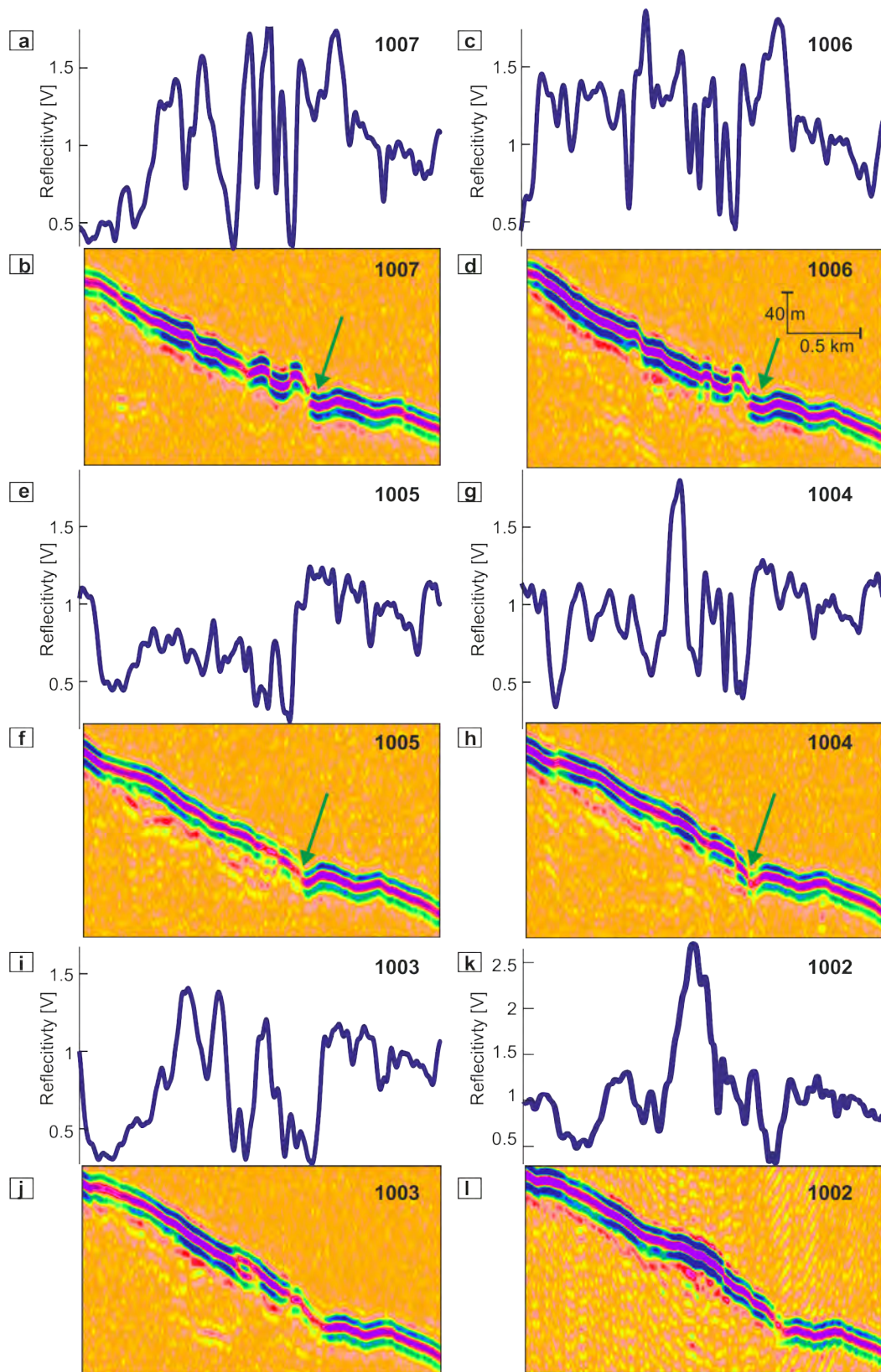
Figure 5.5: Edge of the central ridge towards the western valley of the RIS. Data displayed in line 1007 and 1006 are located upstream of the boundary, lines 1005-1002 are located in the area of basal sliding. a, c, e, g, i, k: Reflectivity. (Caption continued on next page)

Figure 5.5: (Continued) b, d, f, h, j, k: Section of corresponding processed radargram to the reflectivity. X-axes for all graphs have the same scale. The scale of the y-axis in k was modified for illustrative reasons. The feature seen in the radargram of line 1003 (j) is probably caused by an off-nadir reflection. Ice flow is from line 1007 to 1002. Figure 5.4 shows the reflectivity and bed topography for lines further upstream.
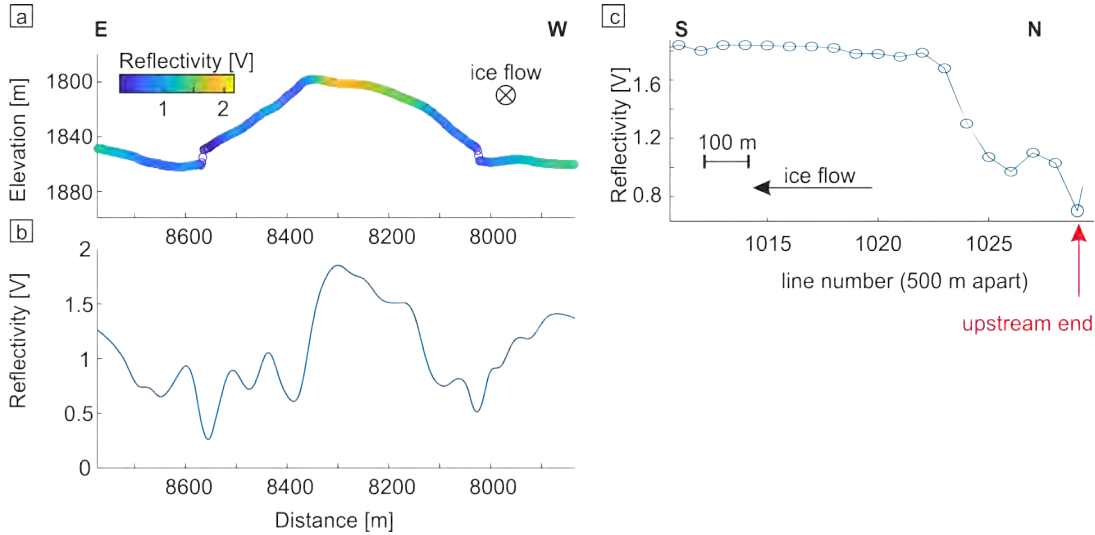
Figure 5.6: The Bump. a) Elevation of the bed of line 1013. Colour-code represents the reflectivity. b) reflectivity along line 1012, c) reflectivity along the crest of the Bump in flow direction. X-axes for graphs a & b are the same.
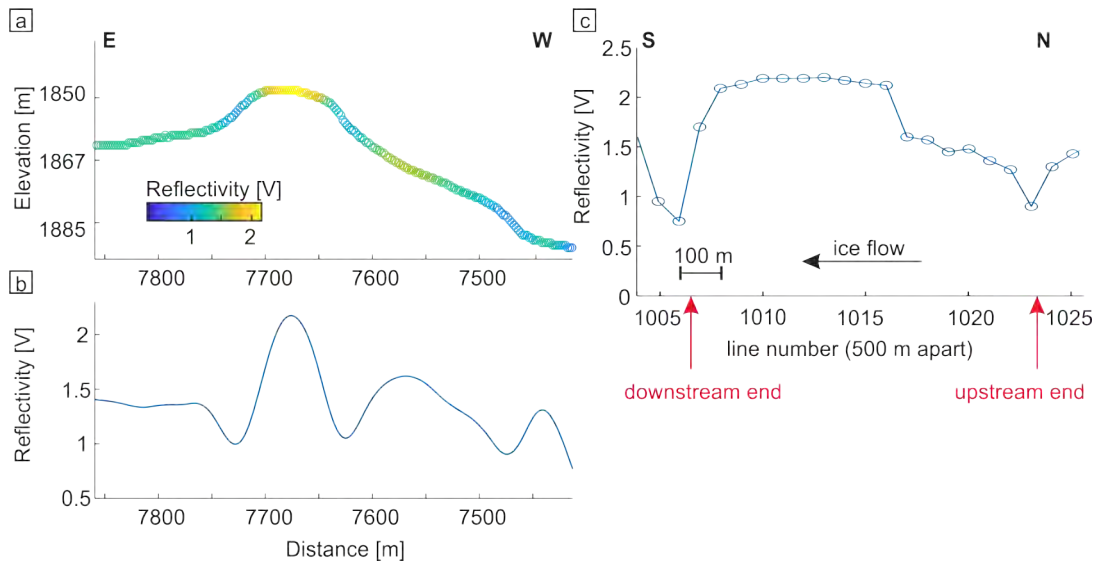
Figure 5.7: The "new" drumlin. a) Elevation of the bed of line 1013. Colour-code represents the reflectivity. b) reflectivity along line 1012, c) reflectivity along the crest of the "new" drumlin in flow direction. X-axes for graphs a & b are the same.

5.1.2.4   Other Landforms

Figure 5.8 shows an interpretation and interpolation of the bed topography based on picks of the twtt of the bed reflection, with values of reflectivity superimposed on the topography. Figure 5.9 shows a close up of the area immediately west (a) and east (b) of the Bump. The Bump and the "new" drumlin, as well as other landforms, are clearly visible as elongated landforms. Contrary to the Bump and "new" drumlin, some other landforms in the valleys show low reflectivity on their crest along the full length of the grid. An increasing reflectivity is only visible for a few landforms like the Bump and the "new" drumlin. However, most landforms in the eastern and western valley are truncated by the survey grid and no increase in reflectivity along the crest was recorded, perhaps because of this truncation.
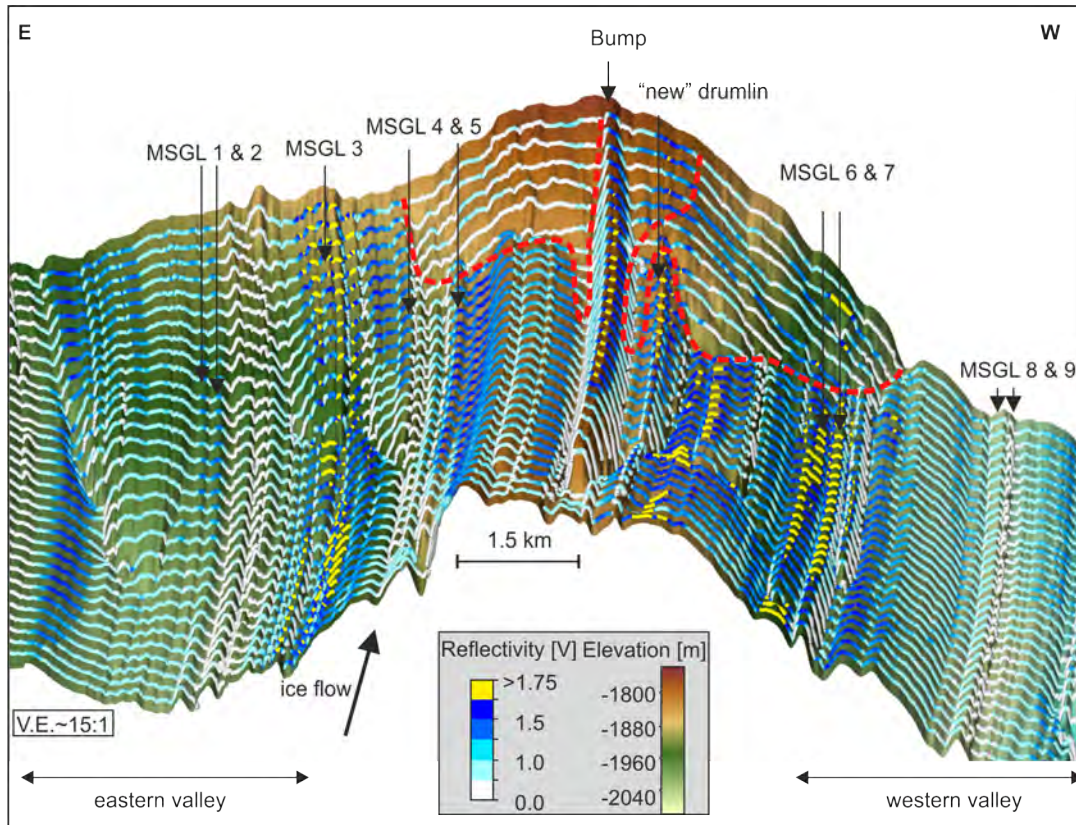
Figure 5.8: Interpretation of the bed topography from interpolation of twtt-picks to a surface with cell size 50×20 m in flow direction. The colour-code of bed topography goes from green for deeper topography to brown for shallower topography. Lines perpendicular to flow show the location of data points superimposed on the bed topography. Lines are spaced 500 m in flow direction, while trace spacing is 2 m in cross-flow direction. Ice flow is pointing into the page along the elongated landforms.
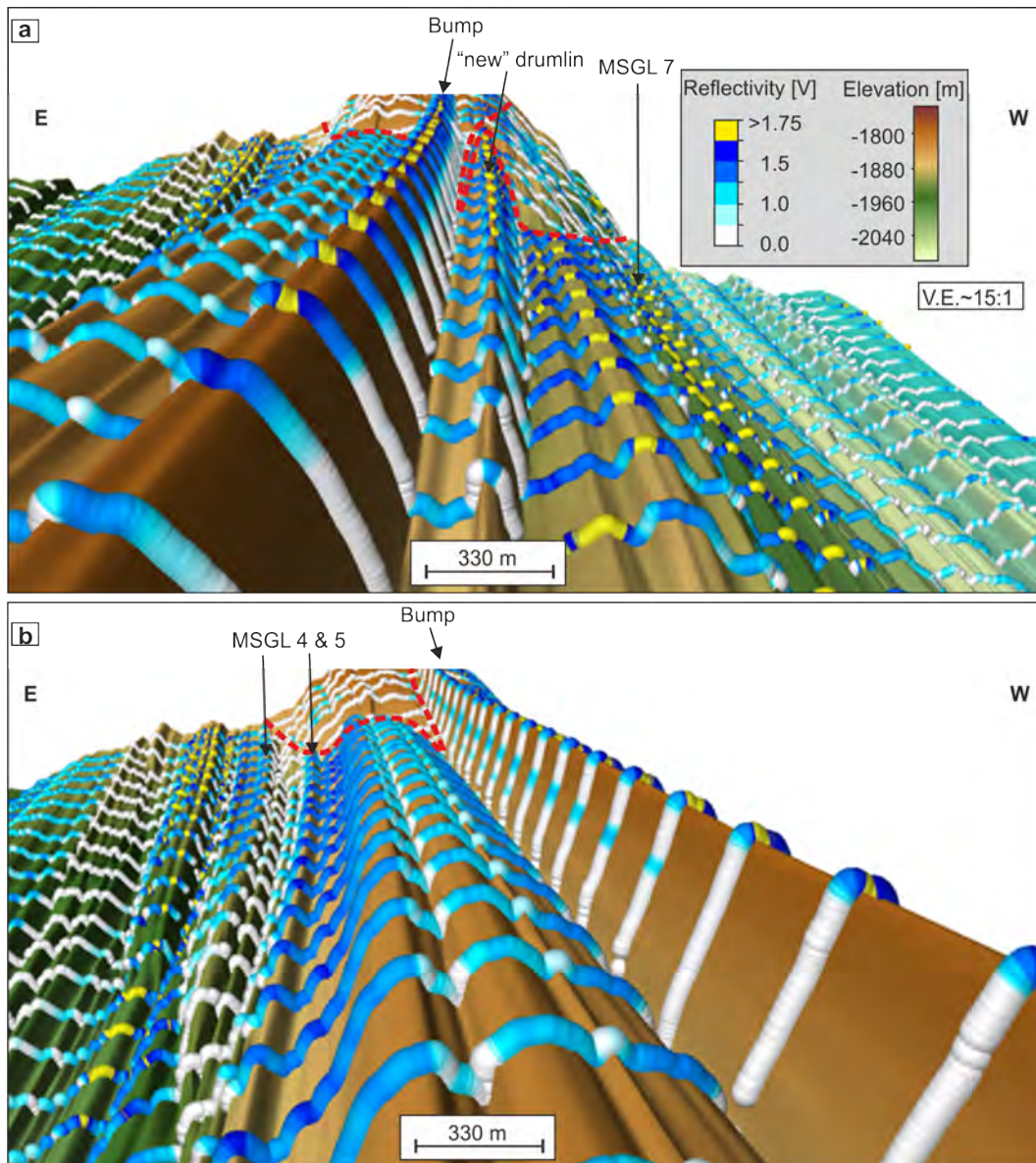
Figure 5.9: Close up of the area west (a) and east (b) of the Bump as shown in Figure 5.8.

5.1.3 Reflectivity Pattern in Comparison With the Interpretation of the Boundary

The interpretation of the boundary separating soft and stiff till by King *et al.* (2009) is concentrated on the central ridge (Figure 5.1 and 5.8). However, changes in reflectivity are observed within the valleys as well as on the central ridge. The eastern sliding area (Figure 5.1) shows on average lower reflectivity ($\sim$0.56 V) compared to the western ($\sim$0.88 V), which also includes a localised area of high reflectivity (see Section 5.1.2.1). The mean reflectivity of the soft bed is $\sim$0.9 V, with areas of low reflectivity (comparable to the eastern sliding area) and areas of high reflectivity. The abruptness of the change in reflectivity around the boundary can be seen in Figure 5.10. Sediment characteristics within the solid grey and black dashed box are assumed to change along flow, while characteristics are assumed to stay constant along flow for areas outside the boxes. Reflectivity received from the area between the grey and black box, also known as the area of the "new" drumlin and Bump, as well as the eastern (and western) area of the image is highly repetitive (therefore shows only little change in ice flow direction) and was described in the previous Section 5.1.1 and 5.1.2. In the following results of the black dashed box are described, followed by the grey box.

Black Dashed Box: The pattern of reflectivity along flow between soft and stiff sediment is changing, with higher reflectivity upstream of the boundary (mean reflectivity line 1012 and 1008: 1.1 V) and lower reflectivity downstream of the boundary (mean reflectivity line 1005: 0.4 V and line 1002: 0.54 V). As indicated in Figure 5.1, the eastern sliding area shows only little variation, therefore reflectivity of lines 1001–1004 is very similar with low reflectivity ($<$1 V). Line 1005 shows lower reflectivity when compared to downstream (most places $<$0.5 V). Further upstream of this line, once the boundary is reached the values of reflectivity increase until line 1007, from where onwards values remain high ($\sim$1.5 V).

Grey Solid Box: The separation of values calculated for lines upstream and downstream of the boundary is not as clear as in the black dashed box. Values are more diffuse and variable. As the boundary is not aligned in flow direction (Figure 5.1), the pattern of reflectivity changes in flow direction, and the location of the boundary changes for every line. Line 1012 lies upstream of the boundary,
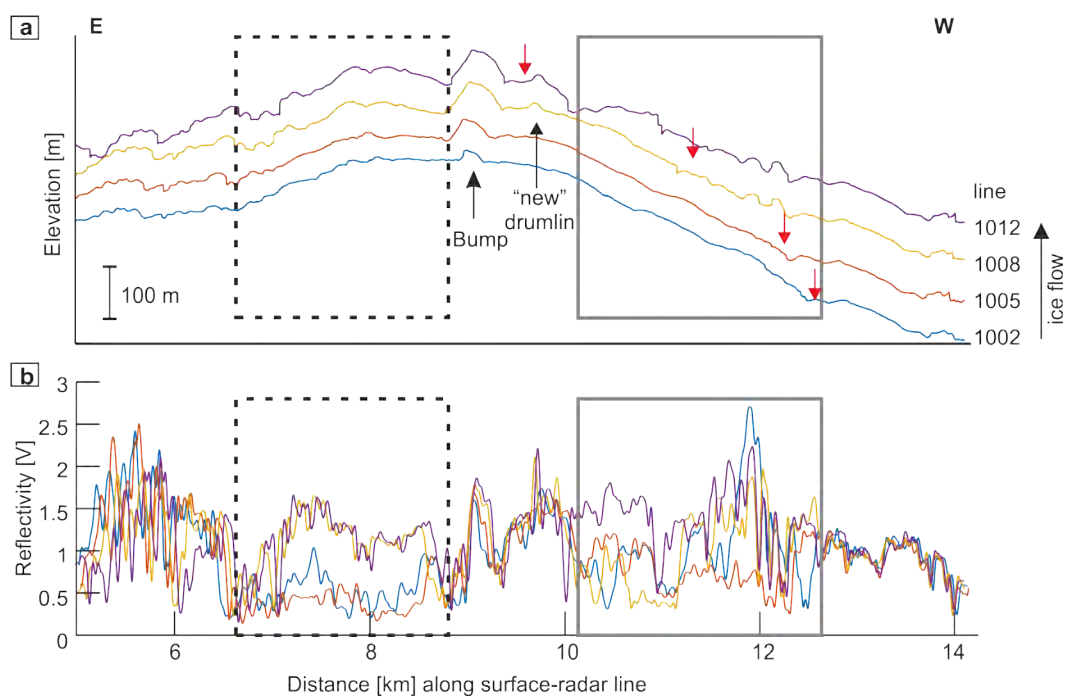
Figure 5.10: Area around the boundary, line 1002, 1005, 1008 and 1012. a) Elevation of the bed and b) reflectivity. Grey and black box mark the area where dynamics are assumed to be switching from deforming bed to sliding in downstream direction. Red arrows in (a) mark the approximate location of the boundary towards the west. The x-axes in graphs a & b are the same.

within the area of soft sediment, as does the western part of line 1008, where both lines show high reflectivity ($>1.5\,$V). The reflectivity in the eastern part of line 1008, located within the stiff sediment, is lower (mean reflectivity: $0.55\,$V), when compared to the western part (mean reflectivity $0.12\,$V), which is assumed to consist of soft sediment. Similarly for line 1005, with higher reflectivity (mean reflectivity: $1.1\,$V) within the soft sediment and lower reflectivity (mean reflectivity: $0.68\,$V) within the stiff sediment. Line 1002 contains a high reflectivity spot (mean reflectivity: $1.5\,$V) which was described before (see Section 5.1.2.1) and is located in the middle of the stiff sediment. Excluding this high reflectivity spot the average reflectivity in the area of the stiff sediment in this line is low (mean reflectivity: $0.84\,$V, $1.1\,$V if high reflectivity sport included). As before, the area along line 1002, located within the soft sediment, shows a high reflectivity (mean reflectivity: $1.06\,$V).

5.1.4 Hydraulic Head

Figure 5.11 shows the hydraulic head under RIS as well as very high values of reflectivity ($>0.75\,$V, yellow dots). The colour-scale for the hydraulic head goes from light green for a low hydraulic head, to dark green, representing a high hydraulic head. Lowest values of hydraulic head can be found in the western valley. The eastern valley as well as the areas around the boundary show a high hydraulic head. Areas of low hydraulic head are in pond-like shapes. High reflectivity values are not preferably located in the area of low hydraulic head. Furthermore, the reflectivity does not follow the spatial variation of the hydraulic head. High reflectivity, aligned in flow direction, is found in the eastern valley, not in the western valley, although the hydraulic head in the western valley is much smaller when compared to the eastern valley. The central ridge of the bed of RIS partly shows high reflectivity, while values of hydraulic head are high. Due to the rise in bed topography and a rise in surface elevation around the location of the boundary, the hydraulic head increases around and downstream of the boundary. The area of basal sliding shows low reflectivity, which coincides with a rise in hydraulic head. Figure 5.12 shows a cross-section (line 1013) of RIS, with ice flowing into the page. As already mentioned, no clear correlation between low values of hydraulic head (green line) and high reflectivity or vice versa can be seen.
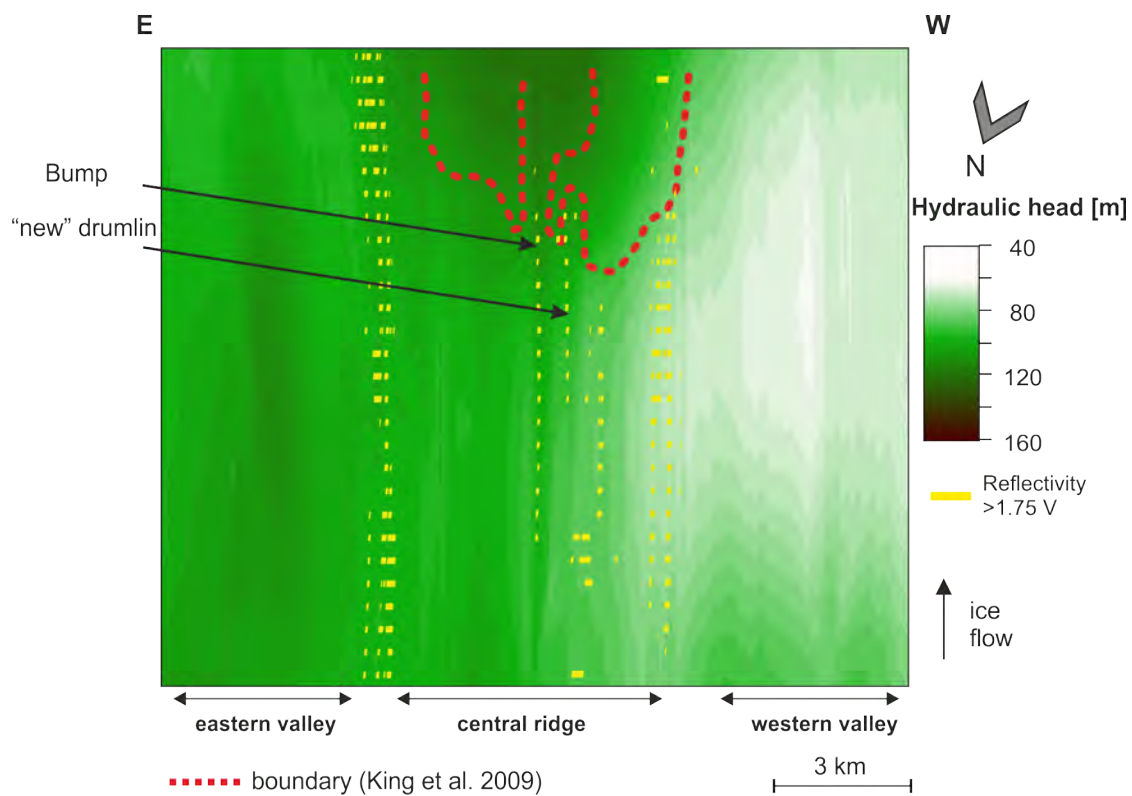
Figure 5.11: Hydraulic head on the bed of RIS superimposed by high values (>1.75 V) of reflectivity. Light green represents low hydraulic head, continuously increasing toward the dark green.
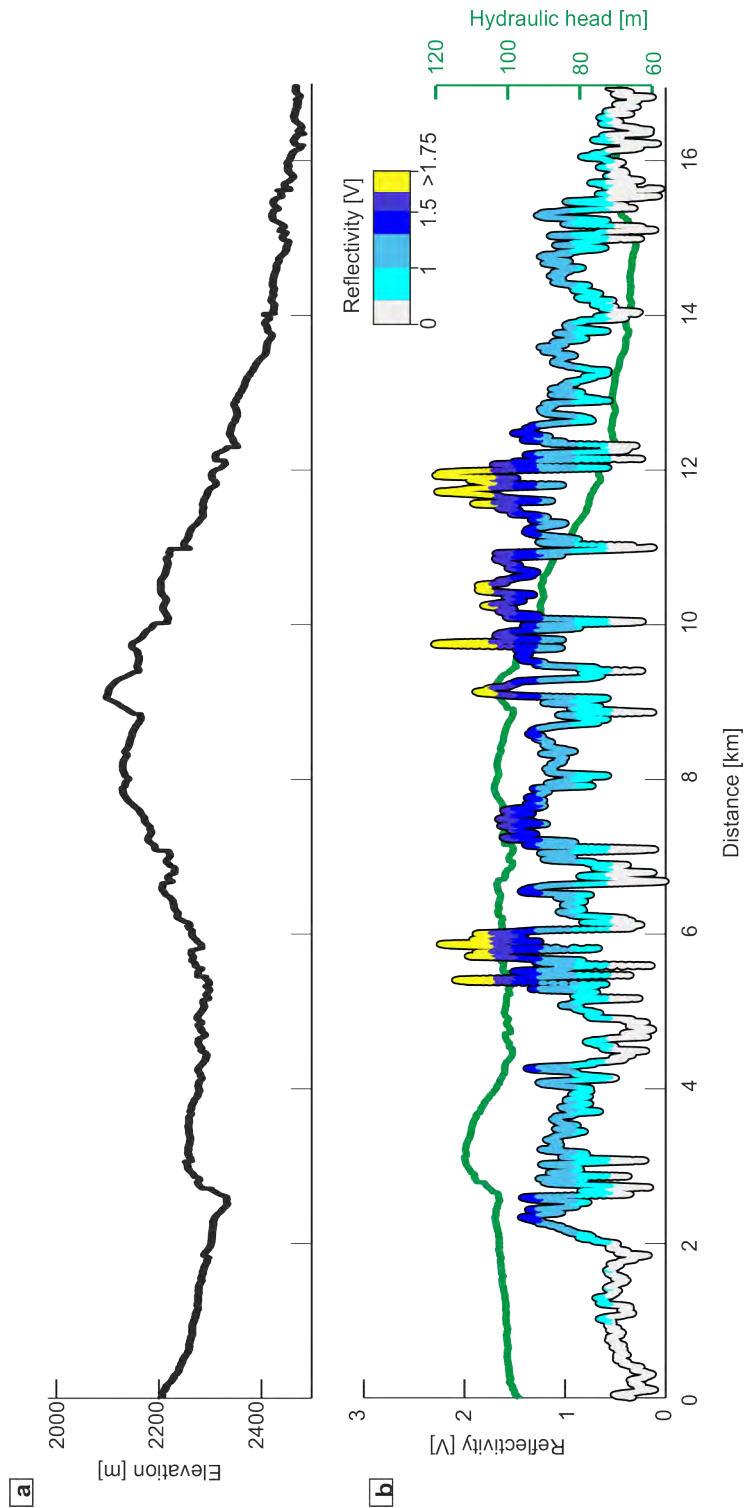
Figure 5.12: Correlation of topography, hydraulic head and reflectivity for line 1013. a) Elevation (black) of the bed and b) reflectivity (similar colour coding to Figure 5.1) and hydraulic head (green). The x-axes in panel a & b span the same values, therefore topographic location, expressed as distance along line 1013.

5.2 Results - Porosities Inferred From Variations in Reflectivity

Figure 5.13 a–c shows a comparison of surface-radar data and seismic data, including topography (a), surface-radar reflectivity (b) and acoustic impedance (c) calculated along line 1007. The vertical bars on the right in Figure 5.13 b indicate the porosities calculated for ranges of reflectivity (see Table 5.1). For most of the areas along the surface-radar line, modelling results in porosities of deforming sediment (porosity= 0.3–0.5), with lower porosities (porosity <0.3) resulting for areas e.g. around km 4, 6–6.5, 8–8.4, 8.7, 9.5, 10 etc. Consistent with modelled porosities from surface-radar reflectivity, acoustic impedance in the area around 8 km suggests porosities below 0.3, similar at 9.5 km. Sediment with porosity higher than 0.5 is indicated for areas around 4.7, 5, 5.2, 8.4, 9, 11.4 km (Figure 5.13).

Table 5.1: Values of reflectivity calculated for different porosities (indicated by vertical bars in Figure 5.13). For values assigned to the reference area see Table 4.1.

porosity	reflectivity [V]
>0.5	>1.78
0.5	0.68–1.78
0.4	0.64–1.67
0.3	0.58–1.53
0.2	0.49–1.33
0.1	0.35–1.02
<0.1	<0.35

5.2.1 High Reflectivity and Locations of Water Interpreted From Airborne-Radar Data

High values in surface-radar reflectivity at 8.4 and 9 km coincide with values of high bulk relative permittivity in airborne-radar data, interpreted as liquid water (bulk relative permittivity=80) by Murray *et al.* (2008). However, high surface-radar reflectivity at km 4.7 and 11.4 are located in an area, where airborne-radar bulk relative permittivity is higher compared to the surrounding, but not sufficiently high to indicate liquid water. These high values of permittivity are interpreted as small water ponds of insufficient thickness (Murray *et al.*, 2008).
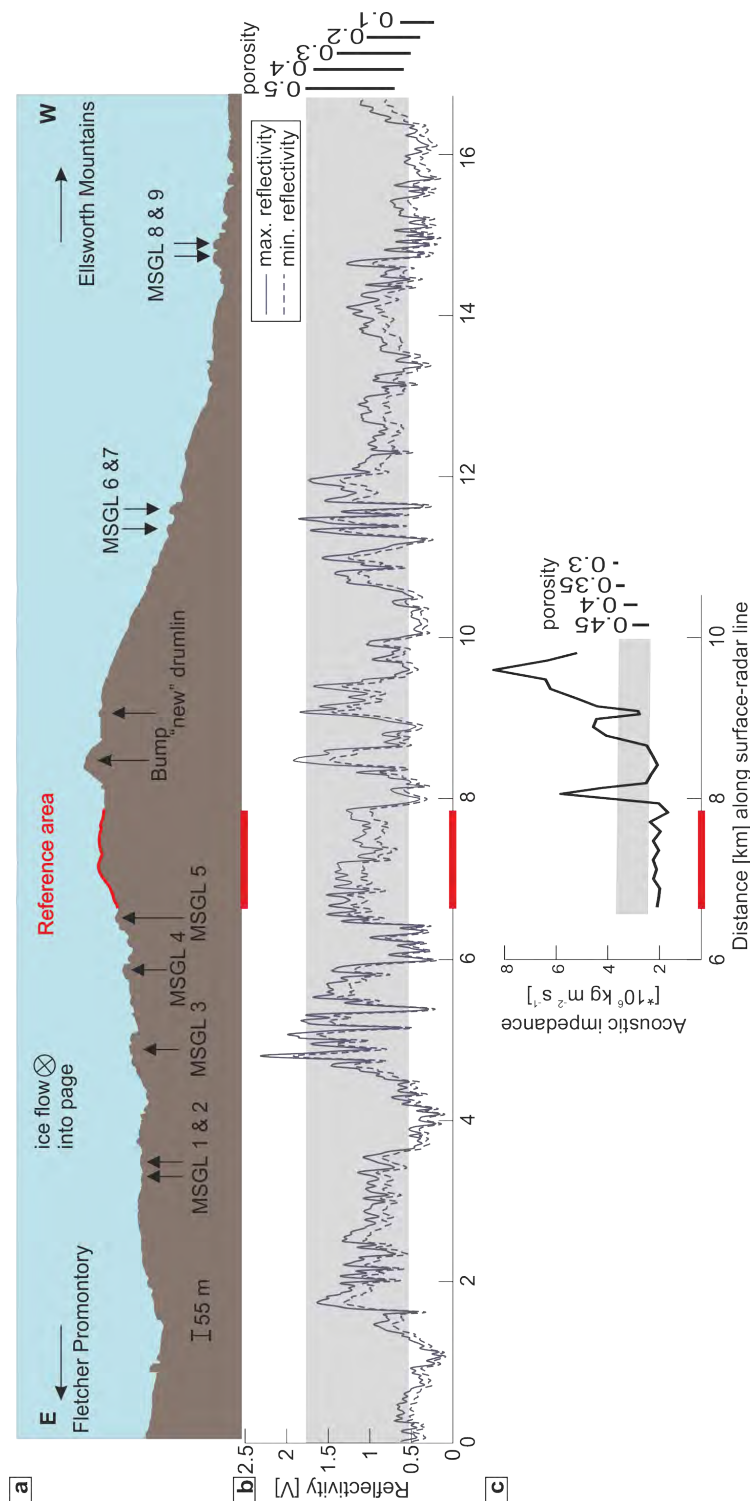
Figure 5.13: Surface-radar reflectivity compared to seismic acoustic impedance along line 1007 (see red arrow in Figure 5.1). a) Bed topography, interpreted from surface radar; ice flows into the page. b) Surface-radar reflectivity. Vertical bars at the right show calculated porosities according to variations in reflectivity compared to the reference area (red line at 6.3–7.7 km). c) Acoustic impedance of line C1-04, with possible porosity ranges (Smith & Murray, 2009). The grey filled boxes in b) and c) mark the range of porosity associated with deforming sediment (corresponding acoustic impedance = 2.2–3.8×10⁶ kg m² s⁻¹).

The high permittivity at 6.8 and 9.4 km (Figure 4.10) is located in an area of high surface-radar reflectivity, although modelled porosities in this region are in the range of deforming sediment (porosity = 0.3–0.5).

5.2.2 Key Observations

- Reflectivity on the bed of RIS is variable on a scale of ~100 m.

- Low reflectivity partly corresponds with areas downstream of the boundary identified by King *et al.* (2009), but areas upstream of the boundary show variations in reflectivity as well.

- Reflectivity drops abruptly once the boundary is reached.

- Some landforms show a high reflectivity on their crest, while others show low reflectivity.

- Reflectivity along the crest of the Bump and the "new" drumlin increases ~2 km downstream of the landforms upstream end.

- The reflectivity pattern around cross-cutting features does not correlate with the orientation of the cross-cutting features.

- Areas of high reflectivity partly coincide with areas interpreted to contain a water layer.

- The spatial pattern of reflectivity does not correlate with the spatial pattern of hydraulic head.

- Calculated porosities indicate the existence of deforming sediment, with some areas of low porosity material and localised areas of very high (>0.5) porosity.

5.3 Discussion - Properties of the Bed and Subglacial Landforms

The following sections discuss the porosities inferred for the bed under RIS (Section 5.3.1) as well as subglacial landforms (Section 5.3.1.1) and cross-cutting features (Section 5.3.1.2) from the reflectivity analysis. Following this, possible origins for sediment with different porosities are discussed (Section 5.3.2). Section 5.3.2.1 focuses on the properties of the low porosity material and addresses whether the low reflectivity that led to the interpretation of a low porosity material is possibly caused by a partly frozen pore space, compressed sediment or a hard bedrock. Moreover, the occurrence of water (Section 5.3.3), in combination with the hydraulic head and geometries of these water bodies, are evaluated. Possible pitfalls and limitations of this study are discussed in Section 5.3.4. Finally, an interpretation of spatial variation of bed properties is given in Section 5.4.

5.3.1 Properties of the Bed

Sediment porosities calculated for the bed indicate the presence of soft sediment (porosity = 0.3–0.5) as well as low porosity material (porosity <0.3). Subglacial landforms seem to be covered by (possibly partly consisting of) soft sediment as well as low porosity material, while the reflectivity calculated for some landform crests suggests porosities of more than 0.5. Porosities of subglacial till recovered from different locations vary between 0.2–0.58 (Evans *et al.*, 2006; Kamb, 2001). Sediment with porosities higher than this is less likely to occur in the subglacial environment due to the compression of the overlying ice (vertical stress ∼20 MPa). Due to this, the high reflectivity observed under RIS can not solely be explained by changes in sediment porosity, and an additional source of reflectivity is mandatory. Comparisons of surface-radar data and interpretation of airborne-radar data (Section 5.2.1; Murray *et al.*, 2008) suggest the high reflectivity signals (reflectivity >1.75 V), e.g., on the crest of some MSGLs, are likely to be caused by water overlying soft sediment. Further implications of this are discussed in Section 5.3.3.

Spatial variations in reflectivity (Figure 5.1) within the deforming and sliding bed indicate that the subglacial material is not homogeneous within these areas, which is consistent with the variations seen in bulk relative permittivity from airborne-radar data (Figure 4.10). However, due to a big overlap of porosities

calculated for a certain range of reflectivity (Figure 5.13 and Table 5.1) a differentiation of porosities within the range of deforming sediment (porosity = 0.3–0.5) is not possible.

5.3.1.1 Properties of Subglacial Landforms

High porosities, indicating soft sediment, are associated with some of the elongated landforms, while the troughs and the upstream end of the landform partly consist of low porosity material, with no indications for liquid water. Analysis of their elongation ratio classifies the landforms upstream of the boundary as MSGLs, rather than drumlins (Section 2.3.2; Everest *et al.*, 2005; King *et al.*, 2009). Those MSGLs are assumed to be deposited rather than the surrounding area eroded (Smith & Murray, 2009), therefore a material difference between the landforms and their surroundings is plausible. In agreement with the airborne-radar data (Murray *et al.*, 2008), this study has identified water occurring at the crest of some MSGLs (Figure 4.10, 5.13, 5.8) extending downstream for up to 10 km, until the downstream end of the landform is reached. Landforms consisting of a hard upstream end and a soft tail and downstream side have been described before by Clyne *et al.* (2020). The transition between the soft and hard material is described as subtle. Furthermore, Clyne *et al.* (2020) and Holschuh *et al.* (2020) described moats and depressions around and at the upstream end of bumps to consist of hard material, which is consistent with the observations of this study. Consistent with the findings of King *et al.* (2009), no free water located at the lee side of MSGLs was identified on the bed of RIS.

5.3.1.2 Cross-Cutting Features

Several cross-cutting features were identified on the bed. Water accumulated in subglacial channels is known to cross-cut the underlying topography (Benn & Evans, 2011), but the reflectivity pattern in the area of cross-cutting features gives no indication for water accumulation in this area. If these features are not part of a water evacuation system, they might be caused by underlying topography that is possibly cropping out in these areas. An underlying geology, like a bedrock, is more resistant to erosion and deformation due to the overriding ice and, therefore might contain a different orientation when compared to the ice flow direction. However, solely from surface-radar data, an interpretation of

the underlying geology is not possible, therefore further information is needed to analyse the origin of these features.

5.3.2 Origin of Different Sediment Porosities

Seismic surveys crossing the central ridge and both valleys or drilling accessing the bed in these locations do not exist yet, and therefore an interpretation of the geology (like the different origins of material or different age (Evans *et al.*, 2006)) in this region was not possible. Changes in reflectivity resulting from variations in sediment properties might be caused by compression and shear deformation (Boulton & Zatsepin, 2006) as well as different source material (Evans *et al.*, 2006) or the particle alignment (Murray & Dowdeswell, 1992). Loose packed sand experiences compression under shearing, therefore a volume decrease, while densely packed sand is known to experience dilation, therefore an increase in porosity under shearing (Craig, 2004; Iverson, 2010). While applying shear stress the interlocking between particles within dense sand is overcome which results in an increase in volume. This might be the case for sediment covering the landforms, where enhanced shear stress around landforms (due to enhanced roughness) might lead to an increase in porosity.

5.3.2.1 Low Porosity Material

The following includes a brief discussion of the low porosity material and the possibility of this material to consists of crystalline rock, compacted sediment or sediment with a partly frozen pore space:

Crystalline Rock vs. Compacted Sediment

Modelling results derived from the surface-radar reflectivity indicate the existence of sediment with low (<0.3) porosities (e.g., around km 4, 6, 8, 8.7, 10). Such low porosities can indicate compacted, unlithified sediment or a sedimentary rock. However, the results presented here can only be used to infer the spatial distribution of porosities. Information about consolidation stages of different rock types can not be inferred solely from surface-radar data. Seismic acoustic impedance calculated for the bed of RIS reaches as high as $8 \times 10^6 \, \mathrm{kg \, m^2 \, s^{-1}}$ (Figure 5.13 c), suggesting a compacted sediment or poorly lithified sedimentary rock, like sandstone, rather than a crystalline basement (Figure 5.14 and Smith *et al.*, 2018). Using dipping seismic reflectors and anomalies in the potential field, Smith *et al.* (2013) identified subglacial crystalline rock under Pine Island
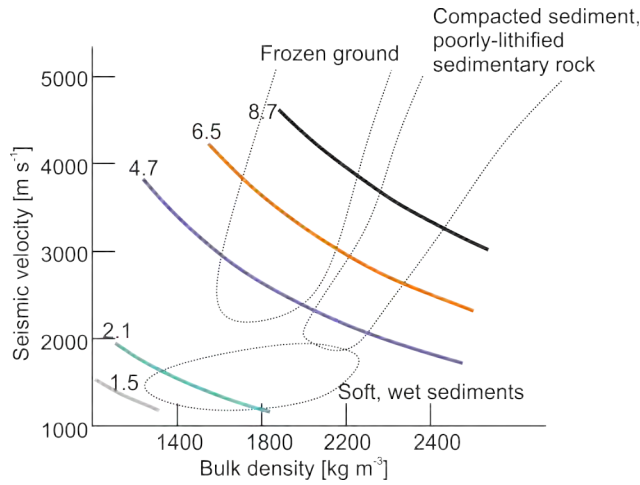
Figure 5.14: Variations of seismic acoustic impedance (coloured lines), by ranges of seismic P-wave velocity and bulk density (graph modified after Smith *et al.*, 2018).

Glacier. The location of the geological boundary coincides with changes in basal roughness, basal drag and ice flow velocity. Nevertheless, acoustic impedance under Pine Island Glacier is not sufficiently high on its own to clearly identify a crystalline basement but does show values comparable to those measured for RIS (Smith *et al.*, 2013). The lack of a clear signal in the impedance on Pine Island Glacier originating from the crystalline rock was attributed to a possible soft sediment layer with a thickness of around $10\,\mathrm{m}$ ($\lambda/2$). This sediment layer is described to possibly superimpose the geological boundary, impeding a clear signal in acoustic impedance. The clear identification of a crystalline rock cropping out in some areas under Pine Island Glacier, even with the lack of a clear acoustic impedance signal, might raise the question of whether a crystalline rock could be present under RIS, considering the acoustic impedance values calculated for the bed, in addition to the sub-bed reflections that were described for RIS by Smith & Murray (2009). However, there is no apparent correlation between magnetic anomalies (Figure 5.15; Ferraccioli & Jordan, 2020) and the areas identified to consist of outcropping low porosity material. From the initial qualitative analysis shown here, the aeromagnetic data do not support the presence of crystalline rock at the ice-bed interface and therefore supports the inference made here of a sedimentary rock or a very compacted unlithified sediment (personal communication Tom Jordan, October 2020).

Frozen Pore Space vs. Water-Saturated Sediment
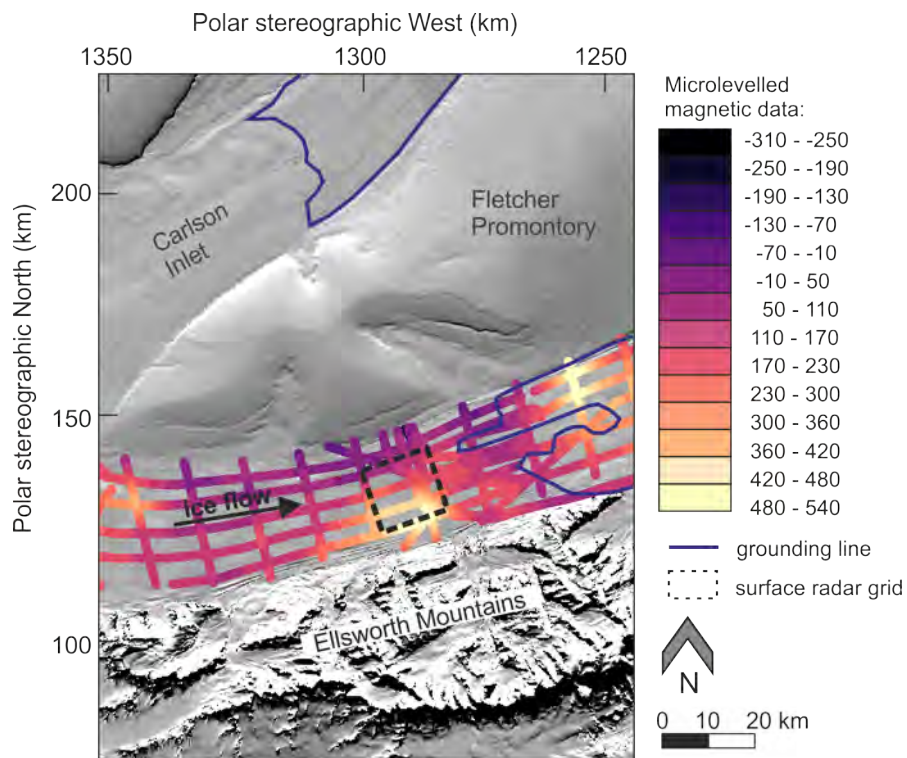
Figure 5.15: Aeromagnetic data acquired in 2006/07 (Ferraccioli & Jordan, 2020). Data were microlevelled following the technique of Ferraccioli & Jordan (2020). Note tie lines are not included in the microlevelled data channel. The blue line marks the grounding line, the black dashed box marks the area of the surface-radar grid.

The sediment under RIS, is interpreted to be water-saturated and at the pressure melting point (Smith & Murray, 2009; Smith *et al.*, 2021). Nevertheless, an alternative interpretation of these low values in reflectivity coinciding with higher values in acoustic impedance might be the existence of a frozen substratum in parts of the bed. This is considered less likely but has not been critically reviewed so far. High values in acoustic impedance could in principle, be explained by a partly frozen pore space as well as the occurrence of compacted material or sedimentary rock, because a clear differentiation of the three cannot be made from the acoustic impedance (Figure 5.14; Smith *et al.*, 2018). However, variations in bulk relative permittivity in areas identified as low porosity material by the surface-radar data are attributed to water at the ice-bed interface by Murray *et al.* (2008), which makes the co-existence with frozen sediment harder to explain in terms of thermodynamics. Furthermore, seismic acoustic impedance values do indicate the possible presence of a thin water layer (Smith & Murray, 2009; Smith *et al.*, 2007). A reliable statement on whether there are frozen patches, or a low porosity material present is only possible combining several observations and methods. The fast and stable ice flow (Gudmundsson, 2006; Gudmundsson & Jenkins, 2009; Murray *et al.*, 2007; Vaughan *et al.*, 2008), the lack of significant spatial changes in basal drag over this area (Joughin *et al.*, 2006), the occurrence of liquid water (Murray *et al.*, 2008) and the correspondence of high acoustic impedance values to the very low surface-radar reflectivity combine to favour the interpretation that areas of very low reflectivity are most likely caused by low porosity material, either compacted sediment or sedimentary rock.

5.3.3   Water on the Bed

Smith *et al.* (2007) reported maximum bed slopes according to seismic data to be >10°, and surface slopes to be below 0.01°, such that at this site, the hydraulic head is more controlled by the bed than the surface slope, consistent with results shown here. Under the assumption of water following the hydraulic head (Vaughan *et al.*, 2008), free water would be expected in the deeper valleys rather than on the central ridge, similarly in the troughs around landforms rather than the crest of landforms (Figure 5.1 and 5.8). However, the results presented here as well as in Smith *et al.* (2007) do not give indications for free water or increased water content around landforms or in the valleys. There are two limitations to with the prediction of water flow here. First, the hydraulic head was calculated

under the assumption of a negligible effective pressure ($\sim 0\,\mathrm{Pa}$), which might be a valid assumption on a larger scale but increasing pressure around landforms unhinges the balance between ice overburden pressure and water pressure; therefore the hydraulic head calculated under these assumptions might not be adequate to describe water flow around small-scale obstacles like MSGLs. Second, variations in permeability and composition of different materials. Subtlety in the topography and therefore the distribution of hydraulic head across the profile of MSGLs possibly drives water towards their crest rather than the flanks or troughs. Depending on the permeability of the sediment, these pressure variations may then result in the formation of a water body at the crest of some landforms. Assuming the landforms to consist of permeable material, whereas the surrounding area is a less permeable material, the water on the landforms might get trapped on the crest, as water possibly cannot (or can only slowly) drain through the underlying material. This might be an important phenomenon, considering that downstream ends of landforms are often located in an area of low porosity material. Water flow through that material might be inhibited, creating an accumulation of water on the landforms. Furthermore, possible anisotropic hydraulic properties of the sediment due to particle alignment might advance water flow through the landforms, rather than the surrounding area, leading to a higher water content in the already water-saturated substratum (Murray & Dowdeswell, 1992).

5.3.3.1 Landforms and Water in Other Studies

The following list gives a brief overview of results and interpretations from different studies investigating water on the bed and a possible link to subglacial landforms:

- Chu *et al.* (2016b) analysed the reflectivity pattern beneath the Greenland Ice Sheet, highlighting the seasonal changes in water distribution. They found isolated water pockets to be stored in cavities on bedrock ridges rather than in troughs in the winter season, while in the melt season these isolated water pockets are connected, and most water is found in the troughs rather than on the ridges. The occurrence of water pockets on the ridges was attributed to a low hydraulic conductivity of the bedrock ridges, highlighting the strong influence of subglacial bed properties on the subglacial drainage development, therefore also the glacier dynamics.

- Riverman *et al.* (2019) identified two wet subglacial landforms under North East Greenland Ice Stream, but their study revealed no evidence for a link between the water movement and the landform development.

- Clyne *et al.* (2020) interpreted water pockets overlying the soft sediment on the lee side of bumps with a length of over 400 m and a depth of <2–6 m.

- Sedimentary evidence of the water system beneath palaeo ice streams comes from eskers and braided deposits interpreted as the relic form of channels and canals, respectively. In the geomorphological record of palaeo ice sheet beds, eskers are usually found tracking along low points in the terrain and sometimes cutting through drumlins and MSGLs. The occurrence of eskers cross-cutting glacial landforms (Benn & Evans, 2011) indicates changes in hydrological system on the bed of former ice sheets. Finding them on top of such landforms is probably unusual and has not been reported to date (personal communication Chris Clark, November 2019). A lack of evidence for canals brings into question whether they were removed, or potentially never existed. McCabe & Dardis (1994) concluded from the sediment analysis of a drumlin in Ireland, the existence of a canal on the crest of the drumlin, as well as lee-side cavities, even though no esker is visible on the crest of the deglaciated landform.

5.3.3.2   Geometry of Water Bodies Beneath RIS

Using evidence from surface and airborne radar as well as seismic surveys the spatial extent of the water layer present on the MSGL crests can be estimated. The appearance of the high reflectivity in adjacent surface-radar lines enables an estimate of the length as well as the width of these water bodies. For the Bump and the "new" drumlin, the signals are visible over a length of 8 km and 4 km along the ice flow and width of 100 m and 50 m, respectively across the ice flow. Other landforms show this pattern over a length of up to 10 km, with a width of up to 100 m. The observations of water overlying the sediment are consistent with the water bodies interpreted as canals by Murray *et al.* (2008). Other studies have used additional evidence to differentiate between canals and channels (Schroeder *et al.*, 2013). However, no additional information on the geometry of the water bodies under RIS to differentiate between a canal or channel is available. Nevertheless, the width of these water bodies suggested a broad and

thin water body, consistent with canals. Furthermore, no statement about these water bodies being part of a water evacuation system can be made because water bodies on the bed of RIS do not have any obvious sink or source, and there is no indication of water beyond the end of the landform (e.g. around the boundary or in the lee of landforms).

A prominent isolated region of free water is located in the area of sliding bed (Figure 5.1, line 1002), while the area immediately around the free water consists of soft sediment. This isolated spot might be linked to the water bodies further upstream, as they are collinear along the ice flow. The isolated spot appears to be the first location downstream of the landform consisting of soft sediment. A more precise interpretation of this area would require a denser acquisition in flow direction as well as additional parameters from e.g. gravity, magnetics or seismics.

5.3.3.3 Differences Between Airborne- and Surface-Radar Data

As mentioned in Section 4.3.2.1.1, the overlap of the surface-radar line with the airborne-radar line could theoretically be used to confirm the distribution of soft sediment and low porosity material inferred from surface-radar data. However, due to issues in the airborne-radar data (described in Section 4.3.2.1.1) the differentiation between signals from soft sediment and low porosity material is not possible. The airborne-radar dataset can only be used to identify the occurrence of water. Nevertheless, when comparing these two radar datasets, the different wavelengths of the different systems, therefore resulting different vertical resolution, has to be kept in mind; $\lambda_{airborne}$=1.2 m while $\lambda_{DELORES}$=48 m. Indications for liquid water on the bed of RIS in most places are present in both radar datasets, although the intensity of the signal varies between the airborne- and surface-radar data. Variations in bulk relative permittivity seen in the airborne data in the western part of line 1007 were interpreted as a water evacuation system at the ice-bed interface by Murray *et al.* (2008). These water bodies might not be within the resolution of the surface-radar data. Some high reflectivity signals, indicating liquid water, might be a transient signal and the amount of water available might change over time, which would explain differences seen between airborne- and surface-radar data. However, signals of water on the Bump and "new" drumlin are present both years, indicating consistency.

5.3.4   Limitations of This Study

Possible reasons that could lead to a misinterpretation of the reflectivity are listed below:

- The interpretation of bed properties in this chapter, is highly dependent on the validity of bed properties chosen for the reference area. Temporal changes in bed properties within the reference area between the seismic and surface-radar survey (12 years) can not be excluded, although seismic acoustic impedance profiles were very consistent in the reference area over several years (personal communication Andy Smith, February 2021), which implies bed properties to be stable.

- An insufficient correction for englacial attenuation losses can be ruled out, since values of reflectivity (Figure 4.7) scatter over the whole length of twtt after correction for englacial attenuation (regardless of which correction was applied). Furthermore, reflections recorded at the same twtt (e.g. along the crest of the Bump, Figure 5.6) show different reflectivity which confirms that changes in reflectivity are twtt independent.

- Thin-layer stratigraphy is reported to possibly cause constructive and deconstructive interference. This process is frequency and layer thickness dependent. No change or spike was observed in the frequency-spectrum in the area of high and low reflectivity, which could indicate interference (Guha et al., 2005). Furthermore, airborne radar data analysed by Murray et al. (2008) led to a similar interpretation, although operated at a wavelength of 1.12 m compared to the wavelength of 48 m in this study, implying no major influence of a possibly layered stratigraphy on the reflectivity and permittivity. However, further investigation is needed to exclude effects of interference on the reflectivity.

- In glaciology, the interpretation of high reflectivity originating from water has typically been made by assuming the glacier bed to be a low-loss medium. However, Tulaczyk & Foley (2020) analysed the validity of this assumption and concluded that for low frequency radars (e.g. the surface radar in this study) the assumption of a low-loss material is not always valid. Reflections at an interface between ice and a material with high conductivity can appear as bright (high reflectivity) or even brighter than a reflection

of a water body (e.g. a subglacial lake). Highly conductive subglacial materials causing such high reflectivity could, for instance, be clay-bearing sediments, materials including seawater- or brine-saturated sediments and bedrock (Foley *et al.*, 2016). The sediments retrieved from the 2018/19 drilling campaign (Smith *et al.*, 2021) have not been analysed yet. The airborne-radar data include high frequencies ($\sim$150 MHz), for which some material possibly still shows high conductivity and, therefore would not fullfill the low-loss assumption. The possibility that the bed in the areas of high reflectivity consists of a high-loss material can not be ruled out; however, the frequency dependence of the reflectivity for different materials makes this less likely. Because in the case of a high-loss material, a major difference in the reflectivity between the airborne and surface radar would be expected (due to the different frequencies of the two datasets), which is not the case here.

5.4 Spatial Interpretation of Bed Properties

The high spatial coverage of reflectivity data enables the interpretation of basal conditions over a wider area than in previous studies on RIS. Figure 5.16 presents the final interpretation of the bed properties. According to this interpretation the bed of RIS partly consists of soft sediment (0.3–0.5 porosity), facilitating basal deformation. Elsewhere, low porosity material (<0.3 porosity) is present at the bed, and basal sliding dominates the flow mechanism. Figure 5.16 suggests that the distribution of different materials is more complex compared to previous studies, where the upstream part of the study area was interpreted to consist entirely of soft sediment (King *et al.*, 2009). Furthermore, the boundary between soft sediment and low porosity material is more complex. Areas assumed to be dominated by sediment deformation partly show localised outcrops of low porosity material, indicating a combination of basal sliding and deformation in that area. The co-existence of a deforming and non-deforming stable bed has also been observed in the palaeo record and has been described as a mosaic-like pattern by Piotrowski (1997) and Piotrowski *et al.* (2004). Within this theory areas with a lower permeability (low pore-water dissipation) tend to deform first. These deforming spots can then expand or shrink under certain conditions. Over a longer timescale, areas can experience multiple phases of deformation and then

become more stable again. Some of the subglacial landforms under RIS are cov-
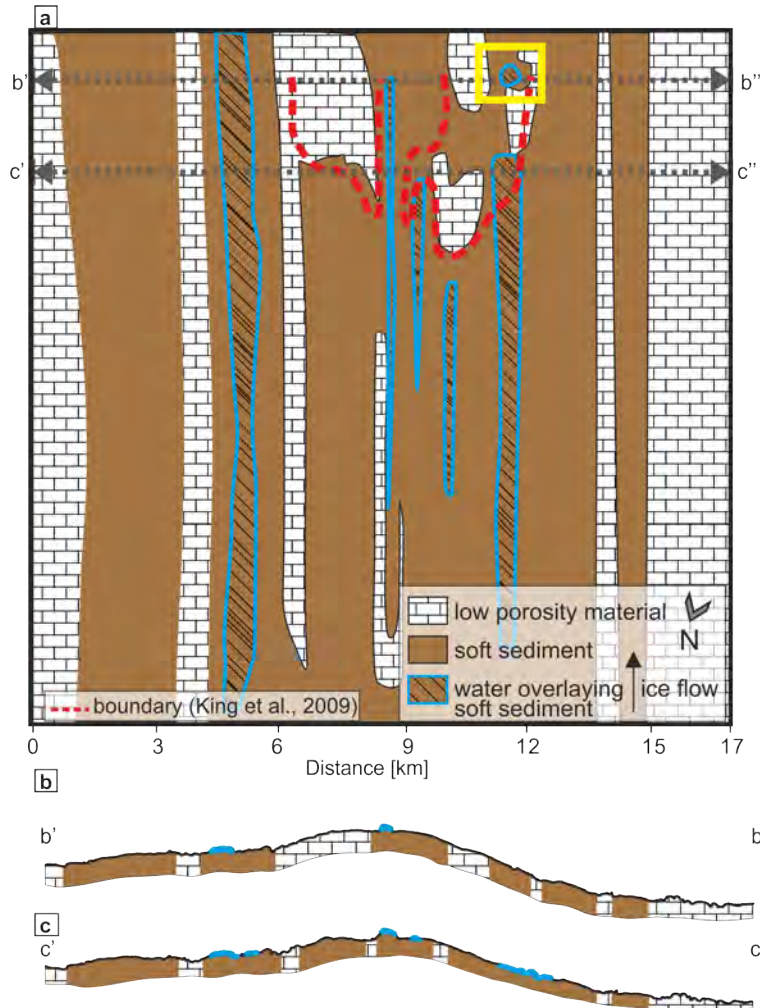
Figure 5.16: Conceptual model of the spatial pattern of bed properties under RIS. a) Plan view, including earlier definitions of the boundary, b) and c) show cross-sections through the bed at surface-radar line 1003 (b' to b") and 1007 (c' to c"), although sediment depth is unconstrained.

ered by soft, water-saturated sediment, while the troughs around some landforms as well as their upstream end consist of a harder material. Water bodies located on the crest of some landforms are aligned in the flow direction over a length of up to 10 km.

5.5 Summary

Surface-radar data were analysed to constrain in-situ bed properties over a wide spatial extent (14.5×18 km), including an area where previous surveys indicate spatial heterogeneities in bed properties. The uncalibrated surface-radar reflectivity was combined with porosities inferred from seismic acoustic impedance to calculate sediment porosities along the grid. The combination of the high spatial coverage of the surface-radar data and the constraints in bed properties from acoustic impedance enabled the interpretation of the distribution of bed properties over a wide area at a scale normally only considered in satellite or offshore studies of deglaciated areas. The spatial distribution of sediment porosities shows a variable bed, consisting of areas of soft sediment, areas of low porosity material and areas of water overlying the soft sediment. The low porosity material is interpreted to consist of compacted sediment or sedimentary rock. Highly porous, soft sediments reduce the basal drag and facilitate fast ice flow.

Bed properties within the pre-defined deforming and sliding bed (King *et al.*, 2009) vary. For most of the bed, excluding the sliding area, bed properties are aligned in the ice flow direction, while bed properties vary across flow on a 100 m scale. The existence of soft sediment and low porosity material upstream of the boundary indicate a combination of basal sliding and deformation in that area, consistent with the co-existence of a deforming and non-deforming stable bed in the palaeo record described as a mosaic-like pattern by Piotrowski (1997) and Piotrowski *et al.* (2004). Subglacial landforms covered by or consisting of, soft sediment, as well as low porosity material, were identified. Some landforms consist of low porosity material at the upstream end, which then transitions into soft sediment. Both airborne- and surface-radar data indicate free water overlying sediment on the crest of some landforms, as well as an isolated spot. The water bodies show a length of up to 10 km, with a maximum width of 100 m. The spatial variation of material properties, and therefore possibly permeability, may be the mechanism behind the occurrence of water on the crest of landforms, rather than in their trough.

Chapter 6

Topographic Changes and their Link to Bed Properties

Erosion and deposition can have an impact on ice dynamics by changing basal properties (Meier & Post, 1987; Post & Motyka, 1995). Furthermore, erosion rates can help to understand how fast a glacier can reorganise its bed. This chapter describes the results (Section 6.1) and discussion (Section 6.2) of the analysis of temporal changes in topography between 2007/08 and 2016/17 (for methods see Section 4.4). Within this thesis, a topographic change is defined as a change in topography of at least 3 m in height and 30 m in length (Section 4.4.1.1). In the following, locations of observed topographic changes are introduced (Section 6.1). To illustrate topographic changes data along radar lines are plotted to see the location and numbering of radar lines on the bed see Figure 3.4. Data used for the analysis and shown in the following figures were acquired perpendicular to the ice flow direction (500 m line spacing) and were 2D processed (Section 3.2.1). Section 6.1.1 describes topographic changes observed over several (neighbouring) lines. Finally, in Section 6.1.2, the locations of changes are compared to locations of sticky spots identified using passive seismics (Kufner *et al.*, 2021; Smith *et al.*, 2015), calculated reflectivity (Section 5.1) and bed properties interpreted from reflectivity (Chapter 5.3.1).

6.1 Results - Overview on Topographic Changes

In total 13 locations with topographic changes were identified (Figure 6.1), all representing a drop in topography, therefore erosion of material. Topographic
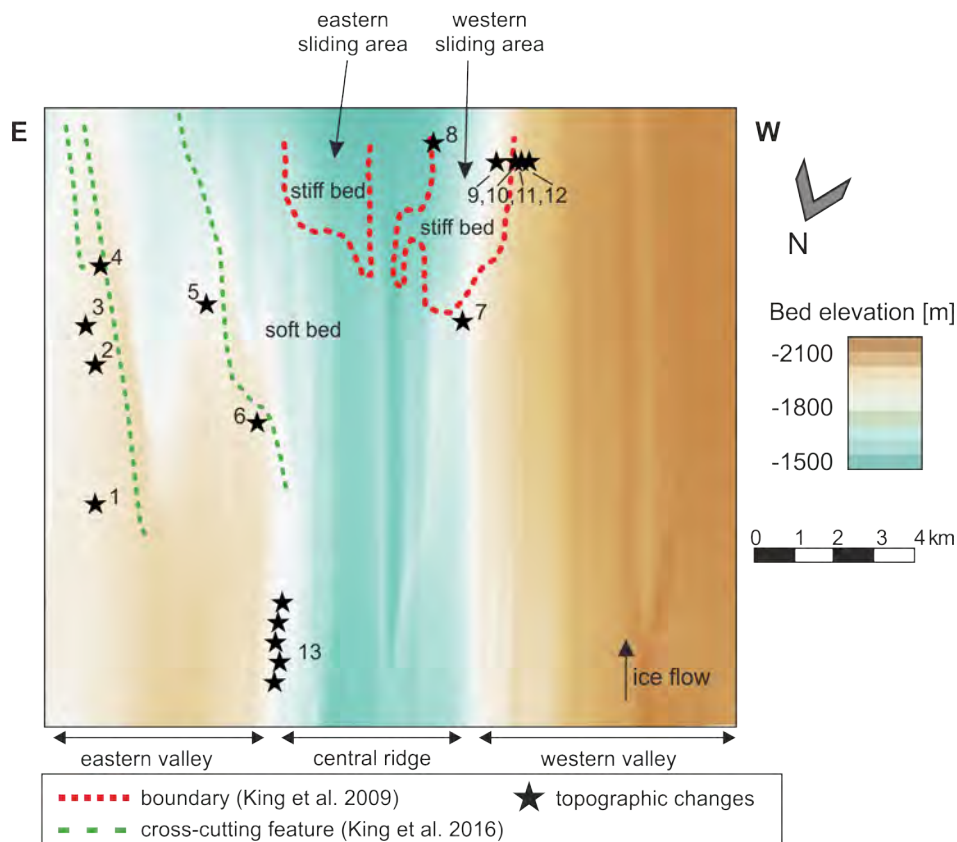
Figure 6.1: Plan view of the bed of the RIS. Colour-coding represents the bed elevation referenced to WGS84 ellipsoid according to King *et al.* (2016). Black stars (numbered 1–13) mark the locations of observed topographic changes.

changes were observed in the eastern valley, close to the cross-cutting feature (green dashed line), but no changes were observed in the western valley. On the central ridge, some changes were observed in the western part of the sliding area and at the boundary (red dashed line) between stiff and soft sediment, according to King *et al.* (2009), but no changes were observed in the eastern part of the sliding area (Figure 6.1). Table 6.1 gives a brief overview of the dimensions of the observed topographic changes, excluding location 13, which is described in more detail in Section 6.1.1. In the following, some of these locations are described in more detail:

Table 6.1: Dimensions of observed topographic changes as seen in Figure 6.1. Location 13 is excluded here but described in Section 6.1.1.

location	line	visible in adjacent lines?	height difference [m]	width [m]
1	1020	yes, line 1019	5.5	120
2	1013	no	3	50
3	1011	no	8	80
4	1008	not clear	6	60
5	1010	no	6.5	80
6	1016	not clear	7.7	60
7	1011	no	6.7	80
8	1002	no	12	60
9	1003	no	15	120
10	1003	no	3	50
11	1003	no	4	100
12	1003	no	6	120

Topography at location 1 (line 1020, Figure 6.2) shows a drop in height of 5.5 m (line 1020). Data within neighbouring line 1019 (downstream) also show some topographic changes but with a smaller volume than in line 1020. The erosion observed in data at location 3 lies approximately 1500 m upstream of location 4. However, data in between these locations show no change in topography (Figure 6.1). The topographic change at location 6 was identified in previous studies (King *et al.*, 2017) and appears in line with the cross-cutting feature (green dashed line in Figure 6.1) downstream of line 1016 (Figure 6.3).

Data at location 9 (Figure 6.4) show a hill with a height of 10 m and a width of 100 m in 2007/08, but a reflection indicating a hill 9 years later is lacking.
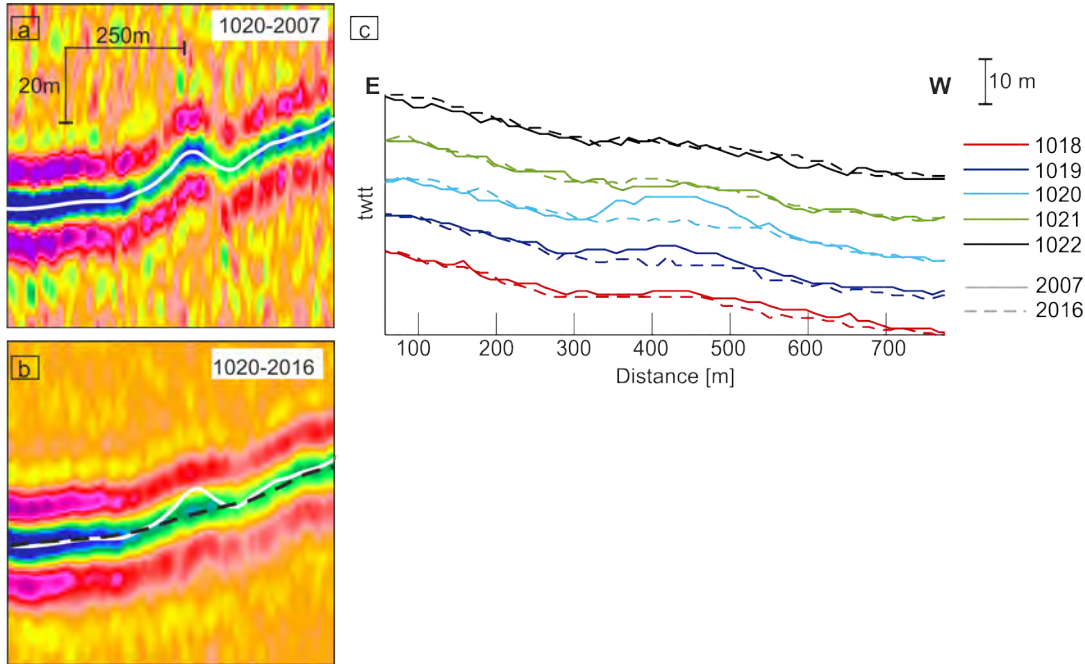
Figure 6.2: Topography around location 1 and adjacent lines: a) Radargram of line 1020 in 2007/08. b) Radargram of line 1020 in 2016/17 in the same geographical location as in (a). Pick of the bed reflection in 2007/08 shown by the white solid line, pick on 2016/17 data by the black dashed line. c) twtt of the bed reflection in 2007/08 (solid line) and 2016/17 (dashed line) for lines 1018–1022.

6.1.1 Erosion Over Several Lines

At the upstream end of the survey grid (location 13) a drop in topography is visible in flow direction along lines 1030 to 1025 (Figure 6.5 and 6.6). This is the only area on the bed where topographic changes in the area of a subglacial landform were observed. The width of the hill that was removed in line 1029 and 1030 accounts to ∼100 m, and the height difference over the 9 years is approximately 5 m, decreasing towards downstream (Figure 6.5 and Figure 6.6), where the hill is present in both years.

6.1.2 Location of Erosions With Respect to Reflectivity and Sticky Spots

Figure 6.7 shows the reflectivity pattern resulting from reflectivity analysis in Section 5.1 and Figure 5.1, as well as the topographic changes (black stars) described in the current chapter. According to the interpretation in Section 5.3.1,
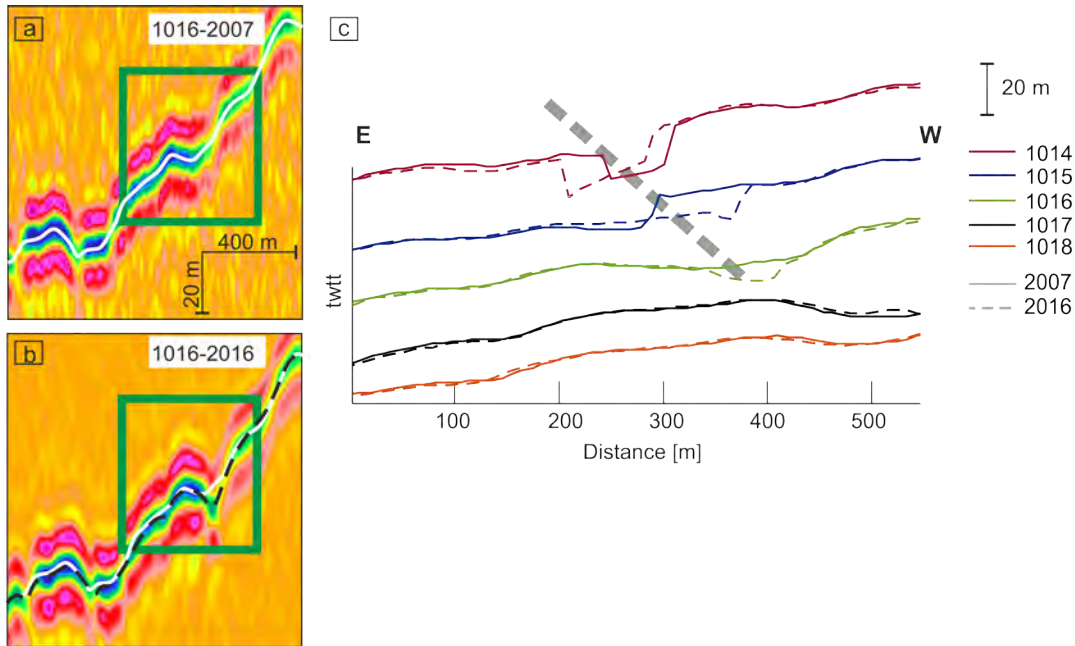
Figure 6.3: Topography around location 6 and adjacent lines, within the area of a cross-cutting feature in the eastern valley. a) Radargram of line 1016 in 2007/08. b) Radargram of line 1016 in 2016/17 in the same geographical location as in (a). Pick of the bed reflection in 2007/08 shown by the white solid line, pick on 2016/17 data by black dashed line. c) twtt of the bed reflection in 2007/08 (solid line) and 2016/17 (dashed line) for lines 1014–1018. The pick of the topography along the cross-cutting feature in line 1015 and 1014 is not possible, an interpolation of the picks is shown, but this might not represent the true bed reflection. The grey dashed line marks the rough orientation of the cross-cutting feature.

areas of reflectivity $<0.6\,\mathrm{V}$ are interpreted to consist of low porosity material while porosity is interpreted to increase with increasing reflectivity (Table 5.1). The reflectivity upstream of the boundary (red dashed line) is aligned in a band-shaped pattern aligned in the flow direction. This pattern is described with little variation along flow, but shows variation on a spatial scale of $100\,\mathrm{m}$ across flow (Section 5.1). Comparison of the locations of topographic change (excluding location 6) and the reflectivity shows topographic changes to be located close to areas where reflectivity varies from very low reflectivity (white, interpreted as low porosity material, Figure 6.7) to low reflectivity (light blue, presumably softer material, Figure 6.7). The pattern of reflectivity in the sliding areas is more diffuse and not aligned in the ice flow direction (Section 5.1). However, topographic changes found in the western part of the sliding area are accompanied by changes in reflectivity, e.g. location 8; reflectivity changes from very low (white) to low

147
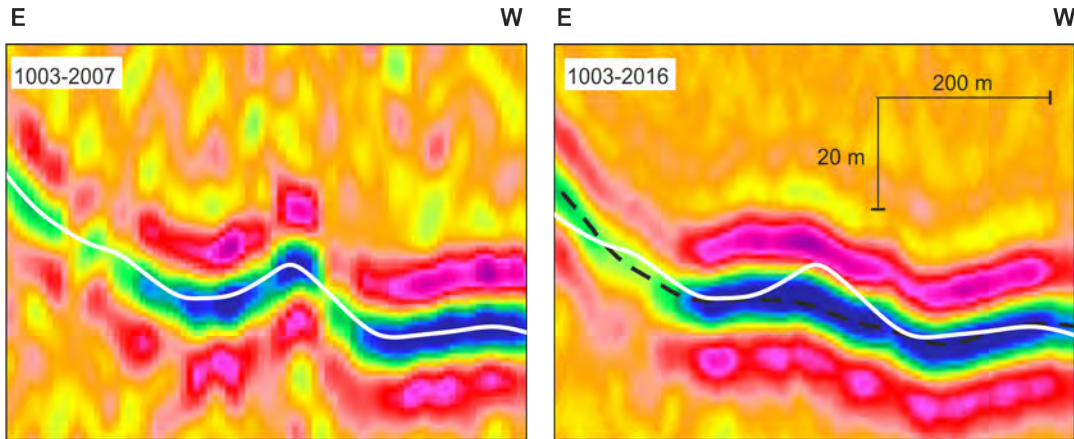
Figure 6.4: Topography around location 9, which is located in the sliding area. Radargram of line 1003 in 2007/08 (left) and 2016/17 (right). Pick of the bed reflection in 2007/08 shown by the white solid line, pick on 2016/17 data by black dashed line.

(light blue, Figure 6.7 c). Bed properties around location 6 (Figure 6.7 b) imply soft sediment, partly with a water layer, to be present. However, as previously mentioned, the erosion at location 6 appears in line with a cross-cutting feature.

Sticky spots identified using passive seismic emissions are limited to the area around the boundary (Figure 6.8), due to the geometry and the location of the seismometers, which were used to record data to identify sticky spots (Kufner et al., 2021; Smith et al., 2015). Therefore, the comparison of locations of sticky spots and erosions shown in Figure 6.8 solely focuses on the area around the boundary. More sticky spots (Kufner et al., 2021; Smith et al., 2015) were identified within the western part of the sliding area compared to the eastern, which is similar to the occurrence of erosion solely observed in the western part of the sliding area. However, topographic changes within the sliding area are located in areas with only few sticky spots, therefore a seismologically quiet zone (Figure 6.8).

6.1.3 Key Observations

- Temporal changes in topography all represent erosion (min. 3 m height difference).

- 13 locations of erosion were observed.
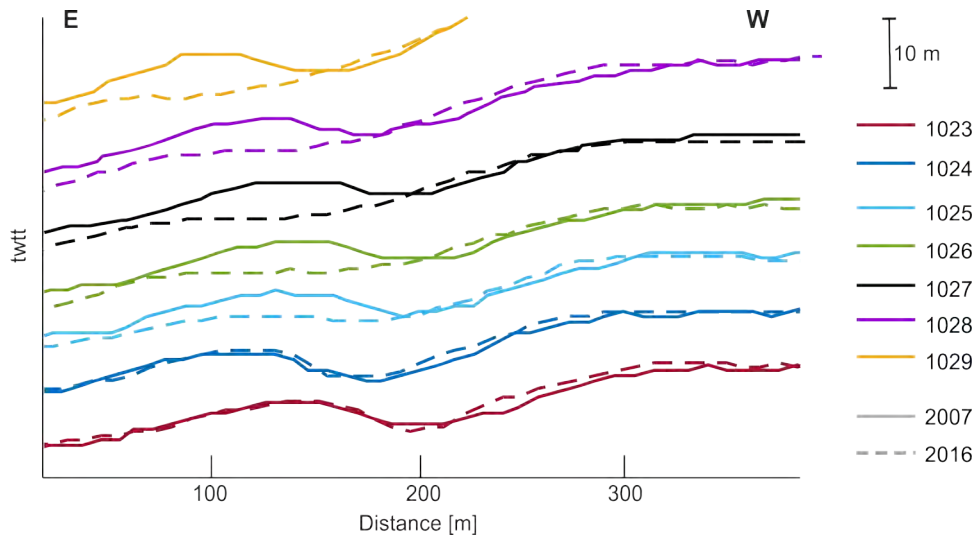
Figure 6.5: Topographic changes observed in data around location 13. This area is located at the upstream end of the survey grid around a subglacial landform. twtt of the bed reflection in 2007/08 (solid line) and 2016/17 (dashed line) for lines 1023–1029.

- 11 locations show local erosion of a mound that is only visible in one radar line (maximum extent on flow direction 900 m).

- Erosion observed at location 6 represents the upstream migration of a cross-cutting feature.

- Erosion in one location is visible over 5 lines, a width of 50–120 m along the line and 3–7.7 m height and represents the erosion of the downstream end of a subglacial landform.

- Most erosion were identified in areas where bed properties are assumed to change from low porosity material to softer material.
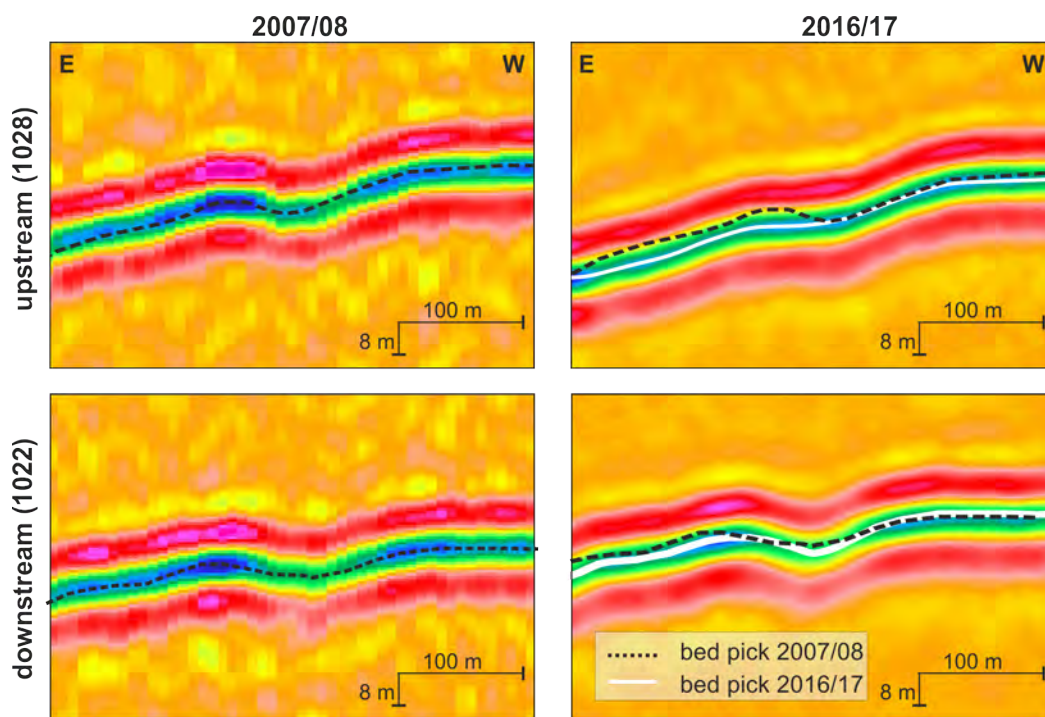
Figure 6.6: Radargrams in 2007/08 (left) and 2016/17 (right) showing data in different lines around location 13. Top: Radargrams of line 1028 (upstream), bottom: Radargrams of line 1022 (downstream). The black dashed lines show the bed pick on repeated lines in 2007/08 and in white for line the pick in 2016/17.
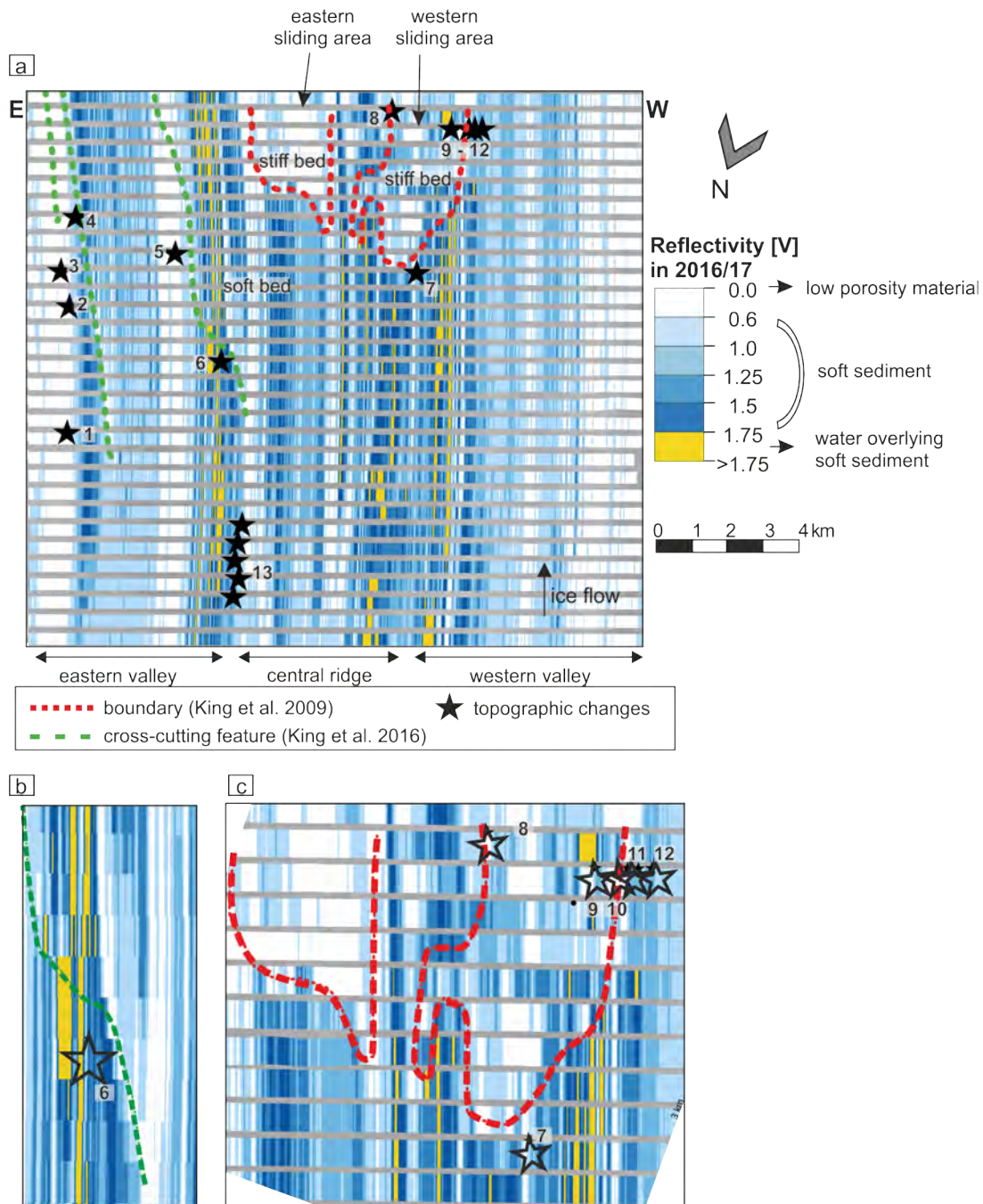
Figure 6.7: Reflectivity of the bed beneath RIS as described in Chapter 5.1 and Figure 5.1. Panel b shows a zoom on the area around location 6, panel c a zoom on the area of the boundary (location 7–12). Yellow marks high reflectivity, interpreted as water overlying sediment, white areas, representing very low reflectivity, interpreted as low porosity material (compacted sediment or sedimentary rock). Black stars mark the location of observed topographic changes.
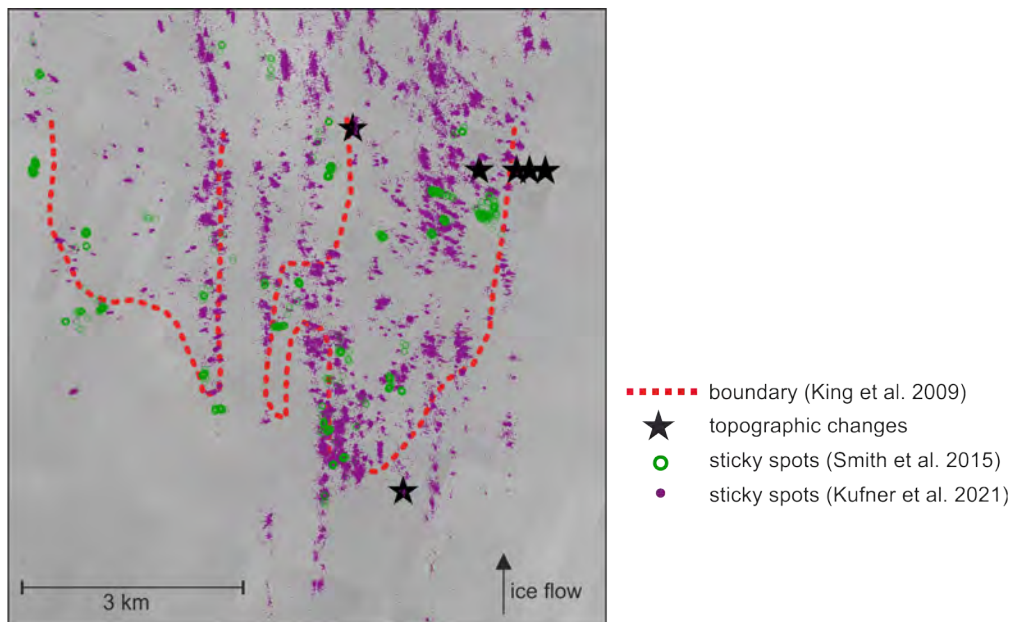
Figure 6.8: Comparison of locations of sticky spots and observed topographic changes within and around the boundary. Black stars mark the location of observed topographic changes. Sticky spots are shown as green circles (according to Smith *et al.* (2015)) and purple dots (according to Kufner *et al.* (2021)).

6.2 Interpretation

In the following, the location and properties of the eroded materials are discussed (Section 6.2.1). Possible mechanisms that can cause erosion of sediment are given in Section 6.2.2. This is followed by different mechanisms that explain the absence of any evidence of deposition of the eroded material (Section 6.2.3). A final interpretation of mechanisms responsible for topographic changes on the bed of RIS is given in Section 6.2.4. A special focus of the discussion is set on the erosion of landforms. Finally, estimations of erosion rates are given.

6.2.1 Erosion of Soft Sediment

Observed erosions located in proximity to or within the soft sediment (Figure 6.7) suggest that soft (high porosity) sediment was eroded rather than low porosity material. This is most apparent for the partial erosion of a landform (location 13), as subglacial landforms under RIS are interpreted to consist of soft sediment (Section 5.3.1.1, Section 5.3.3.1; Smith & Murray, 2009; Smith et al., 2007). The sliding area is assumed to consist mainly of low porosity material and stiff sediment (Figure 5.16). Areas of erosion within and around the sliding area (location 7–12) are located in the vicinity of where reflectivity suggests local spots of soft sediment (Figure 6.7 c). The co-existence of soft sediment (likely subject to basal deformation) as well as low porosity material (presumably non-deforming) is also reflected by the pattern of sticky spots identified in the sliding area (Kufner et al., 2021; Smith et al., 2015).

The majority of erosion events found within the 9 year period are found in a setting consisting of a hill of supportingly soft sediment in only one survey line, therefore with a maximum extent of 900 m in flow direction (possibly much less). This local topography represents a local resistance to the ice flow, hence an easy target for erosion. However, there are numerous of these local hills present on the bed, with no obvious difference that could help to determine which hill is more susceptible to erosion compared to others. Bennett & Glasser (2009) described the regional pattern of erosion to be controlled by the basal thermal regime, while the local pattern is controlled by different variables, including the geology i.e. areas of softer lithology will experience more erosion than harder, more resistant lithologies. Spatial changes in the texture of the bed and/or water availability can lead to small-scale variations in the mobility of the bed, therefore variation

in resistance to ice flow and erosion (Boulton *et al.*, 2001; Menzies, 2002; Van Der Meer *et al.*, 2003). However, small-scale variations, causing some areas to be more resistant to flow than others, might not be within the spatial resolution of identified bed properties (Chapter 5). Moreover, the interpretation of bed properties in Chapter 5 was made on the basis of data acquired in 2016/17, and a temporal change of these bed properties within 9 years can not be excluded. Nevertheless, the stability of the ice flow and temporal consistency of large areas of the bed reported by Smith *et al.* (2007) support the assumption of only very few and local changes in bed conditions over such small periods.

6.2.2   Possible Mechanisms of Erosion

Three mechanisms are known to cause subglacial erosion: (1) influence of water, (2) mechanical and (3 & 4) thermo-mechanical mechanism. In the following, possible mechanisms causing the erosion of local hills are discussed:

1. Erosion by water can occur in canals and/or channels or as discrete flood events:

   1.1. Canals or channels are known to migrate upstream under certain conditions. The upstream migration of a cross-cutting feature could therefore be an indication for a water routing system that is cut into the bed. The absence of high reflectivity (location 6, Figure 6.7), and therefore liquid water in and around these cross-cutting features implies that these cross-cutting features do not represent a water routing system but are possibly formed by the underlying geology (see Section 5.3.1.2).

   1.2. Subglacial floods are known to cause erosion of large amounts of sediment, affecting a large area (Shaw, 1983). Bathymetric evidence indicates large amounts of sediment were removed from Pine Island Bay by water flowing beneath the ice (Lowe & Anderson, 2003). Areas of erosion observed under RIS are spatially limited. Furthermore, erosion by water would be expected in the deeper valleys under RIS due to the hydraulic head (Section 5.1.4), rather than in the locations of erosion found here and in the study of Smith *et al.* (2007). Subglacial lakes have, however, been identified further upstream (Napoleoni *et al.*, 2020), which might provide a source for water.

2. Ploughing as well as clasts and irregularities at the ice base were reported to remove material in the flow direction, over a distance of several kilometres (Alley *et al.*, 2019; Clark *et al.*, 2003):

   2.1. A boulder incorporated into the ice base, ploughing through the glacier bed as the ice moves, would be expected to create a groove along the ~ 3.2 km distance that the ice stream moved over 9 years. No groove upstream or downstream of the erosions was observed. However, the boulder might have created a groove that is not resolvable with the methods presented here (less than 3 m in depth).

   2.2. Sediment might be incorporated into the basal ice in the first place but been interpreted as a hill on the bed. Due to the ice movement, this sediment will move over time. However, no hill has appeared further downstream after 9 years. Assuming the hill represented sediment incorporated into the basal ice in the first instance, this hill was either located between survey lines or sediment was melted out over time.

   2.3. Clasts incorporated in the ice base might lead to local compression of sediments, assuming the ice base to be more rigid than the sediment. Assuming a 0.5 porous sediment a 40% volume decrease could be achieved without significantly changing the reflectivity and therefore interpreted bed properties (Chapter 5). Nevertheless, this would require compression to take place at a localised spot over several metres of depth, while parts of the sediment would still need to be moved to another area.

3. The drag between the sediment and the ice might be sufficiently high in some areas to detach and deform sediment, especially if these areas represent a local hill consisting of soft sediment. The transport of soft sediment by subglacial till deformation was described before by Truffer *et al.* (2000) and Boulton (1996) and is assumed to be capable of transporting significant amounts of material (Alley *et al.*, 1989; Clark & Pollard, 1998). The eroded material could then get incorporated into a thin till layer.

4. Under the assumption of ice being stiffer than the soft sediment regelation and refreezing could lead to the erosion of sediment at the upstream end of the hill and deposition of sediment downstream of the hill (Section 2.1.2, Figure 2.2). However, the process of regelation and refreezing is highly dependent on the conduction of heat through the obstacle (here the hill).

Regelation is described to be most efficient for small obstacles ($<10\,\text{mm}$ (obstacle size described for regelation)) (Alley *et al.*, 1997; Benn & Evans, 2011) and is probably inefficient in the setting described here.

6.2.3 Deposition of Eroded Material

No depositions of material resolvable with the method used were observed. Different options on where the eroded material was moved to are given below:

1. Sediment may have been transported to areas outside the grid. For the erosion observed at the upstream end of the grid, this would imply sediment flux not to be aligned in flow direction or the material to move faster than the ice flows in this area. However, the upper surface of the deforming till layer is assumed to move with or slower than the ice base which makes both options less likely (Alley *et al.*, 1989, 2019; Clark & Pollard, 1998; Zoet & Iverson, 2018).

2. Eroded material might be deposited in thin layers, with insufficient thickness to be resolvable within this dataset. The deposition of sediment in a local hill will be resolvable as a distinct feature if hill height is more than $3\,\text{m}$ (the threshold for detecting difference). Deposition of thin layers could occur (2.1) by sediment incorporation into the basal ice and then slowly melting out, or (2.2), by soft bed deformation, smearing the sediment over a wider area (in flow direction as well as across).

2.1. Sediment might get incorporated into the ice base by freeze-on or via basal faults and crevasses, as is seen for surging glaciers (e.g. Hambrey *et al.*, 1996; Lovell *et al.*, 2015). With the ice advancing over the bed, basal melting might lead to the deposition of englacial sediment over a large distance. The idea of sediment incorporation into the basal ice is supported by the findings of Smith *et al.* (2021), describing the occurrence of englacial sediment close to the bed from hot-water drilling performed in the proximity of the boundary separating deforming and sliding bed. More englacial sediment was retrieved from the area of basal sliding (Hole 3, Smith *et al.* (2021)), when compared to the deforming bed (Hole 1 and 2). Local spots of soft sediment in the sliding area and areas where the soft sediment thins out (e.g. the boundary between sliding and deforming bed) provide a weak

basal interface for the fast ice flow. Moreover, ice moving against the rising bed topography towards downstream might lead to a higher pressure zone (compared to further upstream), possibly presenting another feedback effect. The occurrence of more englacial sediment close to the glacier bed in the sliding area, where we find variations in bed properties and changes in topography along flow, is therefore consistent with the process of erosion by regelation and incorporation of the sediment in the basal ice. However, englacial sediment transport is described as very inefficient (Alley *et al.*, 1987; Boulton & Jones, 1979), as basal heat created by the fast ice flow over the bed will sequentially lead to melt out of englacial sediment.

2.2. Subglacial deformation is described as very efficient to transport large amounts of sediment (Alley *et al.*, 1989; Clark & Pollard, 1998). The amount of sediment transported within different areas will vary according to variations in shear stresses, effective pressure and material properties (Boulton, 1987; Boulton & Jones, 1979), therefore the coupling between bed and the sediment (e.g. water at the ice-sediment interface favours rapid motion by decoupling the bed and therefore reducing sediment deformation (Fischer & Clarke, 2001; Iverson *et al.*, 1995)). Although only local erosion is observed, soft sediment deformation is probably taking place over a large area of the bed without being resolvable with the techniques used in this study.

6.2.4 Final Interpretation of Mechanisms Driving Erosion and the Deposition of Eroded Material

From the dataset presented here, a distinction between interpretation whether the erosion happened as a discrete, rapid event or as a continuous event over the 9 year period can not be made. However, the stability of the ice flow favours the erosion by a continuous ice-bed interaction, like regelation and refreezing or the mechanical deformation of soft sediment (or a combination of both). Due to the size of the hills ($>10\,\text{mm}$), therefore the relatively low amounts of transported sediment, the soft bed deformation is more likely to be the main process driving the observed topographic changes. To where the eroded sediment was moved is unknown, but considering ice flow and subglacial hydraulic gradients, it is most likely to have been transported downstream. This could have happened either by the incorporation of sediment into the ice base and sequentially melting out

of this subglacial sediment, distributing it over large area as well as deforming sediment into thin layers. Both of those options would deposit the sediment in thin layers that are not resolvable with the dataset and technique presented here.

6.2.5 Erosion of a Subglacial Landform

The observed erosion of the downstream end of a landform represents the downstream migration of the landform's upstream end. This shortening of a landform and the extension of the "new" drumlin observed by Smith *et al.* (2007) and Smith & Murray (2009), highlight that landforms on the RIS are not a static and non-dynamic part of the bed but are subject to temporal changes. The interplay between sediment deformation, erosion, transport as well as formation of drumlins was highlighted before by Boulton (1996); Boulton & Hindmarsh (1987) and Hindmarsh (1998).

The bed of the RIS is overprinted by subglacial landforms, which raises the question why was just this one landform eroded, rather than any surrounding landforms. So far a link between the formation of landforms and their erosion has never been discussed or published, which might be related to the lack of observations of such erosions. The erosion of the landform might be linked to:

1. variations in the geometry of the whole landforms, or solely the upstream or downstream ends,

2. variations in the sediment composition of landforms. As landforms possibly were formed at different times, the sediment supply in these times possibly changed and, therefore, the composition of the landforms might changed,

3. spatial variations in the sediment content incorporated into the basal ice, which causes spatial, small-scale variation in ice stiffness.

Theses changes might affect the resistance to erosion of landforms. The different options are evaluated in more detail below:

1. The eroded landform is only partly visible in the dataset, therefore no statement about the geometry of the upstream end of the landform can be made. Due to the coarse line spacing of the data analysed here, a quantitative comparison of the downstream end of this landform and others can not be made and a denser data spacing is needed. Furthermore, due to the

missing upstream end in the data, an estimation of the length, therefore elongation ration is not possible. However, the width of the landform accounts to $\sim$80 m, which is fairly small compared to other landforms on the RIS (mean subglacial landform width is 267 m (Smith & Murray, 2009)).

2. In Chapter 5 spatial variations in sediment porosity of the bed were identified; therefore sediment properties might vary for different landforms. Difference in the composition might lead to variations in stiffness and resistivity of sediment. However, further analysis and preferably seismic acoustic impedance measurements are needed to identify differences in sediment composition between different landforms.

3. Smith *et al.* (2021) reported on variations of englacial sediment content further downstream. However, the occurrence of sediment incorporated into the basal ice in the location of the eroded landform would need to be longitudinal along flow to be affecting solely the landform and not the surrounding topography.

Due to the limited data available to analyse the eroded landform, a clear statement can not be made here. Nevertheless, a mechanical erosion of the landform (soft bed deformation), in which the location of the erosion is dependent on the three parameters: geometry, composition of the landform and the stiffness of basal ice, seems most likely.

6.2.6 Erosion Rates

Averaged over the 9 year period, the minimum local erosion rate was 0.7–$1.3\,\mathrm{m\,a^{-1}}$. These rates are comparable to results from Smith *et al.* (2007) showing erosion rates of $1\,\mathrm{m\,a^{-1}}$ from repeated seismic measurements (Section 2.3.3) but here are derived from data covering a much wider area and a larger number of measurement points. Nevertheless, measured and interpreted erosion rates in most subglacial environments normally range from 0.1–$100\,\mathrm{mm\,a^{-1}}$ (Alley *et al.*, 2003; Hallet *et al.*, 1996; Humphrey & Raymond, 1994), much lower than was observed for the RIS. Erosion rates in only few areas (Iceland and Alaska during the Little Ice Age and Taku Glacier) consisting of soft, poorly lithified sediments, are assumed to be in the order of up to meters per year (Björnsson, 1996; Motyka *et al.*, 2006; Smith *et al.*, 2007). Erosion rates on Pine Island Glacier are determined

to be around $0.6\,\mathrm{m\,a^{-1}}$ for a period between 1960 and 2009. Nowadays, erosion rates under Pine Island Glacier are expected to be higher (around $1\,\mathrm{m\,a^{-1}}$) due to the acceleration of the ice flow of Pine Island Glacier (Smith *et al.*, 2012). However, these high erosion rates under Pine Island Glacier as well as in Iceland and Alaska are found for non-steady glaciers, experiencing major changes in the ice dynamics, e.g. continuous acceleration of the ice flow and surface lowering, whereas the RIS is described as a steady system.

6.2.6.1 Erosion of a Landform

The erosion of the downstream end of a landform, observed over several lines, can be used to estimate the volume of sediment eroded in this area. The length estimate used to calculate the volume is limited by the spacing of the radar lines as well as the extent of the grid. The volume of sediment initially forming this landform approximate accounts to 64–$100.8{\times}10^4\,\mathrm{m^3}$ ($\sim 80\,\mathrm{m}$ wide, 4–$4.5\,\mathrm{m}$ height, 2–$2.8\,\mathrm{km}$ length). Spreading out this volume over the whole study area ($18\,\mathrm{km}\times14.5\,\mathrm{km}$) would result in a $\sim 2.5\,\mathrm{mm}$ thick sediment layer. A layer of such thickness would not be detectable within this study.

6.3   Summary

Repeated surface-radar data were analysed to identify temporal variation in bed topography over a $14.5{\times}18\,\mathrm{km}$ area beneath RIS. Temporal variations in topography beneath RIS were determined before using repeated seismic surveys (Smith *et al.*, 2007), although these measurements only covered relatively small areas. In total 13 locations with topographic changes were identified, each showing a drop in topography, therefore erosion of material. Most erosions represent the removal of local hills, which reduces resistance to ice flow. Observations of erosion also include the upstream migration of a cross-cutting feature and possibly the first observation of partial erosion of a landform. Landforms beneath RIS are shown to be a non-static part of the bed and undergo shortening and extension (Smith & Murray, 2009; Smith *et al.*, 2007). Erosion is interpreted to be dominated by mechanical erosion by soft bed deformation, while the eroded sediment most likely gets deposited in thin layers. The maximum erosion rate beneath RIS is around $1\,\mathrm{m\,a^{-1}}$, which is consistent with results from repeated seismic surveys

on RIS. However, erosions beneath RIS within the 9 years investigated in this chapter only affect local hills.

Chapter 7

3D Migration and Attributes of Basal Reflections

The aim of the acquisition of data compliant with 3D migration and the processing of these data was to create high-resolution images of the topography beneath RIS. By calculating different attributes, the visibility of small-scale detail of this topography is enhanced, and details of subglacial processes can be identified. In the following results of the 3D migration and attribute analysis of data acquired in 2017/18, including two grids covering an area of 3×3 km (Figure 3.7) are described. Grid 1 covers the upstream end of the Bump, and grid 2 the downstream end of landforms terminating against the boundary as well as parts of the boundary.

This chapter is divided into three different parts. First is the description of 3D migration results, which includes examples of the 3D migrated data and the amplitude behaviour of these data (Section 7.1), as well as a comparison of the topography received from 3D migrated data compared to topography received from previously acquired 2D processed data (Section 7.2). The second part of this chapter focuses on the attribute analysis of 3D migrated data, where Section 7.3.1 describes different attributes calculated for the bed reflection. Structural attributes of the bed topography and the envelope of the bed reflection are described in Section 7.3.2 and Section 7.3.3. Section 7.3.4 focuses on the different landforms found within both grids and gives an estimation of the volume of the Bump and the moat in both of the grids. The third part of this chapter comprises a discussion of these results (Section 7.4).

7.1 Amplitude Behaviour in 3D Migrated Data

This section provides a few snapshots of the radar data after 3D migration to demonstrate the data quality and, therefore, clarity of the bed reflection. Figure 7.1 shows examples of an in- and crossline of grid 1 after processing including 3D migration. The spatial evolution of the Bump can be seen in Figure 7.1 b, where the prominence is ∼15 m above the surrounding bed. While the Bump grows along flow (with decreasing line numbering) the bed reflection becomes discontinuous in places, especially around the flanks of the Bump. These discontinuities are also visible within data along crosslines (Figure 7.2), which image the topography along flow (from left to right). Crossline 601 in Figure 7.2 a shows the topography along flow, starting upstream of the Bump, then along the Bump and later on along the eastern flank of the Bump. Crossline 701 (Figure 7.2 b) is located further to the west of the previously described line, imaging the trough around the Bump and partly the flank. The trough around the Bump is from now on referred to as a moat. Other lines show areas further to the west, where small-scale landforms can be found. Crossline 1201 (Figure 7.2 e) is located close to the western edge of grid 1. Here the topography in the flow direction appears smooth and a continuous bed reflection can be seen.

Amplitude nulls in the bed reflection complicate horizon picking, and, as such, the COP attribute (Figure 7.3 and 7.4) is introduced to fill gaps in amplitude coverage (Section 4.5.3.2). Discontinuities in the amplitude are much more pronounced in grid 1 (Figure 7.3) compared to grid 2 (Figure 7.4), where most of the lines show a clear continuous reflection, and only certain areas contain scattered amplitudes for the bed reflection. Even with the use of the COP a continuous pick along the flanks and the moat of the Bump was not always possible.
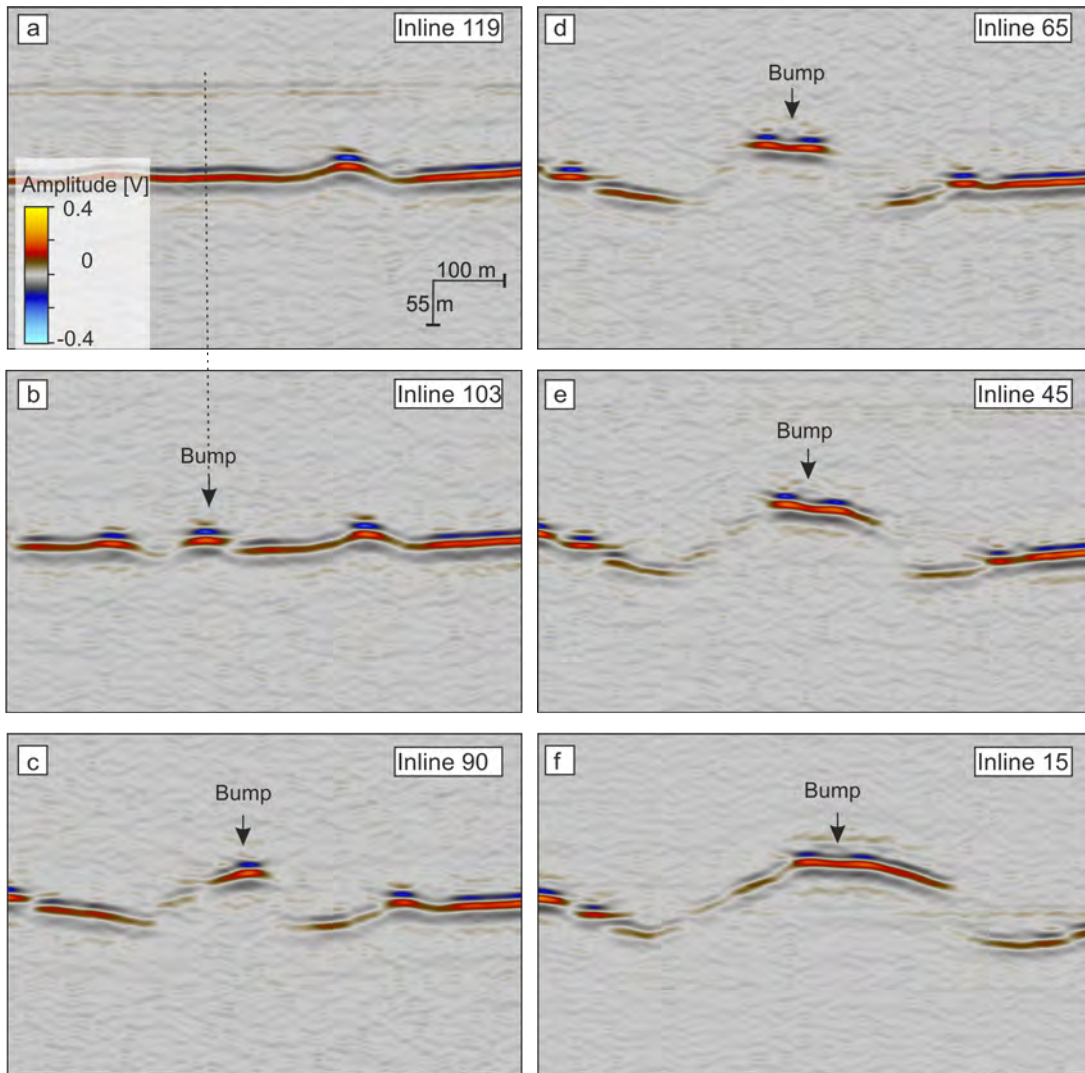
Figure 7.1: Result of 3D migration shown for different inlines of grid 1. Vertical and horizontal scales, as well as colour bars, are kept constant. Ice flowing into the page. The dashed line between a) and b) was drawn to point out the approximate location of the Bump further downstream.
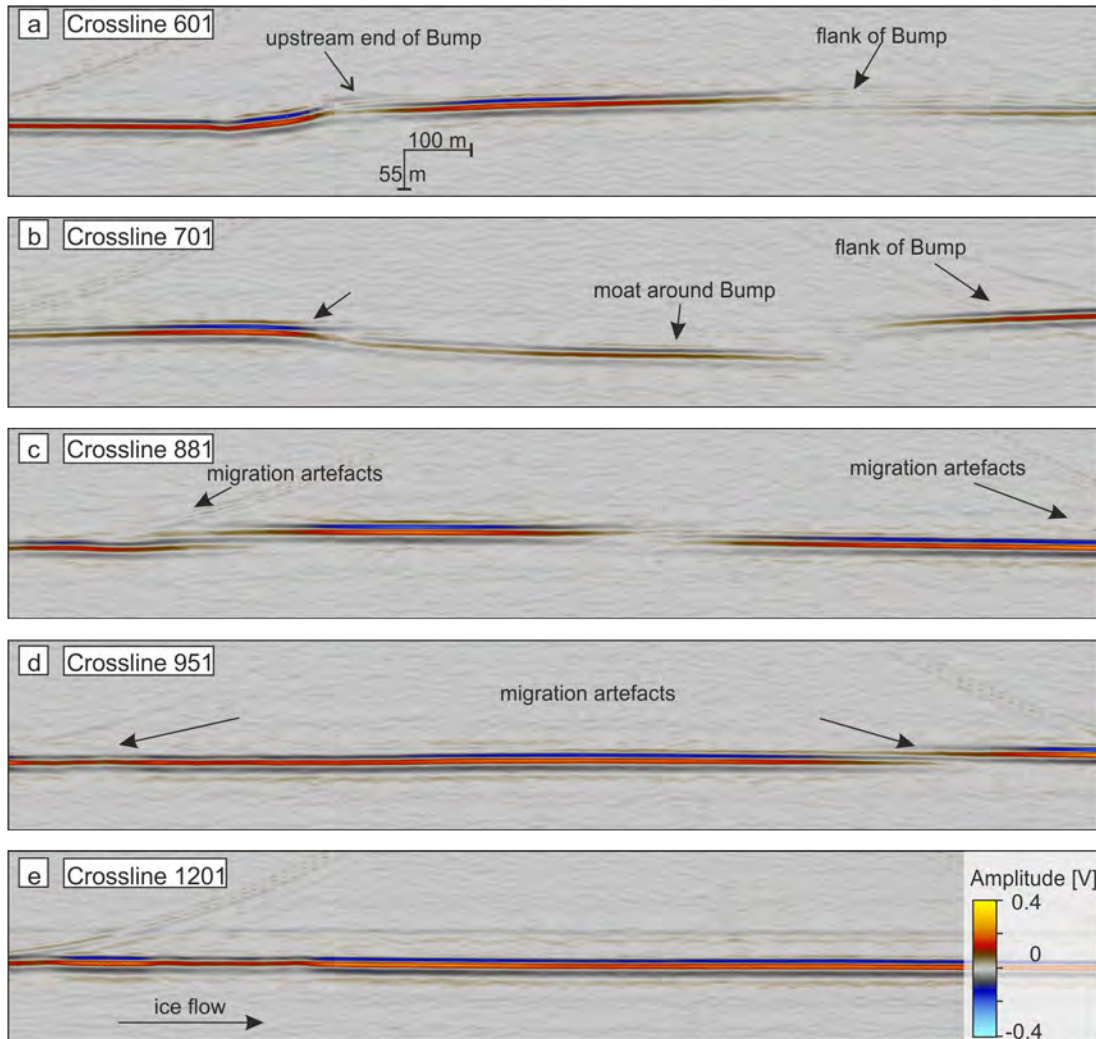
Figure 7.2: Result of 3D migration shown for different crosslines of grid 1. Vertical and horizontal scales, as well as colour bars, are kept constant. Ice flow is from left to right.
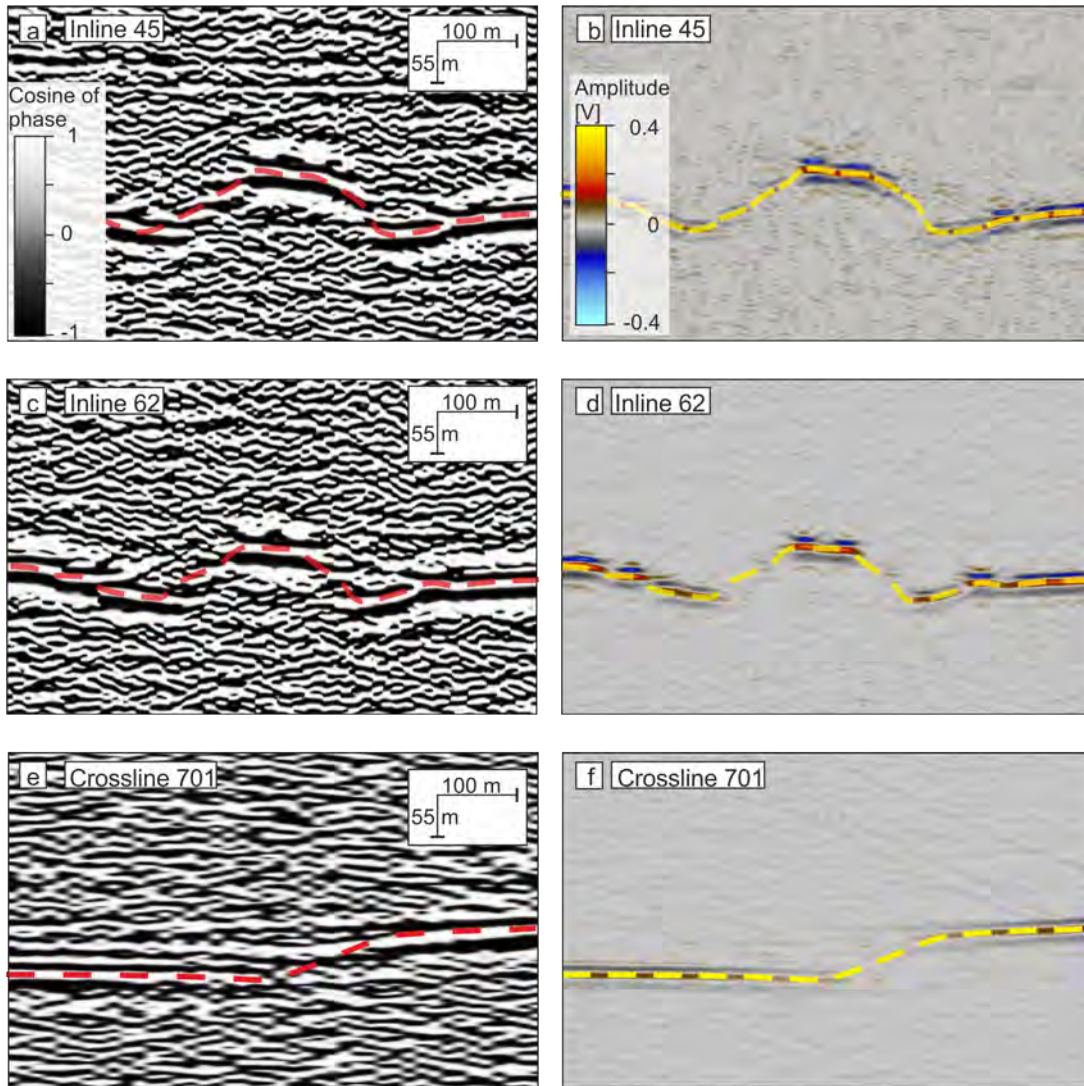
Figure 7.3: Comparison of continuity of the bed reflection in grid 1 using the amplitude and the COP for different in- and crosslines. The yellow and red dashed lines indicate the suggested position of the bed reflection according to picking and interpolation of picks.
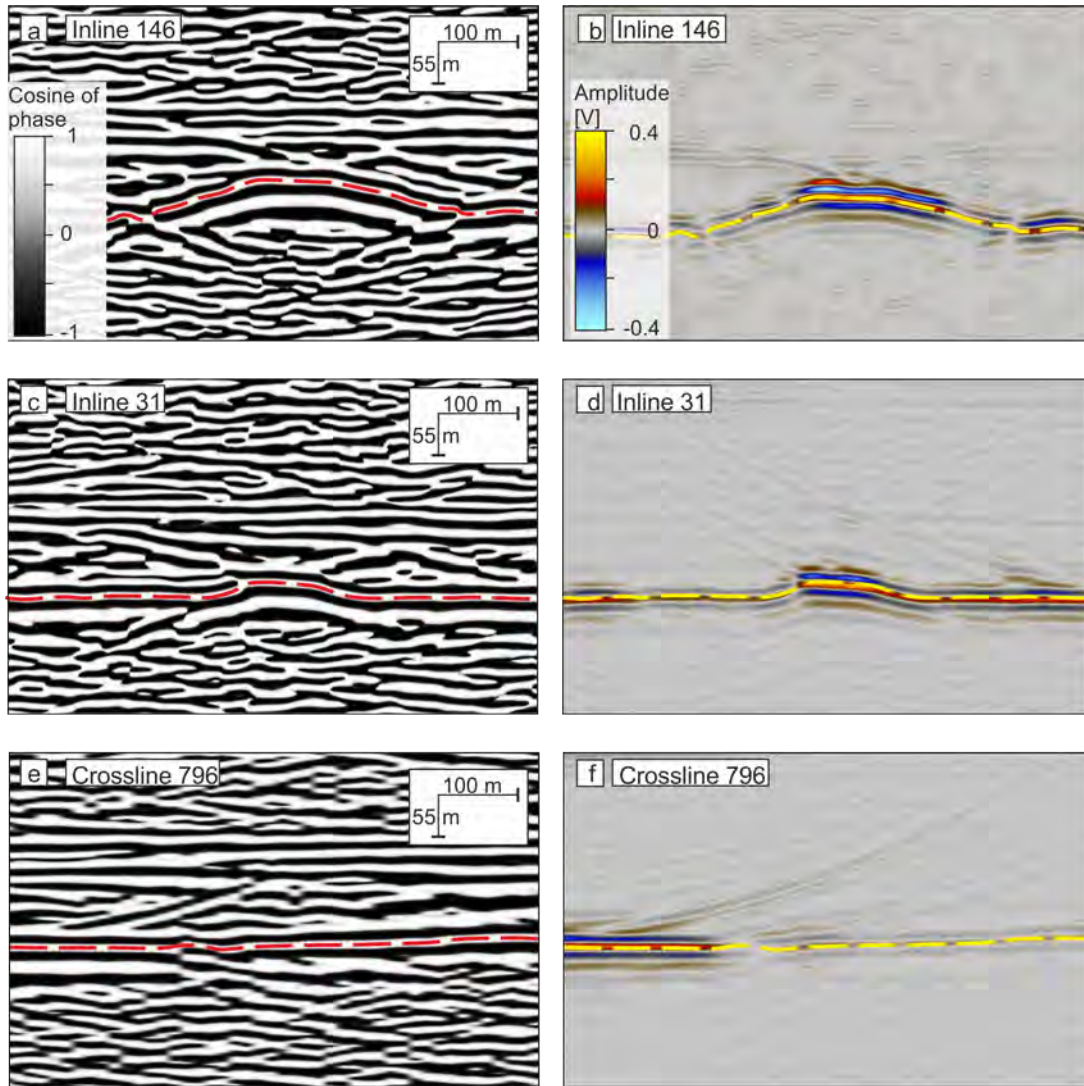
Figure 7.4: Comparison of continuity of the bed reflection in grid 2 using the amplitude and the COP for different in- and crosslines. The yellow and red dashed lines indicate the suggested position of the bed reflection according to picking and interpolation of picks.

7.2 Comparison of 3D Data With Previously Published Data

Figure 7.5 and Figure 7.6 compare the topography interpreted from 3D migrated 20 m spaced data (top) and 2D migrated 500 m spaced (bottom) data acquired in 2016/17 for the area in grid 1 (Figure 7.5) and grid 2 (Figure 7.6).

In grid 1 (Figure 7.5), more detail is visible around the upstream end of a landform at the eastern edge of the grid (blue arrow) and around smaller landforms (red arrow) using the 20 m spaced 3D migrated data. The most significant difference between the two datasets can be seen around the Bump and the moat around the Bump. First, the depth of the moat is shallower in the 500 m spaced data. Second, the moat appears discontinuous on the western flank of the Bump, and therefore the shape of the Bump changes. Third, the upstream end of the Bump shows a gradual increase in topography, whereas the upstream end in the 20 m data shows a steeper topography. The difference in grid 2 (Figure 7.6) is less pronounced: differences can be seen in the moat around the Bump (yellow arrow), and in the downstream area (green and red arrow) where small undulations are visible in the 20 m spaced data. A more significant difference can be seen at the downstream end of a landform (blue arrow). First, the shape of the landform changed, second, the depression between the landform and the downstream topography is more pronounced in the 500 m spaced data. Only little differences can be seen in the topography of the Bump.

Naturally, more detail is lost when increasing the line spacing, which is illustrated in Figure 7.7, showing the radargram of a crossline (in flow direction) in grid 2 along the downstream end of a landform (approximately the area of the blue arrow in Figure 7.6). The different lines superimposing the amplitudes display the picks of the bed reflection on the basis of different datasets. The different picks do agree along most of the line. Picks on 500 m spaced data (white dashed line), smoothed out the depression (at inline location 110), while 200 m and 100 m spaced data shift the location of the depression towards downstream. Additionally to the line spacing, the 3D migration better positions reflections of dipping events into the right location. In 2D migration, these signals can be visible as sub-bed signals, as shown in Figure 7.8. 2D migrated data show a dipping reflector towards the south. The 3D migrated data give no indication of a dipping

Figure 7.5: Comparison of bed topography of grid 1 using 3D migrated 20 m spaced data (top), and 2D migrated 500 m spaced data. Colour coding represents bed elevation referenced to the WGS84 ellipsoid. Ice flow is into the page, parallel to elongated landforms. The prominence of these is exaggerated for display. Areas of differences between the two datasets are highlighted by coloured arrows.
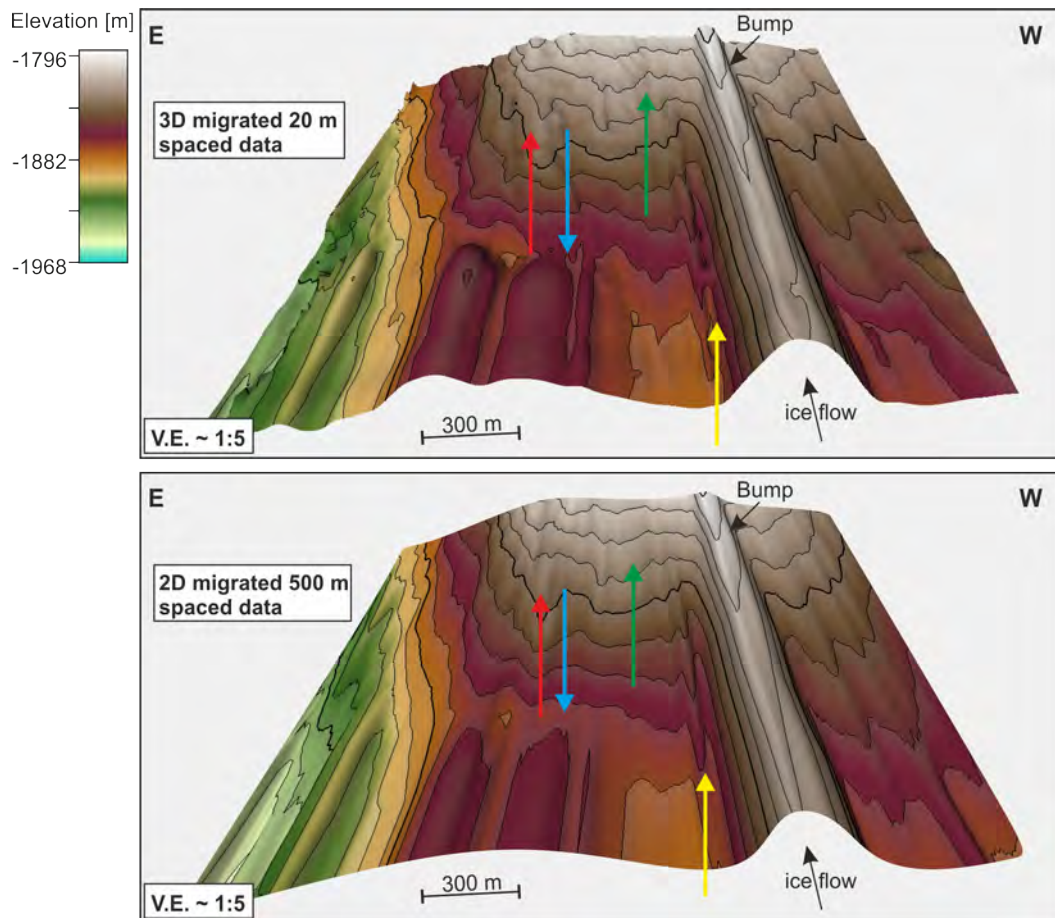
Figure 7.6: Comparison of bed topography of grid 2 using 3D migrated 20 m spaced data (top), and 2D migrated 500 m spaced data. Colour coding represents bed elevation referenced to the WGS84 ellipsoid. Ice flow is into the page, parallel to elongated landforms. The prominence of these is exaggerated for display. Areas of differences between the two datasets are highlighted by coloured arrows.

Figure 7.7: Comparison of picked twtt of the bed reflection on 20, 100, 200, and 500 m spaced data. Radargram shows crossline 599 of 2D migrated 20 m spaced data. Lines superimposing the amplitude of the bed reflection show twtt picks based on different datasets for comparison. For Crossline 599 showing 500 m and 20 m spaced data see Figure 10.19 in the Appendix.
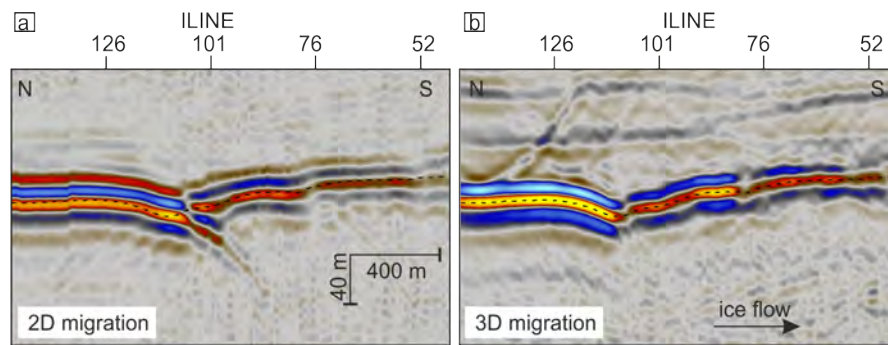
Figure 7.8: Crossline 511 after 2D (a) and 3D (b) migration of 20 m spaced data. The black dashed line shows the picked twtt of the bed reflection on the 3D migrated data. Panel a & b do not show the same colour coding due to amplitude differences originating from different processing.

reflector. Further examples of differences between 2D and 3D migration can be seen in the Appendix Figure 10.20 and 10.21.

7.3 Attribute Analysis of 3D Datasets

The following section focuses on the bed reflection and the topography interpreted from the bed reflection. This includes the analysis of the bed reflection using different attributes to highlight possible discontinuities in the reflection. The second part of this section is focused on highlighting small-scale features, complex structures and the identification of trends in the bed topography (Section 7.3.2). These are then compared to the calculated envelope (Section 7.3.3). Comparison of the envelope calculated in this chapter with the calibrated reflectivity in Chapter 5 enables the assignment of bed properties to the envelope. Calculation of attributes along in- and crosslines of the 3D data cube which were analysed to emphasise lateral and vertical variations within the ice column, along the bed reflection and possibly below the bed reflection, are shown and discussed in Section 10.5.2 in the Appendix.

7.3.1 Physical Attributes of the Bed Reflection Around the Bump

7.3.1.1 Grid 1

A comparison of different attributes calculated for the area around the Bump in grid 1 is shown in Figure 7.9. The left flank (left box) shows a low amplitude (a) as well as low envelope (c, ∼0.05 V), while the frequencies (d) in that area contain more higher frequency components (around 6 MHz), when compared to other areas of the bed reflection (mainly components around 4 MHz). The COP (b) and the GLCM (f) partly show a continuous signal for this flank with discontinuities where the reflection gets less steep (at the ends of the flank). The variance of the signal (e) is low for most of the flank, with a discontinuity (higher variance) at the lower and upper end of the flank (right edge of the left black box). The crest of the Bump (centre box) contains a high amplitude (a) along the reflection, while the envelope (b) shows clear variations although all values are high (>0.10 V). Frequency content (d, ∼4 MHz) is constant and variance (e) is low for this part of the reflection. GLCM (f) and COP (b) shows a clear continuous reflection. The signal of the right flank of the Bump (right box) is very chaotic, with the amplitude (a) and envelope (c, ∼0.01,V) in this region lower compared to the surrounding area. The frequency content (d) of the signal in this region is higher (∼8 MHz) compared to the left flank. No continuous reflection

can be identified using the COP (b). The variance (e) is high along parts of this flank. To summarise, the crest of the Bump shows a continuous, high amplitude reflection, while discontinuities are visible along the low amplitude flanks.

7.3.1.2 Grid 2

The bed reflection of the Bump in grid 2 is more continuous (Figure 7.10), and in most places can be picked using the amplitude display (a). The COP shows small discontinuities in the location where the flank ends and the reflection gets plane/horizontal again (in the right and left box). This discontinuity, which is less pronounced in the right box, is also visible using the variance attribute (e) and the COP (b). Frequency content varies little from 4 MHz for most of the reflection. The variance (e), GLCM (f) as well as the COP (b) not only show the bed reflection as a consistent signal, but also contain artefacts that appear above the bed reflection. However, these artefacts are much less pronounced in the amplitude (a) and envelope (c). The envelope (c) of the bed reflection shows small variation along the crest of the Bump (centre box, values between 0.11–0.25 V), comparable to grid 1. Both flanks (right and left box) show a much weaker envelope ($\sim$0.08 V), with areas of very low envelope ($<$0.04 V) in the right box, comparable to the signal in the background. The location of very low envelope does correlate with areas of discontinues in the COP (b) and variance (e). To summarise, as in grid 1, the crest of the Bump shows a continuous high amplitude reflection. Although not visible in the amplitude display, small discontinuities can be identified for both low amplitude flanks.

7.3.2 Bed Reflection – Structural Attributes

The following contains results of the analysis of the structural (Section 7.3.2) and physical (Section 7.3.3) attributes of the bed reflection within grid 1 and grid 2. Therefore, two different imaging view points are chosen, first a 3D view of the topography of the bed from within the ice, pointing in the ice flow direction, and secondly, a plan view of the bed topography, with ice flowing from the bottom to top.
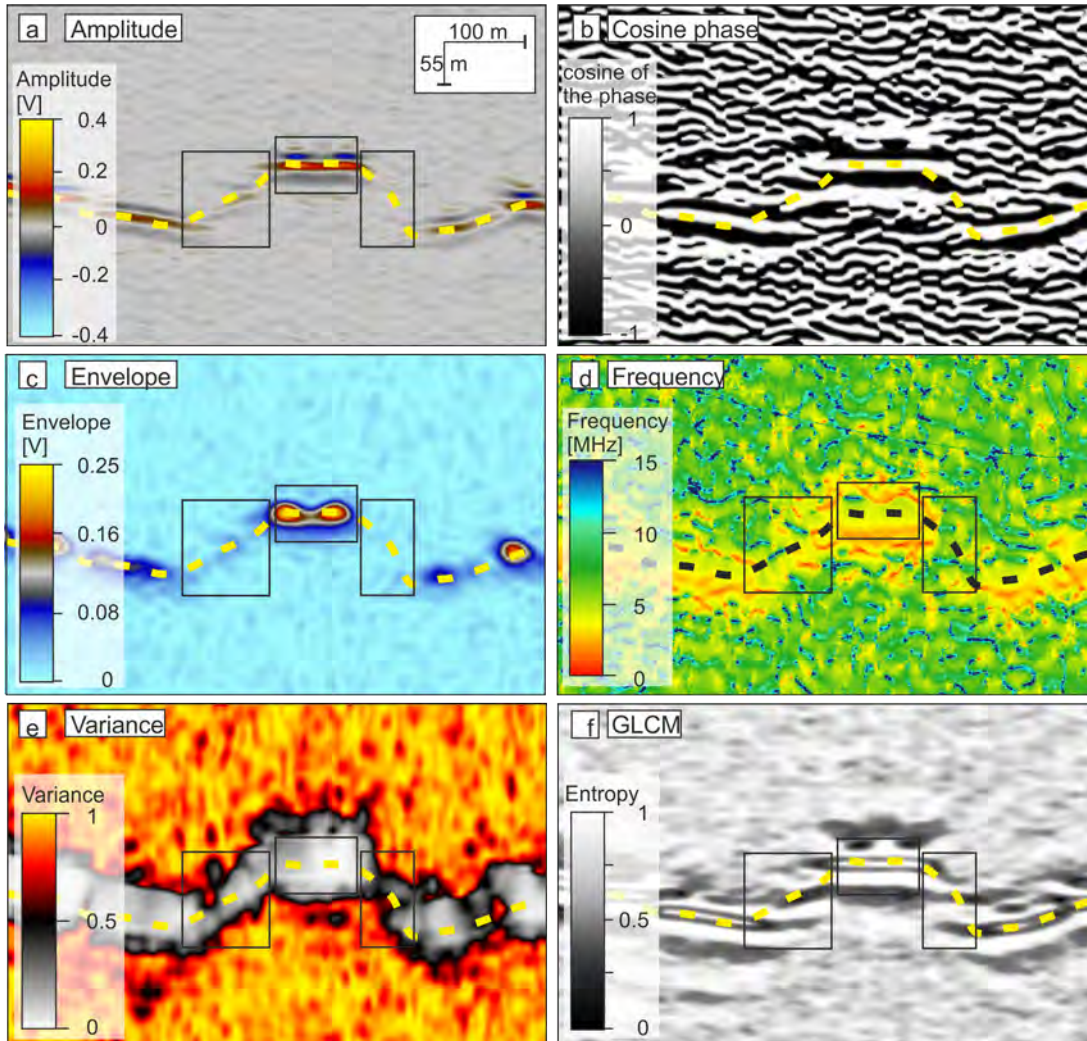
Figure 7.9: Zoom on the Bump in inline 76 of grid 1. The three boxes mark the left flank, the crest and the right flank respectively. Colour coding is chosen to display different attributes as follows: a) amplitude, b) COP, c) envelope, d) dominant frequency, e) variance and f) GLCM with attribute entropy. The yellow and black dashed line indicates the suggested position of the bed reflection according to picking and interpolation of picks.
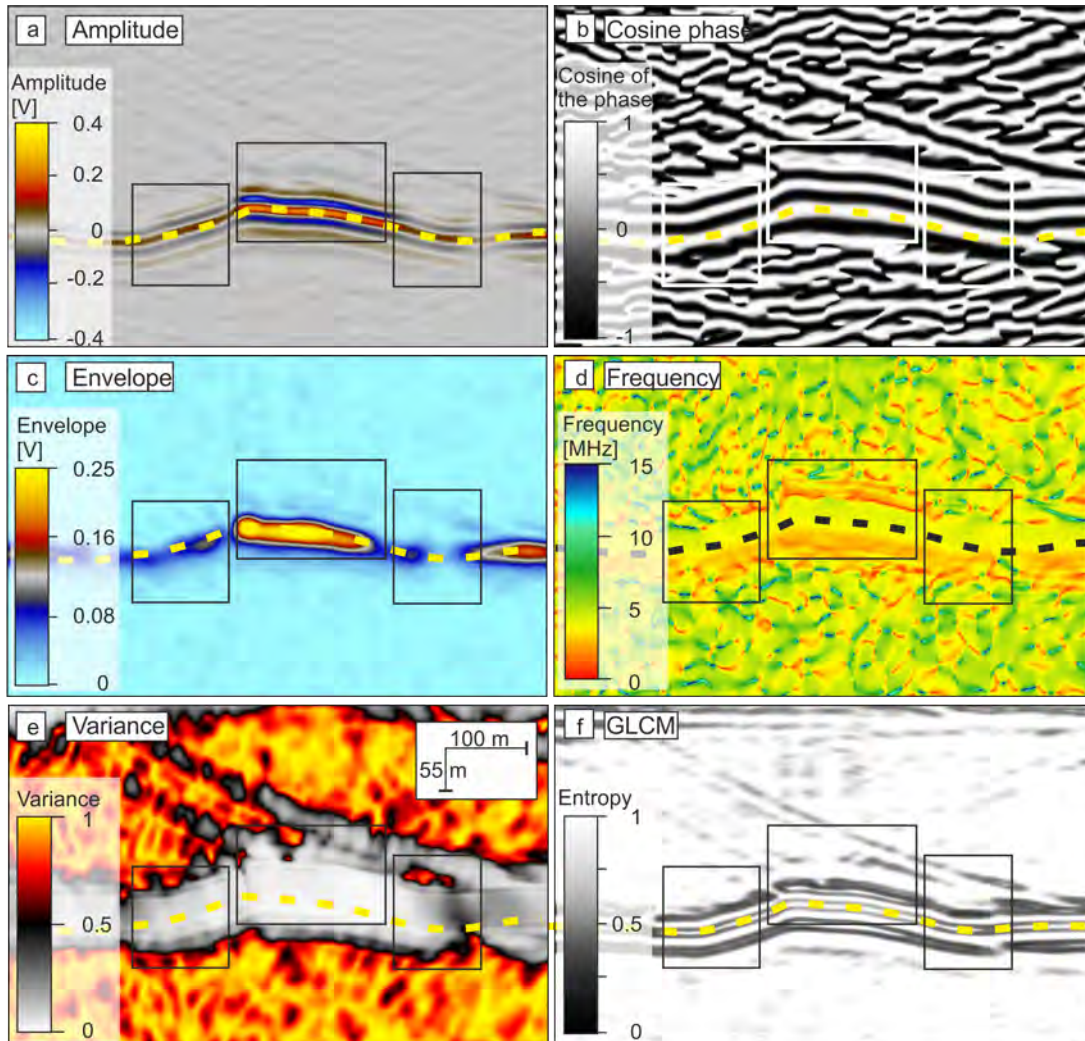
Figure 7.10: Zoom on the Bump in inline 146 of grid 2. The three boxes mark the left flank, the crest and the right flank respectively. Colour coding is chosen to display different attributes as follows: a) amplitude, b) COP, c) envelope, d) dominant frequency, e) variance and f) GLCM with attribute entropy. The yellow and black dashed line indicates the suggested position of the bed reflection according to picking and interpolation of picks.

7.3.2.1 Grid 1

Figures 7.11–7.14 show the picks of the bed reflection interpolated onto a 3D surface, colour coding representing elevation (Figure 7.11), dip (Figure 7.12), azimuth (Figure 7.13) and the curvature (Figure 7.14) of the bed in grid 1, respectively. These attributes are also shown in plan view in Figure 7.15. The topography shows a general increase in elevation from 1930 m below the ellipsoid (light green/blue) to 1840 m below the ellipsoid (brown) perpendicular to the ice flow towards the east. Subglacial landforms aligned in the flow direction are visible and can be found all along the western and eastern part of the grid. The moat surrounds the Bump along its full extent, with the exception of a small interruption at the upstream end (red arrow Figure 7.15 a). The Bump and the moat are described in more detail in Section 7.3.4. Excluding the Bump and the moat, the topography of grid 1 dips at angles below 20° in most of the areas (Figure 7.12), while the flanks of smaller, elongated landforms dip up to 30°. The steepest dips (<50°) can be found for the flanks of the Bump (blue colour in Figure 7.12 and 7.15 b). However, as mentioned before in Section 7.1, the bed reflection along the flanks of the Bump is not clearly visible and the interpretation of topography is subject to interpolation and interpretation, which can lead to the calculation of erroneous dips in this area. The pattern of the dip shows a preferred orientation along flow direction, as highlighted by the black dashed lines. This alignment can also be seen when looking at the pattern of the azimuth calculated for this grid (Figure 7.13 and Figure 7.15 c). Areas pointing against flow (yellow/orange) can only be seen in small localised areas, e.g., the upstream end of a landform at the eastern edge of grid 1 (marked by the yellow arrow in Figure 7.13). Only small localised patches are found that point in flow direction (marked by blue colour, e.g. area highlighted by red arrow, Figure 7.13), coinciding with areas of very low dip. The curvature of the bed (Figure 7.14), is coloured to display troughs and depressions in red, as can be seen for the moat. Furthermore, the visibility of several landforms and troughs between landforms is enhanced and confirms the orientation of features shown by the black dashed lines. The spatial continuity of landforms is enhanced using the curvature attribute, compared to solely imaging the topography. Landforms in the east and west of grid 1 are ∼6–15 m high and ∼40–260 m wide and appear continuous and exist downstream along the whole grid (length >3 km). The landforms upstream of the Bump seem truncated by

176
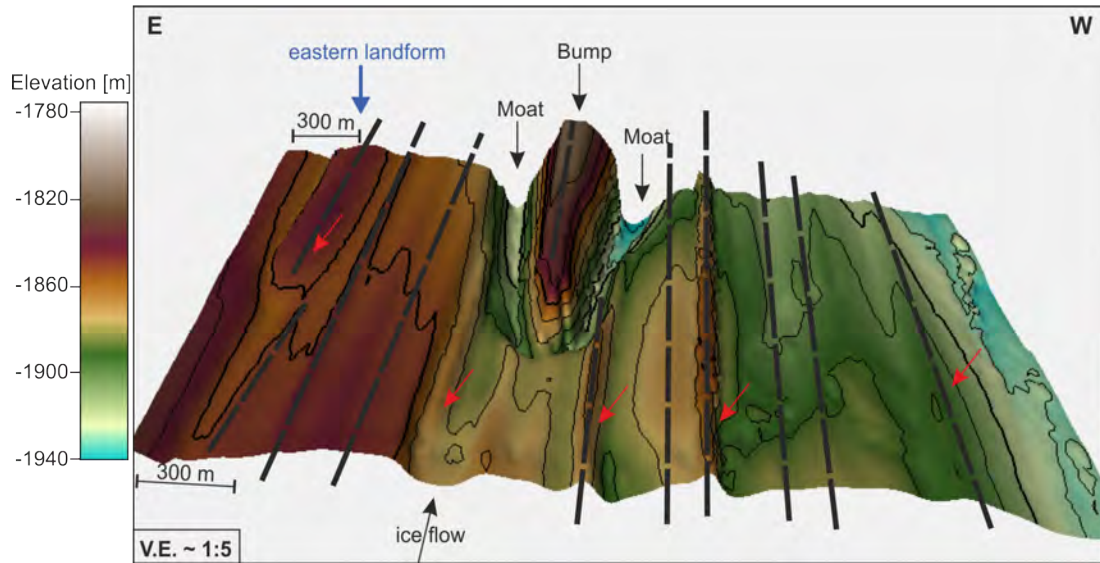
Figure 7.11: 3D bed topography of grid 1. Colour coding represents bed elevation. Ice flow is into the page, parallel to elongated landforms. The prominence of these is exaggerated for display, with vertical exaggeration (V.E.) of 1:5. Black dashed lines represent the orientation of patterns of structural attributes. The red arrow marks the locations of examples of small landforms on the bed. Black contour lines show the topography in 10 m increments.

the moat. Two examples of these terminated landforms are highlighted by the yellow arrow in Figure 7.14.
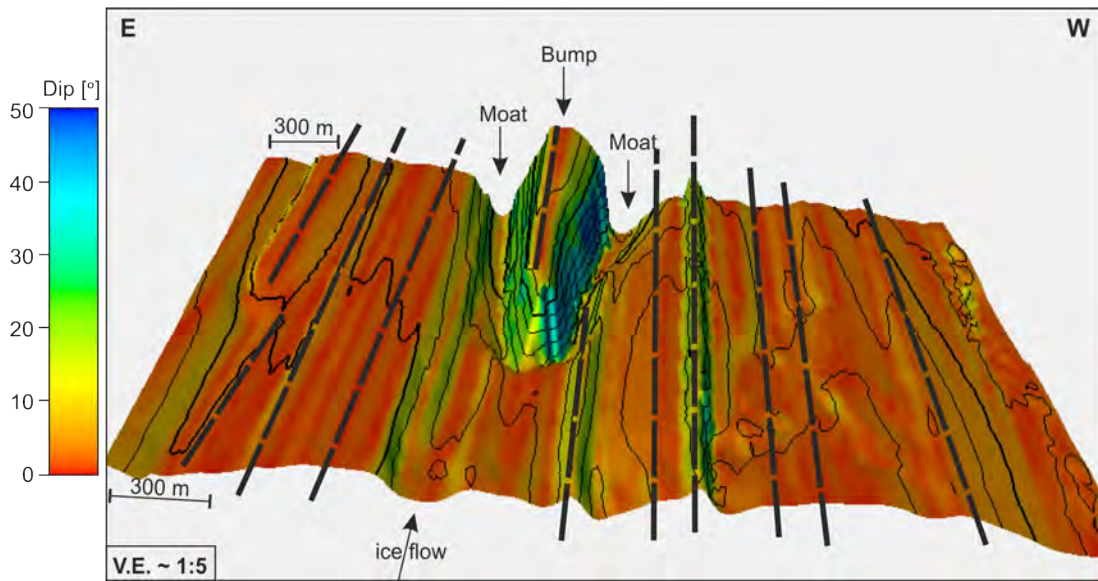
Figure 7.12: 3D bed topography of grid 1. Colour coding represents dip of the bed topography.
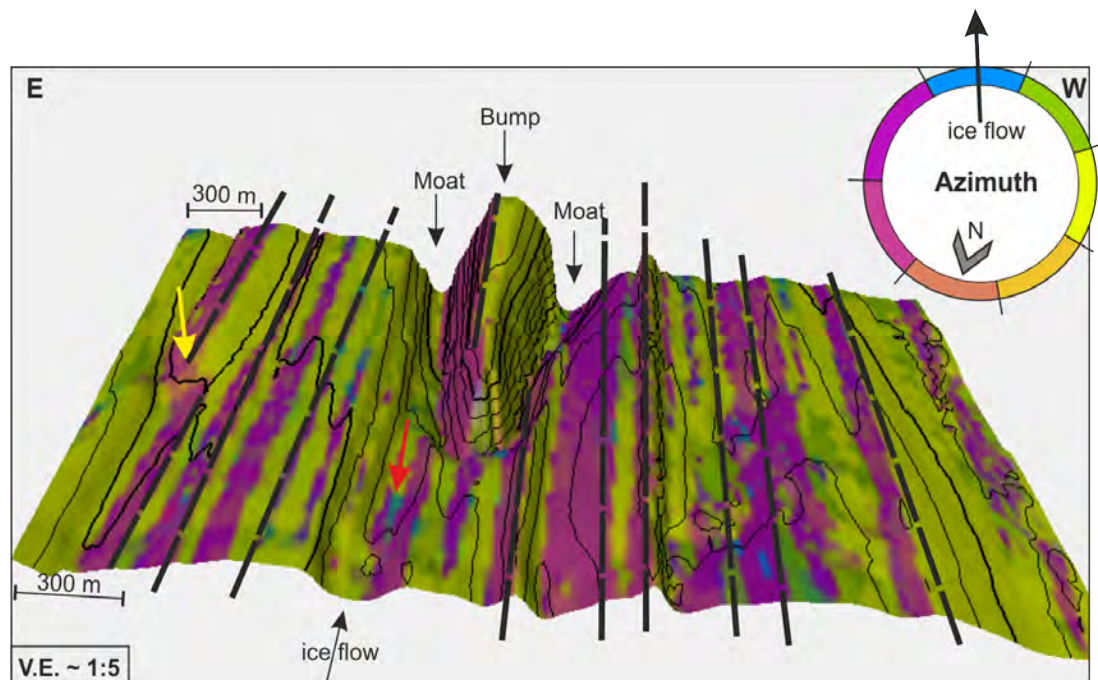
Figure 7.13: 3D bed topography of grid 1. Colour coding represents azimuth of the bed topography. Areas pointing in flow direction are coloured in blue, areas pointing against flow direction are coloured in orange. The red arrow marks an area orientated in flow direction, the yellow arrow an area against flow direction (upstream end of a landform).
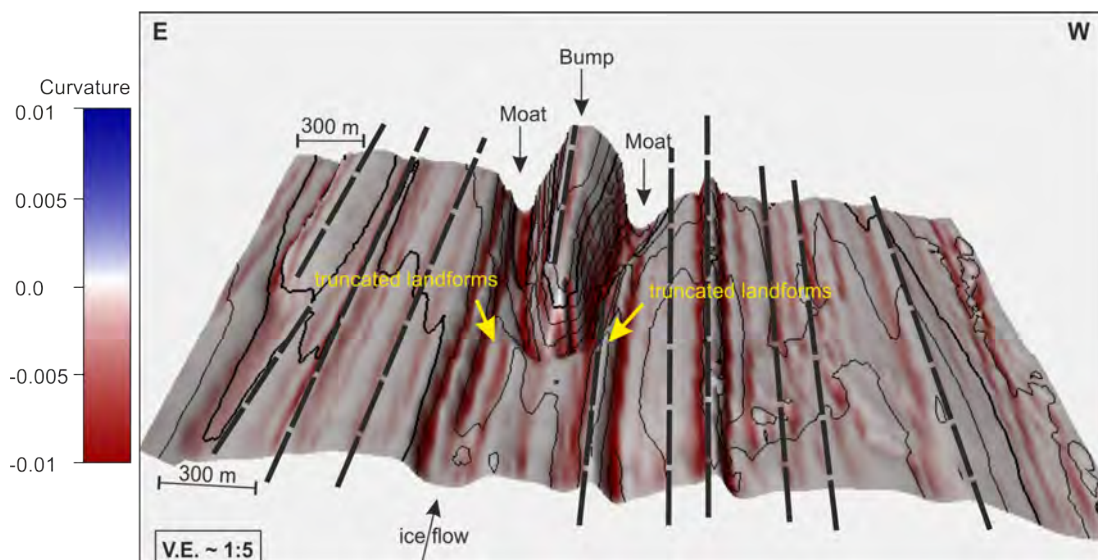
Figure 7.14: 3D bed topography of grid 1. Colour coding represents curvature of the bed topography. Landforms that appear to be terminating against the moat are highlighted by yellow arrows.
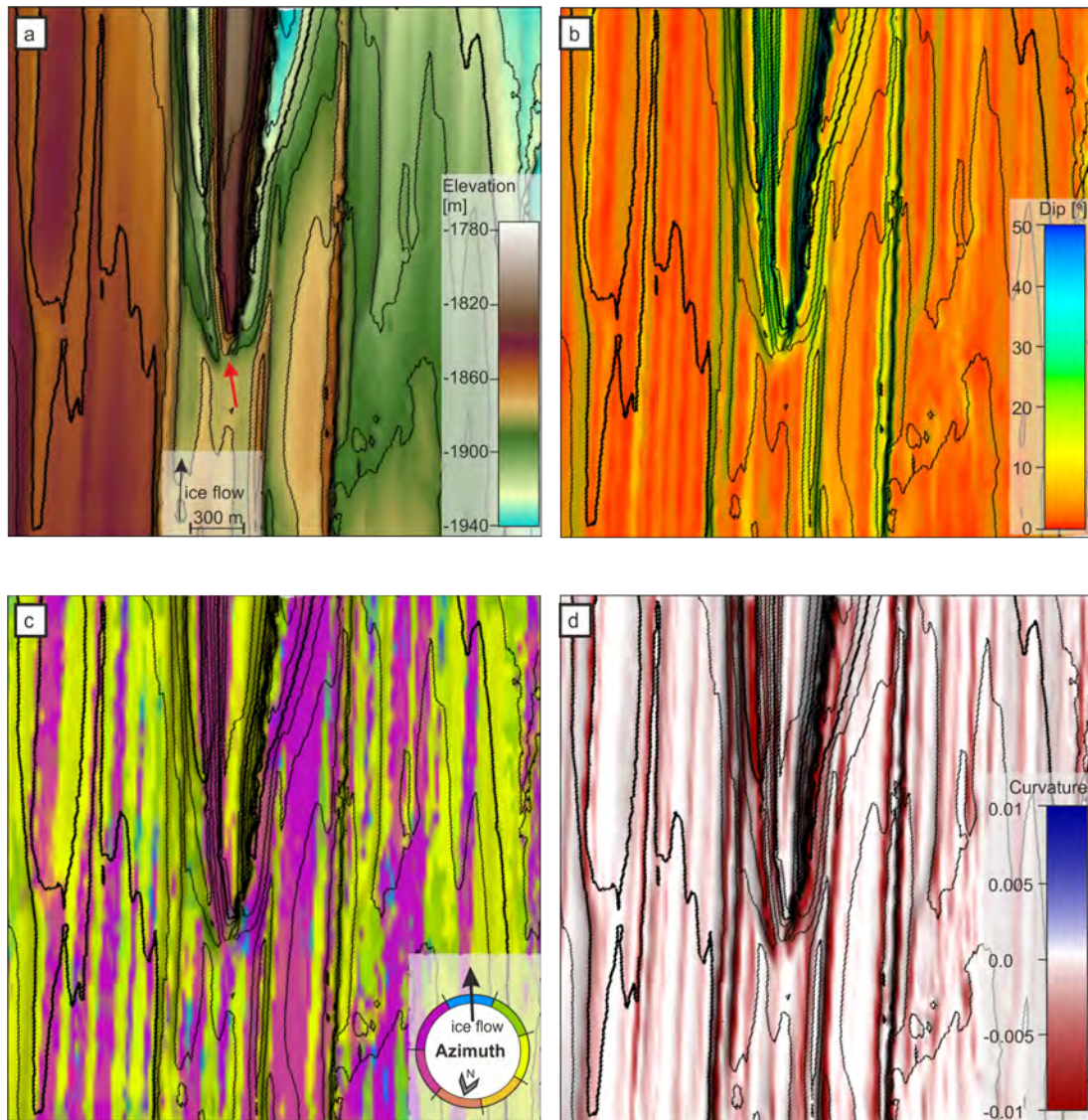
Figure 7.15: Structural attributes of grid 1 in plan view. a) Bed elevation, b) dip, c) azimuth and d) curvature. Ice flow is from bottom to top.

7.3.2.2   Grid 2

Figures 7.16–7.19 show the picks of the bed reflection interpolated onto a 3D surface for grid 2, with colour coding representing elevation (Figure 7.16), dip (Figure 7.17), azimuth (Figure 7.18) and the curvature (Figure 7.19) of the bed, respectively. All three attributes are also shown in plan view in Figure 7.20. The topography of grid 2 shows an increase in elevation along the flow direction and a general decrease in elevation perpendicular to the flow direction towards the east. Elevation in the western part of the grid varies between 1875 and 1790 m below the ellipsoid along flow, and from 1940 and 1890 m below the ellipsoid along flow in the eastern part of the grid. Comparison of the contour lines of the topography highlights a more complex pattern east of the Bump, compared to the west. The orientation of topographic features appears less aligned in flow direction in some areas east of the Bump, where some features cross-cut the topography in a more south-easterly direction. Red dashed lines represent the orientation of structural attributes aligned approximately in flow direction, whereas the orientation of the cross-cutting features is marked by cyan dashed lines. The dip of the bed (Figure 7.17) is around and often below 10°. Steeper dips of up to 25° can be found for the flanks of the Bump. Cross-cutting features (cyan dashed lines) show dips of up to 12°. The azimuths of these features (Figure 7.18 and 7.20 c) imply that they are orientated towards the east, at an angle of 4–15° compared to the flow direction. The crests of small landforms (black dashed lines in the downstream area), which were not identifiable solely analysing the topography, can be identified by the alignment of plan structures in flow direction (~0° dip and a switch in azimuth from purple to yellow-green). These landforms are ~200–300 m long, ~4 m high and ~6 m wide.

The orientations of features against flow (yellow/orange coloured areas) can be seen in some localised areas downstream of the landforms, marked by the black arrow in Figure 7.18. The downstream ends of two landforms (yellow arrows) show orientation in flow direction (blue coloured areas in Figure 7.18). The dip as well as the azimuth (Figure 7.20 b and c) both highlight a more diffuse pattern in the downstream eastern area of the grid, and aligned features in other parts of the grid. The orientation and location of cross-cutting features is enhanced using the curvature. Furthermore, as observed for data in grid 1, the curvature of the bed highlights small landforms, which are not clearly visible looking at the topography.
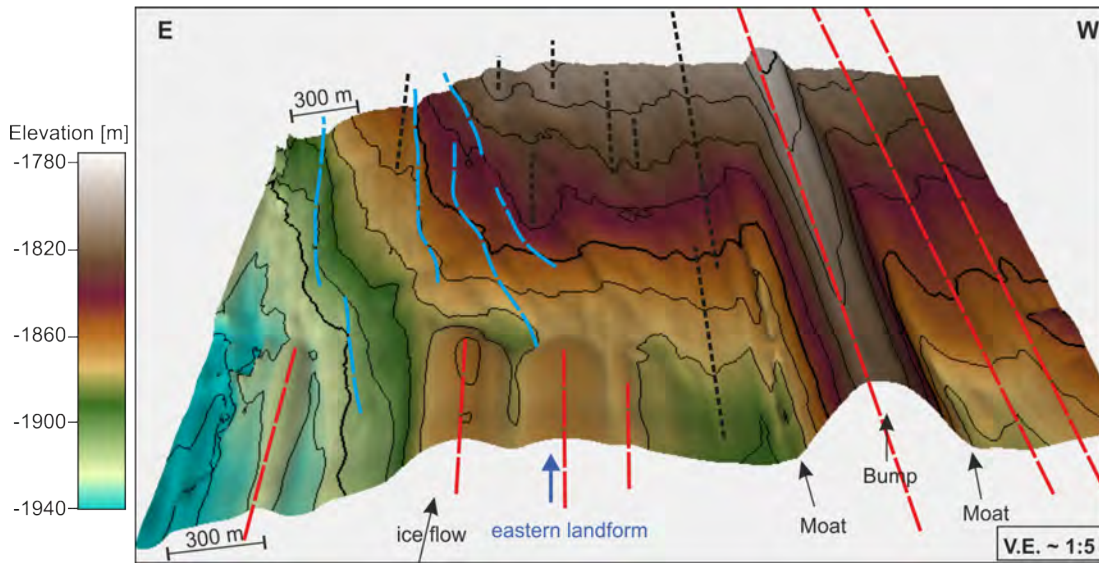
Figure 7.16: 3D bed topography of grid 2. Colour coding represents elevation below surface. Ice flow is into the page, parallel to elongated landforms. The prominence of these is exaggerated for display. Red dashed lines represent the orientation of structural attributes in flow direction, cyan dashed lines orientation with an angle to flow direction.
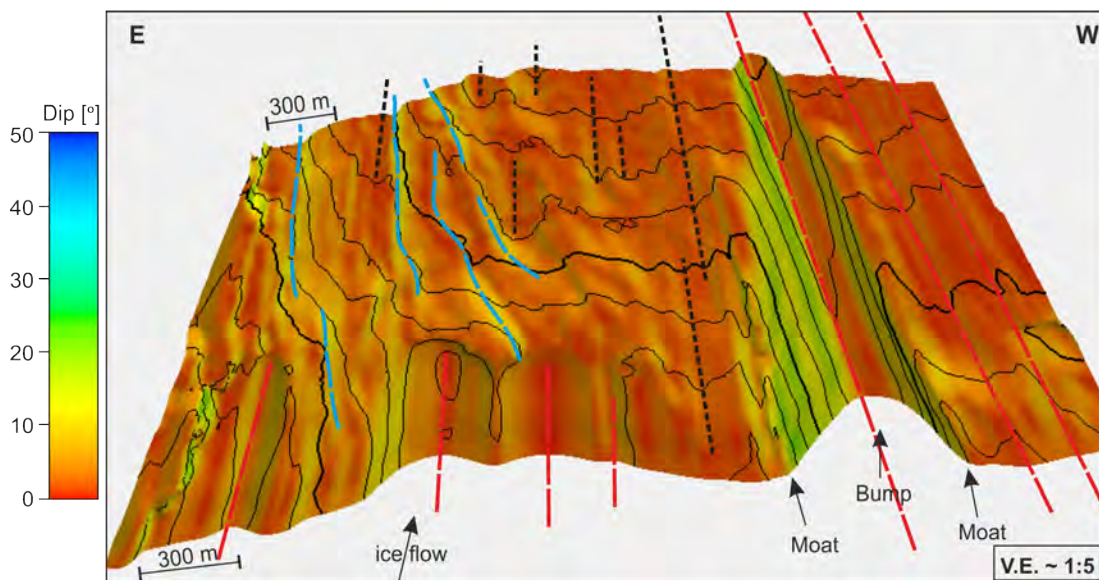
Figure 7.17: 3D bed topography of grid 2. Colour coding represents dip of the bed topography.
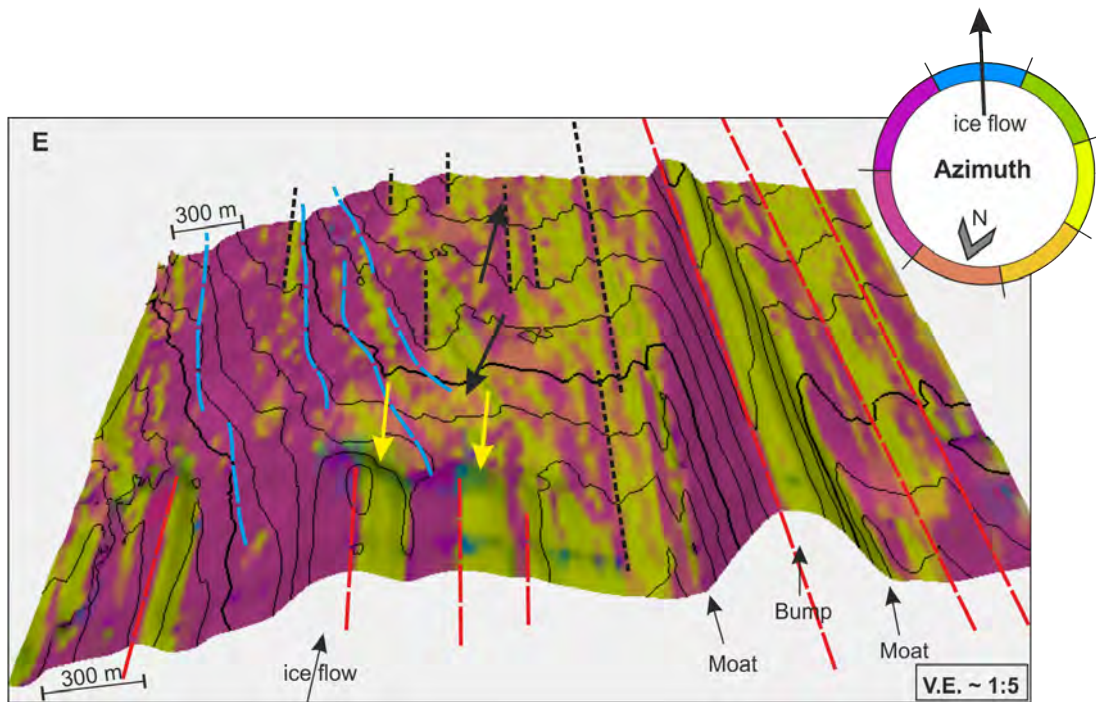
Figure 7.18: 3D bed topography of grid 2. Colour coding represents azimuth of the bed topography. Areas pointing in flow direction are coloured in blue, areas pointing against flow direction are coloured in orange. Yellow arrows mark areas orientated in the ice flow direction (e.g. downstream end of a landform), black arrow marks features orientated against ice flow direction.
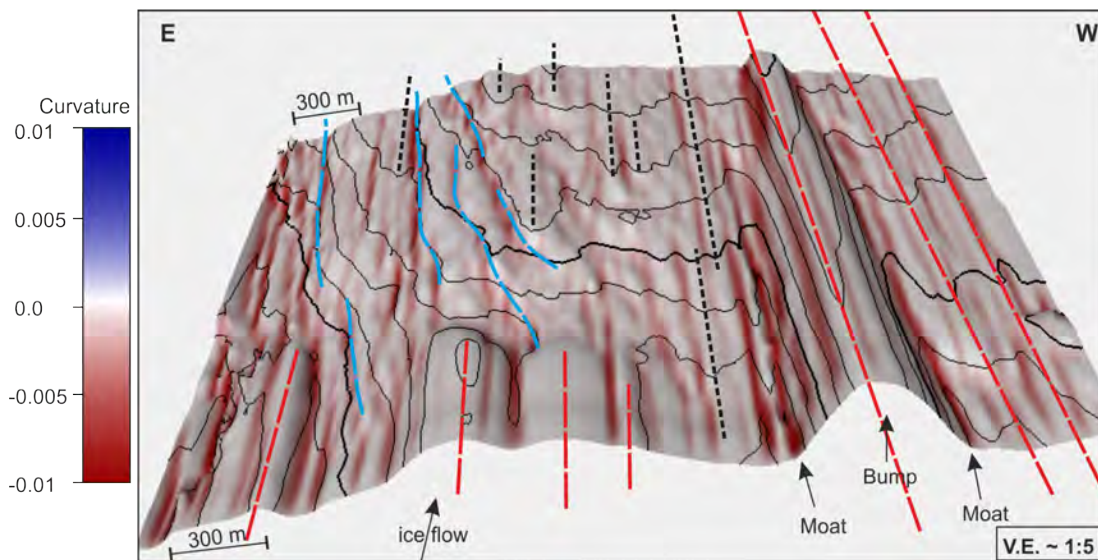
Figure 7.19: 3D bed topography of grid 2. Colour coding represents curvature of the bed topography.
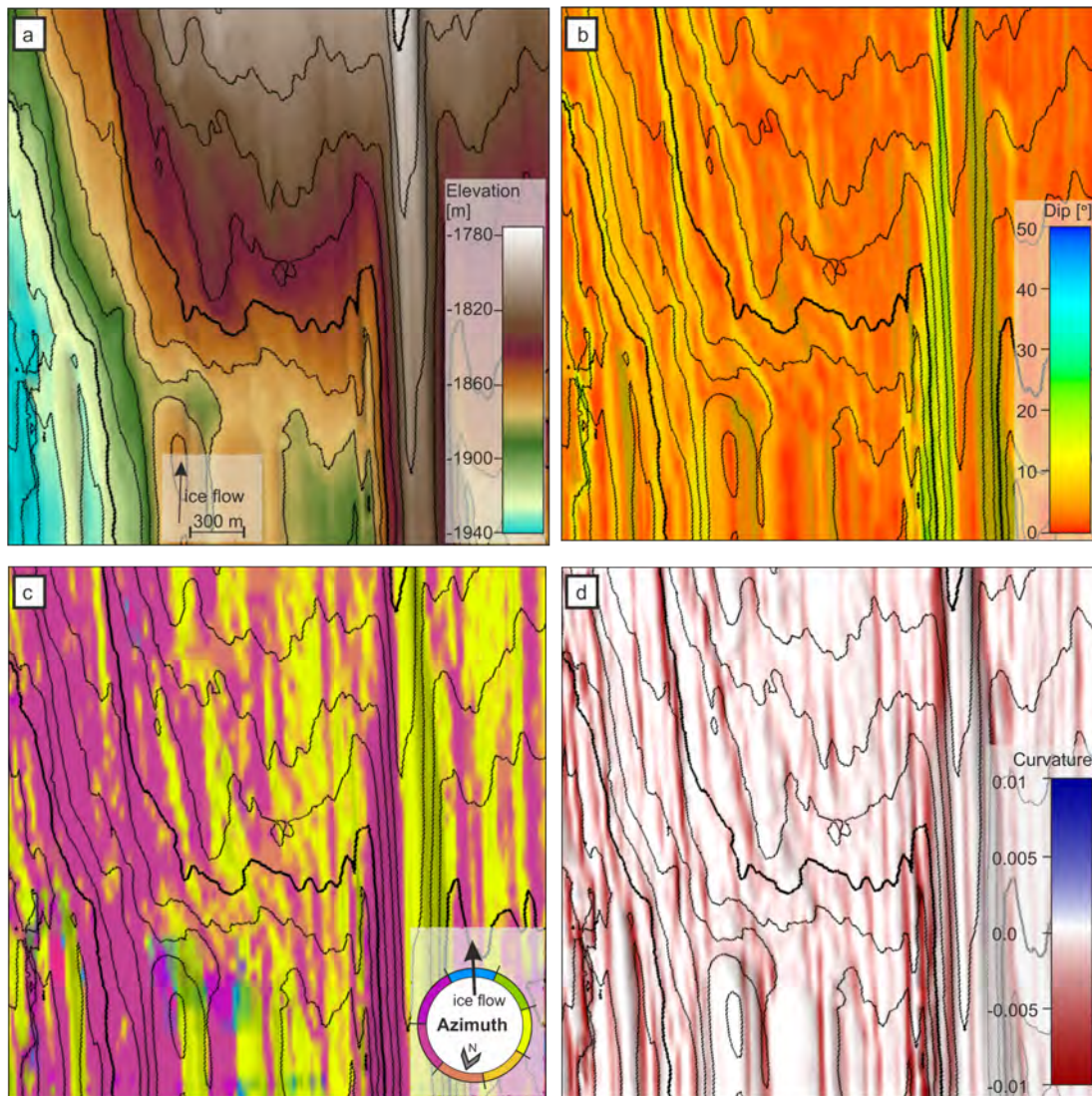
Figure 7.20: Structural attributes of grid 2 in plan view. a) Bed elevation, b) dip, c) azimuth and d) curvature. Ice flow is from bottom to top.

7.3.3   Bed Reflection – Envelope

Figures 7.21 and 7.22 show the calculated envelope (3D migrated bed reflection) overprinted on the 3D topography for the bed in grid 1 and grid 2, respectively. Within grid 1, high envelope is aligned in ice flow direction, similar to the orientation of the topography (black dashed lines in Figure 7.21). An area of high envelope (red arrow) is visible in the eastern upstream end of grid 1, which is partly located along the crest of a landform. A 3D display in Figure 7.21 b is included to highlight the association of this attribute with the topography, with higher envelope on the crest, compared to the flanks and moat of the Bump. In the area of grid 2 (Figure 7.22 a & c) cross-cutting features (cyan dashed line) show a low envelope, comparable to the troughs around landforms, i.e., the moat. The pattern of high envelope is mainly aligned along flow (black and red dashed line). Small landforms, identified during analysis of structural attributes (black dashed lines) show higher envelope ($\sim$0.12 V) when compared to the surrounding, although not as high as e.g., the Bump ($\sim$0.24 V, Figure 7.22 c). Figure 7.22 b shows the 3D topography of grid 2 viewed towards the east (perpendicular to the ice flow). Downstream ends of landforms can be seen on the left-hand side, with a small depression following and then a rise in topography to the right. The high envelope ($\sim$0.24 V) visible on the landforms crest is present until downstream of the landform, where the depression can be seen. Further downstream (to the right) the envelope is low ($<$0.08 V).

A comparison of the reflectivity calculated in Chapter 5 and the envelope calculated within this chapter can be seen in Figure 7.23. Concordant with findings in Chapter 5, high envelope is aligned along some landform crests, while troughs around landforms show low envelope. Much more detail can be seen when comparing the pattern of envelope and reflectivity in the area of grid 2, where spots of medium reflectivity can be identified to be located on the crest of small landforms (highlighted by the black dashed lines in Figure 7.22).

Due to the replacement of components of the DELORES system (Section 3.3.3) the envelope of the bed reflection calculated for data acquired using system 2 appears higher, compared to the envelope of data acquired with system 3 (Figure 7.22 a & b). This can also be seen comparing the amplitude of the direct wave as well as englacial reflections recorded using the two different systems (Appendix Figure 10.32). Therefore, the envelope and amplitude calculated for the most upstream 20 lines of grid 2 should not be taken into account. To avoid loss
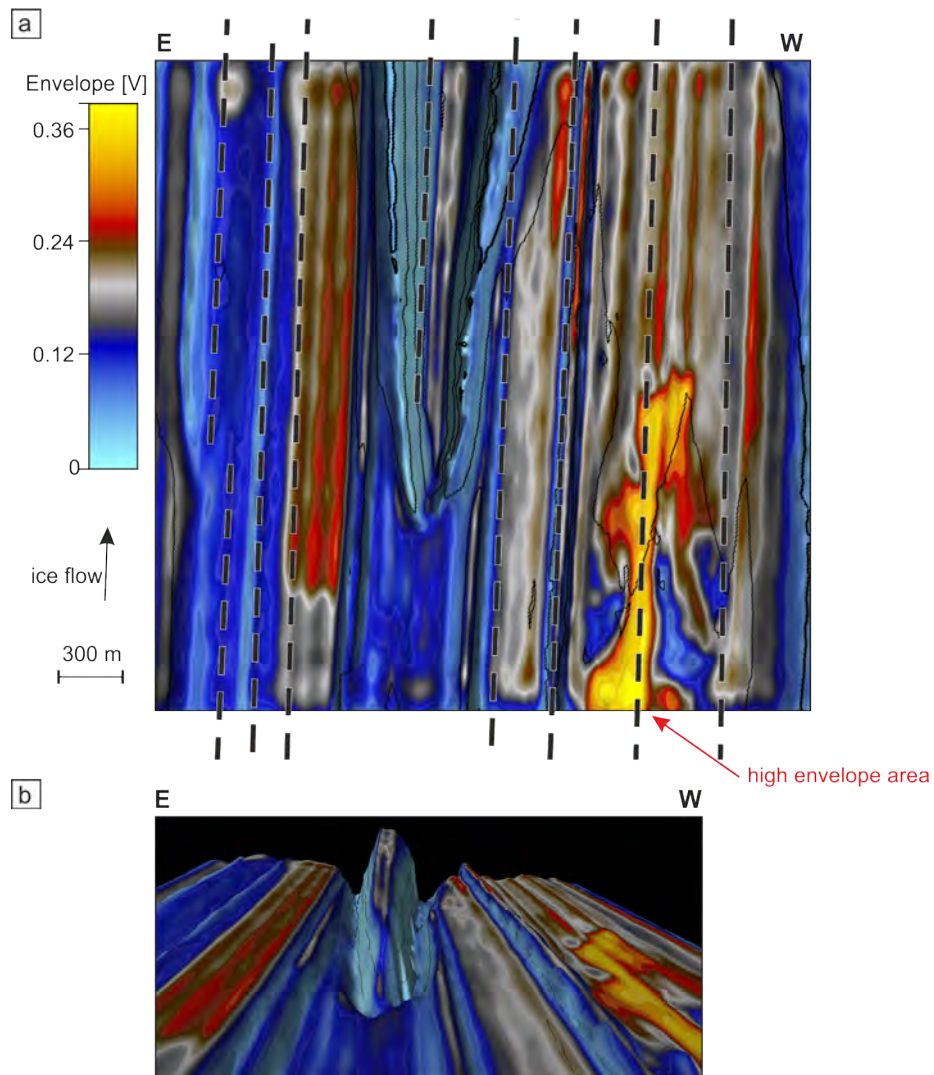
Figure 7.21: Envelope of the bed reflection of grid 1. a) Plan view of the bed. Black dashed lines indicate the orientation of features identified from structural attributes. b) 3D display of the area around the Bump.
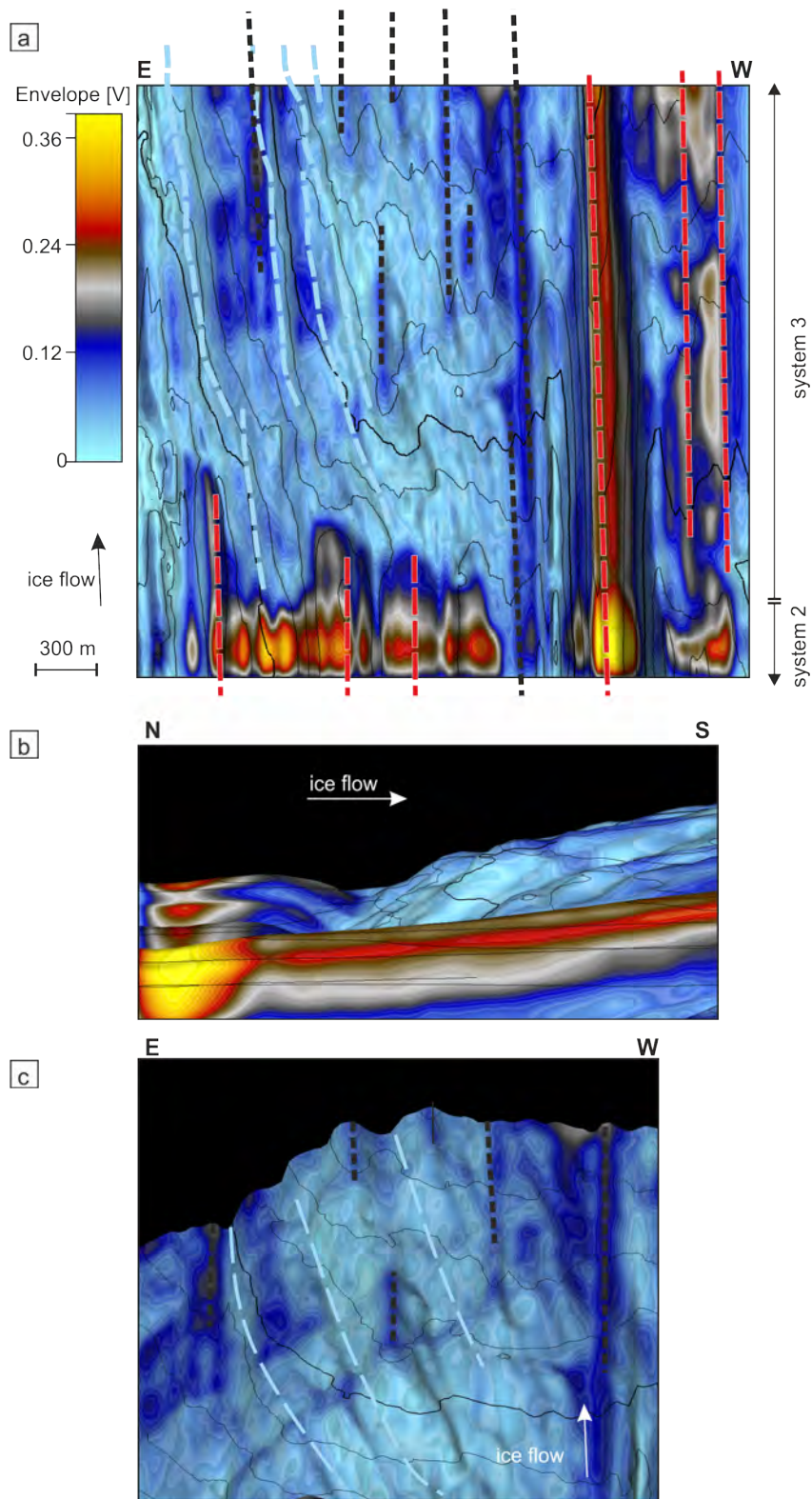
Figure 7.22: Envelope of the bed reflection in grid 2. a) Plan view of the bed. Cyan dashed lines = cross-cutting features. Red dashed lines = well-pronounced features, black dashed lines = landforms that can only be identified using attribute analysis. b) 3D topography, bending towards east, perpendicular to ice flow. c) Zoom onto the sliding area in the downstream part of the grid.
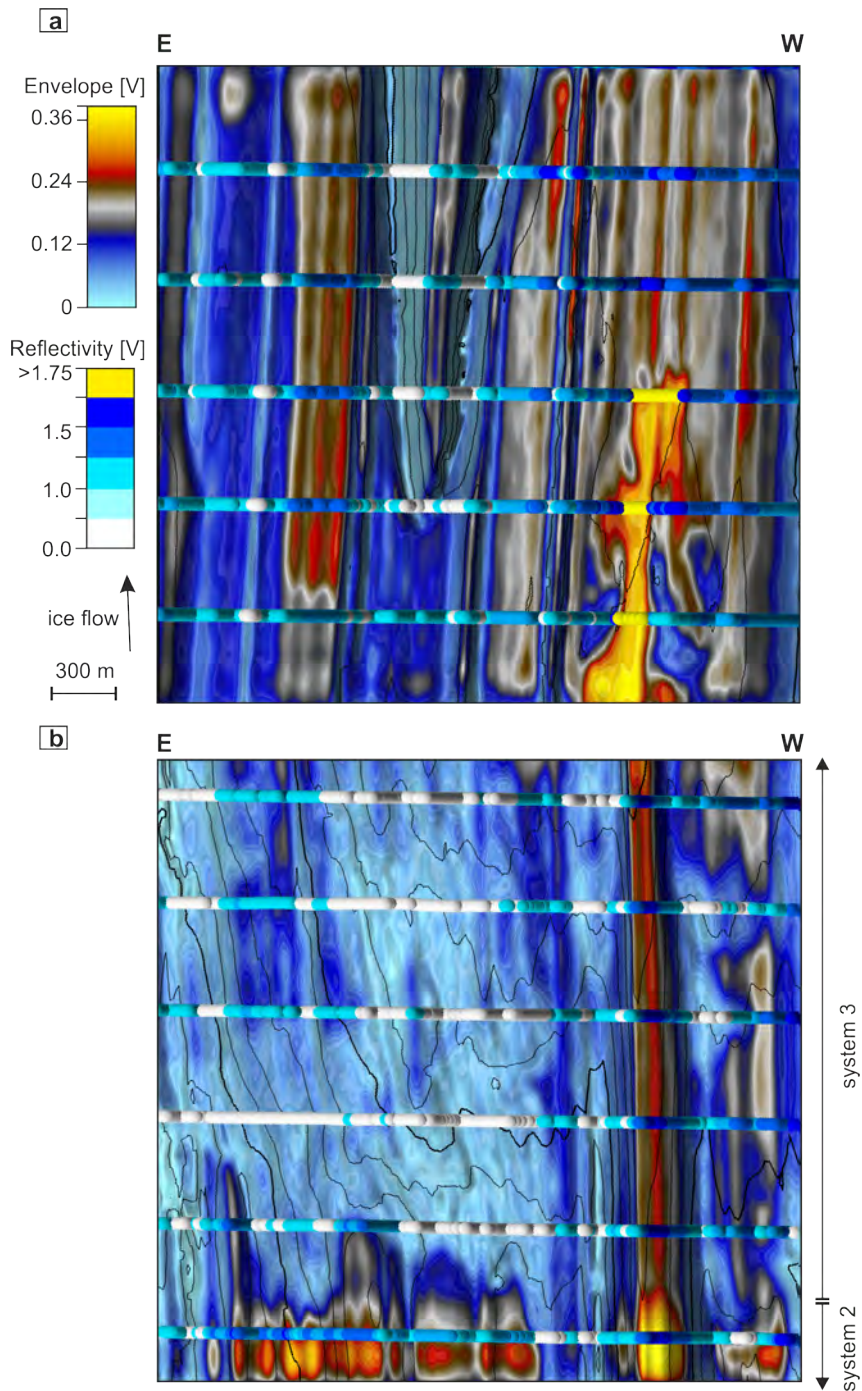
Figure 7.23: Comparison of the pattern of envelope and the pattern of reflectivity as calculated in Chapter 5 for grid 1 (a) and grid 2 (b).

of information in future analysis, the amplitude of different systems needs to be corrected, but for this study the different sensitivities of the antennas were not known prior to processing and a calibration and correction for this effect was not possible within the scope of this thesis.

Figure 7.24 shows an interpretation of bed properties in grid 1 and grid 2 according to bed properties assigned in Chapter 5 (Figure 5.13, Figure 7.23), interpolated over grid 1 and grid 2 using the pattern of envelope. The range of envelope values assigned to a certain property were defined by scaling the reflectivity from Chapter 5 to fit the envelope presented here, as both measure the same property but are scaled differently due to differences in the acquisition and processing. The cut-off values were chosen as follows: Envelope of $>0.3\,\mathrm{V}$ is interpreted as soft sediment overlain by water, envelope less than $0.06\,\mathrm{V}$ as low porosity (porosity <0.3) material, everything in between (envelope $= 0.06$–$0.3\,\mathrm{V}$) is interpreted as soft, water-saturated sediment (porosity $= 0.3$–0.5).

Liquid water is interpreted in the western upstream end of grid 1. No further area in grid 1 and grid 2 is interpreted to contain free water. Most of the area in grid 1 consists of soft sediment. The flanks of some landforms (e.g., the landform in the east of grid 1 and the Bump) as well as the moat around the Bump consist of low porosity material. A large area of the bed in grid 2 is interpreted as low porosity material, with local areas of soft sediment, which coincides with the location of small landforms (black dashed lines). The extent of the low porosity material coincides with parts of the boundary defined by King *et al.* (2009); however, much more detail is visible in the 3D dataset. The colour coding in Figure 7.24 divides the soft sediment in soft sediment with high envelope (dark brown) and lower envelope (light brown), interpreted as sediment with higher porosity (higher envelope) and soft sediment with lower porosity (lower envelope), but still in the range of deforming (porosity= 0.3–0.5) sediment. According to this, the upstream end of the Bump is interpreted to consist of soft sediment with lower porosity, therefore harder sediment, compared to the downstream part (grid 2). Landforms recorded in grid 2 consist of soft sediment until they terminate. The troughs around the downstream end of these landforms consist of low porosity sediment with no indication of liquid water.

Table 7.3.3 summarises the differences between grid 1 and grid 2.
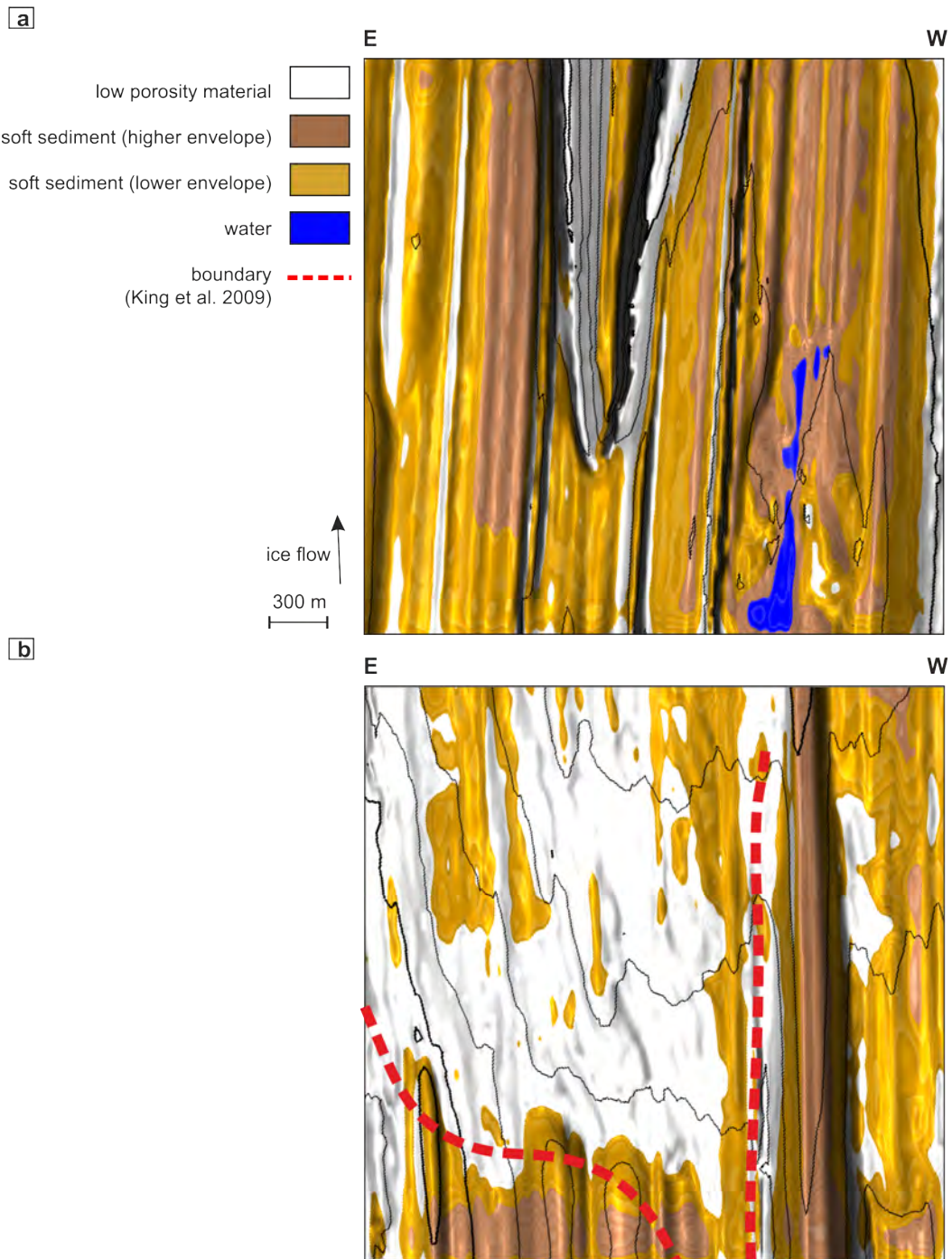
Figure 7.24: Interpretation of bed properties in grid 1 (a) and grid 2 (b). Soft sediment is divided into two categories, with light brown colours representing soft sediment with lower envelope, and dark brown representation soft sediment with high envelope (therefore higher porosity compared to the light brown areas).

Table 7.1: Differences identified from attribute analysis between grid 1 and grid 2.

	Grid 1	Grid 2
cross-cutting features	none	low envelope, 12° dip, 4–15° deviation to ice flow
large-scale elevation	decreasing towards west	abrupt increase in ice flow
dips Bump	<50° (Figure 7.15 b)	<25° (Figure 7.20 b)
dips other landforms	<30°	<15°
reflectivity of Bump	0.18 V	0.24 V

7.3.4 Subglacial Landforms

In the following, the topography along landforms and the moat is described. Using different attributes the geometry and outline of the moat are analysed for both grids (Section 7.3.4.1). This is followed by an estimation of the volume of material eroded to form the moat and the volume of the Bump (Section 7.3.4.2).

The topography along and around some of the landforms in grid 1 and 2 is shown in Figure 7.25 and Figure 7.26. Each figure marks the radargram locations shown in subsequent panels as follows: along a subglacial landform (b), along the eastern moat of the Bump (c), along the crest of the Bump (d), and along the western moat of the Bump (e). The amplitude of the bed reflection along and upstream of a subglacial landform (Figure 7.25 b & d) is clearly identifiable. The amplitude along the moat of the Bump (Figure 7.25 c & e and Figure 7.26 c & e) fades in places but can still be identified. The amplitude along the downstream end of a landform (Figure 7.26 b) as well as along the crest of the Bump (Figure 7.26 d) is high and the reflection appears continuous.

Upstream of the landform (Figure 7.25 f), a small decrease in topography by 4 m followed by an increase in topography by 12 m can be seen. The increase in topography results in a dip of around 2° at the upstream end of the landform. The topography along this landform does not appear constant but shows a decrease in topography by 3 m. The topography of the Bump (Figure 7.27 and Figure 7.25 d) appears very similar to the one of the other landforms described before, but on a different scale. The Bump is the feature with the highest topographic relief in the study area. The topography upstream of the Bump shows a general decrease by around 7 m over an 80 m distance. This is followed by a small depression of 5 m. The height difference between the depression and the crest of the Bump is around 34 m, causing a dip of 8° along this line (Figure 7.12). The topography on the crest of the Bump shows a constant increase, with a dip ~1° for 900 m.
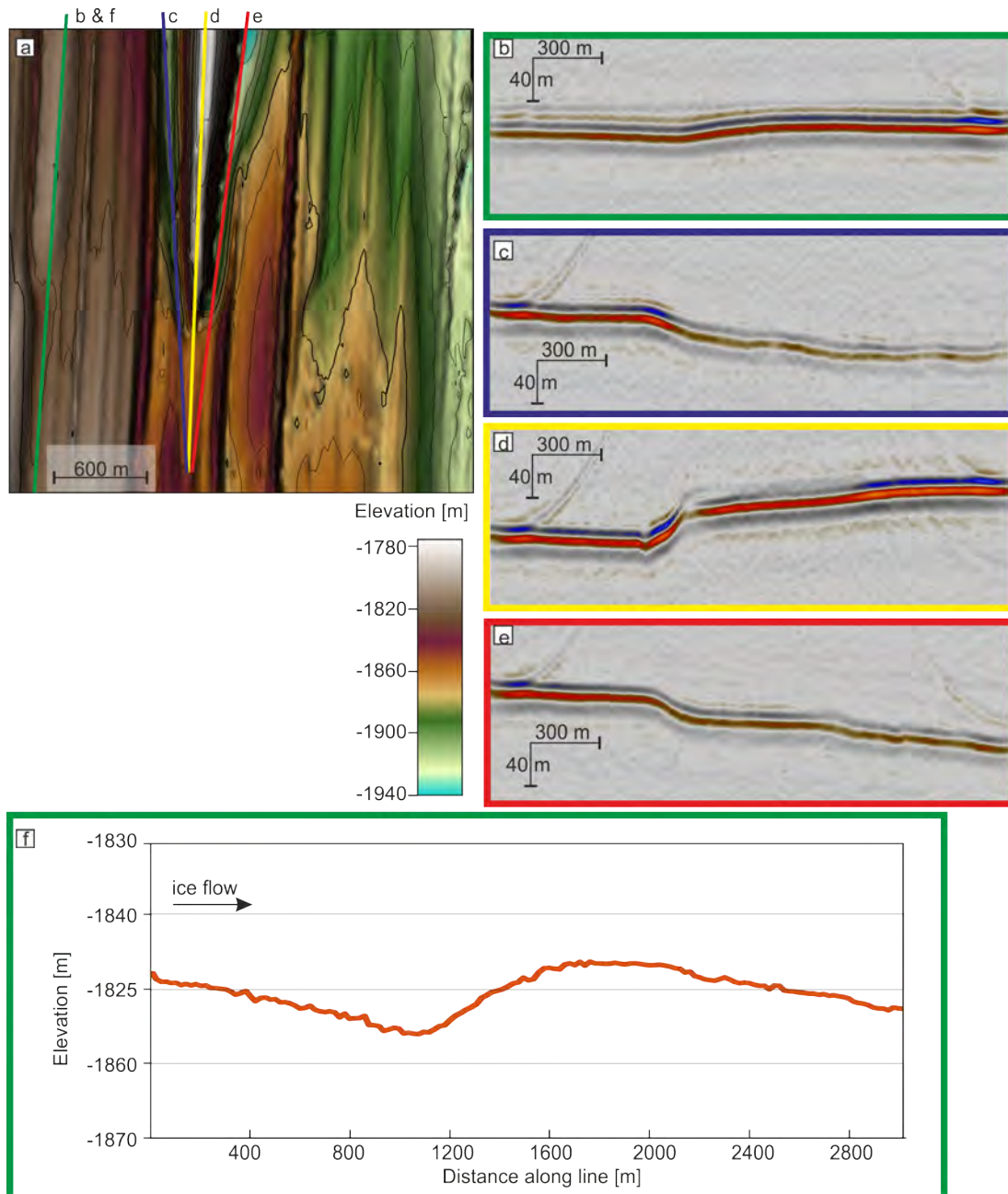
Figure 7.25: Grid 1, a) plan view, colour coding shows the bed elevation. Ice flow from bottom to top. Coloured lines represent the locations of profiles shown in b) – e) showing radargram along b) the upstream end of a landform, c) the moat on the east of the Bump, d) the upstream end and the crest of the Bump, e) the moat on the west of the Bump, f) bed elevation along flow across the upstream end of a subglacial landform. The topography was determined using the radargram shown in b. Ice flow in b) – f) is from left to right.
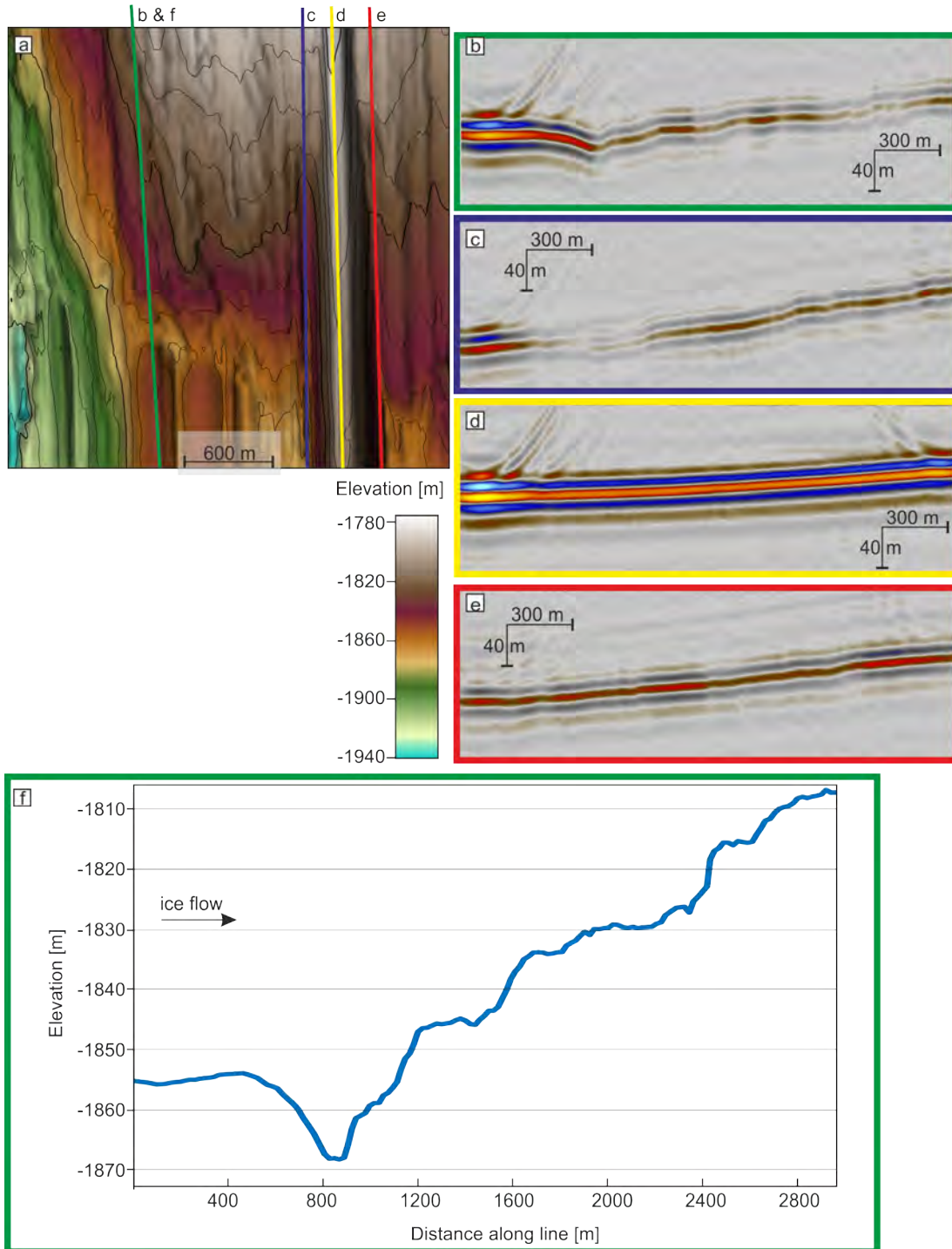
Figure 7.26: Grid 2, a) plan view, colour coding shows the bed elevation. Ice flow from bottom to top. Coloured lines represent the locations of profiles shown in b) – e) showing radargram along b) the downstream end of a landform, c) the moat on the east of the Bump, d) the crest of the Bump, e) the moat on the west of the Bump, f) bed elevation along flow across the upstream end of a subglacial landform. The topography was determined using the radargram shown in b). Ice flow in b) – f) is from left to right.

Further downstream a small topographic step of 9 m over 300 m distance can be seen followed by a smooth constant increase in topography. The downstream end of the landform in grid 2 shows an abrupt decrease in topography of around 15 m, resulting in a dip angle of around 2–4°. This depression is followed by an increasing topography for the rest of the profile. After around 300 m in flow direction, the height of the landform is reached again; the size of the depression downstream of the landform is around 300 m wide and 15 m deep.

7.3.4.1 Outline Size of the Bump and Moat

The outline of the moat was picked based on spatial changes in topography, dip and azimuth (Figure 7.28 and 7.29). Mapping of the outline of the moat in grid 1 was easier compared to grid 2, as the moat is very pronounced in grid 1, due to its significant volume, whereas in grid 2, the appearance of the moat in the topography is very subtle, preventing clear identification from the elevation, although the outline becomes more clear using the dip and azimuth. Comparisons of the depth of the moat and the height of the Bump (Figure 7.27) shows both features develop abruptly. The Bump's crest (green line) shows a topographic increase at 2100 m distance, while the eastern side of the moat (red line) shows a decrease in topography at 2000 m. The moat in grid 1 is up to 45 m deep and 60–360 m wide. The Bump is 13–51 m high and 100–360 m wide (height-to-width ratio 1:7). The geometry of the Bump and the moat is not symmetric in grid 1; in the downstream part, the moat and the Bump get wider on the western side but not on the eastern side (Figure 10.27 and 7.28). The downstream end of the moat on either side of the Bump in grid 2 is shifted by 150 m in flow direction, whereas the western moat advances further downstream. According to this definition of the outline of the moat, the width of the moat in grid 2 varies between 90–140 m, depending on the location where the moat ends and where the Bump starts. The moat in grid 2 is up to 11 m deep. The Bump in this grid is 20–50 m high and around 190–450 m wide (height-to-width ratio 1:10). The height-to-width shows an increase from 1:7 to 1:10 in flow direction. This can also be seen by the decrease in dip on the flanks of the Bump towards downstream. In grid 1, the flanks can be up to 50° steep, whereas further downstream in grid 2 the flanks dip at up to 20°.
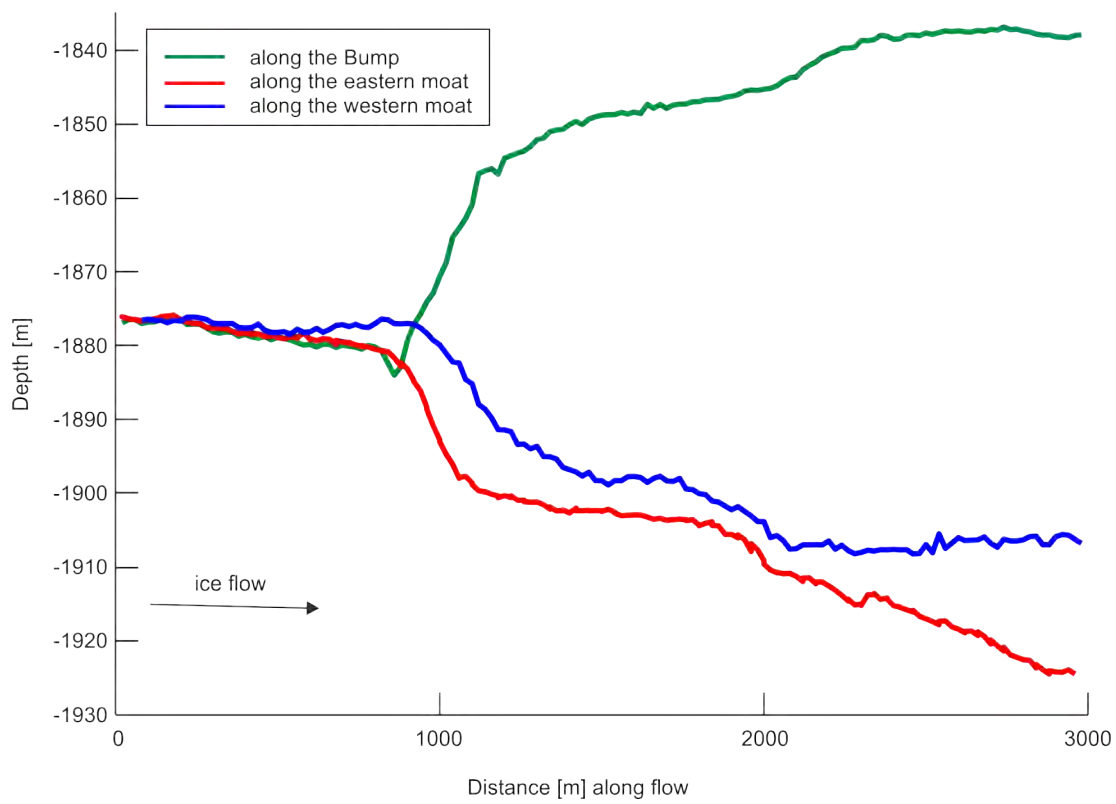
Figure 7.27: Elevation along the crest of the Bump (green) and the eastern (red) and western (blue) moat of the Bump.
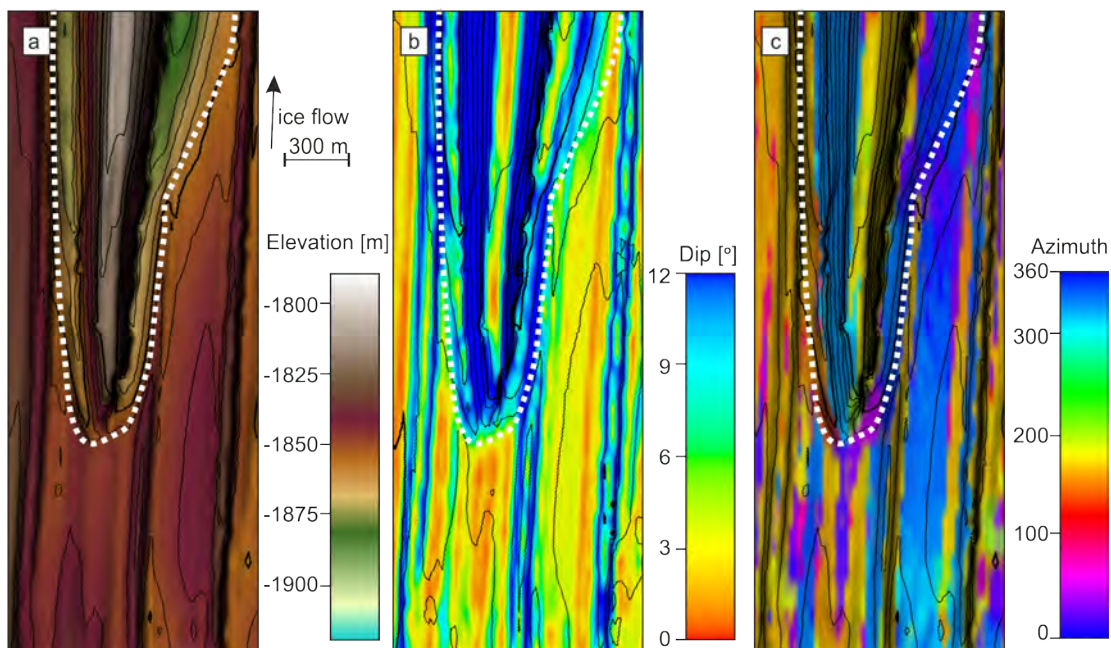
Figure 7.28: Plan view of the bed in grid 1. White dashed line represents the approximate outline of the moat. a) Elevation, b) dip (limited to values between 0–12° to enhance visibility), c) azimuth. Radargram of the upstream end of the Bump and the downstream end of the grid is shown in Figure 10.27 in the Appendix.
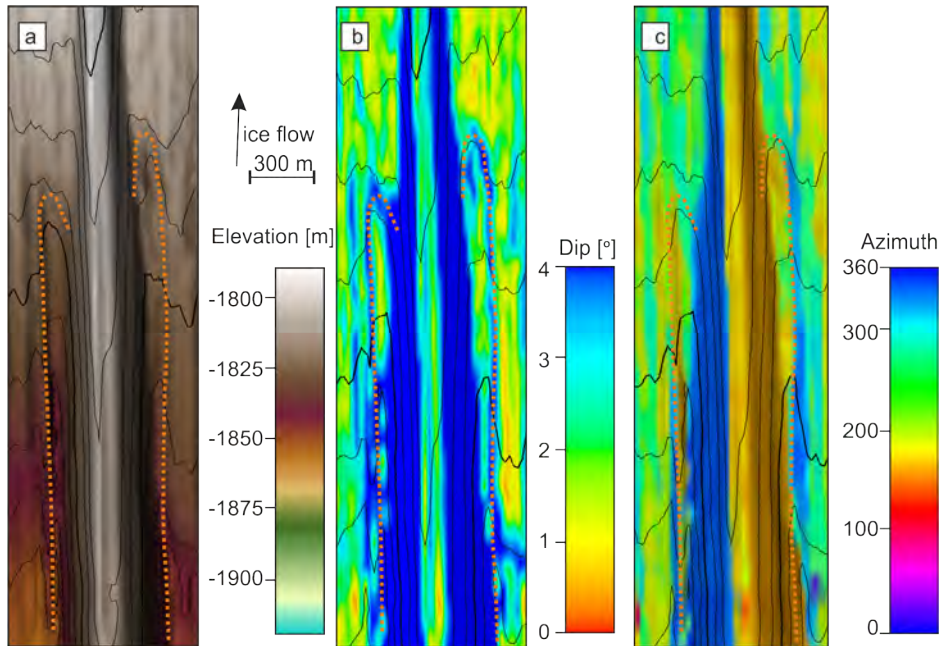
Figure 7.29: Plan view of the bed in grid 2. Orange dashed line represents the approximate outline of the moat. a) Elevation, b) dip (limited to values between 0–4° to enhance visibility), c) azimuth. Radargram of the upstream end of the grid and the downstream end of the moat is shown in Figure 10.27 in the Appendix.

7.3.4.2 Volume of the Moat and the Bump

Analysis of the 3D dataset reveals a larger moat than implied in previous studies. Furthermore, in being able to define the Bump and the moat, the volume for both can be calculated. Omitting the structure of the Bump and the moat from the bed surface and interpolation of the data east and west of the Bump an interpretation of the "initial" topography can be calculated. By subtracting the initial topography and the actual topography the volume of the Bump and moat was calculated. For the interpretation of the initial topography see Figure 10.27 and 10.31. The volume that forms the Bump is around $1.4 \times 10^7 \, \text{m}^3$ in grid 1 and $2.4 \times 10^7 \, \text{m}^3$ in grid 2. The volume of the moat is around $2.0 \times 10^7 \, \text{m}^3$ in grid 1 and $1.9 \times 10^6 \, \text{m}^3$ in grid 2.

7.3.5 Key Observations

- More detail of the topography is visible in 3D migrated 20 m spaced data compared to the 2D migrated 500 m spaced data.

- COP attributes can enhance the visibility of continuous reflectors, specifically in areas of low amplitude returns.

- Topography in grid 1 is more aligned to the ice flow than to grid 2.

- The spatial pattern of attributes is more chaotic in the downstream area of grid 2 compared to grid 1.

- Small landforms were identified using variation in dip and azimuth.

- Cross-cutting features identified in grid 2 show a low envelope, possibly caused by low porosity material.

- Landforms in both grids consist of soft sediment.

- A moat exists around the upstream end of the Bump, extending 10.5 km along flow.

- The moat around the Bump consists of low porosity material.

- Landforms upstream of the moat are truncated by the moat.

- The outlines of the Bump and moat were mapped using different attributes. Estimated volumes of the Bump and moat are of the same order for grid 1, while the volume of the Bump is an order of magnitude higher compared to the volume of the moat in grid 2.

7.4 Discussion

The following includes the discussion of results obtained from 3D migration and attribute analysis on 3D migrated data. The first part discusses the improvement of data quality by the calculation of attributes on 3D migration data. The second part of the discussion focuses on the different features identified on the bed, including cross-cutting features (Section 7.4.2.1.1), small landforms (Section 7.4.2.1.2), the moat (Section 7.4.2.2) and the different shape and properties of landforms (Section 7.4.2.3). The final part of this chapter discusses influences on the reliability of the signal received from the bed, especially the interpreted bed properties, which were inferred from variation in amplitude.

7.4.1 3D Topography and Attribute Analysis

The acquisition of data compliant with 3D migration and processing of these data is time and labour intensive, yet the high detail received for the ends of landforms represents a major improvement to the interpretation of topography from sparsely spaced data and has an important influence on the understanding of subglacial processes and the formation of landforms. Section 10.5.4 in the Appendix includes some suggestions to consider for future studies. The usage of the COP and GLCM to identify discontinuities is very useful as demonstrated here when picking the bed reflection in areas of low amplitude return. The additional value of attribute analysis is highlighted with the enhanced visibility of small features, such as the small landforms and cross-cutting features identified in grid 2. Furthermore, structural attributes like azimuth and curvature were identified to be useful tools to identify landform crests, troughs and to map the outline of the moat.

7.4.2 Bed Properties and Topography

The discussion of bed properties first focuses on a comparison of bed properties and topography in grid 1 and grid 2, with a special focus on the boundary and the sliding area. This is then followed by a discussion of the Bump and the moat.

7.4.2.1 Spatial Changes in Topography and Link to Bed Properties

Coherent across all geometric attributes, the bed topography is different in grid 1 and grid 2 (Figure 7.15 & Figure 7.20). In grid 1 the topography appears more

abrupt perpendicular to ice flow but very continuous along flow (Figure 7.11). In contrast, topographic changes in grid 2 appear steady perpendicular to ice flow, but topography changes noticeably along flow (Figure 7.16). The changes in bed topography in flow direction in grid 2 are accompanied by changes in bed properties. Landforms terminate against the area, which is interpreted to consist of low porosity material. Small landforms (200–300 m length, 6 m width) compared to further upstream as well as cross-cutting features are located within the area of low porosity material (Figure 7.24 b), whereas none of these are found in the area of grid 1, an area laced with landforms and interpreted to consist mainly of soft sediment (Figure 7.24 a; Smith *et al.*, 2007). A transition of soft sediment to stiffer sediment in the area of grid 2 has already been described by King *et al.* (2009) as well as in Chapter 5 (Figure 5.16). Concordant with results in Chapter 5 (Figure 7.23 b), the interpretation of the spatial pattern of bed properties in this chapter does confirm a transition, although 3D migrated data in grid 2 provide more detail on the pattern of bed properties. In the following possible origins for the cross-cutting features and explanations for the occurrence of smaller landforms in grid 2 compared to grid 1 are given.

7.4.2.1.1 Cross-Cutting Features: Cross-cutting features are located in an area of low porosity material, where the spatial pattern of structural attributes indicates abrupt changes in topography. The orientation of cross-cutting features deviates from ice flow to the east by 4–15°. Using the 2007/08 dataset King *et al.* (2016) also identified cross-cutting features with similar orientation but topographically more pronounced in the eastern trough of RIS (see Figure 2.7). Cross-cutting features in the palaeo record are often interpreted as relics of former phases of ice flow (Clark, 1993) or channels incised into underlying impermeable bedrock (Lowe & Anderson, 2003). The first would imply a change in ice flow direction, and the orientation of these features would represent the orientation of the former ice flow. However, this seems less likely, considering the clear topographically-constrained valley which the whole of RIS flows (Section 2.3). Assuming the cross-cutting features represent channels, one might expect water to be present along the features. The reflectivity in 2016/17 data (Figure 5.16 and 5.1), as well as envelope in data presented in this chapter (Figure 7.24), give no indication for the existence of water in and around the cross-cutting features identified in grid 2. Water identified on the bed of RIS in Chapter 5

seems to be orientated along the flow direction, contradictory to the orientation of cross-cutting features. As already implied in Section 5.3.1.2, the rise in topography downstream of the boundary and the occurrence of cross-cutting features, together with changes in bed properties, likely express components of the underlying geology e.g., the outcrop of the inherited underlying geology, similar to the interpretation of an inherited underlying geology causing subtle changes in subglacial topography under Pine Island Glacier (Bingham *et al.*, 2017; Brisbourne *et al.*, 2017).

7.4.2.1.2 Influences on Landform Length: The elongation ratio of the small landforms ($\sim$200–300 m length, $\sim$6 m width) in grid 2 categorises them as MSGLs. Apart from the difference in length (200–300 m vs. 10 km) and density, no obvious difference can be seen in the geometry of landforms between grid 1 and grid 2. Both are interpreted to consist of soft sediment (Figure 7.24); however, the small landforms in grid 2 are located in an area of low porosity material, which implies an influence of the underlying substratum on the landform length. In previous studies, the landform elongation was linked to the ice flow velocity (e.g., Briner, 2007; Hart, 1999; Shaw, 1994; Stokes *et al.*, 2013). However, ice flow velocity does not vary between grid 1 and grid 2. Modelling results by Jamieson *et al.* (2016) imply the elongation of MSGLs to be a function of ice flow velocity as well as basal shear stress. Furthermore, Clyne *et al.* (2020) found longer tails of potential crag-and-tail features beneath Thwaites Glacier in areas of the bed that consist of soft sediment and low surface slope compared to areas of hard bed, great topographic relief and steeper ice surface slope. Coherent with modelling results (Jamieson *et al.*, 2016) and observations in the palaeo record (Evans *et al.*, 2005; Reinardy *et al.*, 2011) as well as beneath active ice streams (Clyne *et al.*, 2020; Holschuh *et al.*, 2020), data presented in this Chapter imply the length and density of landforms to be influenced by ice flow velocities and basal properties.

Both the occurrence of small landforms and cross-cutting features are linked to the occurrence of low porosity material, therefore the topographic rise in grid 2. The lack of both explains the absence of cross-cutting features and small landforms in grid 1.

7.4.2.2 The Moat Around the Bump

7.4.2.2.1 Geometry of the Moat: Moats identified in the palaeo record (Graham & Hogan, 2016; Larter *et al.*, 2019; Ó Cofaigh *et al.*, 2005) and beneath Thwaites Glacier (Holschuh *et al.*, 2020) are located around the upstream ends of crag-and-tail features, whereas the moat beneath the RIS is located around and along a MSGL (Figure 7.30). The shape of the moat in Figure 7.30 a, imaged in a palaeo-ice stream offshore from Greenland, appears similar to the moat around the Bump (Figure 7.30 e), with similar depth of the moat (54 m (a) and 45 m (RIS)). Furthermore, similar to the RIS the depth of the moat seems to be on the order of the height of the Bump (Figure 7.30 a). However, the moat appears continuous around the bump in Figure 7.30 a, whereas the moat under RIS has a small interruption at the upstream end (e). The moat beneath RIS is visible over a length of around 10.5 km, which is much longer than (<3 km) reported by Graham & Hogan (2016). This could imply three things: (1) the topographic difference between the moat and surrounding area in grid 2 is very subtle, such differences might be below the resolution of data from palaeo ice stream beds, (2) processes during deglaciation possibly changed the topography in this region and (3) the moat length possibly scales with the length of the landform as the Bump (e) is longer than landforms in Figure 7.30 a–d. However, further studies are needed to identify a possible link. An additional difference between the moat beneath RIS and the palaeo record shown here is that moats are visible around large as well as small landforms in the palaeo record (red arrow in Figure 7.30 a-2 & a-4), whereas under RIS the Bump appears to be the only feature surrounded by a moat. Implications of this are discussed in Section 8.2.3.

7.4.2.2.2 Properties Along the Moat: The moats identified beneath Thwaites Glacier (Clyne *et al.*, 2020; Holschuh *et al.*, 2020) and in the palaeo record (Larter *et al.*, 2019) are interpreted to be cut into hard material. This is consistent with observations at RIS, where the moat and flanks of the Bump consist of low porosity material. Soft sediment upstream of and around the moat could imply that soft sediment was eroded during the formation of the moat and underlying material got exposed, with this harder underlying material possibly then being eroded too. This would imply soft sediment interpreted in this area to consist of a layer of several metres thickness, overlying low porosity material underneath. Furthermore, small landforms upstream of the Bump are truncated by the moat, which

implies that these landforms and the surrounding topography were eroded during the formation of the moat. Formation theories of moats are discussed later in Section 8.2.3.

7.4.2.3 The Bump and Other Landforms on the Bed of RIS

7.4.2.3.1 Symmetry of Landforms: In the past, the asymmetry of landforms in deglaciated areas was used to reconstruct the past ice flow direction. However, Spagnolo *et al.* (2010) stated that the asymmetry of landforms is not necessarily indicative of the ice flow direction, as symmetric, asymmetric and reverse drumlins can be found next to each other within the same flow set. Moreover, Spagnolo *et al.* (2010) questioned, whether the symmetry of drumlins evolves over time, due to erosion and deposition, or if their shape represents shapes on formation, which are subsequently not modified. The eastern edge of grid 1 covers the upstream end of a landform (referred to as eastern landform), which extends into and truncates in grid 2 (see Figure 7.11, 7.16, 5.8 and 5.9). The width of this landform ($\sim$300 m) appears constant over the distance of 10.5 km (Figure 5.8). The upstream and downstream sides appear smooth (Figure 7.25 f and 7.26 f) and both sides appear similarly steep, although the dip spans slightly higher values at the downstream end (2–4°) compared to the upstream end (2°). The landform is therefore classified as symmetric. The Bump, which is the other feature visible in both grids, appears tapered (in height, and therefore width) at the upstream end (Figure 7.11) and towards downstream (King *et al.*, 2016). Furthermore, the flanks at the upstream end of the Bump dip at <50°, while the flanks further downstream dip at <25°. However, the downstream end of the Bump lies outside the acquired grid, but variations seen in grid 1 and grid 2 imply a change in shape of the Bump towards downstream, which implies a possible asymmetry. Other landforms visible in the 3×3 km grid do not appear tapered. No information on when the landforms under RIS were formed is available, but observations of the active extension of a landform (Smith & Murray, 2009; Smith *et al.*, 2007) imply that at least some of the landforms were formed recently or are still in the process of formation (Spagnolo *et al.*, 2010). This implies that the symmetry of landforms visible under RIS is a product of their formation. Furthermore, the 3D shape of a landform can lead to fundamental insights into landform morphology and therefore inspire and test/validate formation theories.
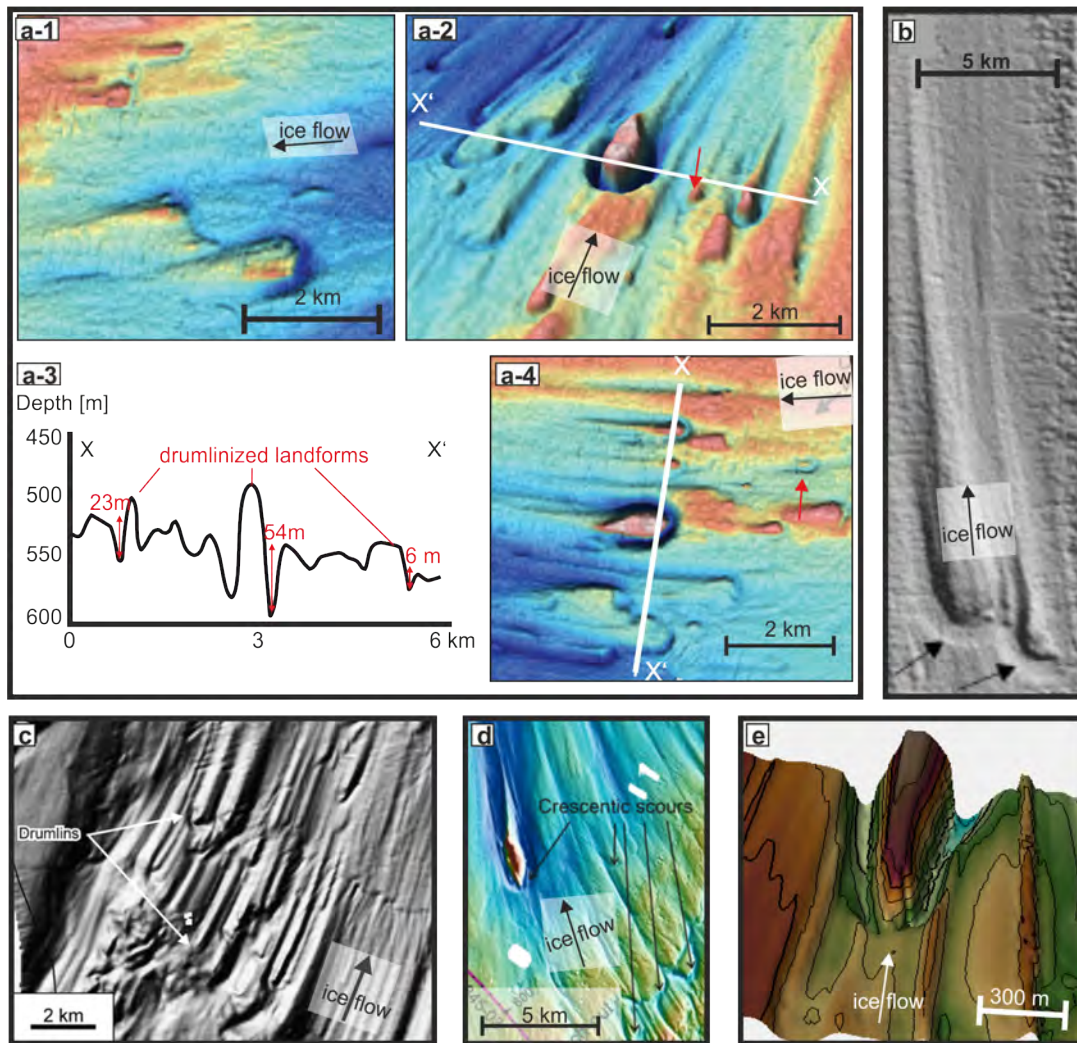
Figure 7.30: Moats around landforms observed in the marine record in a-1 – a-4) offshore from Greenland (Graham & Hogan, 2016), b) on a palaeo ice stream in Antarctica (Ó Cofaigh *et al.*, 2005), c) on a palaeo ice stream in Antarctica (Graham *et al.*, 2009), d) on a palaeo ice stream in Antarctica (Larter *et al.*, 2019) and for comparison, e) beneath RIS. a-2 & a-4 show the area around the same landform, a-3 shows the topography of this landform and the surrounding in a cross-section.

7.4.2.3.2 Landform Properties: Coherent with interpretations in Chapter 5 the upstream end of the Bump appears to consist of harder material compared to downstream. However, the envelope is not sufficiently low to indicate low porosity material. The moat and flanks around the Bump consist of low porosity material. Observations of softening of material along the downstream coincide with observations from Thwaites Glacier (Clyne *et al.*, 2020; Muto *et al.*, 2019) and the onset region of RIS (King *et al.*, 2007) where they report a hard bed on the upstream side of bumps followed by a soft tail.

7.4.3 Reliability of Bed Returns

In most areas, the bed reflection is clearly identifiable using different attributes. For instance, the bed reflection is often the signal containing the highest amplitude. However, parts of the Bump flanks and cross-cutting features do not show a clear return. In the following the reliability of bed picks and their subsequent topography and attributes are analysed. First, the continuity of the bed reflection is evaluated and areas, where the bed can not be identified reliably, are highlighted. This includes possible reasons for the unreliability of some areas. Secondly, an evaluation of the reliability of the envelope as an attribute to determine bed properties is given.

7.4.3.1 Continuity of the Signal

To evaluate the continuity of the bed reflection, the variance of the COP was calculated. Figure 7.31 and Figure 7.32 show the overlay of the variance of the COP over the topography. Low coherency areas (variance >0.1) are coloured in blue, high coherency areas (low variance) are chosen to be transparent, therefore the topography is displayed. Low coherency of the bed reflection was calculated for areas of the flank of the Bump, as well as the moat, although the reflection of the Bump and the moat seem more continuous in grid 2, compared to grid 1. Furthermore, flanks of other landforms as well as some features on the eastern end of grid 2 contain low coherency. Apart from small areas which are interpreted to contain discontinuities in the bed reflection, most of the bed in grid 2 and grid 1 appears continuous.

Different factors might influence the continuity of the signal as follows:
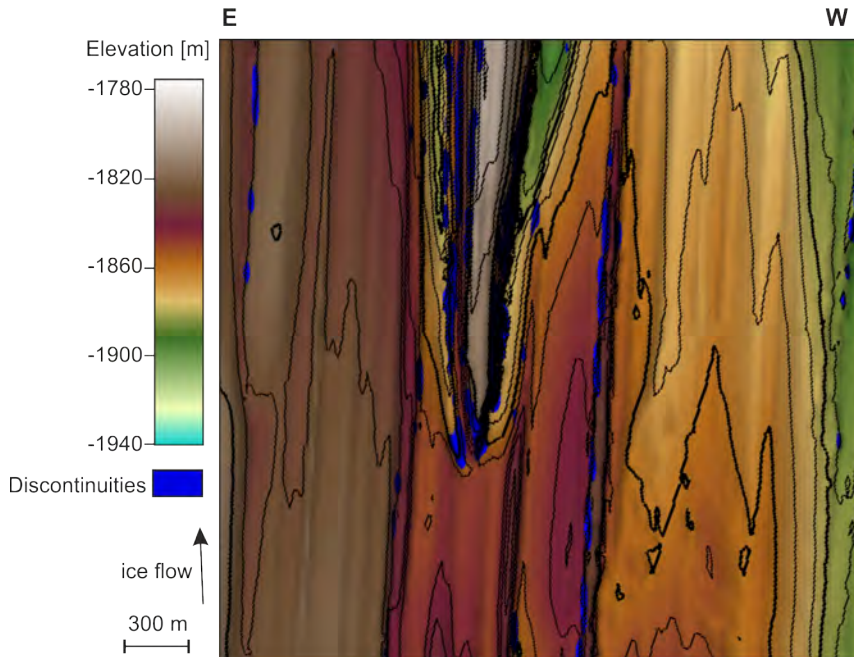
Figure 7.31: Evaluation of the continuity of bed reflection in grid 1. Discontinuity is expressed by the variance of the COP. The variance was calculated using a range of 3 inlines, 6 crosslines and a vertical smoothing of 15 samples. Areas with variance less than 0.1 are not displayed (transparent).

Bed Topography and Acquisition Parameters: The structural analysis of the topography in both grids revealed that the topography in grid 2 is less abrupt compared to grid 1. An increase in discontinuities (high variance) can be seen with increasing dip of the surface (Figure 7.33), where all signals reflected at a surface dipping at 55° show discontinuities, while for signals reflected at a surface at 25° around 50% of the signals show discontinuities. An insufficient length of radar lines, compared to the dip of the target, will result in a lack of recorded reflections for dipping reflectors (see Section 3.3.2.2). Dips up to 50° were observed for the flanks of the Bump, where the majority of the reflections contain discontinuities. Considering the acquisition geometry for grid 1, the distance of the western flank to the outer edge of the grid is around 1.5–1.7 km. Assuming a linear ray path (therefore neglecting the firn) would allow for a maximum dip of 34–37° in this area, for the bed return to be recorded (see Section 3.3.2.2). Reflections from steeper dipping topography will not be recorded. Furthermore, due to the gradual decrease of velocities in the firn column and the resulting bending of the ray path away from the source, resolvable dips will be smaller. A second parameter to take into account is the radiation pattern. The radiation pattern of
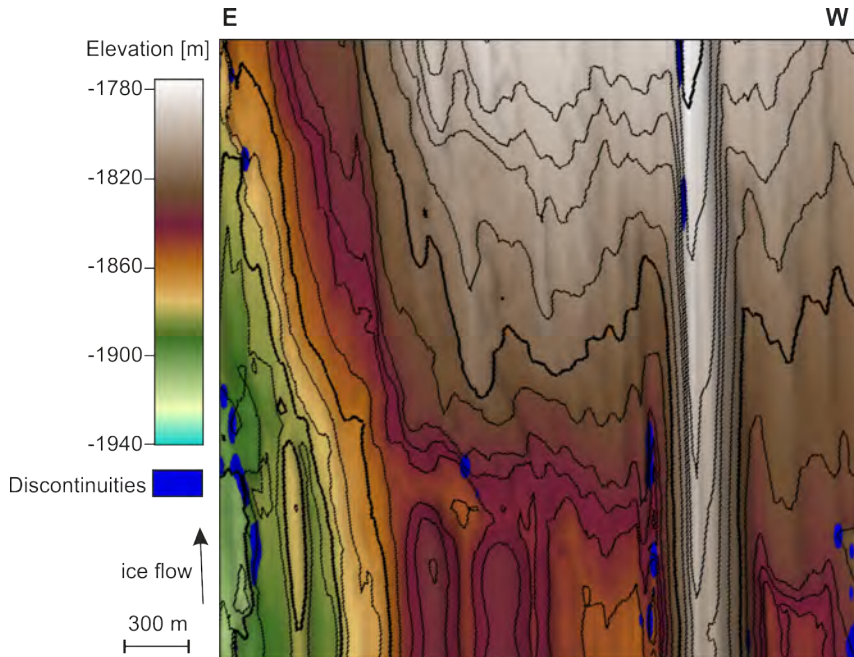
Figure 7.32: Evaluation of the continuity of bed reflection in grid 2. Discontinuity is expressed by the variance of the COP. The variance was calculated using a range of 3 inlines, 6 crosslines and a vertical smoothing of 15 samples. Areas with variance less than 0.1 are not displayed (transparent).

the DELORES system was not analysed so far. Based on the characteristics of the system, the radiation pattern is assumed to be comparable to that described by Langhammer *et al.* (2019). They describe several configurations, for which the pattern for an EM infinitesimal dipole in a full space for antenna heights of 20 m (Figure 7.34) is most likely to represent the radiation pattern of the DELORES system on an ice stream (personal communication Ed King, March 2021). According to the radiation pattern described for this configuration, less energy is transmitted and recorded with an incoming angle of more than 25° (compared to the vertical). This decrease in recorded energy influences the amplitude of the signal, as well as the continuity of the bed reflection.

Interference Effects: The interpretation of physical attributes is often based on the assumption of an isolated interface, which might not be the case for a subglacial environment where sediments are possibly deposited in several thin layers. Reflections of these thin layers can cause interference of signals, which is also known as thin-layer tuning. This phenomenon would change the frequency as well as the amplitude of the signal (Booth *et al.*, 2012; Guha *et al.*, 2005;
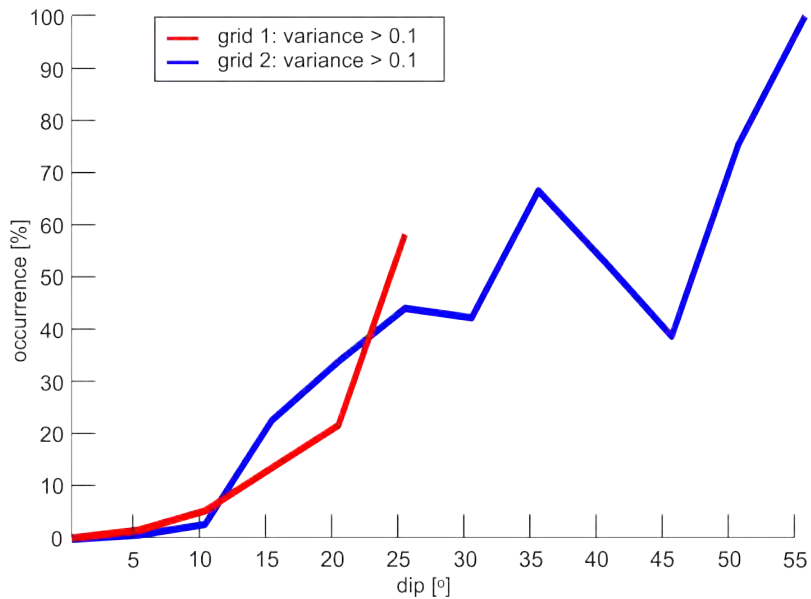
Figure 7.33: Occurrence of discontinuities (variance >0.1) for surfaces dipping at different angles. The dip increment for the calculation of the occurrence of signals with high variance in comparison to the total amount of signals is chosen to be 5°.
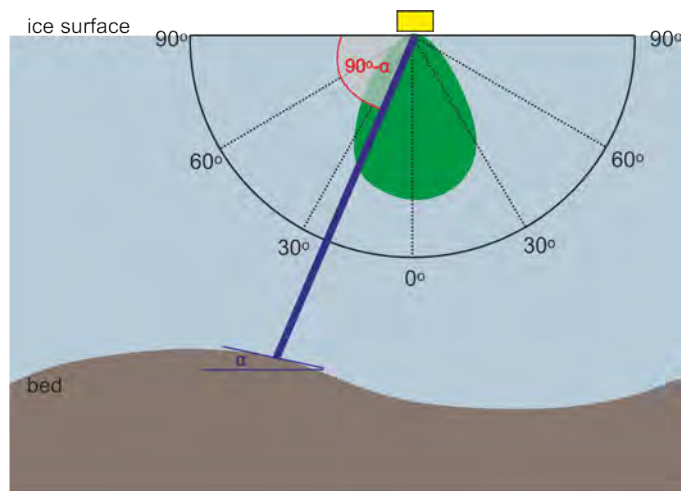
Figure 7.34: Assumed radiation pattern (in the E-plane) of the DELORES system. The radiation pattern of the DELORES system on an ice stream (consisting of snow, firn and ice) is assumed to be comparable to the radiation pattern of the antenna configuration described in Langhammer *et al.* (2019) over air (20 m) and ice, rather than just ice, to account for the high air content in firn (graph modified after Langhammer *et al.*, 2019).

Widess, 1973), causing some regions to have a lower or higher amplitude due to deconstructive or constructive interference. Figure 7.35 shows the frequency overprinted on the bed topography with frequencies below 3 MHz displayed in blue and frequencies above 4.5 MHz displayed in green. Frequencies below 3 MHz can not be seen in grid 1 and grid 2, but part of the flanks of the Bump as well as other landforms show higher frequency content ($\sim$7 MHz). Areas with higher frequency content might indicate possible interference effects, but more work is needed to verify the possible effects of interference on these data presented here.

Insufficient Change in Bed Properties: A gradual change in properties might not represent a sufficient contrast in dielectric properties and therefore no clear reflection can be recorded. Such a gradual change might occur if sediment is incorporated into the basal ice.

7.4.3.2   Reliability of the Amplitude Information

Previous parts of this thesis highlighted that the amplitude of an arrival can be influenced by many different factors other than bed properties, such as roughness and attenuation (Section 2.4.3 and 4.3.1). Variations in the frequency and phase content of the wavelet were used in the previous section to evaluate the influence of these factors. Figure 7.36 shows the interpretation of bed properties as seen in Figure 7.24, with areas of low confidence coloured in red. Low confidence areas are defined as areas of high frequency content, areas where the bed reflection shows a low continuity and/or where the bed is dipping steeper than 25°. In grid 1 the low confidence areas are located along the flanks of landforms. Areas of low confidence are mostly located in areas interpreted as low porosity sediment, implying that the amplitude received from this area and the resulting interpretation of the bed properties are possibly not reliable. However, other areas of the flank and moat of the Bump that do not show low confidence indicate the existence of low porosity material, supporting the interpretation that the flank and the moat around the Bump at least partly consists of low porosity material.

Low confidence areas in grid 2 are spatially limited and mostly located in the moat or the flanks of the Bump, as well as areas at the eastern edge of the grid. Due to the limited data availability, and therefore limitation of the migration aperture at the edges of the grid, these areas have to be interpreted with caution and more complex geometries will not be resolved nor imaged if located at the
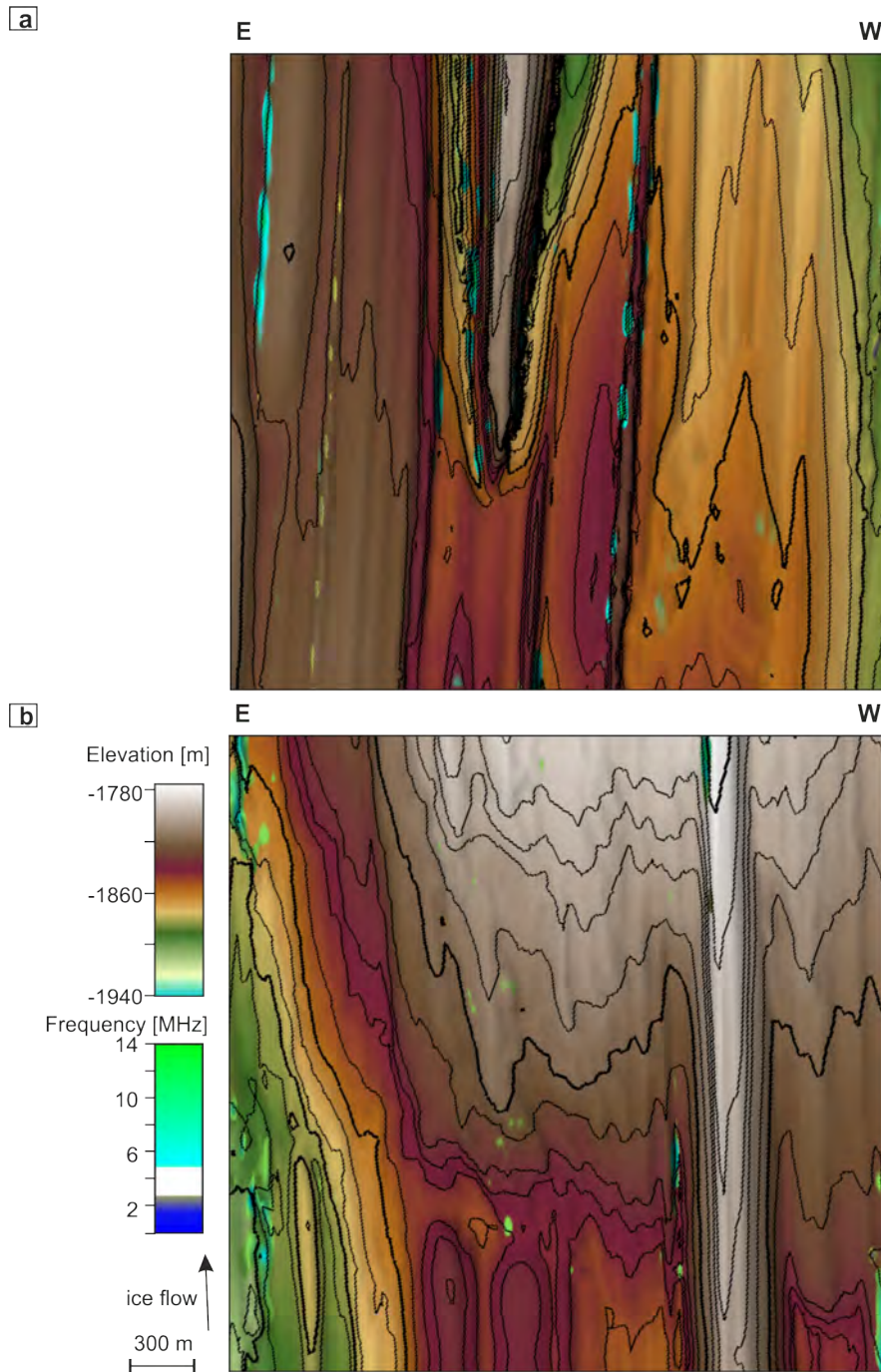
Figure 7.35: Elevation of the bed overprinted with the frequency of the bed reflection in grid 1 (a) and grid 2 (b). Frequencies between 3 and 4.5 MHz are chosen not to be displayed, as these represent frequencies expected from the bed return, not affected by interference.

edges of a grid. Apart from local areas, the interpretation of bed properties in grid 2 seems valid.

To conclude, after this initial analysis, most of the arrivals received from the bed appear to contain reliable amplitude information. Areas that should be interpreted with caution are located along parts of the flank of the Bump and the moat.
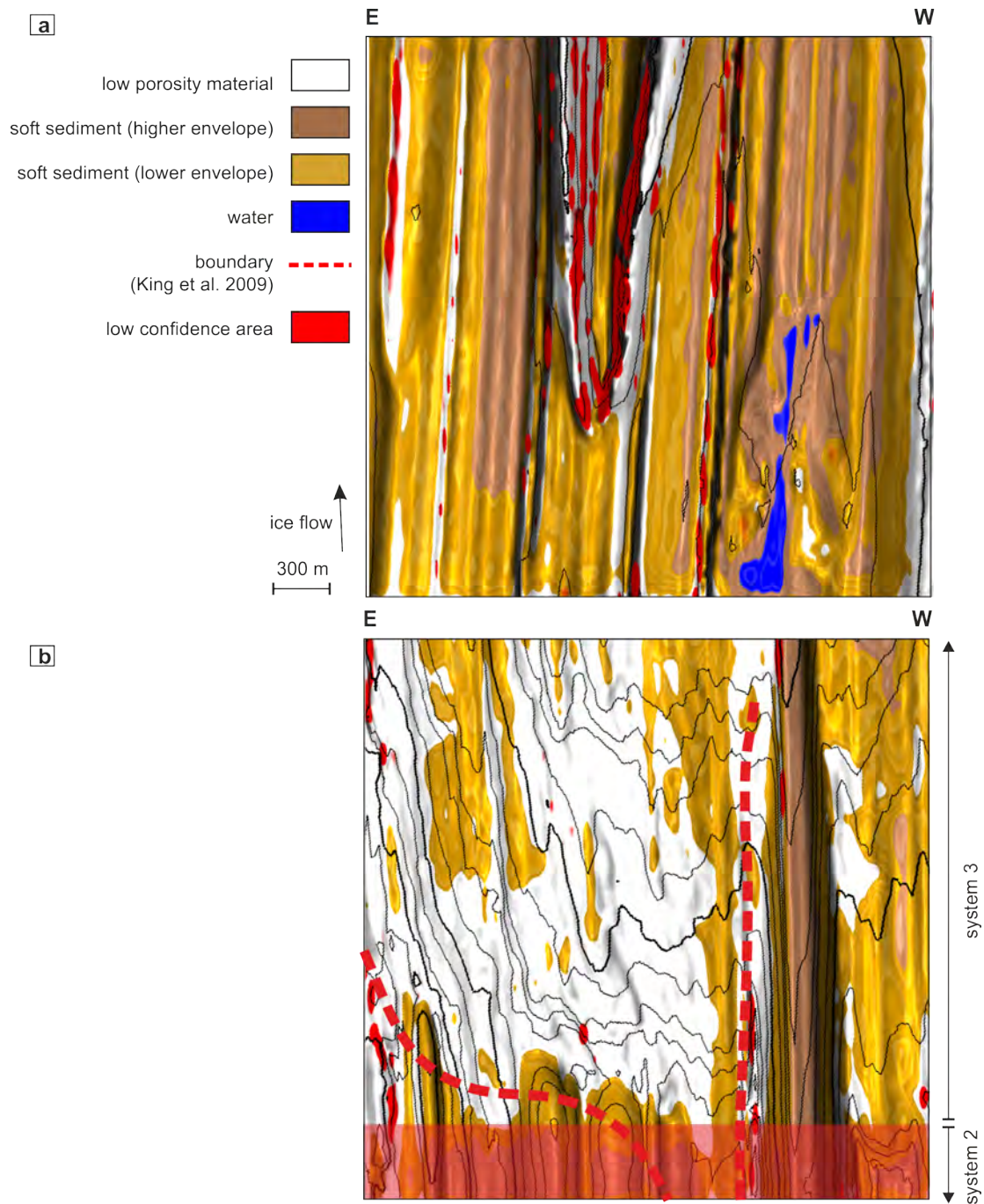
Figure 7.36: Interpretation of bed properties in grid 1 (a) and grid 2 (b) with identification of areas of low confidence. Soft sediment is divided into two categories, with light brown colours representing soft sediment with lower envelope, therefore interpreted as possibly lower porosity, compared to soft sediment with higher envelope coloured dark brown. Areas of low confidence due to steep (>25°) dipping topography, discontinuities in bed reflection and high frequency content are coloured in red. Additionally, the upstream area of grid 2 is coloured in red, as data in this area were acquired with different antennas, which results in an inconsistency of the recorded amplitude.

7.5   Summary

Two 3D migrated datasets, each covering a $3{\times}3$ km area, were analysed to retrieve high-resolution architecture of the up- and downstream end of landforms and the area around the boundary (King *et al.*, 2009). Following the 3D processing, structural and physical attributes were calculated for the surface-radar data. The resulting resolution of this dataset is compliant with morphological analysis on DEMs from deglaciated areas. The data reveal small landforms consisting of soft sediment, within an area of low porosity material. The limited length of these landforms implies landform length to be dependent on ice flow velocity, basal properties and basal topography. High-resolution data reveal a moat around the upstream end of the Bump, that consists along the landform for more than 10 km. The moat is interpreted to be formed by the erosion of sediment, which exposes underlying low porosity material. The depth of the moat and the height of the Bump is of the same scale at the upstream end of the Bump. Comparison of the up- and downstream end of landforms reveals that some landforms are symmetric, while the Bump appears tapered and less steep towards downstream. Analysis of the reliability of the amplitude received from the bed, and therefore the interpretation of bed properties, revealed that the properties determined for the moat and the flanks of the Bump in some places contain high uncertainties, whereas in other places the variation in amplitude can be attributed to variation in bed properties. The use of attributes in 3D data interpretation has significantly enhanced the visibility of subtle features such as small landforms and the outline of the moat.

Chapter 8

Subglacial Environment and Landforms Beneath *Rutford Ice Stream*

From a wider perspective, the main aim of studying active flowing ice and the deglaciated environment is to get a better understanding of the mechanisms and controls of glacier flow, in order to reliably predict their future behaviour. While the dynamics in formerly glaciated areas were studied in various locations (e.g., Alley *et al.*, 1997; Clark *et al.*, 2018; Clarke, 2005; Ely *et al.*, 2016; Stokes & Clark, 2001; Stokes *et al.*, 2007), insights into conditions beneath active ice flow have only been gained over the last 30 years (e.g., Alley, 1993; Alley *et al.*, 1986; Bingham *et al.*, 2017; Blankenship *et al.*, 1987; Brisbourne *et al.*, 2017; Davies *et al.*, 2018; Holschuh *et al.*, 2020; King *et al.*, 2016). The broad aim of this thesis was to investigate the basal properties beneath RIS with a special focus on the subglacial landforms. To investigate contemporary conditions beneath RIS a combination of surface-radar data was utilised: (1) a radar grid acquired in 2007/08 covering 14.5×18 km ~40 km upstream of the grounding line; (2) the repetition of the radar grid, covering the same location, acquired in 2016/17; and (3) two high-resolution 3D radar datasets acquired in 2017/18, both covering an area of 3×3 km.

The main outcomes of this thesis are:

- Detailed surveys and analyses of basal properties, including the identification of areas of high water content, low porosity material (referred to as stiff sediment) and soft sediment (Section 5.3.1). Properties of subglacial

landforms were identified to vary between low porosity material and soft sediment (Section 5.3.1.1).

- Repeated radar lines reveal high local erosion rates of $1 \, \text{m a}^{-1}$ (Section 6.2.6), which includes the extensive erosion of the downstream end of a landform (over 2.5 km) (Chapter 6.2.6.1).

- The upstream end of the Bump is surrounded by a moat, which is inferred to continue for 10.5 km (Section 7.3.4.1).

- Detailed topography of subglacial landforms, including their up- and downstream ends revealed a variety of landform shapes on the bed, some symmetric, others asymmetric.

In the following, outcomes of these analyses are combined with findings from other studies to evaluate the current understanding of subglacial properties and their link to ice flow (Section 8.1) and to the elongation of landforms (Section 8.1.1.1). In particular, Section 8.1.2.1 discusses implications for the future stability of the ice flow of RIS. Considering the detailed images received of the subglacial environment, theories of landform formation are evaluated and tested (Section 8.2.3).

8.1 Bed Properties Beneath RIS and Basal Dynamics

The analysis of surface-radar reflectivity calculated for the bed (Chapter 5) revealed a combination of basal properties over the 14.5×18 km area (Figure 8.1). The bed consists of alternations of low porosity material (black and grey coloured areas), which is possibly non-deforming, and soft (brown areas), deforming sediment across the flow. The existence of deforming and non-deforming sediment and therefore a partitioning of flow between basal sliding and basal deformation was confirmed from several studies on RIS (King *et al.*, 2009; Smith, 1997a,b; Smith & Murray, 2009; Smith *et al.*, 2007) and from the palaeo record (Piotrowski *et al.*, 2004). However, data analysed in this thesis show that spatial variation of properties beneath RIS is more complex than previously assumed (King *et al.*, 2009), with properties varying along and across flow (see Figure 8.1). To highlight differences in the spatial extent of low porosity material in this and other studies, low porosity material is coloured in black and grey in Figure 8.1. Areas that are

Figure 8.1: Summary of basal environment of RIS. a) Composition of the bed beneath RIS as interpreted in Chapter 5. Low porosity material is divided into two colours; low porosity confirmed by active and passive seismics (black coloured areas), no information from active and passive seismics (grey coloured areas). The pink (b) and blue (c) boxes show zooms on the upstream end of the Bump and the boundary, respectively.

interpreted to consist of low porosity material in this thesis and in other studies (e.g., acoustic impedance data in Smith & Murray (2009); Smith *et al.* (2007)), which also coincides with spatial variation in topography, are coloured in black. The low porosity material interpreted in both areas (grey and black) implies these regions of the bed to be dominated by basal sliding. However, passive and active seismic surveys were focused on the area around the boundary. Information about basal microseismicity, which could support the idea of changes in basal motion in the eastern and western valleys, is not available. The idea of bands of low porosity sediment, and therefore higher basal drag, is consistent with findings beneath MacAyeal Ice Stream (former Ice Stream E), where bands of higher basal drag (several kilometres in length and width), referred to as "sticky strings" were identified (MacAyeal *et al.*, 1995). The dimensions of these sticky strings are comparable to the area of low porosity material identified in the eastern and western valleys of RIS (Figure 8.1 MacAyeal *et al.*, 1995).

Differences between the boundary drawn by King *et al.* (2009) and the area interpreted to consist of low porosity material in this thesis imply that the interpretation of the boundary should be altered to fit the extent of the low porosity material (shown as the black dashed line in Figure 8.1). The amount of microseismicity located downstream of the boundary (Figure 8.2) together with findings by Kufner *et al.* (2021), imply a mixture of sediment in this region. More microseismic events are located in the western sliding area, compared to the eastern sliding area, which is consistent with interpretations of Chapter 5, that bed properties in the western sliding area are more diverse, compared to the eastern sliding area.

8.1.1 Basal Conditions and Their Influence on Ice Flow

Fast-flowing ice streams, like RIS, often have low driving stress. To facilitate fast flow, the resistance at the bed must be low, which can be achieved by basal lubrication. Fast basal sliding is attributed to lubricating water at the bed (Cuffey *et al.*, 1999; Rose, 1979), while fast flow over a deforming bed is attributed to the deformation of soft, water-saturated sediment (Alley *et al.*, 1986). Clearly, water is a key component for fast flow. Furthermore, Vaughan *et al.* (2003) stated that basal drag beneath ice steams is highly dependent on the porosity of the subglacial material. They calculated higher basal shear stress for ice streams underlain by lodged sediment (e.g., Carlson Inlet), which are flowing slower compared to fast-flowing ice streams (e.g., Evans Ice Stream) underlain by dilated sediment and
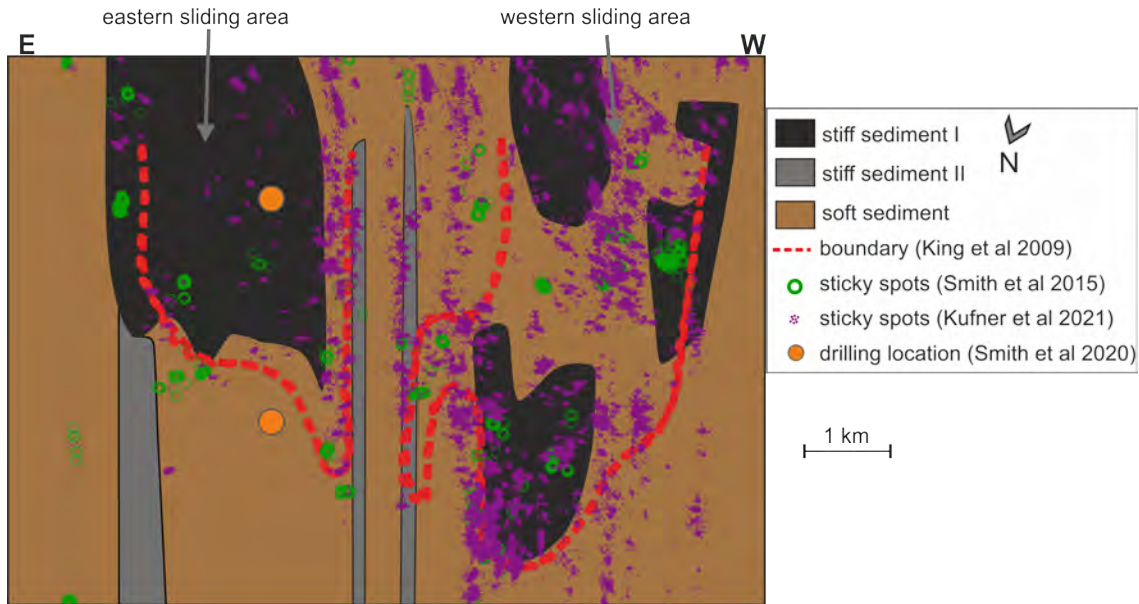
Figure 8.2: Comparison of interpretations of bed composition (Chapter 5) and the boundary between stiff and soft sediment by King *et al.* (2009) (red dashed line) and the occurrence of sticky spots by Kufner *et al.* (2021) and Smith *et al.* (2015).

low basal shear stress. RIS which is underlain by a mixture of dilated (high porosity) and lodged sediment (low porosity), was calculated to have a higher shear stress compared to Evans Ice Stream, which is consistent with the slower ice flow velocity of RIS.

Although numerous locations of sticky spots (areas of enhanced basal drag) (Kufner *et al.*, 2021; Smith, 2006; Smith *et al.*, 2015) were identified around the boundary defined by King *et al.* (2007), only little spatial correspondence between sticky spots and the surface velocity was found (Smith, 1997a). This is consistent with modelling results by Raymond (2007), showing that short scale (few ice thicknesses) variations in surface flow velocity of RIS are attributed to variations in basal topography rather than variations in basal lubrication.

8.1.1.1 Basal Properties and Influence on Subglacial Landforms

Stokes *et al.* (2007) suggested a deviation of landform orientation and the termination of landforms in areas of sticky spots due to increased basal drag. Apart from the Bump all landforms terminate at the boundary. However, landforms are present downstream of the boundary (although their length is drastically reduced) as well as in the area of low porosity material in the eastern and western

valley (Figure 8.1 a). Furthermore, the orientation of landforms located in the area of low porosity material does not deviate strongly from landforms further upstream, which implies no deviation in ice flow over the area of low porosity material and the sticky spots. The slip direction of sticky spots was identified to be predominantly parallel, with some events orientated towards the east (Kufner et al., 2021). The latter was attributed to flow-oblique deformation during the formation of landforms or by local distortion of the stress regime at outcropping bedrock (Kufner et al., 2021). The lack of landform-orientation deviations implies that variations in basal drag in this area are not sufficiently high to deviate ice flow. However, the variation clearly has an influence on landform size.

Drumlins and MSGLs were proposed to be part of a continuum (e.g., Ely et al., 2016; Stokes et al., 2013), with MSGLs representing an extension of drumlins. Drumlins are assumed to be present in areas of lower ice flow velocity, therefore presumably further upstream, compared to further downstream, where ice flow is expected to be accelerated, and MSGLs occur. This hypothesis applies to the landforms beneath RIS, with drumlins located in the onset region (Figure 8.3 a; King et al., 2007) and several km long MSGL located further downstream (Figure 8.3 b & c). The high-resolution 3D dataset presented in this thesis also resolved small landforms located in the area of stiff sediment (downstream of the boundary, Figure 8.3 c). Their elongation classifies these as MSGLs; however, their length is limited to 200–300 m. No significant variation in ice surface velocity were reported between upstream and downstream of the boundary. This implies not only ice flow velocity to influence the landform length but basal properties as well. This is consistent with findings by Graham et al. (2009) who found that landform signature is dependent on basal conditions. Areas of shorter landforms are interpreted to be indicative of sticky spots (Stokes et al., 2007). Together with findings from Clyne et al. (2020) and Holschuh et al. (2020), the results of this thesis highlight that landform length is dependent on ice flow velocity and basal properties as well as basal topography.

8.1.2 External vs. Internal Influences on Ice Dynamics

Several studies on the Siple Coast ice streams found oscillations between stagnation and reactivations, accompanied by variability of grounding line position and shear margin position (e.g., Catania et al., 2012, 2006; Stearns et al., 2005) which are interpreted to have been ongoing since the Last Glacial Maximum (Anderson

	a	**b**	**c**
sediment stiffness	soft sediment	soft sediment	stiff sediment
flow mechanism	basal deformation	basal deformation	basal sliding
ice flow velocity	~72 m a^{-1}	~377 m a^{-1}	~377 m a^{-1}
length & height landforms	1.5 km long 74 m high	in places > 14 km long 10-50 m high	<300 long 3-5 m high
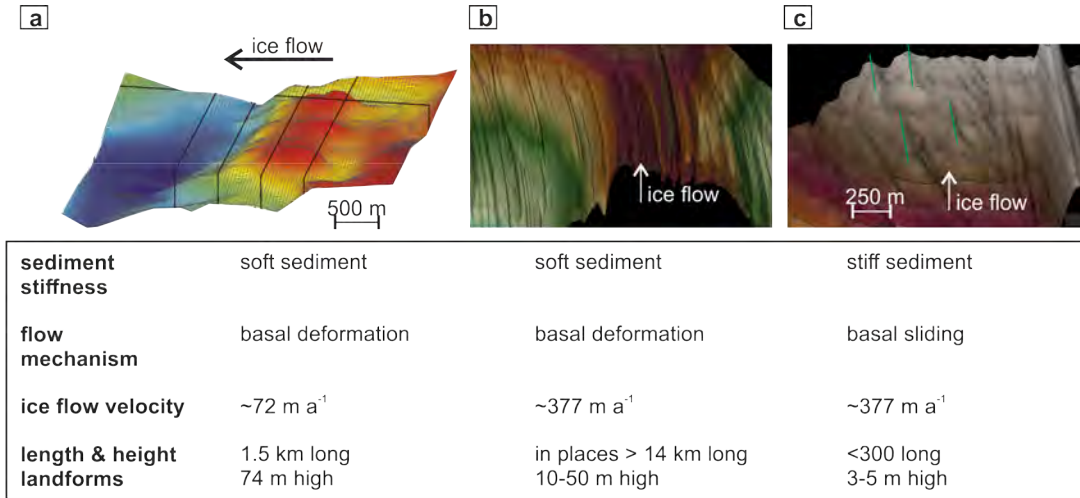
Figure 8.3: Subglacial landforms in the (a) onset region of the RIS (King *et al.*, 2007) and (b) & (c) ~40 km upstream of the grounding line. The green lines in (c) highlight small subglacial landforms. Ice flow velocities, bed properties and dimensions of landforms in (a) are taken from King *et al.* (2007) and King *et al.* (2004) and velocity in (b) and (c) is taken from Smith *et al.* (2007). Dimensions of landforms in panel c were measured from data acquired in 2017/18.

et al., 2002; Dowdeswell *et al.*, 2008; Mosola & Anderson, 2006). These variations in ice flow velocity are not linked to external forcing but are assumed to be mainly caused by variations in basal water and thermal conditions at the bed. Ice stream thinning can lead to changes in the thermal condition at the base, and a switch from basal melting to basal freezing, which removes water from the sediment and increases the sediment stiffness, which in turn increases the basal resistance due to the absence of a lubricating water layer to ice flow. The resulting slow down of ice flow will lead to an increase in ice thickness (Christoffersen & Tulaczyk, 2003; Hulbe & Fahnestock, 2004).

Figure 8.4 shows a selection of ice streams in West Antarctica, and analyses the influence of basal water and sticky spots on ice flow velocity. The figure comprises a schematic comparison of the different influences. Axes are neither to scale nor linear. The following gives a description of the conditions of the ice streams, while the ice streams are grouped geographically by the ice sheet or ocean into which they drain.

Ross Ice Streams

Kamb Ice Stream stagnated ~175 years ago (Retzlaff & Bentley, 1993) which
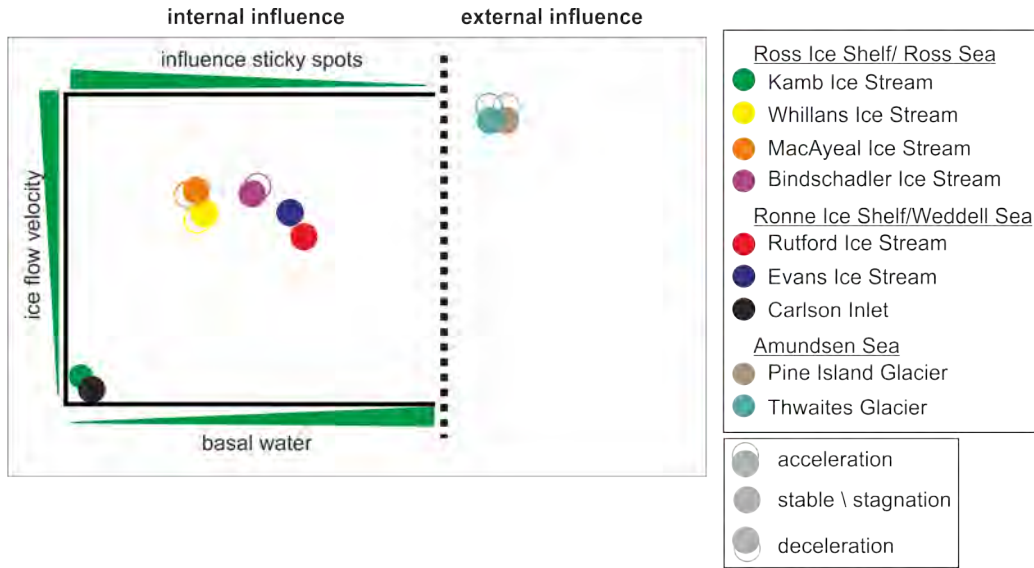
Figure 8.4: Evaluation of influence of sticky spots and basal water on ice flow velocity of a selection of West Antarctic Ice Streams. This represents a non-quantitative comparison of the different influences; axes are neither to scale nor linear.

was attributed to increased basal resistance from a sticky spot, composed of de-watered till. The neighbouring Whillans and MacAyeal Ice Streams are currently experiencing a slow down (Joughin & Bamber, 2005; Stearns *et al.*, 2005), which is attributed to increased drag by sticky spots, attributed to a decrease in basal water. Modelling of the future flow of Whillans Ice Stream predicts a shut down in the next century if trends of slow down and thickening of the ice stream are not reversed (Bougamont *et al.*, 2003; Joughin & Bamber, 2005). Contrary to this, Bindschadler Ice Stream is experiencing an increase in ice flow velocity, which is possibly driven by an increase in basal water and therefore enhanced lubrication at the bed (Scheuchl *et al.*, 2012).

Ronne Ice Streams

Observations over several decades confirmed the stability of ice flow velocity for RIS. Indications of accelerating or decelerating ice flow of Evans Ice Stream are missing. Modelling studies infer the influence of sticky spots on both ice streams (Joughin *et al.*, 2006). For Evans Ice Stream, a sticky spot was interpreted to consist of de-watered till (Ashmore & Bingham, 2014). Carlson Inlet, which is adjacent to RIS, has similar geometry and therefore driving stress to RIS but is stagnant and was suggested to be a relict ice stream (Vaughan *et al.*, 2008).

The stagnation of Carlson Inlet is attributed to loss of lubricating basal water. Estimations on when Carlson Inlet stagnated vary between 240 (Vaughan *et al.*, 2008) to 3500–6800 years ago (King, 2011).

Amundsen Sea Ice Streams

Pine Island Glacier and Thwaites Glacier both show an acceleration of ice flow which is attributed to ocean forcing, due to loss of resistance at the grounding line (Section 1.1.2).

The fast ice flow of ice streams in Antarctica is attributed to their lubrication by basal water. Basal water is either generated locally (e.g., melting at sticky spots) or produced in the upstream region. Part of the water under RIS and Whillans Ice Stream is proposed to originate from enhanced water piracy from the neighbouring Carlson Inlet and Kamb Ice Stream, respectively (Catania *et al.*, 2012; Vaughan *et al.*, 2008). Rerouting of water under Carlson Inlet might occur if RIS thickens, which might lead to a reactivation of Carlson Inlet concomitant with a slow down on RIS (Vaughan *et al.*, 2008). Figure 8.4 implies the influence of sticky spots to be inversely linked to the basal water. However, the ice thickness has an important control on the thermal state at the bed. Nevertheless, Carlson Inlet demonstrates a first-order dependence on basal water availability.

Consider the end members of this illustration: Ice flow variations of Siple Coast ice streams are dominated by internal forces and water piracy of neighbouring ice streams (Catania *et al.*, 2012), whereas variations of Pine Island and Thwaites Glacier are driven by external forces (oceanic and climatic). Ice streams draining into the Ronne Ice Shelf appear to lie between these two extremes. In the current state neither is known to be significantly influenced by climatic forcing nor water piracy. Even though the neighbouring Carlson Inlet is hypothesised to represent a relict ice stream that stagnated due to water piracy towards RIS. If the latter hypothesis proves true, the timescale involved in temporal changes in dynamics of RIS is much lower compared to the timescale of changes observed for Siple Coast ice streams. The following section evaluates the possible prognosis for the future stability of RIS.

8.1.2.1   Future Stability of *Rutford Ice Stream*

Under current conditions, the ice flow of RIS is considered as stable (Gudmundsson, 2007; Gudmundsson & Jenkins, 2009; Pralong & Gudmundsson, 2011). However, temporal changes in water pressure or the erosion of soft sediment might cause variations in basal drag. In the following, both of these processes are evaluated.

Removal of Soft Sediment

High erosion rates beneath Pine Island Glacier were proposed to possibly expose crystalline bedrock to the ice base within a few decades, and as a consequence it is assumed that the ice flow velocity will decrease due to increased basal drag (Smith *et al.*, 2012). Erosion rates beneath RIS calculated in Chapter 6 are as high as found beneath Pine Island Glacier ($\sim 1\,\mathrm{m\,a^{-1}}$). However, areas of erosion found beneath the RIS are spatially isolated and occur locally and do not show the removal of an area of large spatial extent. A complete removal of the soft sediment under the RIS in the next few decades is less likely.

Temporal Variation in Bed Stiffness

Consistent with observations from the Siple Coast ice streams, Piotrowski *et al.* (2004) suggested temporal variability of sediment stiffness caused by variations in water pressure. Although hot-water drilling on RIS (Smith *et al.*, 2021) as well as on other ice streams (Whillans, Kamb, Bindschadler Ice stream; Engelhardt & Kamb, 1997; Kamb, 2001) indicates that the overall water pressure at the bed is close to the ice overburden pressure, local variations in water pressure (Engelhardt & Kamb, 1997) can drive stiff spots to grow and shrink and therefore be the main control on stick-slip behaviour of ice flow (Boulton *et al.*, 2001). Furthermore, temporal variations in basal water pressure induced by tidal forcing were modelled to penetrate to the study area of this thesis (Rosier *et al.*, 2015).

Sediment stiffness was interpreted over a 30 year period under RIS by repeated acoustic impedance measurements (Smith, 1997b; Smith & Murray, 2009; Smith *et al.*, 2007). Within this period, local changes in sediment stiffness were observed after 7 years over a length of $\sim 800\,\mathrm{m}$, which were attributed to de-watering and compaction of sediment (Smith & Murray, 2009; Smith *et al.*, 2007). No further change in sediment stiffness was observed during subsequent studies in this area. Furthermore, the remaining part of the bed along the seismic line ($\sim 2.5\,\mathrm{km}$) shows

no temporal variation in stiffness (Smith *et al.*, 2007). Temporal consistency at the bed is also consistent with the stability of ice flow (Gudmundsson & Jenkins, 2009; Pralong & Gudmundsson, 2011).

The question remains: what makes RIS less susceptible to internal and external forces compared to the Siple Coast ice streams and Pine Island and Thwaites Glacier? The flow variability of the Siple Coast ice streams is attributed to the interaction of adjacent ice streams (in the trunk or the ice plains), which is facilitated by the shallow basal topography (ice thickness ∼1000 m). In contrast, the basal topography of RIS is characterised a deep trough (Figure 2.5), which, together with the higher ice thickness of RIS (∼2000 m) results in a higher driving stress. Furthermore, small-scale variations in basal drag beneath RIS are attributed to variations in basal topography rather than variations in basal lubrication (Raymond, 2007). Variations in basal drag, caused by the enlargement or reduction of sticky spots, are therefore unlikely over decadal timescales (Gudmundsson & Jenkins, 2009), which makes RIS very different to the Siple Coast ice streams. Concerning the effect of external climate forcing on the dynamics, modelling of ocean circulation beneath the Ronne Ice Shelf (Jenkins *et al.*, 2006) implied that there is a lack in significant seasonal variation in melt at the grounding line, which could initiate a retreating grounding line due to enhanced melt.

Combining these observations, the stability of the ice flow of RIS can be attributed to the geometry of the RIS and the limited potential for external (oceanic and climatic) forcing to influence the ice flow under the current setting (Gudmundsson & Jenkins, 2009) and only localised erosion of soft sediment.

8.2 Landforms and Moat Beneath RIS

8.2.1 Properties of Subglacial Landforms

Landform properties vary across the bed, with some landforms consisting[4] of low porosity material (white lines in Figure 8.1) while others are interpreted to consist of soft sediment (black and yellow lines). The latter was also confirmed from acoustic impedance measurements across some landforms (Smith & Murray, 2009; Smith *et al.*, 2007). Sediment porosities along some landforms e.g., the Bump and "new" drumlin, imply a harder upstream end (brown colour) and softer sediment further downstream (Section 5.3.1.1). However, calculated porosities lie within the range of deforming sediment (porosity = 0.3–0.5) along the whole crest, except for areas that are interpreted to consist of soft sediment overlain by a water body (blue coloured area). The interpretation of a harder upstream end and a soft tail of subglacial landforms as well as water on the crest of some landforms is consistent with findings from Thwaites Glacier (Clyne *et al.*, 2020; Holschuh *et al.*, 2020) as well as the palaeo record (McCabe & Dardis, 1994).

Figure 8.6 shows a schematic that could explain the existence of a harder upstream end and the occurrence of water along the crest of landforms. The driving force of the ice flow against an obstacle, in this case, the upstream end of the landform, will create a high-pressure area. Sediment at the upstream end of landforms will be compressed which results in a pore space reduction and drainage of pore water. The size of this high-pressure area is dependent on the geometry of the landform, but also on the elastic properties of the sediment (Craig, 2004; Yilmaz, 2001). The compression of the sediment will decrease with distance to the upstream end, which will result in an increase in porosity along the landform. During the extension of the "new" drumlin the deposition of soft sediment onto low porosity material was observed (Smith & Murray, 2009; Smith *et al.*, 2007). Underlying low porosity material possibly represents a non-permeable material or material with low permeability, which might create a sealed system. Water trapped in the landform would possibly be routed to areas of lower ice overburden pressure, in this case, the crest of landforms. Differences in sediment composition of landforms and the surrounding area might explain the absence of water

---

[4]As the radar energy likely does not penetrate much into the landform and no sub-bed reflections are recorded, results from reflectivity analysis can only provide information about the top most sediment layer. For simplicity, the term "consists of" rather than "is covered by and possibly consists of" is chosen here.
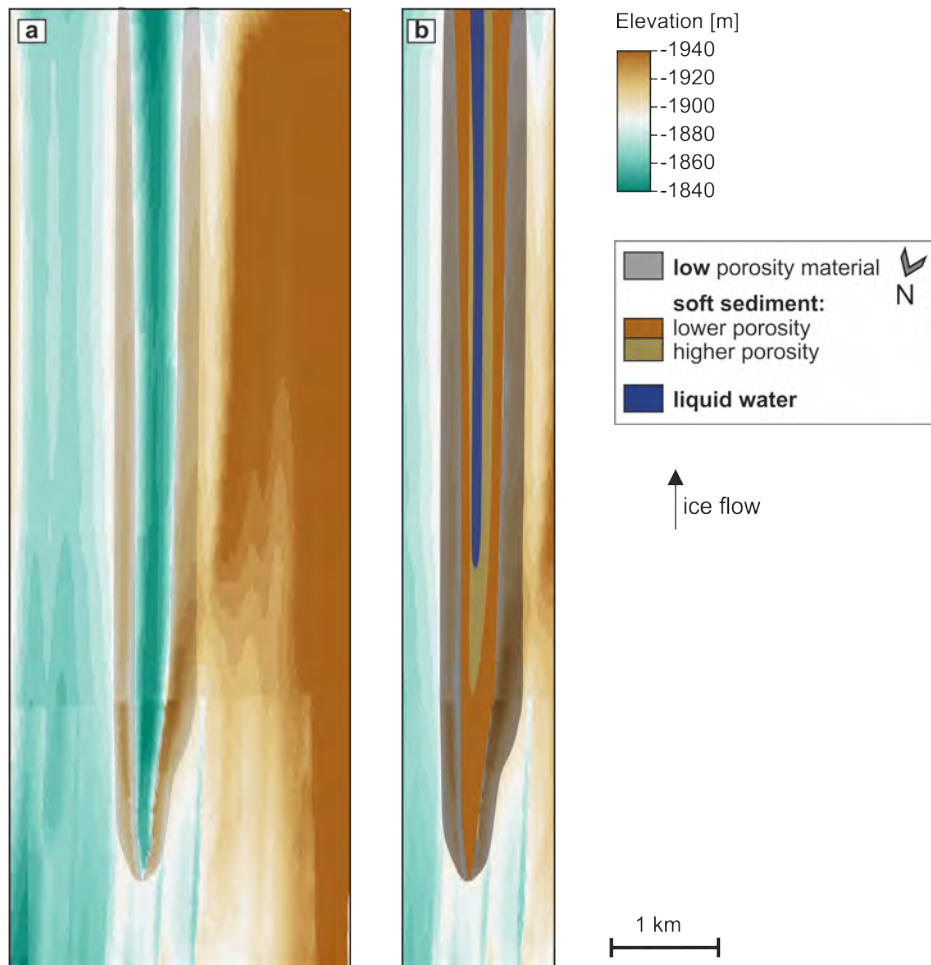
Figure 8.5: Interpretation of properties along the Bump. a) Topography of the Bump, with the moat around the Bump shaded in grey. b) Interpreted sediment properties along the Bump according to results of reflectivity analysis described in Section 5.3.1.1.

layers on other landforms, where water can possibly drain into deeper layers. Furthermore, a water layer was identified on landforms that are shorter than the dimension of the grid. The dimension of the landform therefore possibly relates to the existence of a water layer. However, modelling including variations in sediment porosities, permeability and the exact topography of landforms is needed to prove this hypothesis.
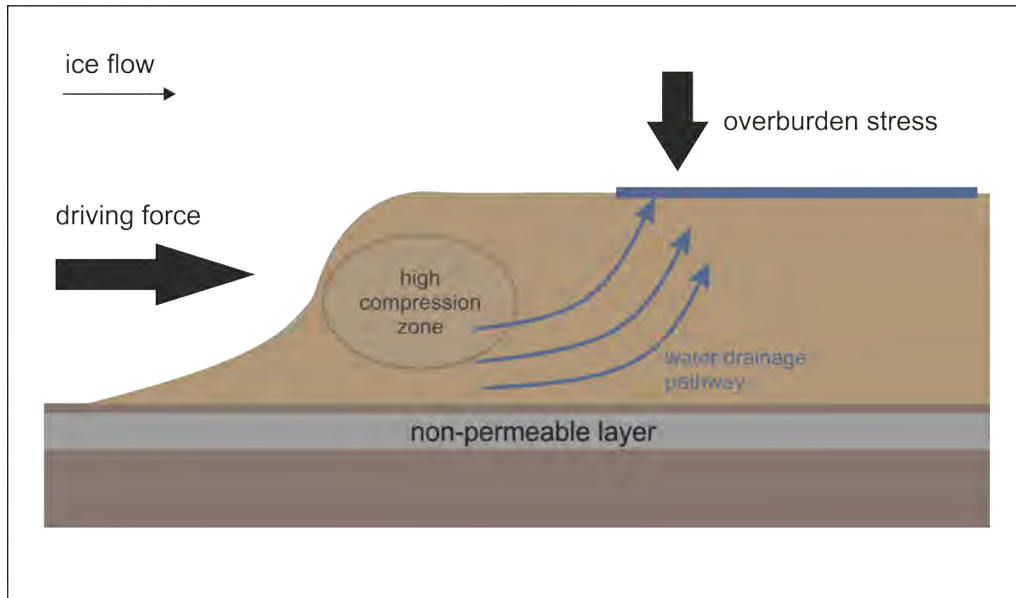
Figure 8.6: Schematic illustrating the hypothesis that pressure-perturbations caused by flow against landforms might cause variations in landforms properties and water content along flow, if these landforms are deposited on a non-permeable layer.

8.2.2 Properties of Moat Around the Subglacial Landforms

3D high-resolution data reveal a moat around the upstream end of the Bump, continuing for about 10.5 km along the Bump. The moat is interpreted to result from erosion of material (indicated by the truncated landforms upstream of the moat), which results in the exposure of low porosity material along the moat (Figure 8.5 b). The occurrence of moats consisting of low porosity material is consistent with findings in the marine record (Larter *et al.*, 2019), as well as beneath contemporary ice streams (Holschuh *et al.*, 2020). The existence of low porosity material in the moat beneath RIS is consistent with recent work by Kufner *et al.* (2021), who identified sticky spots along the moats of landforms (Figure 8.1 b and 8.2). Furthermore, the occurrence of low porosity material in the moat surrounding the Bump supports the hypothesis of a less permeable or possibly non-permeable material underneath the Bump (Figure 8.6). A moat was only identified around the Bump. This might be linked to the limited existence of 3D data available around the upstream ends. The 2D processed data, which is spaced at 500 m, do not provide sufficient coverage and horizontal resolution

227

to resolve such a feature. Nevertheless, no obvious moat was found around the upstream end of another subglacial landform that is also located within the 3D high-resolution grid (left edge of Figure 7.11). This might imply a link between the existence of the moat and the size of the landform, as the Bump is the landform with the greatest topographic relief in the study area.

8.2.3 Implications for Mechanisms of MSGL and Moat Formation Beneath RIS

The following tests possible formation mechanisms for landforms and the moat around the Bump, and evaluate their consistency with observations beneath RIS. Analysis by King *et al.* (2009) revealed the groove ploughing hypothesis to be inconsistent with observations beneath RIS. Therefore this theory is not further discussed here. The findings in this thesis revealed some new detail of the landforms including the existence of the moat around the Bump. However, it is not clear if the erosion of the moat and the formation of landforms, specifically the Bump, constitute the result of one process or if both represent individual processes, possibly with a time offset. In the following, four ideas of landform and moat formation are discussed. First the possibility of formation by instability theory. Second, the formation of landforms and the erosion of the moat caused by a meltwater event. Third, formation by soft sediment deformation around an obstacle. And finally, the coupled formation of the landforms and the moat by pressure perturbation.

- The instability theory proposed by Schoof & Clarke (2008) models the formation of landforms with a formation time of 1800 years. This is contradictory to the extension of a landform within a 7 years time beneath RIS. Furthermore, Holschuh *et al.* (2020) highlighted that instability theories, aim to reproduce landforms in a regular pattern. However, landforms beneath RIS and other ice streams (Holschuh *et al.*, 2020) are variable in size and composition. For instance, the small landforms that seem to be truncated by the moat show very different geometries to the Bump. This questions whether an instability theory would be capable of producing such different features.

- Erosion by meltwater could be caused by a catastrophic discharge of basal water (Graham *et al.*, 2009; Larter *et al.*, 2019; Shaw, 1994) or processes

linked to localised meltwater during deglaciation (Ó Cofaigh *et al.*, 2005). Either option seems less likely beneath RIS for various reasons mostly discussed in King *et al.* (2009), such as the hydraulic head, lack of surface speed up during the extension of the "new" drumlin and lack of sufficient water for a catastrophic event. An additional argument against a catastrophic event is the occurrence of small landforms which are truncated by the moat. These landforms, which are interpreted to consist of soft sediment, would have been eroded by a catastrophic flood event. Furthermore, analysis beneath Thwaites Glacier revealed incompatibilities between subglacial landform orientations and predicted subglacial water pathways but consistency of landform orientation and the ice flow direction. Following these observations the main driver in initiating the development of landforms beneath Thwaites Glacier was interpreted to be ice, not water (Holschuh *et al.*, 2020).

- The theory by Clark (1993) of soft sediment deformation was reported to fit most of the observations made on contemporary and palaeo ice stream bed (Stokes, 2018). At least some of the landforms beneath RIS are interpreted to consist of soft sediment (Section 5.3.1.1; Smith & Murray, 2009; Smith *et al.*, 2007). Furthermore, the observation of the extension of the "new" drumlin, therefore the attenuation of a landform, confirms the principle of this theory. Nevertheless, this theory requires a rigid obstacle, which acts as a seeding point of a landform. Reflectivity analysis indicates the upstream end of some landforms to be harder when compared to sediment further downstream, which could imply the core of the upstream end to consist of a rigid material. However, seismic impedance measurements along the upstream end of landforms are needed to investigate this further. Nevertheless, from surface-radar data, which only gives information about the top layer of sediment, a rigid obstacle at the upstream end of landforms can not be excluded.

- The erosion of the moat beneath Thwaites Glacier was linked to enhanced coupling of the bed and the ice due to high pressure upstream of the landforms (Holschuh *et al.*, 2020). This enhanced coupling is assumed to remove sediment upstream of and around the landform (Alley *et al.*, 2019, 2021;

Holschuh *et al.*, 2020). Material that was eroded can then possibly get deposited at the downstream end of the landform and extend the landform as the moat gets eroded. This is an interesting theory as the volume of the Bump is of a similar order to the volume of the moat in the upstream area; however, the volume of the Bump is a magnitude of order more compared to the volume of the moat further downstream. However, modelling results by Alley *et al.* (2021) indicate a limited length of the landform and the moat for this formation which might imply a combination of mechanisms that form the landforms and moats around landforms.

To the current stage, no individual theory can explain the variety of landforms as well as the timescale at which landform are shown to change on the bed of RIS. Furthermore, the existence of a long moat around the Bump complicates the formation processes. The truncation of landforms by the moat gives an indication of the relative chronology of subglacial processes. The erosion of landforms during the creation of the moat is consistent with observations of a constantly changing bed in other areas of RIS, such as shortening and extension of landforms (Section 6.1.1 Smith *et al.*, 2007) over decadal timescales. Further studies (including modelling) are needed to investigate a link between the formation of the Bump and the moat. Although a moat around landforms was stated to be indicative of a coupled formation of landform and moat by water (Graham & Hogan, 2016), this seems unlikely beneath RIS. With current knowledge, the enhanced coupling of sediment and ice, caused by pressure perturbations seems most likely for the formation of the moat and Bump. Additional deposition of material to form the Bump might be supplied by soft bed deformation, which appears to be a plausible theory for the formation of landforms that are not surrounded by moats.

8.3 Summary

Variations in landform length and the basal properties imply the length to be dependent on ice flow velocity, basal properties and topography. Basal drag from variation in bed properties beneath RIS is not sufficiently high to cause deviation of landforms but most landforms terminate in an area where basal properties change along flow. Ice flow of RIS is stable and is proposed not to undergo rapid changes in the near future due to its current insensitivity to external forces and the geometry which impede rapid variations in internal forces. Only one moat

surrounding a landform, which is interpreted as an erosional feature, was observed beneath RIS. Some of the landforms beneath RIS, with a length up to 17 km, contain a harder upstream end compared to the softer material further downstream. This pattern is possibly caused by pressure-perturbations causing compression at the upstream end and pore water migration to the ice-sediment interface, assuming a non-permeable layer beneath the landform. Although observations of landforms beneath RIS (timescale of formation, variety of properties and geometry) do not confirm an individual formation theory, a formation by pressure variation (Alley *et al.*, 2021) and soft bed deformation (Clark, 1993) is compatible with most of the observations.

Chapter 9

Conclusions and Recommendations for Further Work

In the following, a summary of the findings of this thesis with respect to the three research objectives are given (Section 9.1). Limitations of the work and suggestions for future work are given in Section 9.2. Finally, Section 9.3 offers conclusions to this thesis.

9.1 Review of Research Objectives

The combination of (1) a repeated (2007/08 and 2016/17) radar survey, (2) a radar dataset (2016/17) covering a relatively large portion of the ice stream and (3) a high-resolution dataset (2017/18) focusing on areas of interest, facilitated a quantitative and qualitative analysis of the topography and bed properties over a large area and with high detail. The analysis was focused on different research aims defined in Section 1.2. The outcomes from this thesis are summarised with respect to the three initial research objectives. To recap, the research objectives were:

1. **What is the spatial pattern of bed properties beneath RIS and how does this pattern modulate ice flow?** *Basal properties are variable along and across flow, with areas of low porosity material (porosity<0.1) presumably dominated by basal sliding and areas of high porosity material (porosity=0.3–0.5) presumably dominated by basal deformation. Variations*

in drag are not sufficient to cause surface flow variations (e.g., visible as crevasses at the surface), implying basal water pressure to be high in all areas on the bed.

The uncalibrated surface-radar reflectivity acquired in 2016/17 was combined with porosities inferred from seismic acoustic impedance to model sediment porosities along the radar grid. The combination of the spatial coverage of the surface-radar data and the constraints in bed properties from acoustic impedance enabled the interpretation of the distribution of bed properties over a wide area, at a scale normally only considered in satellite or offshore studies of deglaciated areas. Bed properties vary on a 100 m scale across flow, interpreted as areas of non-deforming material and areas of deforming sediment (Section 5.4). Spatial variation in the dominance of basal sliding and deformation over the bed was interpreted by previous studies (e.g., Kufner *et al.*, 2021; Smith *et al.*, 2015). However, the pattern identified in this thesis is more variable and complex than previously assumed, with areas consisting of soft sediment in a region previously interpreted as being dominated by basal sliding. The mixture of deforming and non-deforming sediment implies a complex pattern of basal drag and, therefore a combination of basal motion mechanisms on the bed of RIS. Spatial variation in bed properties and bed topography is reflected in the landform length (Section 7.4.2.1.2). Landforms terminate in areas of enhanced basal drag along flow, caused by variations in basal properties and topography. Smaller landforms (<300 m) were identified downstream and within the area of these variations. Long landforms (>10 km) are found in areas of limited variation in flow direction. Furthermore, the landforms in areas of higher basal drag do not show a deviation in orientation which implies the influence of variation in basal drag are small enough to modulate the mechanism of basal motion but do not cause deviation in ice flow direction over areas of higher basal drag (Section 8.1.1.1). This implies that the water pressure at the bed beneath RIS is high enough to facilitate fast sliding over harder bed (lubricated by a basal water) and sediment deformation of soft, water-saturated sediment.

2. **How mobile or stable is the bed beneath RIS and what are the possible implications for the stability of the ice flow?** *Erosion rates are high, but locally constrained, with most of the bed being stable. The*

complete removal of a soft sediment layer beneath RIS in the near future is less likely, which implies a future stability of the ice flow.

Repeated (9 years) surface-radar lines covering an 14.5×18 km area were analysed for topographic changes. Erosion occurred in 13 isolated locations, interpreted to consist of soft sediment, including the removal of the downstream end of a landform (therefore shortening of a landform). No deposition of material was observed. Consistent with basal motion partly accommodated by basal deformation of soft sediment, topographic changes were attributed to the erosion of soft sediment by soft bed deformation. The resulting local erosion rate was $1 \, \mathrm{m \, a^{-1}}$ and implied that the bed can be reorganized over short timescales. However, the observed changes were spatially constrained, which highlights the stability over most of the bed. Implications about the future stability of the RIS are discussed in Section 8.1.2.1, with the outcome that the overall temporal consistency of bed topography and properties implies only little temporal changes in basal drag, therefore highlighting the temporal stability of the flow of RIS. Nevertheless, the stability of the ice flow does not imply the bed to be static. The active extension of a landform (Smith & Murray, 2009; Smith *et al.*, 2007) and the shortening of a landform observed in this thesis imply the bed to be constantly mobile with subglacial landforms representing a dynamic part of the bed.

3. **What does the upstream and downstream end of landforms beneath RIS look like, and what are the implications for the formation process of landforms?** *Landforms beneath RIS are variable with respect to their shape, length and sediment properties. The upstream end of landforms vary between individual landforms, but the up- and downstream ends of landforms imaged along their whole length appear symmetric, with no obvious difference. None of the current formation theories can on its own explain the variety of landform properties found beneath RIS.*

Data compliant with 3D migration were acquired as part of this PhD project. These data were 3D processed and different attributes were calculated to enhance the visibility of small-scale features and discontinuities. The high-resolution images reveal a moat wrapped around the upstream end and along most of the length of the Bump (Section 7.4.2.2 and 7.3.4.1). This moat is interpreted to be eroded, which reveals low porosity material

around the landform. Reflectivity analysis along the moat gave no indication of water in the moat. The depth of the moat is comparable to the height of the Bump at the upstream end of the Bump. However, at the downstream end of the moat, the Bump is an order of magnitude higher than the moat. Small landforms which are truncated by the moat imply the erosion of these landforms during the formation of the moat. This highlights that landforms on the bed develop at different times. Combining the high-resolution data with data of higher spatial extent (14.5×18 km acquired in 2016/17) variations in landform composition across the bed were identified (Section 8.2.1). Some landforms are interpreted to be covered by, or consist of, sediment with lower porosity (porosity<0.3) compared to landforms consisting of soft sediment (porosity$=0.3$–0.5). Landforms with a length exceeding the dimensions of the grid (>14.5 km) show no significant variation in properties along flow. Landforms recorded along their entire length (e.g., the "new" drumlin) contain a harder upstream end when compared to the soft sediment interpreted along their crest (Section 5.3.1.1). Furthermore, some of these landforms contain a water body (<10 km length and <100 m width) along their crest. Effects of pressure-perturbations were proposed to cause the water body on the crest (Section 8.2.1), but, further studies are needed to validate this hypothesis. Different theories of landform and moat formation were tested in Section 8.2.3. However, incompatibilities between existing theories and observations in this thesis highlight that either a combination of processes created the landforms beneath RIS or existing theories need to be modified to fit the observations in this thesis.

9.2 Limitations of This Study and Suggestions for Future Research

The following includes suggestions for further investigations to (1) overcome limitations of the methods applied in this thesis and therefore test the conclusions of this thesis (Section 9.2.1 and 9.2.2), and (2) expand the knowledge received from this thesis (Section 9.2.3).

9.2.1 Limited Sampling of Bed Properties

One of the limitations of the bed properties inferred in this thesis is that solely using the surface-radar data only allows assumptions about the top layer of the sediment to be made. For instance, only properties of the top layer of landforms rather than the composition along the whole depth of the landform, can be analysed by surface-radar data due to the limited penetration of EM energy in high attenuation material (such as wet sediment). The analysis of seismic reflection data acquired along the upstream end of the Bump could be used to identify the composition of the Bump. Acoustic impedance values could confirm the existence of the harder upstream and possible sub-bed reflections might reveal more detail of the composition of the Bump and the transition of harder material into softer material. Furthermore, seismic data could possibly reveal if the Bump contains a rigid core at the upstream end of if only the top sediment layer is compressed due to for instance enhanced stresses at the upstream end.

9.2.2 Calibration of Surface-Radar Reflectivity

The calibration of surface-radar reflectivity with porosities inferred from seismic acoustic impedance revealed bed properties over a large spatial extent, with high horizontal resolution. Applying this technique to other areas would broaden the knowledge of spatial variation in bed properties (especially in areas where a calibration at an ice-water interface is not possible). However, this calibration approach is not a standard technique and further investigations could be used to validate this approach and possibly adopt the method to other surveys. Acquisition of a seismic line in the valleys of the RIS could confirm the existence of lower porosity material in this area and therefore validate the robustness of this method.

9.2.3 Further Suggestions

- This study showed how the detailed architecture of basal topography differs from the architecture inferred from previous studies, yet even the 3D methods used here were limited to a resolution of 24 m. A SAR approach to processing could add even more detail into the interpretation (Legarsky *et al.*, 2001; Paden *et al.*, 2010). As described in Section 3.3.1, the data

acquisition in 2017/18 aimed to create a dataset compliant with 3D migration and SAR processing. Nevertheless, one condition for the application of SAR processing and, therefore the implementation of the phase into the processing is the reliability of the phase recorded by the DELORES system. This could be tested e.g., by comparing the phase in areas of crossing radar lines, or by analysing the phase consistency of the system over time, while the system is static.

- From all the findings to date, it is not clear if water identified along the crest of some landforms is linked to their formation or is a result of interaction with ice flow. Water on the crest of landforms rather than in the troughs around them can not be explained by the hydraulic head. This implies that modelling of water routing has to include more components, such as the pressure field around landforms and variations in sediment properties within and amongst landforms. The detailed topography of the landforms should be used to model the effects of pressure-perturbation on the sediment consolidation (Section 8.2.1). The results of this could discern whether spatial variation of sediment properties and the water body along the crest of landforms is a result of ice flow or the formation. Furthermore, requirements for the existence of a water layer, such as a maximum landform length can be evaluated.

- The identification of the moat expanded the number of possible formation mechanisms for landforms. Following the theory by Alley *et al.* (2021), the Bump could partly consist of material eroded from the moat. So far, a moat was only observed around the upstream end of the Bump. This might be (1.) due to the lack of high 3D resolution data around other landforms, or (2.) because potentially a certain height or width of an obstacle or landform is a minimum requirement for the erosion of moats. To understand if the moat represents an isolated case, and is therefore possibly created by a different and individual process compared to other landforms, high-resolution data are required around the upstream end of other landforms. A 3D grid around the upstream end of the "new" drumlin, which is also a feature of high topographic relief, will help understand conditions of moat formation. Furthermore, a moat continuing to the area where the extension of the "new" drumlin was observed would imply a link between both and clearly eliminate water as a cause of the erosion.

- The amplitude and resolution of information on the geometry and properties as well as temporal variation in the length of landforms beneath RIS provide a rich foundation to test and adapt possible formation theories. In this thesis, a combination of soft bed deformation (Clark, 1993) and pressure variations causing decoupling (Alley *et al.*, 2021) is favoured to explain the formation of landforms and moats. However, modelling studies are mandatory to validate this, and evaluate if a combined model is capable of e.g., creating the observed length of landform and moat, depth of moat and landform height, variation in properties along and amongst landforms.

9.3 Conclusions

Surface-radar data covering a 14.5×18 km area and 3D imaging of 3×3 km grids covering the up- and downstream ends of subglacial landforms beneath RIS revealed the complex interplay between basal properties, subglacial landforms and the flow dynamics of RIS.

Variations in bed properties imply a combination of basal motion by deforming of porous, soft sediment and sliding over low porosity, non-deforming sediment at the bed of RIS. The pattern of dominance of either of these processes is more complex than previously assumed. The bed consists of numerous elongated landforms, classified by their elongation ratio as MSGLs. Observed spatial variation in landform length was attributed to variation in basal properties and basal topography. Landforms beneath RIS are depositional features (Smith & Murray, 2009; Smith *et al.*, 2007), which interact with the ice overriding these features. The resulting forces on the landforms together with heterogeneities in sediment are assumed to cause spatial variation of properties along the landforms and the creation of water bodies along the crest of some landforms. The observed shortening of a landform over 9 years, together with observations of landform extension over 7 years, highlight the mobility of the bed and imply landforms to be part of a constantly active system rather than a static component of the bed. Using 3D migrated data, a moat was identified around the upstream end and along the flanks of one landform. Small-scale features imply this moat to be eroded, exposing low porosity material to the ice-bed interface. The unprecedented detail with which basal landforms were imaged more than justifies the time-consuming

acquisition and processing of radar data. The resolution of this dataset is compliant with morphological analysis on DEMs from deglaciated areas. Furthermore, the combination of the high spatial coverage of the surface-radar data and the constraints in bed properties from acoustic impedance enabled the interpretation of the distribution of bed properties over a wide area at a scale normally only considered in satellite or offshore studies of deglaciated areas.

The data presented in this thesis form a good basis to test formation theories and compare landforms in deglaciated areas with landforms beneath RIS. These observations should motivate further studies of the basal properties of the RIS, specifically to explore the link between the spatial variation in sediment properties along landforms and the formation of landforms as well as possible links between the formation of landforms and the moat.

References

ADALGEIRSDÓTTIR, G., SMITH, A., MURRAY, T., KING, M., MAKINSON, K., NICHOLLS, K. & BEHAR, A. (2008). Tidal influence on Rutford Ice Stream, West Antarctica: observations of surface flow and basal processes from closely spaced GPS and passive seismic stations. *Journal of Glaciology*, **54**, 715–724. 26

ALLEY, R., BLANKENSHIP, D., ROONEY, S. & BENTLEY, C. (1989). Sedimentation beneath ice shelves — the view from ice stream B. *Marine Geology*, **85**, 101–120. 155, 156, 157

ALLEY, R., CUFFEY, K., EVENSON, E., STRASSER, J., LAWSON, D. & LARSON, G. (1997). How glaciers entrain and transport basal sediment: Physical constraints. *Quaternary Science Reviews*, **16**, 1017–1038. 156, 214

ALLEY, R.B. (1993). In search of ice-stream sticky spots. *Journal of Glaciology*, **39**, 447–454. 214

ALLEY, R.B., BLANKENSHIP, D.D., BENTLEY, C.R. & ROONEY, S.T. (1986). Deformation of till beneath ice stream B, West Antarctica. *Nature*, **322**, 57–59. 13, 214, 217

ALLEY, R.B., BLANKENSHIP, D.D., ROONEY, S.T. & BENTLEY, C.R. (1987). Continuous till deformation beneath ice sheets. *The Physical Basis of Ice Sheet Modelling (Proceedings of the Vancouver Symposium, August 1987)*, 81–92. 157

ALLEY, R.B., LAWSON, D.E., LARSON, G.J., EVENSON, E.B. & BAKER, G.S. (2003). Stabilizing feedbacks in glacier-bed erosion. *Nature*, **424**, 758–760. 17, 159

ALLEY, R.B., CUFFEY, K.M. & ZOET, L.K. (2019). Glacial erosion: status and outlook. *Annals of Glaciology*, **60**, 1–13. 155, 156, 229

ALLEY, R.B., HOLSCHUH, N., MACAYEAL, D.R., PARIZEK, B.R., ZOET, L., RIVERMAN, K., MUTO, A., CHRISTIANSON, K., CLYNE, E., ANANDAKRISHNAN, S., STEVENS, N. & GHOST COLLABORATION (2021). Bedforms of Thwaites Glacier, West Antarctica: Character and Origin. *Journal of Geophysical Research: Earth Surface*, **126**. 22, 229, 230, 231, 237, 238

ALSADI, H.N. (2017). 3D Seismic Reflection Surveying. In *Seismic Hydrocarbon Exploration*, 139–168, Springer International Publishing. 45

ANANDAKRISHNAN, S. & ALLEY, R.B. (1997). Stagnation of Ice Stream C, West Antarctica by water piracy. *Geophysical Research Letters*, **24**, 265–268. 15

ANANDAKRISHNAN, S., BLANKENSHIP, D.D., ALLEY, R.B. & STOFFA, P.L. (1998). Influence of subglacial geology on the position of a West antarctic ice stream from seismic observations. *Nature*, **394**, 62–65. 26

ANANDAKRISHNAN, S., VOIGT, D.E., ALLEY, R.B. & KING, M.A. (2003). Ice stream D flow speed is strongly modulated by the tide beneath the Ross Ice Shelf. *Geophysical Research Letters*, **30**, 1361. 15

ANDERSON, J.B., SHIPP, S.S., LOWE, A.L., WELLNER, J.S. & MOSOLA, A.B. (2002). The Antarctic Ice Sheet during the Last Glacial Maximum and its subsequent retreat history: a review. *Quaternary Science Reviews*, **21**, 49–70. 219

ANDREASSEN, K. & WINSBORROW, M. (2009). Signature of ice streaming in Bjørnøyrenna, Polar North Atlantic, through the Pleistocene and implications for ice-stream dynamics. *Annals of Glaciology*, **50**, 17–26. 5

ASHMORE, D.W. & BINGHAM, R.G. (2014). Antarctic subglacial hydrology: Current knowledge and future challenges. *Antarctic Science*, **26**, 758–773. 30, 86, 221

ASTRATTI, D., AARRE, D., VEJBÆK, O.V. & WHITE, G. (2015). Mapping and time-lapse analysis of South Arne Chalk fault network using new developments in seismic dip computation. *Geological Society Special Publication*, **406**, 331–358. 37

ATRE, S.R. & BENTLEY, C.R. (1993). Laterally varying basal conditions beneath ice streams B and C, West Antarctica. *Journal of Glaciology*, **39**, 507–514. 16, 25, 95, 97

ATRE, S.R. & BENTLEY, C.R. (1994). Indication of a dilatant bed near Downstream B Camp, Ice Stream B, Antarctica. *Annals of Glaciology*, **20**, 177–182. 95

BAMBER, J.L., RIVA, R.E., VERMEERSEN, B.L. & LEBROCQ, A.M. (2009). Reassessment of the potential sea-level rise from a collapse of the west antarctic ice sheet. *Science*, **324**, 901–903. 1

BENN, D. & EVANS, J. (2011). *Glaciers and Glaciation*. Routledge, 2nd edn. 1, 11, 12, 13, 14, 16, 17, 18, 46, 79, 131, 137, 156

BENNETT, M.R. & GLASSER, N.F. (2009). *Glacial geology: Ice sheets and landforms, 2nd edn.*. 5, Wiley-Blackwell, Cambridge. 13, 153

BENTLEY, C.R., LORD, N. & LIU, C.J. (1998). Radar reflections reveal a wet bed beneath stagnant Ice Stream C and a frozen bed beneath ridge BC, West Antarctica. *Journal of Glaciology*, **44**, 149–156. 79

BINDSCHADLER, R., CHOI, H., WICHLACZ, A., BINGHAM, R., BOHLANDER, J., BRUNT, K., CORR, H., DREWS, R., FRICKER, H., HALL, M., HINDMARSH, R., KOHLER, J., PADMAN, L., RACK, W., ROTSCHKY, G., URBINI, S., VORNBERGER, P. & YOUNG, N. (2011). Getting around Antarctica: new high-resolution mappings of the grounded and freely-floating boundaries of the Antarctic ice sheet created for the International Polar Year. *The Cryosphere*, **5**, 569–588. 2, 23

BINDSCHADLER, R.A. (2003). Tidally Controlled Stick-Slip Discharge of a West Antarctic Ice. *Science*, **301**, 1087–1089. 15

BINGHAM, R.G. & SIEGERT, M.J. (2009). Quantifying subglacial bed roughness in Antarctica: implications for ice-sheet dynamics and history. *Quaternary Science Reviews*, **28**, 223–236. 84

BINGHAM, R.G., KING, E.C., SMITH, A.M. & PRITCHARD, H.D. (2010). Glacial geomorphology: Towards a convergence of glaciology and geomorphology. *Progress in Physical Geography: Earth and Environment*, **34**, 327–355. 97

BINGHAM, R.G., VAUGHAN, D.G., KING, E.C., DAVIES, D., CORNFORD, S.L., SMITH, A.M., ARTHERN, R.J., BRISBOURNE, A.M., DE RYDT, J., GRAHAM, A.G.C., SPAGNOLO, M., MARSH, O.J. & SHEAN, D.E. (2017). Diverse landscapes beneath Pine Island Glacier influence ice flow. *Nature Communications*, **8**, 1618. 5, 201, 214

BJÖRNSSON, H. (1996). Scales and rates of glacial sediment removal: a 20 km long, 300 m deep trench created beneath Breidamerkurjökull during the Little Ice Age. *Annals of Glaciology*, **22**, 141–146. 159

BLANKENSHIP, D.D., BENTLEY, C.R., ROONEY, S.T. & ALLEY, R.B. (1986). Seismic measurements reveal a saturated porous layer beneath an active Antarctic ice stream. *Nature*, **322**, 54–57. 13

BLANKENSHIP, D.D., BENTLEY, C.R., ROONEY, S.T. & ALLEY, R.B. (1987). Till beneath ice stream B: 1. Properties derived from seismic travel times. *Journal of Geophysical Research*, **92**, 8903–8911. 13, 16, 25, 78, 95, 214

BOGODOROSKY, V., BENTLEY, C. & GUDMANDSEN, P. (1985). *Radioglaciology*. Dordrecht, Reidel Publishing Co. 33, 82, 284

BOOTH, A.D., CLARK, R.A., KULESSA, B., MURRAY, T., CARTER, J., DOYLE, S. & HUBBARD, A. (2012). Thin-layer effects in glaciological seismic amplitude-versus-angle (AVA) analysis: implications for characterising a subglacial till unit, Russell Glacier, West Greenland. *The Cryosphere*, **6**, 909–922. 207

BOUGAMONT, M., TULACZYK, S. & JOUGHIN, I. (2003). Numerical investigations of the slow-down of Whillans Ice Stream, West Antarctica: is it shutting down like Ice Stream C? *Annals of Glaciology*, **37**, 239–246. 221

BOULTON, A.G.S., DENT, D.L., MORRIS, E.M., GEOGRAFISKA, S., SERIES, A. & GEOGRAPHY, P. (1974). Subglacial Shearing and Crushing, and the Role of Water Pressures in tills from South- East Iceland. *Geografiska Annaler. Series A: Physical Geography*, **56**, 135–145. 16

Boulton, G. (1972). The role of thermal regime in glacial sedimentation. *Polar Geomorphology 4. Special Publication*, 1–9. 12, 13

Boulton, G. (1996). Theory of glacial erosion, transport and deposition as a consequence of subglacial sediment deformation. *Journal of Glaciology*, **42**, 43–62. 155, 158

Boulton, G. & Dent, D.L. (1974). The Nature and Rates of Post-Depositional Changes in Recently Deposited Till from South-East Iceland. *Geografiska Annaler: Series A, Physical Geography*, **56**, 121–134. 16

Boulton, G. & Zatsepin, S. (2006). Hydraulic impacts of glacier advance over a sediment bed. *Journal of Glaciology*, **52**, 497–527. 132

Boulton, G., Dobbie, K. & Zatsepin, S. (2001). Sediment deformation beneath glaciers and its coupling to the subglacial hydraulic system. *Quaternary International*, **86**, 3–28. 154, 223

Boulton, G.S. (1976). The origin of glacially fluted surfaces - observations and theory. *Journal of Glaciology*, **17**, 287–309. 16

Boulton, G.S. (1987). A theory of drumlin formation by subglacial sediment deformation. *Drumlin symposium. Manchester, 1985*, 25–80. 157

Boulton, G.S. & Clark, C.D. (1990). A highly mobile Laurentide ice sheet revealed by satellite images of glacial lineations. *Nature*, **346**, 813–817. 4

Boulton, G.S. & Dobbie, K.E. (1993). Consolidation of sediments by glaciers: relations between sediment geotechnics, soft-bed glacier dynamics and subglacial ground-water flow. *Journal of Glaciology*, **39**, 26–44. 16

Boulton, G.S. & Hindmarsh, R.C.A. (1987). Sediment deformation beneath glaciers: Rheology and geological consequences. *Journal of Geophysical Research*, **92**, 9059–9082. 13, 14, 16, 26, 158

Boulton, G.S. & Jones, A.S. (1979). Stability of Temperate Ice Caps and Ice Sheets Resting on Beds of Deformable Sediment. *Journal of Glaciology*, **24**, 29–43. 14, 157

BRINER, J.P. (2007). Supporting evidence from the New York drumlin field that elongate subglacial bedforms indicate fast ice flow. *Boreas*, **36**, 143–147. 19, 201

BRISBOURNE, A.M., SMITH, A.M., VAUGHAN, D.G., KING, E.C., DAVIES, D., BINGHAM, R.G., SMITH, E.C., NIAS, I.J. & ROSIER, S.H. (2017). Bed conditions of Pine Island Glacier, West Antarctica. *Journal of Geophysical Research: Earth Surface*, **122**, 419–433. 201, 214

CATANIA, G., HULBE, C., CONWAY, H., SCAMBOS, T. & RAYMOND, C. (2012). Variability in the mass flux of the Ross ice streams, West Antarctica, over the last millennium. *Journal of Glaciology*, **58**, 741–752. 219, 222

CATANIA, G.A., CONWAY, H.B., GADES, A.M., RAYMOND, C.F. & ENGELHARDT, H. (2003). Bed reflectivity beneath inactive ice streams in West Antarctica. *Annals of Glaciology*, **36**, 287–291. 83

CATANIA, G.A., SCAMBOS, T.A., CONWAY, H. & RAYMOND, C.F. (2006). Sequential stagnation of Kamb Ice Stream, West Antarctica. *Geophysical Research Letters*, **33**, L14502. 78, 219

CHAPWANYA, M., CLARK, C.D. & FOWLER, A.C. (2011). Numerical computations of a theoretical model of ribbed moraine formation. *Earth Surface Processes and Landforms*, **36**, 1105–1112. 20

CHOPRA, S. & MARFURT, K.J. (2005). Seismic attributes — A historical perspective. *GEOPHYSICS*, **70**, 3SO–28SO. 79, 103, 108

CHORLEY, R.J. (1959). The shape of drumlins. *Journal of Glaciology*, **3**, 339–344. 4

CHRISTOFFERSEN, P. & TULACZYK, S. (2003). Response of subglacial sediments to basal freeze-on 1. Theory and comparison to observations from beneath the West Antarctic Ice Sheet. *Journal of Geophysical Research: Solid Earth*, **108**, 2222. 220

CHU, W., CREYTS, T.T. & BELL, R.E. (2016a). Rerouting of subglacial water flow between neighboring glaciers in West Greenland. *Journal of Geophysical Research: Earth Surface*, **121**, 925–938. 90

CHU, W., SCHROEDER, D.M., SEROUSSI, H., CREYTS, T.T., PALMER, S.J. & BELL, R.E. (2016b). Extensive winter subglacial water storage beneath the Greenland Ice Sheet. *Geophysical Research Letters*, **43**, 12,484–12,492. 136

CHURCH, G.J., BAUDER, A., GRAB, M., HELLMANN, S. & MAURER, H. (2018). High-resolution helicopter-borne ground penetrating radar survey to determine glacier base topography and the outlook of a proglacial lake. In *2018 17th International Conference on Ground Penetrating Radar (GPR)*, 1–4, IEEE. 44

CLARK, C.D. (1993). Mega-scale glacial lineations and cross-cutting ice-flow landforms. *Earth Surface Processes and Landforms*, **18**, 1–29. 4, 17, 18, 19, 29, 46, 200, 229, 231, 238

CLARK, C.D. (2011). Emergent drumlins and their clones: From till dilatancy to flow instabilities. *Journal of Glaciology*, **56**, 1011–1025. 4

CLARK, C.D., TULACZYK, S.M., STOKES, C.R. & CANALS, M. (2003). A groove-ploughing theory for the production of mega-scale glacial lineations, and implications for ice-stream mechanics. *Journal of Glaciology*, **49**, 240–256. 16, 17, 19, 155

CLARK, C.D., ELY, J.C., SPAGNOLO, M., HAHN, U., HUGHES, A.L. & STOKES, C.R. (2018). Spatial organization of drumlins. *Earth Surface Processes and Landforms*, **43**, 499–513. 214

CLARK, P.U. & POLLARD, D. (1998). Origin of the Middle Pleistocene Transition by ice sheet erosion of regolith. *Paleoceanography*, **13**, 1–9. 155, 156, 157

CLARKE, G.K. (2005). Subglacial Processes. *Annual Review of Earth and Planetary Sciences*, **33**, 247–276. 16, 78, 214

CLARKE, G.K.C. (1987). Fast glacier flow: Ice streams, surging, and tidewater glaciers. *Journal of Geophysical Research*, **92**, 8835–8841. 15

CLOUGH, J.W. (1977). Radio-Echo Sounding: Reflections From Internal Layers In Ice Sheets. *Journal of Glaciology*, **18**, 3–14. 306

CLYNE, E.R., ANANDAKRISHNAN, S., MUTO, A., ALLEY, R.B. & VOIGT, D.E. (2020). Interpretation of topography and bed properties beneath Thwaites Glacier, West Antarctica using seismic reflection methods. *Earth and Planetary Science Letters*, **550**. 79, 131, 137, 201, 202, 205, 219, 225

COOPER, M.A., JORDAN, T.M., SCHROEDER, D.M., SIEGERT, M.J., WILLIAMS, C.N. & BAMBER, J.L. (2019). Subglacial roughness of the Greenland Ice Sheet: Relationship with contemporary ice velocity and geology. *Cryosphere*, **13**, 3093–3115. 84, 85

COPLAND, L. & SHARP, M. (2001). Mapping thermal and hydrological conditions beneath a polythermal glacier with radio-echo sounding. *Journal of Glaciology*, **47**, 232–242. 78, 79, 83, 100, 107

CRAIG, R. (2004). *Craig's Soil Mechanics, 7th edn.*. CRC Press. 25, 100, 132, 225

CUFFEY, K. & PATERSON, W.S.B. (2010). *The Physics of Glaciers*. Butterworth-Heinemann, Oxford, 4th edn. 11, 14, 46

CUFFEY, K.M., CONWAY, H., HALLET, B., GADES, A.M. & RAYMOND, C.F. (1999). Interfacial water in polar glaciers and glacier sliding at -17C. *Geophysical Research Letters*, **26**, 751–754. 217

DANIELS, D. (1996). Surface-penetrating radar. *Electronics and Communication Engineering Journal*, **8**, 165–182. 34, 92

DAVIES, D., BINGHAM, R.G., KING, E.C., SMITH, A.M., BRISBOURNE, A.M., SPAGNOLO, M., GRAHAM, A.G., HOGG, A.E. & VAUGHAN, D.G. (2018). How dynamic are ice-stream beds? *Cryosphere*, **12**, 1615–1628. 6, 14, 29, 30, 214

DAVIS, J.L. & ANNAN, A.P. (1989). Ground-Penetrating Radar for High-Resolution Mapping of Soil and Rock Stratigrapphy. *Geophysical Prospecting*, **37**, 531–551. 30, 34, 46, 92, 94

DELF, R., SCHROEDER, D.M., CURTIS, A., GIANNOPOULOS, A. & BINGHAM, R.G. (2020). A comparison of automated approaches to extracting englacial-layer geometry from radar data across ice sheets. *Annals of Glaciology*, **61**, 234–241. 107

DIEZ, A., MATSUOKA, K., JORDAN, T.A., KOHLER, J., FERRACCIOLI, F., CORR, H.F., OLESEN, A.V., FORSBERG, R. & CASAL, T.G. (2019). Patchy Lakes and Topographic Origin for Fast Flow in the Recovery Glacier System, East Antarctica. *Journal of Geophysical Research: Earth Surface*, **124**, 287–304. 100

DOAKE, C.S.M., FROLICH, R.M., MANTRIPP, D.R., SMITH, A.M. & VAUGHAN, D.G. (1987). Glaciological studies on Rutford Ice Stream, Antarctica. *Journal of Geophysical Research*, **92**, 8951–8960. 5

DOAKE, C.S.M., CORR, H.F.J., JENKINS, A., MAKINSON, K., NICHOLLS, K.W., NATH, C., SMITH, A.M. & VAUGHAN, D.G. (2001). Rutford Ice Stream, Antarctica. In *The West Antarctic Ice Sheet: Behavior and Environment; Antarctic Research Series*, vol. 77, 221–235, American Geophysical Union. 16, 22, 46

DOWDESWELL, J.A., COFAIGH, C.Ó. & PUDSEY, C.J. (2004). Thickness and extent of the subglacial till layer beneath an Antarctic paleo–ice stream. *Geology*, **32**, 13–16. 13, 14

DOWDESWELL, J.A., OTTESEN, D., EVANS, J., COFAIGH, C.Ó. & ANDERSON, J.B. (2008). Submarine glacial landforms and rates of ice-stream collapse. *Geology*, **36**, 819–822. 220

DOWDESWELL, J.A., CANALS, M., JAKOBSSON, M., TODD, B.J., DOWDESWELL, E.K. & HOGAN, K.A. (2016). The variety and distribution of submarine glacial landforms and implications for ice-sheet reconstruction. *Geological Society, London, Memoirs*, **46**, 519–552. 79

DREIMANIS, A. (1993). Water-eroded crescentic scours and furrows associated with subglacial flutes at Breidamerkurjökull, Iceland. *Boreas*, **22**, 110–112. 21

DUSSAUGE-PEISSER, C., WATHELET, M., JONGMANS, D., HANTZ, D., COUTURIER, B. & SINTES, M. (2003). Investigation of a fractured limestone cliff (Chartreuse Massif, France) using seismic tomography and ground-penetrating radar. *Near Surface Geophysics*, **1**, 161–170. 30

EISEN, O., NIXDORF, U., WILHELMS, F. & MILLER, H. (2002). Electromagnetic wave speed in polar ice: Validation of the common-midpoint technique

with high-resolution dielectric-profiling and γ-density measurements. *Annals of Glaciology*, **34**, 150–156. 33, 284

ELY, J.C., CLARK, C.D., SPAGNOLO, M., STOKES, C.R., GREENWOOD, S.L., HUGHES, A.L., DUNLOP, P. & HESS, D. (2016). Do subglacial bedforms comprise a size and shape continuum? *Geomorphology*, **257**, 108–119. 19, 46, 79, 214, 219

ENDRES, A.L., MURRAY, T., BOOTH, A.D. & WEST, L.J. (2009). A new framework for estimating englacial water content and pore geometry using combined radar and seismic wave velocities. *Geophysical Research Letters*, **36**, 1–5. 97

ENGELHARDT, H. (1998). Basal sliding of Ice Stream B, West Antarctica. *Journal of Glaciology*, **44**, 223–230. 14, 29

ENGELHARDT, H. & KAMB, B. (1997). Basal hydraulic systetn of a West Antarctic ice streatn.: constraints frotn borehole observations. *Journal Glaciology*, **43**, 207–230. 12, 15, 223

ENGELHARDT, H., HUMPHREY, N., KAMB, B. & FAHNESTOCK, M. (1990). Physical conditions at the base of a fast moving Antarctic ice stream. *Science*, **248**, 57–59. 5, 15

EVANS, D.J., PHILLIPS, E.R., HIEMSTRA, J.F. & AUTON, C.A. (2006). Subglacial till: Formation, sedimentary characteristics and classification. *Earth-Science Reviews*, **78**, 115–176. 130, 132

EVANS, J., PUDSEY, C.J., ÓCOFAIGH, C., MORRIS, P. & DOMACK, E. (2005). Late Quaternary glacial history, flow dynamics and sedimentation along the eastern margin of the Antarctic Peninsula Ice Sheet. *Quaternary Science Reviews*, **24**, 741–774. 201

EVEREST, J., BRADWELL, T. & GOLLEDGE, N. (2005). Subglacial landforms of the tweed palaeo-ice stream. *Scottish Geographical Journal*, **121**, 163–173. 131

FALCINI, F.A., RIPPIN, D.M., KRABBENDAM, M. & SELBY, K.A. (2018). Quantifying bed roughness beneath contemporary and palaeo-ice streams. *Journal of Glaciology*, **64**, 822–834. 84

FERRACCIOLI, F. & JORDAN, T. (2020). Airborne magnetic data covering the Evans, and Rutford Ice Streams, and ice rises in the Ronne Ice Shelf (2006/07) (Version 1.0) [Data set]. UK Polar Data Centre, https:\\doi.org/10.5285/7504BE9B-93BA-44AF-A17F-00C84554B819. 133, 134

FISCHER, U.H. & CLARKE, G.K. (2001). Review of subglacial hydro-mechanical coupling: Trapridge Glacier, Yukon Territory, Canada. *Quaternary International*, **86**, 29–43. 157

FLOWERS, G.E. (2015). Modelling water flow under glaciers and ice sheets. *Proceedings of the Royal Society A: Mathematical, Physical and Engineering Sciences*, **471**, 20140907. 13

FOLEY, N., TULACZYK, S., AUKEN, E., SCHAMPER, C., DUGAN, H., MIKUCKI, J., VIRGINIA, R. & DORAN, P. (2016). Helicopter-borne transient electromagnetics in high-latitude environments: An application in the McMurdo Dry Valleys, Antarctica. *Geophysics*, **81**, WA87–WA99. 140

FORTE, E., PIPAN, M., CASABIANCA, D., DI CUIA, R. & RIVA, A. (2012). Imaging and characterization of a carbonate hydrocarbon reservoir analogue using GPR attributes. *Journal of Applied Geophysics*, **81**, 76–87. 103, 106, 108, 109

FOWLER, A.C. (2009). Instability modelling of drumlin formation incorporating lee-side cavity growth. *Proceedings of the Royal Society A: Mathematical, Physical and Engineering Sciences*, **465**, 2681–2702. 13

FOWLER, A.C. (2010). The formation of subglacial streams and mega-scale glacial lineations. *Proceedings of the Royal Society A: Mathematical, Physical and Engineering Sciences*, **466**, 3181–3201. 4

FOWLER, A.C. & CHAPWANYA, M. (2014). An instability theory for the formation of ribbed moraine, drumlins and mega-scale glacial lineations. *Proceedings of the Royal Society A: Mathematical, Physical and Engineering Sciences*, **470**, 20140185. 20

FRETWELL, P., PRITCHARD, H.D., VAUGHAN, D.G., BAMBER, J.L., BARRAND, N.E., BELL, R., BIANCHI, C., BINGHAM, R.G., BLANKENSHIP,

D.D., Casassa, G., Catania, G., Callens, D., Conway, H., Cook, A.J., Corr, H.F.J., Damaske, D., Damm, V., Ferraccioli, F., Forsberg, R., Fujita, S., Gim, Y., Gogineni, P., Griggs, J.A., Hindmarsh, R.C.A., Holmlund, P., Holt, J.W., Jacobel, R.W., Jenkins, A., Jokat, W., Jordan, T., King, E.C., Kohler, J., Krabill, W., Riger-Kusk, M., Langley, K.A., Leitchenkov, G., Leuschen, C., Luyendyk, B.P., Matsuoka, K., Mouginot, J., Nitsche, F.O., Nogi, Y., Nost, O.A., Popov, S.V., Rignot, E., Rippin, D.M., Rivera, A., Roberts, J., Ross, N., Siegert, M.J., Smith, A.M., Steinhage, D., Studinger, M., Sun, B., Tinto, B.K., Welch, B.C., Wilson, D., Young, D.A., Xiangbin, C. & Zirizzotti, A. (2013). Bedmap2: improved ice bed, surface and thickness datasets for Antarctica. *The Cryosphere*, **7**, 375–393. 30

Fujita, S. & Mae, S. (1994). Causes and nature of ice-sheet radio-echo internal reflections estimated from the dielectric properties of ice. *Annals of Glaciology*, **20**, 80–86. 306

Fujita, S., Maeno, H., Uratsuka, S., Furukawa, T., Mae, S., Fujii, Y. & Watanabe, O. (1999). Nature of radio echo layering in the Antarctic Ice Sheet detected by a two-frequency experiment. *Journal of Geophysical Research: Solid Earth*, **104**, 13013–13024. 307

Fujita, S., Maeno, H. & Matsuoka, K. (2006). Radio-wave depolarization and scattering within ice sheets: a matrix-based model to link radar and ice-core measurements and its application. *Journal of Glaciology*, **52**, 407–424. 35

Fukui, K., Sone, T., Strelin, J.A., Torielli, C.A., Mori, J. & Fujii, Y. (2008). Dynamics and GPR stratigraphy of a polar rock glacier on James Ross Island, Antarctic Peninsula. *Journal of Glaciology*, **54**, 445–451. 30

Gades, A.M. (1998). *Spatial and Temporal Variations of Basal Conditions Beneath Glaciers and Ice Sheets Inferred From Radio Echo-Sounding Measurements*. https:\\earthweb.ess.washington.edu/glaciology/dissertations /gades_dissertation.pdf, University of Washington. 47

GADES, A.M., RAYMOND, C.F., CONWAY, H. & JACOBEL, R.W. (2000). Bed properties of Siple Dome and adjacent ice streams, West Antarctica, inferred from radio-echo sounding measurements. *Journal of Glaciology*, **46**, 88–94. 79, 83, 86, 87, 88

GARDNER, G.H.F., GARDNER, L.W. & GREGORY, A.R. (1974). Formation velocity and density—The diagnostic basics for stratigraphic traps. *Geophysics*, **39**, 770–780. 96

GASCON, G., SHARP, M., BURGESS, D., BEZEAU, P. & BUSH, A.B.G. (2013). Changes in accumulation-area firn stratigraphy and meltwater flow during a period of climate warming: Devon Ice Cap, Nunavut, Canada. *Journal of Geophysical Research: Earth Surface*, **118**, 2380–2391. 33, 284

GHOSE, R. & SLOB, E.C. (2006). Quantitative integration of seismic and GPR reflections to derive unique estimates for water saturation and porosity in subsoil. *Geophysical Research Letters*, **33**, L05404. 97

GLEN, J.W. & PAREN, J.G. (1975). The Electrical Properties of Snow and Ice. *Journal of Glaciology*, **15**, 15–38. 33, 284

GRAHAM, A.G., LARTER, R.D., GOHL, K., HILLENBRAND, C.D., SMITH, J.A. & KUHN, G. (2009). Bedform signature of a West Antarctic palaeo-ice stream reveals a multi-temporal record of flow and substrate control. *Quaternary Science Reviews*, **28**, 2774–2793. 17, 18, 20, 21, 204, 219, 228

GRAHAM, A.G.C. & HOGAN, K.A. (2016). Crescentic scours on palaeo-ice stream beds. *Geological Society, London, Memoirs*, **46**, 221–222. 20, 21, 202, 204, 230

GRASMUECK, M., WEGER, R. & HORSTMEYER, H. (2005). Full-resolution 3D GPR imaging. *Geophysics*, **70**, K12–K19. 30, 44, 45, 46, 60

GRAY, S.H. (2004). Gaussian beam migration of common-shot records. *2004 SEG Annual Meeting*, **70**, 71–77. 40

GREENWOOD, S.L. & CLARK, C.D. (2009a). Reconstructing the last Irish Ice Sheet 1: changing flow geometries and ice flow dynamics deciphered from the glacial landform record. *Quaternary Science Reviews*, **28**, 3085–3100. 4

Greenwood, S.L. & Clark, C.D. (2009b). Reconstructing the last Irish Ice Sheet 2: a geomorphologically-driven model of ice sheet growth, retreat and dynamics. *Quaternary Science Reviews*, **28**, 3101–3123. 4

Gudmundsson, G.H. (2006). Fortnightly variations in the flow velocity of Rutford Ice Stream, West Antarctica. *Nature*, **444**, 1063–1064. 22, 135

Gudmundsson, G.H. (2007). Tides and the flow of Rutford Ice Stream, West Antarctica. *Journal of Geophysical Research*, **112**. 223

Gudmundsson, G.H. & Jenkins, A. (2009). Ice-flow velocities on Rutford Ice Stream, West Antarctica, are stable over decadal timescales. *Journal of Glaciology*, **55**, 339–344. 22, 135, 223, 224

Guha, S., Kruse, S.E., Wright, E.E. & Kruse, U.E. (2005). Spectral analysis of ground penetrating radar response to thin sedimentary layers. *Geophysical Research Letters*, **32**, L23304. 139, 207

Hale, D. (1990). Stable, explicit depth extrapolation of seismic wavefields. *1990 SEG Annual Meeting*, **56**, 1301–1304. 40

Hallet, B., Hunter, L. & Bogen, J. (1996). Rates of erosion and sediment evacuation by glaciers: A review of field data and their implications. *Global and Planetary Change*, **12**, 213–235. 159

Hambrey, M.J., Dowdeswell, J.A., Murray, T. & Porter, P.R. (1996). Thrusting and debris entrainment in a surging glacier: Bakaninbreen, Svalbard. *Annals of Glaciology*, **22**, 241–248. 156

Hart, J.K. (1999). Identifying fast ice flow from landform assemblages in the geological record: a discussion. *Annals of Glaciology*, **28**, 59–66. 19, 201

Heilig, A., Schneebeli, M. & Eisen, O. (2009). Upward-looking ground-penetrating radar for monitoring snowpack stratigraphy. *Cold Regions Science and Technology*, **59**, 152–162. 33

Hess, D.P. & Briner, J.P. (2009). Geospatial analysis of controls on subglacial bedform morphometry in the New York Drumlin Field - Implications for Laurentide Ice Sheet dynamics. *Earth Surface Processes and Landforms*, **34**, 1126–1135. 4

HINDMARSH, R.C. (1998). Drumlinization and drumlin-forming instabilities: Viscous till mechanisms. *Journal of Glaciology*, **44**, 293–314. 20, 158

HINKEL, J., JAEGER, C., NICHOLLS, R.J., LOWE, J., RENN, O. & PEIJUN, S. (2015). Sea-level rise scenarios and coastal risk management. *Nature Climate Change*, **5**, 188–190. 1

HOLLAND, C.W. & ANANDAKRISHNAN, S. (2009). Subglacial seismic reflection strategies when source amplitude and medium attenuation are poorly known. *Journal of Glaciology*, **55**, 931–937. 95

HOLSCHUH, N., CHRISTIANSON, K., PADEN, J., ALLEY, R. & ANANDAKRISHNAN, S. (2020). Linking postglacial landscapes to glacier dynamics using swath radar at Thwaites Glacier, Antarctica. *Geology*, **48**, 268–272. 4, 5, 7, 20, 21, 30, 79, 131, 201, 202, 214, 219, 225, 227, 228, 229, 230

HOOKE, R.L. & IVERSON, N.R. (1995). Grain-size distribution in deforming subglacial tills: Role of grain fracture. *Geology*, **23**, 57–60. 15

HOOKE, R.L.B., HANSON, B., IVERSON, N.R., JANSSON, P. & FISCHER, U.H. (1997). Rheology of till beneath Storglaciären, Sweden. *Journal of Glaciology*, **43**, 172–179. 15

HUGHES, T.J. (1981). The weak underbelly of the West Antarctic ice sheet. *Journal of Glaciology*, **27**, 518–525. 3

HULBE, C.L. & FAHNESTOCK, M.A. (2004). West Antarctic ice-stream discharge variability: mechanism, controls and pattern of grounding-line retreat. *Journal of Glaciology*, **50**, 471–484. 220

HUMPHREY, N.F. & RAYMOND, C.F. (1994). Hydrology, erosion and sediment production in a surging glacier: Variegated Glacier, Alaska, 1982-83. *Journal of Glaciology*, **40**, 539–552. 159

IPCC (2021). Sixth Assessment Report. In *Summary for Policymakers. In: Climate Change 2021: The Physical Science Basis. Contribution of Working Group I to the Sixth Assessment Report of the Intergovernmental Panel on Climate Change [Masson-Delmotte, V., P. Zhai, A. Pirani, S.L. Connors, C. Péan,*, Cambridge University Press. 1

IVERSON, N.R. (2010). Shear resistance and continuity of subglacial till: hydrology rules. *Journal of Glaciology*, **56**, 1104–1114. 132

IVERSON, N.R. & IVERSON, R.M. (2001). Distributed shear of subglacial till due to Coulomb slip. *Journal of Glaciology*, **47**, 481–488. 16

IVERSON, N.R., HANSON, B., HOOKE, R.L. & JANSSON, P. (1995). Flow Mechanism of Glaciers on Soft Beds. *Science*, **267**, 80–81. 15, 157

JACOBEL, R., WELCH, B.C., OSTERHOUSE, D., PETTERSSON, R. & MAC-GREGOR, J.A. (2009). Spatial variation of radar-derived basal conditions on Kamb Ice Stream, West Antarctica. *Annals of Glaciology*, **50**, 10–16. 86

JACOBEL, R.W., LAPO, K.E., STAMP, J.R., YOUNGBLOOD, B.W., WELCH, B.C. & BAMBER, J.L. (2010). A comparison of basal reflectivity and ice velocity in East Antarctica. *The Cryosphere*, **4**, 447–452. 90

JAMIESON, S.S., STOKES, C.R., LIVINGSTONE, S.J., VIELI, A., COFAIGH, C., HILLENBRAND, C.D. & SPAGNOLO, M. (2016). Subglacial processes on an Antarctic ice stream bed. 2: Can modelled ice dynamics explain the morphology of mega-scale glacial lineations? *Journal of Glaciology*, **62**, 285–298. 201

JENKINS, A., CORR, H.F., NICHOLLS, K.W., STEWART, C.L. & DOAKE, C.S. (2006). Interactions between ice and ocean observed with phase-sensitive radar near an Antarctic ice-shelf grounding line. *Journal of Glaciology*, **52**, 325–346. 224

JISKOOT, H. (2011). Dynamics of Glaciers. In *Encyclopedia of Earth Sciences Series*, 245–256, Springer Netherlands. 10

JONES, I.F. (2014). Tutorial: Migration imaging conditions. *First Break*, **32**, 45–55. 38, 40

JOUGHIN, I. & ALLEY, R.B. (2011). Stability of the West Antarctic ice sheet in a warming world. *Nature Geoscience*, **4**, 506–513. 3

JOUGHIN, I. & BAMBER, J.L. (2005). Thickening of the ice stream catchments feeding the Filchner-Ronne Ice Shelf, Antarctica. *Geophysical Research Letters*, **32**. 221

JOUGHIN, I., BAMBER, J.L., SCAMBOS, T., TULACZYK, S., FAHNESTOCK, M. & MACAYEAL, D.R. (2006). Integrating satellite observations with modelling: Basal shear stress of the Filcher-Ronne ice streams, Antarctica. *Philosophical Transactions of the Royal Society A: Mathematical, Physical and Engineering Sciences*, **364**, 1795–1814. 135, 221

JOUGHIN, I., TULACZYK, S., BAMBER, J.L., BLANKENSHIP, D., HOLT, J.W., SCAMBOS, T. & VAUGHAN, D.G. (2009). Basal conditions for Pine Island and Thwaites Glaciers, West Antarctica, determined using satellite and airborne data. *Journal of Glaciology*, **55**, 245–257. 3, 46

JOUGHIN, I., SMITH, B.E. & HOLLAND, D.M. (2010). Sensitivity of 21st century sea level to ocean-induced thinning of Pine Island Glacier, Antarctica. *Geophysical Research Letters*, **37**. 3

JOUGHIN, I., SMITH, B.E. & MEDLEY, B. (2014). Marine ice sheet collapse potentially under way for the thwaites glacier basin, West Antarctica. *Science*, **344**, 735–738. 3

JOUGHIN, I., SHAPERO, D., SMITH, B., DUTRIEUX, P. & BARHAM, M. (2021). Ice-shelf retreat drives recent Pine Island Glacier speedup. *Science Advances*, **7**. 3

KAMB, B. (1991). Rheological nonlinearity and flow instability in the deforming bed mechanism of ice stream motion. *Journal of Geophysical Research*, **96**, 16585–16595. 13

KAMB, B. (2001). Basal Zone of the West Antarctic Ice Streams and its Role in Lubrication of Their Rapid Motion. In *The West Antarctic Ice Sheet: Behavior and Environment; Antarctic Research Series*, vol. 77, 157–199, American Geophysical Union. 5, 14, 15, 16, 101, 130, 223

KEAREY, P., BROOKS, M. & HILL, I. (2002). *Introduction To Geophysical Exploration*, vol. 3rd edn. Blackwell Science, Oxford. 36, 38, 39

KIEMAN, J. & BORGSTRÖM, I. (1996). Reconstruction of palaeo-ice sheets: The use of geomorphological data. *Earth Surface Processes and Landforms*, **21**, 893–909. 4

King, E. (2020). The precision of radar-derived subglacial bed topography: a case study from Pine Island Glacier, Antarctica. *Annals of Glaciology*, **61**, 154–161. 33, 278

King, E., Pritchard, H., Brisbourne, A., Smith, A., Lewington, E. & Clark, C. (2017). Comparison of contemporary subglacial bedforms beneath Rutford Ice Stream and Pine Island Glacier, Antarctica. In *EGU 2017*, 1, https:\\meetingorganizer.copernicus.org/EGU2017/EGU2017-1885-1. 145

King, E.C. (2009). Flow dynamics of the Rutford Ice Stream ice-drainage basin, West Antarctica, from radar stratigraphy. *Annals of Glaciology*, **50**, 42–48. 22

King, E.C. (2011). Ice stream or not? Radio-echo sounding of Carlson Inlet, West Antarctica. *The Cryosphere*, **5**, 907–916. 222

King, E.C., Woodward, J. & Smith, A.M. (2004). Seismic evidence for a water-filled canal in deforming till beneath Rutford Ice Stream, West Antarctica. *Geophysical Research Letters*, **31**, 4–7. 6, 22, 25, 26, 79, 220

King, E.C., Woodward, J. & Smith, A.M. (2007). Seismic and radar observations of subglacial bed forms beneath the onset zone of Rutford Ice Stream, Antarctica. *Journal of Glaciology*, **53**, 665–672. 5, 29, 47, 79, 205, 218, 219, 220

King, E.C., Hindmarsh, R.C.A. & Stokes, C.R. (2009). Formation of mega-scale glacial lineations observed beneath a West Antarctic ice stream. *Nature Geoscience*, **2**, 585–588. 5, 6, 19, 23, 26, 27, 28, 29, 30, 46, 56, 79, 112, 113, 122, 129, 131, 140, 142, 145, 189, 200, 213, 215, 217, 218, 228, 229

King, E.C., Pritchard, H.D. & Smith, A.M. (2016). Subglacial landforms beneath Rutford Ice Stream, Antarctica: detailed bed topography from ice-penetrating radar. *Earth System Science Data*, **8**, 151–158. 5, 22, 23, 24, 25, 27, 28, 47, 48, 50, 52, 55, 101, 113, 144, 200, 203, 214

Kleman, J., Hättestrand, C., Borgström, I. & Stroeven A. (1997). Fennoscandian palaeoglaciology using a glacialological inversion model. *Journal of Glaciology*, **43**, 283–299. 4

KNOLL, M.D. (1996). *A petrophysical basis for ground penetrating radar and very early time electromagnetics: electrical properties of sand-clay mixtures*. Ph.D. thesis. 35

KUFNER, S.K., BRISBOURNE, A.M., SMITH, A.M., HUDSON, T.S., MURRAY, T., SCHLEGEL, R., KENDALL, J.M., ANANDAKRISHNAN, S. & LEE, I. (2021). Not all Icequakes are Created Equal: Basal Icequakes Suggest Diverse Bed Deformation Mechanisms at Rutford Ice Stream, West Antarctica. *Journal of Geophysical Research: Earth Surface*, **126**. 26, 77, 143, 148, 152, 153, 217, 218, 219, 227, 233

LANGHAMMER, L., RABENSTEIN, L., SCHMID, L., BAUDER, A., GRAB, M., SCHAER, P. & MAURER, H. (2019). Glacier bed surveying with helicopter-borne dual-polarization ground-penetrating radar. *Journal of Glaciology*, **65**, 123–135. 207, 208

LARTER, R.D., GRAHAM, A.G., HILLENBRAND, C.D., SMITH, J.A. & GALES, J.A. (2012). Late Quaternary grounded ice extent in the Filchner Trough, Weddell Sea, Antarctica: new marine geophysical evidence. *Quaternary Science Reviews*, **53**, 111–122. 20, 21

LARTER, R.D., HOGAN, K.A., HILLENBRAND, C.D., SMITH, J.A., BATCHELOR, C.L., CARTIGNY, M., TATE, A.J., KIRKHAM, J.D., ROSEBY, Z.A., KUHN, G., GRAHAM, A.G.C. & DOWDESWELL, J.A. (2019). Subglacial hydrological control on flow of an Antarctic Peninsula palaeo-ice stream. *The Cryosphere*, **13**, 1583–1596. 20, 21, 202, 204, 227, 228

LEGARSKY, J., GOGINENI, S. & AKINS, T. (2001). Focused synthetic aperture radar processing of ice-sounder data collected over the Greenland ice sheet. *IEEE Transactions on Geoscience and Remote Sensing*, **39**, 2109–2117. 236

LEMKE, R.W. (1958). Narrow linear drumlins near Velva, North Dakota. *American Journal of Science*, **256**, 270–283. 18

LESEMANN, J.E., ALSOP, G.I. & PIOTROWSKI, J.A. (2011). Subglacial deposition and deformation of glaciofluvial sediments during episodic glacier-bed decoupling events. In *Geohydro2011*, January, https:\\www.researchgate.net/publication/262934436. 15

LEUCCI, G. & NEGRI, S. (2006). Use of ground penetrating radar to map subsurface archaeological features in an urban area. *Journal of Archaeological Science*, **33**, 502–512. 30

LICCIARDI, J.M., CLARK, P.U., JENSON, J.W. & MACAYEAL, D.R. (1998). Deglaciation of a soft-bedded Laurentide Ice Sheet. *Quaternary Science Reviews*, **17**, 427–448. 16

LINDSEY, J.P. (1989). The Fresnel zone and its interpetive significance. *The Leading Edge*, **8**, 33–39. 52, 58

LIVINGSTONE, S.J., CLARK, C.D., WOODWARD, J. & KINGSLAKE, J. (2013). Potential subglacial lake locations and meltwater drainage pathways beneath the Antarctic and Greenland ice sheets. *The Cryosphere*, **7**, 1721–1740. 100, 101

LOVELL, H., FLEMING, E.J., BENN, D.I., HUBBARD, B., LUKAS, S., REA, B.R., NOORMETS, R. & FLINK, A.E. (2015). Debris entrainment and landform genesis during tidewater glacier surges. *Journal of Geophysical Research: Earth Surface*, **120**, 1574–1595. 156

LOWE, A.L. & ANDERSON, J.B. (2003). Evidence for abundant subglacial meltwater beneath the paleo-ice sheet in Pine Island Bay, Antarctica. *Journal of Glaciology*, **49**, 125–138. 19, 154, 200

LOWRIE, W. (2007). *Fundamentals of Geophysics*. Cambridge University Press, Cambridge. 33

LUO, Y., HIGGS, W.G. & KOWALIK, W.S. (1996). Edge detection and stratigraphic analysis using 3D seismic data. In *SEG Technical Program Expanded Abstracts 1996*, 324–327, Society of Exploration Geophysicists. 109

LUTHRA, T., PETERS, L.E., ANANDAKRISHNAN, S., ALLEY, R.B., HOLSCHUH, N. & SMITH, A.M. (2017). Characteristics of the sticky spot of Kamb Ice Stream, West Antarctica. *Journal of Geophysical Research: Earth Surface*, **122**, 641–653. 78, 79

LYTHE, M.B. & VAUGHAN, D.G. (2001). BEDMAP: A new ice thickness and subglacial topographic model of Antarctica. *Journal of Geophysical Research: Solid Earth*, **106**, 11335–11351. 3

MacAyeal, D.R., Bindschadler, R.A. & Scambos, T.A. (1995). Basal friction of Ice Stream E, West Antarctica. *Journal of Glaciology*, **41**, 247–262. 17, 217

MacGregor, J.A., Winebrenner, D.P., Conway, H., Matsuoka, K., Mayewski, P.A. & Clow, G.D. (2007). Modeling englacial radar attenuation at Siple Dome, West Antarctica, using ice chemistry and temperature data. *Journal of Geophysical Research*, **112**. 86

MacGregor, J.A., Catania, G.A., Conway, H., Schroeder, D.M., Joughin, I., Young, D.A., Kempf, S.D. & Blankenship, D.D. (2013). Weak bed control of the eastern shear margin of Thwaites Glacier, West Antarctica. *Journal of Glaciology*, **59**, 900–912. 83, 84, 85

MacGregor, J.A., Li, J., Paden, J.D., Catania, G.A., Clow, G.D., Fahnestock, M.A., Gogineni, S.P., Grimm, R.E., Morlighem, M., Nandi, S., Seroussi, H. & Stillman, D.E. (2015). Radar attenuation and temperature within the Greenland Ice Sheet. *Journal of Geophysical Research: Earth Surface*, **120**, 983–1008. 307

Marfurt, K., Duncan, W.S. & Constance, P. (2002). Comparison of 3-d edge detection seismic attributes to Vinton Dome Louisiana. In *SEG Technical Program Expanded Abstracts 2002*, 577–580, Society of Exploration Geophysicists. 109

Martinez, A. & Byrnes, A.P. (2001). Modeling Dielectric-Constant Values of Geologic Materials: An Aid to Ground-Penetrating Radar Data Collection and Interpretation. *Current Research in Earth Sciences*, **247**. 34, 35, 92

Matsuoka, K. (2011). Pitfalls in radar diagnosis of ice-sheet bed conditions: Lessons from englacial attenuation models. *Geophysical Research Letters*, **38**. 86

McCabe, A. & Dardis, G.F. (1994). Glaciotectonically induced water-throughflow structures in a Late Pleistocene drumlin, Kanrawer, County Galway, western Ireland. *Sedimentary Geology*, **91**, 173–190. 137, 225

McClymont, A.F., Green, A.G., Streich, R., Horstmeyer, H., Tronicke, J., Nobes, D.C., Pettinga, J., Campbell, J. & Langridge, R.

(2008). Visualization of active faults using geometric attributes of 3D GPR data: An example from the Alpine Fault Zone, New Zealand. *Geophysics*, **73**, B11–B23. 103

MCGRANAHAN, G., BALK, D. & ANDERSON, B. (2007). The rising tide: Assessing the risks of climate change and human settlements in low elevation coastal zones. *Environment and Urbanization*, **19**, 17–37. 1

MEIER, M.F. & POST, A. (1987). Fast tidewater glaciers. *Journal of Geophysical Research*, **92**, 9051–9058. 80, 143

MENZIES, J. (1979). A review of the literature on the formation and location of drumlins. *Earth Science Reviews*, **14**, 315–359. 4, 18

MENZIES, J. (2002). Glacial environments — Modern and past. In *Modern and Past Glacial Environments*, 1–13, Elsevier. 154

MENZIES, J. & SHILTS, B.W. (2002). Subglacial environments. In *Modern and Past Glacial Environments*, 183–278, Elsevier. 20

MERCER, J.H. (1978). West Antarctic ice sheet and CO2 greenhouse effect: a threat of disaster. *Nature*, **271**, 321–325. 3

MILLAR, D.H.M. (1981). Radio-echo layering in polar ice sheets and past volcanic activity. *Nature*, **292**, 441–443. 307

MOHEBIAN, R., RIAHI, M.A. & YOUSEFI, O. (2018). Detection of channel by seismic texture analysis using Grey Level Co-occurrence Matrix based attributes. *Journal of Geophysics and Engineering*, **15**, 1953–1962. 103

MOSOLA, A.B. & ANDERSON, J.B. (2006). Expansion and rapid retreat of the West Antarctic Ice Sheet in eastern Ross Sea: possible consequence of overextended ice streams? *Quaternary Science Reviews*, **25**, 2177–2196. 220

MOTYKA, R.J., TRUFFER, M., KURIGER, E.M. & BUCKI, A.K. (2006). Rapid erosion of soft sediments by tidewater glacier advance: Taku Glacier, Alaska, USA. *Geophysical Research Letters*, **33**, L24504. 80, 159

MOUNT, G.J. & COMAS, X. (2014). Estimating porosity and solid dielectric permittivity in the Miami Limestone using high-frequency ground penetrating radar (GPR) measurements at the laboratory scale. *Water Resources Research*, **50**, 7590–7605. 35, 91

MURRAY, T. & CLARKE, G.K.C. (1995). Black-box modeling of the subglacial water system. *Journal of Geophysical Research: Solid Earth*, **100**, 10231–10245. 15

MURRAY, T. & DOWDESWELL, J.A. (1992). Water throughflow and the physical effects of deformation on sedimentary glacier beds. *Journal of Geophysical Research*, **97**, 8993. 132, 136

MURRAY, T., SMITH, A.M., KING, M.A. & WEEDON, G.P. (2007). Ice flow modulated by tides at up to annual periods at Rutford Ice Stream, West Antarctica. *Geophysical Research Letters*, **34**. 22, 135

MURRAY, T., CORR, H., FORIERI, A. & SMITH, A.M. (2008). Contrasts in hydrology between regions of basal deformation and sliding beneath Rutford Ice Stream, West Antarctica, mapped using radar and seismic data. *Geophysical Research Letters*, **35**. 5, 6, 14, 16, 28, 30, 44, 77, 79, 84, 85, 86, 91, 92, 93, 94, 95, 98, 127, 130, 131, 135, 137, 138, 139

MUTO, A., ANANDAKRISHNAN, S., ALLEY, R.B., HORGAN, H.J., PARIZEK, B.R., KOELLNER, S., CHRISTIANSON, K. & HOLSCHUH, N. (2019). Relating bed character and subglacial morphology using seismic data from Thwaites Glacier, West Antarctica. *Earth and Planetary Science Letters*, **507**, 199–206. 95, 205

NAPIERALSKI, J. & NALEPA, N. (2010). The application of control charts to determine the effect of grid cell size on landform morphometry. *Computers and Geosciences*, **36**, 222–230. 7

NAPOLEONI, F., JAMIESON, S.S.R., ROSS, N., BENTLEY, M.J., RIVERA, A., SMITH, A.M., SIEGERT, M.J., PAXMAN, G.J.G., GACITÚA, G., URIBE, J.A., ZAMORA, R., BRISBOURNE, A.M. & VAUGHAN, D.G. (2020). Subglacial lakes and hydrology across the Ellsworth Subglacial Highlands, West Antarctica. *The Cryosphere*, **14**, 4507–4524. 154

NAVARRO, F. & EISEN, O. (2009). Ground-penetrating radar in glaciological applications. In *Remote Sensing of Glaciers*, 195–229, Taylor and Francis. 33, 58, 82

NAVARRO, F.J., MACHERET, Y.Y. & BENJUMEA, B. (2005). Application of radar and seismic methods for the investigation of temperate glaciers. *Journal of Applied Geophysics*, **57**, 193–211. 96, 97

NEUBAUER, W., EDER-HINTERLEITNER, A., SEREN, S. & MELICHAR, P. (2002). Georadar in the Roman civil town Carnuntum, Austria: an approach for archaeological interpretation of GPR data. *Archaeological Prospection*, **9**, 135–156. 30

NEWTON, A.M. & HUUSE, M. (2017). Glacial geomorphology of the central Barents Sea: Implications for the dynamic deglaciation of the Barents Sea Ice Sheet. *Marine Geology*, **387**, 114–131. 5

NICHOLLS, R.J. & CAZENAVE, A. (2010). Sea-level rise and its impact on coastal zones. *Science*, **328**, 1517–1520. 1

NYGÅRD, A., SEJRUP, H., HAFLIDASON, H., LEKENS, W., CLARK, C. & BIGG, G. (2007). Extreme sediment and ice discharge from marine-based ice streams: New evidence from the North Sea. *Geology*, **35**, 395–398. 13

NYQUIST, H. (1928). Certain Topics in Telegraph Transmission Theory. *Transactions of the American Institute of Electrical Engineers*, **47**, 617–644. 56

Ó COFAIGH, C., PUDSEY, C.J., DOWDESWELL, J.A. & MORRIS, P. (2002). Evolution of subglacial bedforms along a paleo-ice stream, Antarctic Peninsula continental shelf. *Geophysical Research Letters*, **29**, 41–1–41–4. 14, 17, 18, 19, 29

Ó COFAIGH, C., DOWDESWELL, J.A., ALLEN, C.S., HIEMSTRA, J.F., PUDSEY, C.J., EVANS, J. & EVANS, D.J. (2005). Flow dynamics and till genesis associated with a marine-based Antarctic palaeo-ice stream. *Quaternary Science Reviews*, **24**, 709–740. 13, 14, 20, 21, 29, 202, 204, 229

Ó COFAIGH, C., EVANS, J., DOWDESWELL, J.A. & LARTER, R.D. (2007). Till characteristics, genesis and transport beneath Antarctic paleo-ice streams. *Journal of Geophysical Research*, **112**, F03006. 13, 14

OGILVY, J.A. & MERKLINGER, H.M. (1991). Theory of Wave Scattering from Random Rough Surfaces. *The Journal of the Acoustical Society of America*, **90**, 3382–3382. 83

ORLANDO, L. (2003). Semiquantitative evaluation of massive rock quality using ground penetrating radar. *Journal of Applied Geophysics*, **52**, 1–9. 30

PADEN, J., AKINS, T., DUNSON, D., ALLEN, C. & GOGINENI, P. (2010). Ice-sheet bed 3-D tomography. *Journal of Glaciology*, **56**, 3–11. 236

PAKISER, L.C. & BLACK, R.A. (1957). Exploring for ancient channels with the refraction seismograph. *Geophysics*, **22**, 32–47. 97

PATTYN, F. & MORLIGHEM, M. (2020). The uncertain future of the Antarctic Ice Sheet. *Science*, **367**, 1331–1335. 4

PIOTROWSKI, J.A. (1997). Subglacial hydrology in north-western germany during the last glaciation: groundwater flow, tunnel valleys and hydrological cycles. *Quaternary Science Reviews*, **16**, 169–185. 140, 142

PIOTROWSKI, J.A. & KRAUS, A.M. (1997). Response of sediment to ice-sheet loading in northwestern Germany: effective stresses and glacier-bed stability. *Journal of Glaciology*, **43**, 495–502. 16

PIOTROWSKI, J.A., LARSEN, N.K. & JUNGE, F.W. (2004). Reflections on soft subglacial beds as a mosaic of deforming and stable spots. *Quaternary Science Reviews*, **23**, 993–1000. 14, 46, 140, 142, 215, 223

POLLARD, D. & DECONTO, R.M. (2012). A simple inverse method for the distribution of basal sliding coefficients under ice sheets, applied to Antarctica. *The Cryosphere*, **6**, 953–971. 3, 46

POPOV, M. (1982). A new method of computation of wave fields using Gaussian beams. *Wave Motion*, **4**, 85–97. 40

POST, A. & MOTYKA, R.J. (1995). Taku and LeConte Glaciers, Alaska: Calving-speed control of Late-Holocene asynchronous advances and retreats. *Physical Geography*, **16**, 59–82. 80, 143

PRALONG, M.R. & GUDMUNDSSON, G.H. (2011). Bayesian estimation of basal conditions on Rutford Ice Stream, West Antarctica, from surface data. *Journal of Glaciology*, **57**, 315–324. 223, 224

RAYMOND, C., ECHELMEYER, K., WHILLANS, I. & DOAKE, C. (2001). Ice stream shear margins. In *The West Antarctic Ice Sheet: Behavior and Environment; Antarctic Research Series*, 137–155, American Geophysical Union, Washington, DC, American Geophysical Union, antarctic edn. 17

RAYMOND, M.J. (2007). *Estimating basal properties of glaciers and ice streams from surface measurements*. https:\\doi.org/10.3929/ethz-a-005485106, Eidgenössische Technische Hochschule ETH Zürich. 218, 224

REINARDY, B.T., LARTER, R.D., HILLENBRAND, C.D., MURRAY, T., HIEMSTRA, J.F. & BOOTH, A.D. (2011). Streaming flow of an Antarctic Peninsula palaeo-ice stream, both by basal sliding and deformation of substrate. *Journal of Glaciology*, **57**, 596–608. 201

RETZLAFF, R. & BENTLEY, C.R. (1993). Timing of stagnation of Ice Stream C, West Antarctica, from short-pulse radar studies of buried surface crevasses. *Journal of Glaciology*, **39**, 553–561. 220

REYNOLDS, J.M. (1997). *An Introduction To Applied and Environmental Geophysics*. John Wiley and Sons. 31, 34, 35

RIGNOT, E., VELICOGNA, I., VAN DEN BROEKE, M.R., MONAGHAN, A. & LENAERTS, J.T.M. (2011). Acceleration of the contribution of the Greenland and Antarctic ice sheets to sea level rise. *Geophysical Research Letters*, **38**. 2, 23

RIGNOT, E., MOUGINOT, J., SCHEUCHL, B., VAN DEN BROEKE, M., VAN WESSEM, M.J. & MORLIGHEM, M. (2019). Four decades of Antarctic Ice Sheet mass balance from 1979–2017. *Proceedings of the National Academy of Sciences*, **116**, 1095–1103. 3

RIPPIN, D., BINGHAM, R., JORDAN, T., WRIGHT, A., ROSS, N., CORR, H., FERRACCIOLI, F., LE BROCQ, A., ROSE, K. & SIEGERT, M. (2014). Basal roughness of the Institute and Möller Ice Streams, West Antarctica: Process determination and landscape interpretation. *Geomorphology*, **214**, 139–147. 84

Ritz, C., Edwards, T.L., Durand, G., Payne, A.J., Peyaud, V. & Hindmarsh, R.C.A. (2015). Potential sea-level rise from Antarctic ice-sheet instability constrained by observations. *Nature*, **528**, 115–118. 3, 46

Riverman, K.L., Anandakrishnan, S., Alley, R.B., Holschuh, N., Dow, C.F., Muto, A., Parizek, B.R., Christianson, K. & Peters, L.E. (2019). Wet subglacial bedforms of the NE Greenland Ice Stream shear margins. *Annals of Glaciology*, **60**, 91–99. 44, 79, 137

Roberts, A. (2001). Curvature attributes and their application to 3D interpreted horizons. *First Break*, **19**, 85–100. 104

Rose, K.E. (1979). Characteristics of Ice Flow in Marie Byrd Land, Antarctica. *Journal of Glaciology*, **24**, 63–75. 217

Rosier, S.H.R., Gudmundsson, G.H. & Green, J.A.M. (2015). Temporal variations in the flow of a large Antarctic ice stream controlled by tidally induced changes in the subglacial water system. *The Cryosphere*, **9**, 1649–1661. 223

Russell, A.J., Roberts, M.J., Fay, H., Marren, P.M., Cassidy, N.J., Tweed, F.S. & Harris, T. (2006). Icelandic jökulhlaup impacts: Implications for ice-sheet hydrology, sediment transfer and geomorphology. *Geomorphology*, **75**, 33–64. 19

Salisbury, M.H., Harvey, C.W. & Matthews, L. (2003). The Acoustic Properties of Ores and Host Rocks in Hardrock Terranes. In *Hardrock Seismic Exploration*, 9–19, Society of Exploration Geophysicists. 96

Scambos, T., Bell, R., Alley, R., Anandakrishnan, S., Bromwich, D., Brunt, K., Christianson, K., Creyts, T., Das, S., DeConto, R., Dutrieux, P., Fricker, H., Holland, D., MacGregor, J., Medley, B., Nicolas, J., Pollard, D., Siegfried, M., Smith, A., Steig, E., Trusel, L., Vaughan, D. & Yager, P. (2017). How much, how fast?: A science review and outlook for research on the instability of Antarctica's Thwaites Glacier in the 21st century. *Global and Planetary Change*, **153**, 16–34. 3

SCHEUCHL, B., MOUGINOT, J. & RIGNOT, E. (2012). Ice velocity changes in the Ross and Ronne sectors observed using satellite radar data from 1997 and 2009. *Cryosphere*, **6**, 1019–1030. 221

SCHNEIDER, W.A. (1978). Integral formulation for migration in two and three dimensions. *Geophysics*, **43**, 49–76. 40, 41

SCHOOF, C.G. & CLARKE, G.K. (2008). A model for spiral flows in basal ice and the formation of subglacial flutes based on a Reiner-Rivlin rheology for glacial ice. *Journal of Geophysical Research: Solid Earth*, **113**. 20, 228

SCHROEDER, D.M., BLANKENSHIP, D.D. & YOUNG, D.A. (2013). Evidence for a water system transition beneath Thwaites Glacier, West Antarctica. *Proceedings of the National Academy of Sciences*, **110**, 12225–12228. 137

SCHROEDER, D.M., GRIMA, C. & BLANKENSHIP, D.D. (2016). Evidence for variable grounding-zone and shear-margin basal conditions across Thwaites Glacier, West Antarctica. *Geophysical Research Letters*, **81**, WA35–WA43. 86

SHAW, J. (1983). Drumlin formation related to inverted melt-water erosional marks. *Journal of Glaciology*, **29**, 461–479. 154

SHAW, J. (1988). Subglacial erosional marks, Wilton Creek, Ontario. *Canadian Journal of Earth Sciences*, **25**, 1256–1267. 19

SHAW, J. (1994). Hairpin erosional marks, horseshoe vortices and subglacial erosion. *Sedimentary Geology*, **91**, 269–283. 19, 21, 201, 228

SHAW, J., RAINS, B., EYTON, R. & WEISSLING, L. (1996). Laurentide subglacial outburst floods: landform evidence from digital elevation models. *Canadian Journal of Earth Sciences*, **33**, 1154–1168. 19, 21

SHAW, J., FARAGINI, D.M., KVILL, D.R. & RAINS, R.B. (2000). The Athabasca fluting field, Alberta, Canada: Implications for the formation of large-scale fluting (erosional lineations). *Quaternary Science Reviews*, **19**, 959–980. 18, 19

SHAW, J., PUGIN, A. & YOUNG, R.R. (2008). A meltwater origin for Antarctic shelf bedforms with special attention to megalineations. *Geomorphology*, **102**, 364–375. 19

SHEPHERD, A., WINGHAM, D. & RIGNOT, E. (2004). Warm ocean is eroding West Antarctic Ice Sheet. *Geophysical Research Letters*, **31**. 3

SHERIFF, R.E. & GELDART, L.P. (1995). *Exploration Seismology — Solid Earth Geophysics*. Cambridge University Press, 2nd edn. 57, 278

SHIPP, S., ANDERSON, J. & DOMACK, E. (1999). Late Pleistocene-Holocene retreat of the West Antarctic Ice-Sheet system in the Ross Sea: Part 1 - Geophysical results. *Bulletin of the Geological Society of America*, **111**, 1486–1516. 29

SIEGERT, M.J. & RIDLEY, J.K. (1998). Determining basal ice-sheet conditions in the Dome C region of East Antarctica using satellite radar altimetry and airborne radio-echo sounding. *Journal of Glaciology*, **44**, 1–8. 79

SIEGERT, M.J., KULESSA, B., BOUGAMONT, M., CHRISTOFFERSEN, P., KEY, K., ANDERSEN, K.R., BOOTH, A.D. & SMITH, A.M. (2018). Antarctic subglacial groundwater: a concept paper on its measurement and potential influence on ice flow. *Geological Society, London, Special Publications*, **461**, 197–213. 78

SIMM, R. & BACON, M. (2014). *Seismic Amplitude - An Interpreter's Handbook*. Cambridge University Press, Cambridge. 54, 106

SMITH, A.M. (1997a). Basal conditions on Rufford Ice Stream, West Antarctica, from seismic observations. *Journal of Geophysical Research*, **102**, 543–552. 25, 26, 28, 77, 79, 95, 215, 218

SMITH, A.M. (1997b). Variations in basal conditions on Rutford Ice Stream, west Antarctica. *Journal of Glaciology*, **43**, 245–255. 5, 6, 14, 22, 25, 26, 28, 29, 46, 77, 95, 97, 215, 223

SMITH, A.M. (2006). Microearthquakes and subglacial conditions. *Geophysical Research Letters*, **33**. 14, 26, 77, 218

SMITH, A.M. & MURRAY, T. (2009). Bedform topography and basal conditions beneath a fast-flowing West Antarctic ice stream. *Quaternary Science Reviews*, **28**, 584–596. 5, 6, 14, 16, 22, 23, 25, 26, 28, 46, 56, 80, 89, 92, 93, 95, 128, 131, 133, 135, 153, 158, 159, 160, 203, 215, 217, 223, 225, 229, 234, 238

SMITH, A.M., MURRAY, T., NICHOLLS, K.W., MAKINSON, K., ADAL-GEIRSDÓTTIR, G., BEHAR, A.E. & VAUGHAN, D.G. (2007). Rapid erosion, drumlin formation, and changing hydrology beneath an Antarctic ice stream. *Geology*, **35**, 127–130. 5, 6, 14, 23, 25, 26, 28, 29, 30, 46, 79, 80, 92, 93, 95, 135, 153, 154, 158, 159, 160, 200, 203, 215, 217, 220, 223, 224, 225, 229, 230, 234, 238

SMITH, A.M., BENTLEY, C.R., BINGHAM, R.G. & JORDAN, T.A. (2012). Rapid subglacial erosion beneath Pine Island Glacier, West Antarctica. *Geophysical Research Letters*, **39**. 160, 223

SMITH, A.M., JORDAN, T.A., FERRACCIOLI, F. & BINGHAM, R.G. (2013). Influence of subglacial conditions on ice stream dynamics: Seismic and potential field data from Pine Island Glacier, West Antarctica. *Journal of Geophysical Research: Solid Earth*, **118**, 1471–1482. 132, 133

SMITH, A.M., WOODWARD, J., ROSS, N., BENTLEY, M.J., HODGSON, D.A., SIEGERT, M.J. & KING, E.C. (2018). Evidence for the long-term sedimentary environment in an Antarctic subglacial lake. *Earth and Planetary Science Letters*, **504**, 139–151. 132, 133, 135

SMITH, A.M., ANKER, P.G.D., NICHOLLS, K.W., MAKINSON, K., MURRAY, T., RIOS-COSTAS, S., BRISBOURNE, A.M., HODGSON, D.A., SCHLEGEL, R. & ANANDAKRISHNAN, S. (2021). Ice stream subglacial access for ice-sheet history and fast ice flow: the BEAMISH Project on Rutford Ice Stream, West Antarctica and initial results on basal conditions. *Annals of Glaciology*, **62**, 203–211. 5, 13, 23, 55, 97, 135, 140, 156, 159, 223

SMITH, E.C., SMITH, A.M., WHITE, R.S., BRISBOURNE, A.M. & PRITCHARD, H.D. (2015). Mapping the ice-bed interface characteristics of Rutford Ice Stream, West Antarctica, using microseismicity. *Journal of Geophysical Research: Earth Surface*, **120**, 1881–1894. 17, 26, 77, 143, 148, 152, 153, 218, 233

SPAGNOLO, M., CLARK, C.D., HUGHES, A.L., DUNLOP, P. & STOKES, C.R. (2010). The planar shape of drumlins. *Sedimentary Geology*, **232**, 119–129. 18, 203

SPAGNOLO, M., CLARK, C.D., ELY, J.C., STOKES, C.R., ANDERSON, J.B., ANDREASSEN, K., GRAHAM, A.G. & KING, E.C. (2014). Size, shape and spatial arrangement of mega-scale glacial lineations from a large and diverse dataset. *Earth Surface Processes and Landforms*, **39**, 1432–1448. 17, 18, 19, 46, 79

STEARNS, L.A., JEZEK, K.C. & VAN DER VEEN, C. (2005). Decadal-scale variations in ice flow along Whillans Ice Stream and its tributaries, West Antarctica. *Journal of Glaciology*, **51**, 147–157. 219, 221

STOKES, C.R. (2018). Geomorphology under ice streams: Moving from form to process. *Earth Surface Processes and Landforms*, **43**, 85–123. 29, 229

STOKES, C.R. & CLARK, C.D. (2001). Palaeo-ice streams. *Quaternary Science Reviews*, **20**, 1437–1457. 17, 214

STOKES, C.R. & CLARK, C.D. (2002). Are long subglacial bedforms indicative of fast ice flow? *Boreas*, **31**, 239–249. 4, 17, 19

STOKES, C.R., CLARK, C.D., LIAN, O.B. & TULACZYK, S. (2007). Ice stream sticky spots: A review of their identification and influence beneath contemporary and palaeo-ice streams. *Earth-Science Reviews*, **81**, 217–249. 17, 214, 218, 219

STOKES, C.R., SPAGNOLO, M. & CLARK, C.D. (2011). The composition and internal structure of drumlins: Complexity, commonality, and implications for a unifying theory of their formation. *Earth-Science Reviews*, **107**, 398–422. 18

STOKES, C.R., FOWLER, A.C., CLARK, C.D., HINDMARSH, R.C. & SPAGNOLO, M. (2013). The instability theory of drumlin formation and its explanation of their varied composition and internal structure. *Quaternary Science Reviews*, **62**, 77–96. 17, 18, 19, 46, 201, 219

TANER, M.T. (2001). Seismic Attributes. *CSEG Recorder*, **26**, 48–56. 103

TANER, M.T., KOEHLER, F. & SHERIFF, R.E. (1979). Complex seismic trace analysis. *Geophysics*, **44**, 1041–1063. 105, 106, 107, 108

TRUFFER, M. & HARRISON, W.D. (2006). In situ measurements of till deformation and water pressure. *Journal of Glaciology*, **52**, 175–182. 14

TRUFFER, M., MOTYKA, R., HARRISON, W., ECHELMEYER, K.A., FISK, B. & TULACZYK, S. (1999). Subglacial drilling at Black Rapids Glacier, Alaska, U.S.A.: drilling method and sample descriptions. *Journal of Glaciology*, **45**, 495–505. 14, 16

TRUFFER, M., HARRISON, W.D. & ECHELMEYER, K.A. (2000). Glacier motion dominated by processes deep in underlying till. *Journal of Glaciology*, **46**, 213–221. 155

TULACZYK, S., KAMB, B., SCHERER, R.P. & ENGELHARDT, H.F. (1998). Sedimentary processes at the base of a West Antarctic ice stream; constraints from textural and compositional properties of subglacial debris. *Journal of Sedimentary Research*, **68**, 487–496. 15, 16

TULACZYK, S., KAMB, W.B. & ENGELHARDT, H.F. (2000). Basal mechanics of Ice Stream B, west Antarctica: 1. Till mechanics. *Journal of Geophysical Research: Solid Earth*, **105**, 463–481. 16

TULACZYK, S.M. & FOLEY, N.T. (2020). The role of electrical conductivity in radar wave reflection from glacier beds. *The Cryosphere*, **14**, 4495–4506. 139

TULACZYK, S.M., SCHERER, R.P. & CLARK, C.D. (2001). A ploughing model for the origin of weak tills beneath ice streams: a qualitative treatment. *Quaternary International*, **86**, 59–70. 16, 19

ULABY, F.T., MOORE, R.K. & FUNG, A.K. (1982). *Microwave remote sensing: active and passive, Volume II. Radar remote sensing and surface scattering and emission theory.*. Artech House. 83

VAN DER MEER, J.J., MENZIES, J. & ROSE, J. (2003). Subglacial till: The deforming glacier bed. *Quaternary Science Reviews*, **22**, 1659–1685. 154

VAUGHAN, D., COMISO, J., ALLISON, I., CARRASCO, J., KASER, G., KWOK, R., MOTE, P., MURRAY, T., PAUL, F., REN, J., RIGNOT, E., SOLOMINA, O., K., S. & T., Z. (2013). Observations: Cryosphere. In Intergovernmental Panel on Climate Change, ed., *Climate Change 2013 the Physical Science Basis: Working Group I Contribution to the Fifth Assessment Report of the Intergovernmental Panel on Climate Change*, vol. 9781107057, 317–382, Cambridge University Press, Cambridge. 1

VAUGHAN, D.G., SMITH, A.M., NATH, P.C. & LE MEUR, E. (2003). Acoustic impedance and basal shear stress beneath four Antarctic ice streams. *Annals of Glaciology*, **36**, 225–232. 14, 16, 25, 217

VAUGHAN, D.G., CORR, H.F., SMITH, A.M., PRITCHARD, H.D. & SHEPHERD, A. (2008). Flow-switching and water piracy between Rutford ice stream and Carlson inlet, West Antarctica. *Journal of Glaciology*, **54**, 41–48. 22, 23, 25, 135, 221, 222

WANG, B., TIAN, G., CUI, X. & ZHANG, X. (2008). The internal COF features in Dome A of Antarctica revealed by multi-polarization-plane RES. *Applied Geophysics*, **5**, 230–237. 30

WEERTMAN, J. (1964). The Theory of Glacier Sliding. *Journal of Glaciology*, **5**, 287–303. 12

WEERTMAN, J. (1974). Stability of the Junction of an Ice Sheet and an Ice Shelf. *Journal of Glaciology*, **13**, 3–11. 3

WELCH, B.C. & JACOBEL, R.W. (2003). Analysis of deep-penetrating radar surveys of West Antarctica, US-ITASE 2001. *Geophysical Research Letters*, **30**, 1444. 47

WELLNER, J., HEROY, D. & ANDERSON, J. (2006). The death mask of the antarctic ice sheet: Comparison of glacial geomorphic features across the continental shelf. *Geomorphology*, **75**, 157–171. 20

WELLNER, J.S., LOWE, A.L., SHIPP, S.S. & ANDERSON, J.B. (2001). Distribution of glacial geomorphic features on the Antarctic continental shelf and correlation with substrate: Implications for ice behavior. *Journal of Glaciology*, **47**, 397–411. 18, 19, 29

WEST, L.J., HANDLEY, K., HUANG, Y. & POKAR, M. (2003). Radar frequency dielectric dispersion in sandstone: Implications for determination of moisture and clay content. *Water Resources Research*, **39**, 1026. 35

WIDESS, M.B. (1973). How thin is a thin bed? *Geophysics*, **38**, 1176–1180. 209

WRIGHT, P.J., HARPER, J.T., HUMPHREY, N.F. & MEIERBACHTOL, T.W. (2016). Measured basal water pressure variability of the western Greenland Ice Sheet: Implications for hydraulic potential. *Journal of Geophysical Research: Earth Surface*, **121**, 1134–1147. 100

YILMAZ, Ö. (2001). *Seismic Data Analysis*, vol. 10 (2 volu. Society of Exploration Geophysicists, Tulsa. 31, 38, 39, 40, 41, 44, 57, 58, 225, 287

YORK, D., EVENSEN, N.M., MARTINEZ, M.L. & DE BASABE DELGADO, J. (2004). Unified equations for the slope, intercept, and standard errors of the best straight line. *American Journal of Physics*, **72**, 367–375. 99

ZHAO, W., FORTE, E., PIPAN, M. & TIAN, G. (2013). Ground Penetrating Radar (GPR) attribute analysis for archaeological prospection. *Journal of Applied Geophysics*, **97**, 107–117. 103, 106

ZHAO, W., FORTE, E., LEVI, S.T., PIPAN, M. & TIAN, G. (2015). Improved high-resolution GPR imaging and characterization of prehistoric archaeological features by means of attribute analysis. *Journal of Archaeological Science*, **54**, 77–85. 103

ZHAO, W., FORTE, E., COLUCCI, R.R. & PIPAN, M. (2016). High-resolution glacier imaging and characterization by means of GPR attribute analysis. *Geophysical Journal International*, **206**, 1366–1374. 103, 107, 108

ZOET, L.K. & IVERSON, N.R. (2018). A healing mechanism for stick-slip of glaciers. *Geology*, **46**, 807–810. 156

Chapter 10

Appendix

10.1 Data Acquisition and Data Summary

week	Monday	Tuesday	Wednseday	Thursday	Friday	Saturday	Sunday
1				Arrival	Digging and setting up camp		
2	Setting up DELORES		GRID 3				
3	GRID 3			Plane visit	GRID 3		GRID 3
4		GRID 2	Plane visit and new antennas			GRID 1	
5	GRID 1						
6				GRID 2			GRID 2
7	GRID 2						

Figure 10.1: Timetable for field season 2017/18 (21.12.2017–04.02.2018). Colour-code is chosen to indicate the different antennas and systems used for the grids.

Table 10.1: Translation of line numbering in 2016/17 to 2007/08.

line numbering 2016/17	line numbering 2007/08
1001	1200
1002	1205
1003	2210
1004	2215
1005	2220
1006	2225
1007	1230
1008	2235
1009	2240
1010	2245
1011	1250
1012	2255
1013	2260
1014	1265
1015	1270
1016	1275
1017	1280
1018	line not acquired
1019	1290
1020	1295
1021	1300
1022	1305
1023	1310
1024	2315
1025	2320
1026	1325
1027	line not acquired
1028	2335
1029	1340
1030	2350

10.2 Inaccuracies during GPS Position Assignment

The following describes how inaccuracies when assigning GPS positions to radar traces were identified. This is followed by the analysis and evaluation of possible origins for these inaccuracies and finally an approach how to correct for parts of these inaccuracies is given.

10.2.1 Identification of Mis-locations

After assigning the GPS positions to each of the radar traces, processing and importing the lines into Petrel (Schlumberger Software) the bed refection within grid 2 was picked using a semi-automated picking algorithm. Using the resulting twtt of the bed reflection, a surface with the dimensions 3×3 km was created, interpolating the picked twtt to 5×5 m grid cells. Comparisons of the picked lines showed that every odd line was shifted horizontally when compared to the even lines, causing topographic features to appear as wavy structures. To analyse the origin of these shifts, the bed reflection was picked in two different groups. Group number one included data acquired on all the lines acquired driving towards the Ellsworth Mountains and group number two included data acquired on lines driving towards the Fletcher Promontory (see Figure 2.4 for location).

Figure 10.2 shows the difference of the two different groups. Contour lines of topography based on picks on lines towards the Ellsworth Mountains are displayed in black, whereas contour lines of topography based on picks on lines towards the Fletcher Promontory are marked in red. The inset in Figure 10.2 shows the two separate picks, but also the contour lines, in case all the data were picked and interpolated together (shown in blue). A mis-location or horizontal shift of the contour lines using different datasets is visible. Figure 10.3 a shows the mis-location calculated as the distances between the location of the two contour lines (red and black) along the radar tracks (see green arrows along the mis-location in Figure 10.2). These mis-locations vary in amplitude and over time (Figure 10.3 a). Comparison of topography calculated using all data and only data acquired in one direction shows mis-locations of up to 12 m. During some days the mis-location was more than 5 m at all times, increasing over time (e.g. around line number 80 Figure 10.3 a).
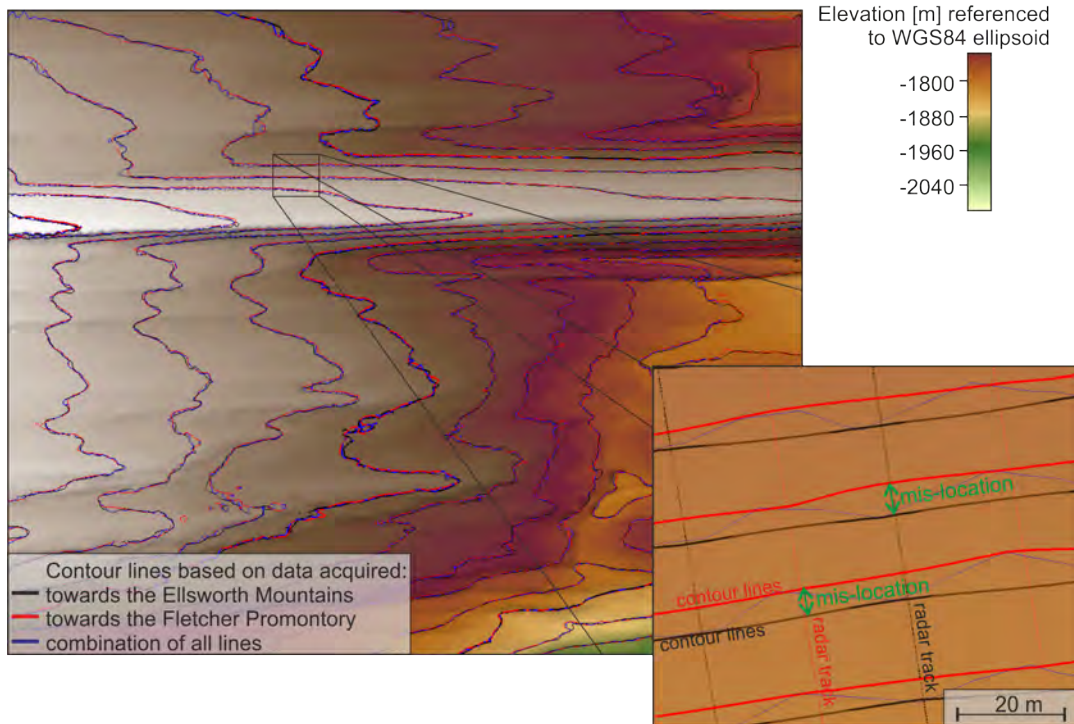
Figure 10.2: Plan view of the bed of grid 2. Section of the interpolated data with 5×5 m grid cells. Black contour lines are created using data acquired towards the Ellsworth Mountains, red contour lines are generated using data acquired towards the Fletcher Promontory. The inset shows a zoom on the flank of the Bump, facing towards the Ellsworth Mountains. Contour lines are displayed in red and black, as in the main image. Additionally the tracks along which the data were acquired are displayed in dashed red (towards the Ellsworth Mountains) and in dashed black (towards the Fletcher Promontory). The blue line marks the position of contour lines, if all the data were combined to create an interpolated grid.
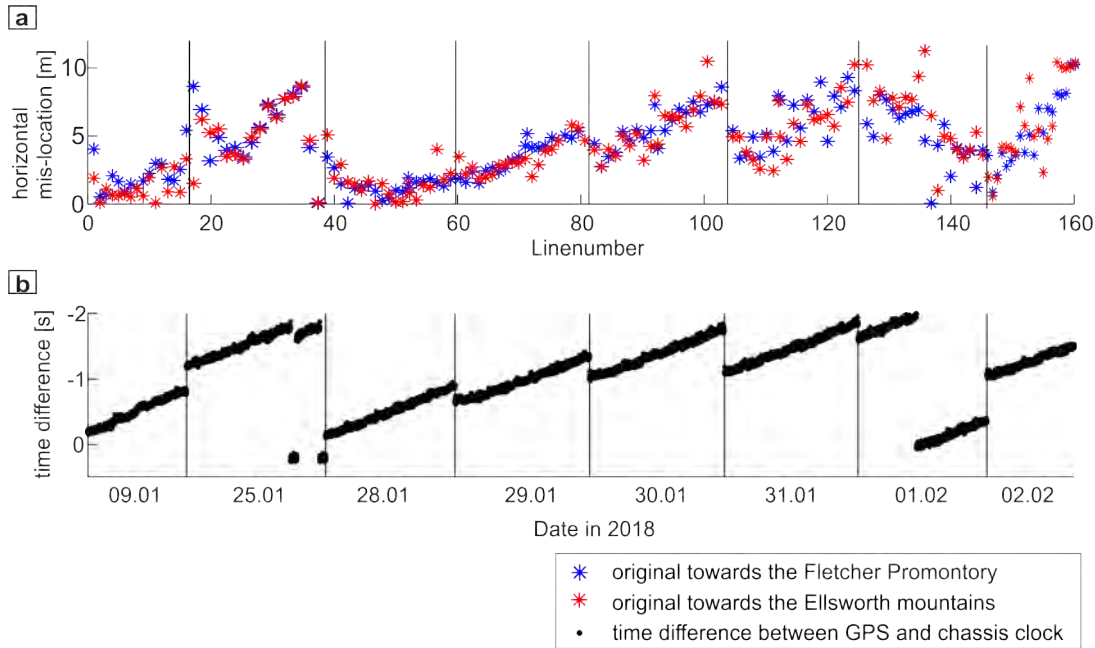
Figure 10.3: Comparison of a) calculated mis-location for grid 2 in day-sections and b) difference in clock time between the chassis computer clock and the UTC time recorded by the single-frequency GPS receiver in day sections.

10.2.2 Potential Explanations for Mis-Locations

To evaluate the source of these shifts, the horizontal resolution of the data post-processing as well as other factors during and after acquisition that might cause these shifts, are discussed.

10.2.2.1 Horizontal Resolution of Data After Processing

The horizontal resolution is dependent on the system parameters as well as the processing. After migration the Fresnel zone has a radius of 12 m. However, it is known that the relation between energy against radius is a Gaussian distribution ($\sqrt{(2)}$) (Sheriff & Geldart, 1995), which is why 12 m radius can be considered as the maximum Fresnel zone radius. The fact that the wavy structures (even less than 12 m shifts) are visible within those data show, together with findings by King (2020), that trace-to-trace precision is much higher than the theoretical horizontal resolution.
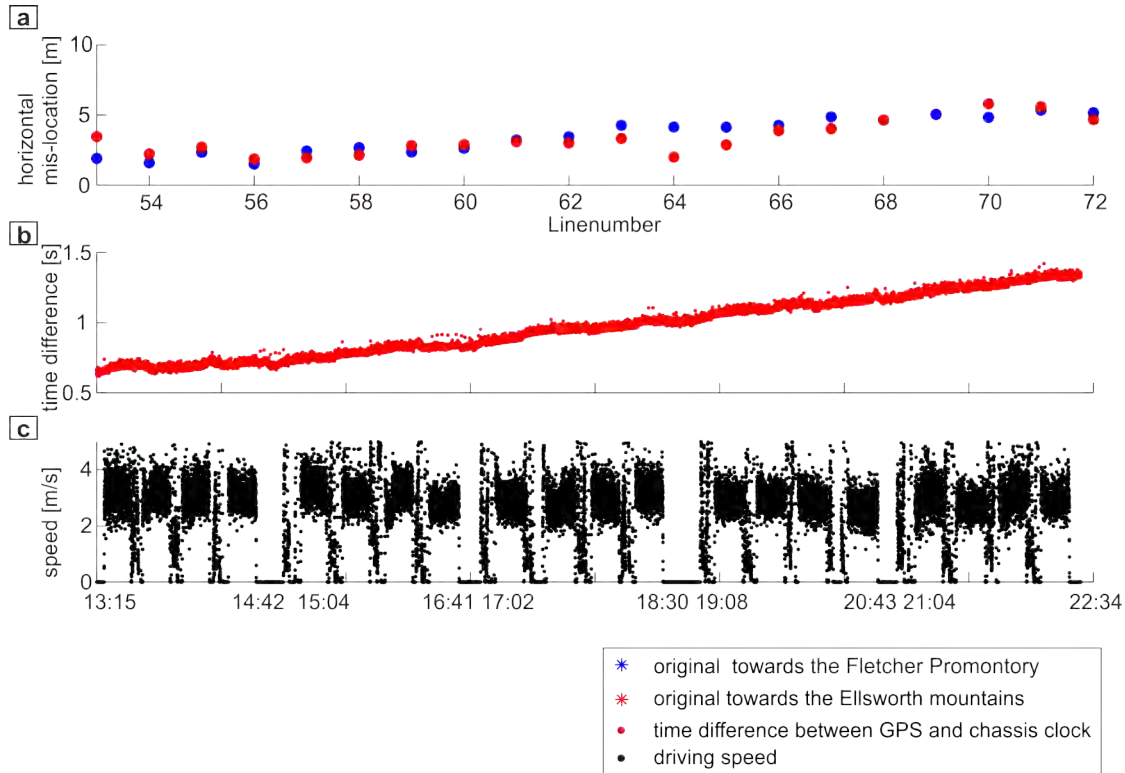
Figure 10.4: Correlation of mis-location (a), time difference (b) and surface speed (c) on the 29/01/2018. The spikes in velocity speed seen in (c) are caused by phases of faster driving (while turning) as well as stops during breaks.

10.2.2.2 Possible Sources of Inaccuracies During Processing in ReflexW and Petrel:

Possible sources may include the interpolation of GPS positions to 2 m trace intervals as well as the interpolation of twtt to a surface (e.g. due to inappropriate grid cell size).

Effects caused by processing could have all induced errors, but these would be constant over time, e.g. inaccuracies due to trace interpolation. The 2 m trace spacing does not vary over time, therefore no correlation can be seen between parameters during processing and the variations in mis-location. Therefore, reasons during and after processing have been ruled out. As a result, the shifts were assumed to be caused during data acquisition. In the following influences of different aspects during data acquisition are discussed in more detail.

10.2.2.3 Possible Sources of Inaccuracies During Acquisition:

Influence of Topography: A correlation of bed topography and the mis-location is not visible. The topography of the ice stream bed is known to be consistent over several kilometres, hence data acquired with an inline spacing of 20 m would therefore be expected to show a similar topography for neighbouring lines. A dependency of the mis-location on topography would therefore cause a repetitive signal within every second line but no variations or trend in mis-location over time.

Influence of Driving Speed: The single-frequency GPS recorded a position every second, and between each of those recordings the position was saved in a buffer. When synchronizing the chassis clock to the UTC time, an error of up to 999 ms could be induced, as the chassis time is synchronized to the UTC time saved in the buffer. This uncertainty could cause a mis-location of up to 3.3 m (assuming a driving speed of 11 km h^{-1}). Together with variations in driving speed, this could theoretically explain the variance of mis-location over time. Figure 10.4 shows the mis-location over time (a) and variations in driving speed (b) over time. The driving speed generally shows variations over the day but no clear trend that could cause the variations in mis-location over the day, which makes this as a source of inaccuracies less likely.

Influence of Clock Drift: A clock drift of the chassis clock could cause an increasing mis-location over time with a possible dependence on temperature in the chassis computer. The "Events.CSV" file created during acquisition includes the timestamp of when GPS positions are written to the file (according to the chassis clock) and the corresponding UTC time recorded by the single-frequency GPS receiver. The chassis clock could be synchronized to UTC time using the single-frequency GPS receiver (which is attached to the chassis). However, during acquisition in season 2017/18 the synchronization of the chassis clock was only performed four times. Figure 10.3 shows the mis-location of data (a) and the time difference between the UTC time in the GPS record and chassis clock over the day (b). For most sections a correlation between the trend in time difference and mis-location can be seen. The chassis is equipped with a low frequency cylindrical watch crystal as a real-time clock source. The typical frequency stability at a temperature of between -10 °C and 10 °C is -40 dF/F (ppm) and -10 dF/F (ppm).

With a frequency of $2^{15}=32768$ Hz a temperature of -10 °C could cause a drift of 1.31 s. Together with a driving speed of 11 km h^{-1} this would lead to a mis-location of 4.4 m. Variations of the temperature in the chassis over time might lead to a drifting clock, therefore, inaccuracies which will accumulate over time. As the GPS assignment is linked to the chassis clock, which experiences drifts in time, the accuracy of this assignment will vary depending on the clock drift.

Delays in Recording, Stacking and Writing: The chassis processing time, to stack the 256 shots and save/write them to the disk, might vary with memory usage as well as temperature. This could lead to a slowdown of the processes over the day. To test this, the sampling rate was increased for a trial recording during acquisition. Although the shot repetition was kept constant, fewer traces were recorded, when compared to a lower sampling rate, indicating that due to increased data volume the process of stacking and/or writing of data to a file has been slowed down, leading to the loss of data. Under the assumption that the time required to stack and record 256 traces drifts, the assignment of location to the stacked trace will drift as well. The location of the stacked trace is determined as the midpoint of the position of the first and the last trace location that has been stacked. If recording of trace number 265 is delayed, the GPS position will be recorded further along radar track than the radar signal was actually received. This delay in recording, especially considering a dependency of the chassis computer power on the temperature and memory usage, might be responsible for mis-location of the data.

10.2.2.4 Final Interpretation of Possible Sources for Inaccuracies

Considering all the possible reasons for this mis-location, the time dependent drift seen for the mis-location is most likely caused by a combination of clock drift and delays within the chassis recording. However, the strong correlation of the time difference between UTC time and chassis clock to the trend in mis-location imply a stronger dependency on clock drift than memory usage. A mis-location of 2 m is within the natural limits of the data due to stacking and the definition of a trace increment of 2 m. These small-scale mis-locations can not be corrected for. In the following the procedure for correction of observed clock drift are explained.

10.2.3 Corrections for Clock Drift

The "Events.CSV" file produced by the chassis contains a time stamp when GPS locations are recorded (every second) as well as the chassis time when the GPS positions were written to the file. To correct the data for the observed clock drift, the chassis time was synchronized to the GPS time and interpolated in between. All data used for 3D processing were corrected using this approach. After this correction, a mis-location can still be seen (red circles in Figure 10.5). However, the mis-location after clock drift removal is mainly below 5 m (therefore 2.5 m for each line) and therefore smaller than the initial mis-location (black stars). Furthermore, after drift removal the mis-location does not show any clear trend but is scattered. The correction for clock drift improves the positioning of radar data as it is now within the natural limits of resolution.
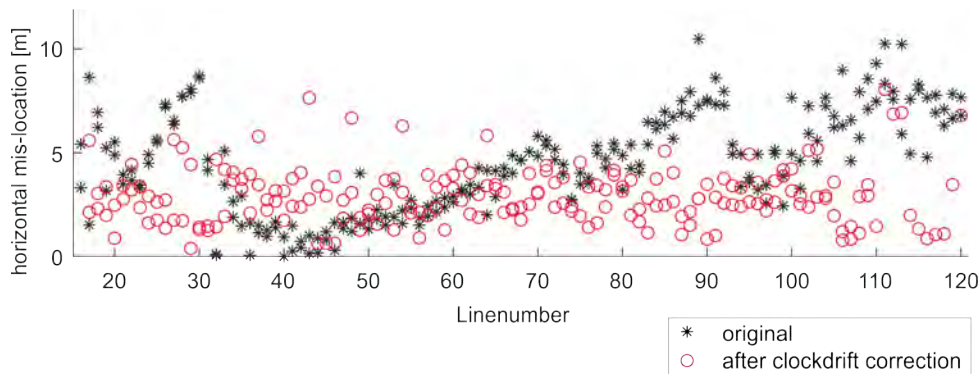
Figure 10.5: Comparison of mis-location over time before correction (black) and after correction for clock drift (red).

10.2.4 Advice for Future Data Acquisition Compliant with 3D Processing and Attribute Analysis

A mis-location of radar data has probably been an issue for all data acquired in previous surveys with the DELORES system. However, survey lines of previous studies were spaced with coarser spacing, impeding the identification of such mis-location of radar data. Considering the horizontal resolution of unmigrated data (228 m Fresnel radius; Section 3.3.2.2), inaccuracies on the scale of the mis-locations are well within the limits of resolution. The following gives a

set of solutions which might help to minimise the mis-location during future data acquisition of dense (<50 m) spaced lines:

- the time sampling frequency should be reduced, to reduce the amount of data that needs to be written into files

- synchronisation of the internal clock and the UTC time as often as possible (minimum 4 times a day)

- replacement of hardware to install a ring buffer with higher capacity.

10.3 Design of Migration Aperture

Different parameters need to be determined for migration, to enable an adequate result. One of those is the velocity at which the wave is assumed to travel within the medium (Section 10.3.1), in this case the ice. Furthermore, another crucial parameter is the design of the migration aperture (Section 10.3.2).

10.3.1 Velocity Analysis

10.3.1.1 Theoretical Values of Velocity

In the case of an ice stream the ice column is assumed to consist of firn and ice. Table 10.2 shows values of EM wave velocity in firn and ice.

Table 10.2: EM wave velocity in firn and ice.

material	velocity $[\mathrm{m\,ns^{-1}}]$ according to literature
firn	0.225–0.245 (Gascon *et al.*, 2013)
firn	0.160–0.225 (Eisen *et al.*, 2002)
ice	0.167–0.168 (Bogodorosky *et al.*, 1985; Glen & Paren, 1975)

For the RIS the firn-ice transition zone is expected at around 70 m depth (personal communication Ed King, Andy Smith, October, 2017). Applying different interval velocities for the firn and ice, results in RMS-velocity (Equation 2.3) between 0.168–0.169 $\mathrm{m\,ns^{-1}}$ (Table 10.3).

Table 10.3: RMS-velocities calculated for different interval velocities in ice and firn. Firn thickness is assumed to be 70 m and ice thickness 2200 m.

velocity in firn $[\mathrm{m\,ns^{-1}}]$	velocity in ice $[\mathrm{m\,ns^{-1}}]$	RMS-velocity in whole ice column $[\mathrm{m\,ns^{-1}}]$
0.2	0.168	0.168
0.224	0.168	0.169
0.2	0.167	0.168
0.224	0.167	0.168
0.245	0.167	0.169

10.3.1.2 Velocity Panels

A migration velocity analysis was performed in SeisSpace/ProMAX (LGC-Halliburton Software) using different RMS-velocities, while other migration parameters were kept constant. Data have been processed as described in Section 3.3.4.3. For
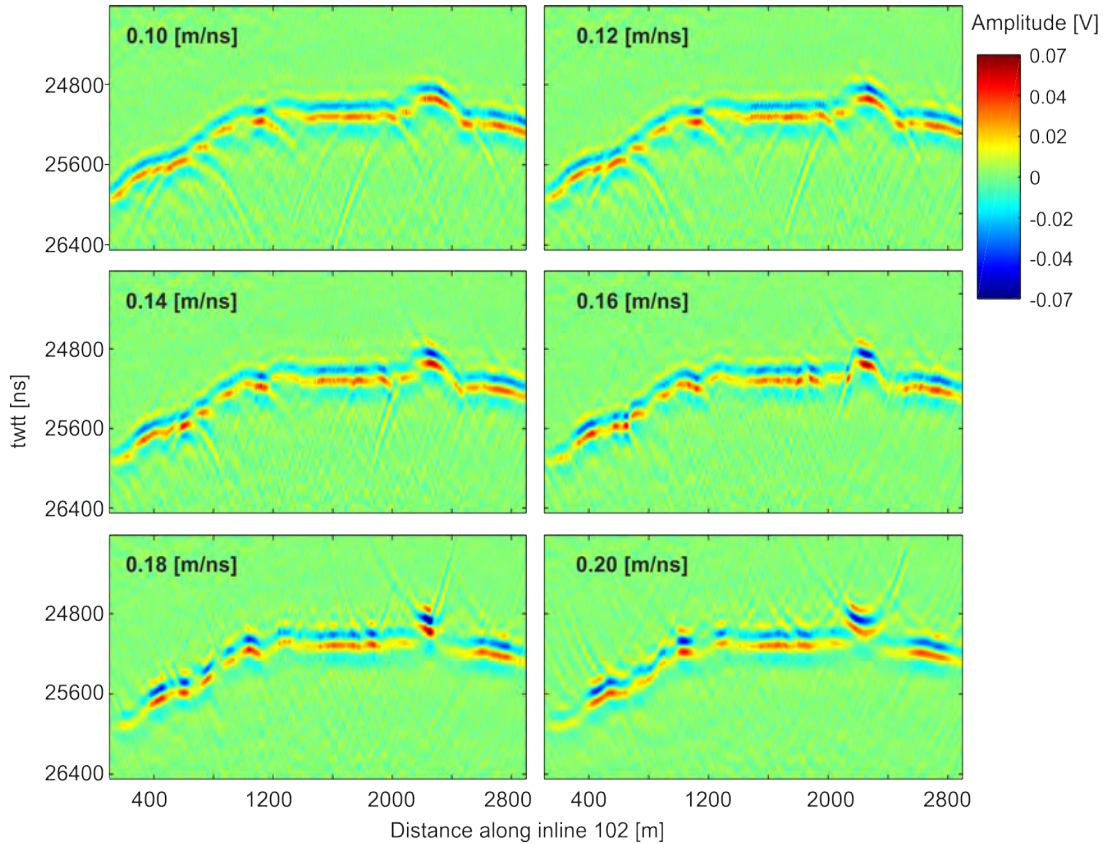
Figure 10.6: Data of inline 2 migrated using different RMS-velocities. The colour-code shows the amplitude of the samples, while the scale for the panels is constant. Figure 10.7 shows a zoom on the same dataset migrated with velocities between 0.162–$0.172 \, \mathrm{m \, ns^{-1}}$.

illustrative reasons, a *Automatic gain control* (AGC)-gain (window size $4000 \, \mathrm{ns}$) has been applied to data prior to migration, however this does only apply for data shown in the following images. Data of inline 2 migrated using RMS-velocities ranging from 0.10–$0.20 \, \mathrm{m \, ns^{-1}}$ are shown in Figure 10.6 as well as 0.162–$0.172 \, \mathrm{m \, ns^{-1}}$ in Figure 10.7. Data migrated using a velocity of 0.10–$0.14 \, \mathrm{m \, ns^{-1}}$ (Figure 10.6) appear undercorrected (migration smile visible, see Section 2.4.4.3.4). Panels with velocity of 0.18 and $0.20 \, \mathrm{m \, ns^{-1}}$ (Figure 10.6) show overcorrected data (migration frowns). In the panel with velocity of $0.16 \, \mathrm{m \, ns^{-1}}$ no migration smile of frowns are visible, therefore no under- or overcorrection of the data can be observed.

Comparison of the amplitude of the positive phase (yellow-red colours) of the bed reflection shows a higher occurrence of higher amplitudes for velocities between 0.168–$0.172 \, \mathrm{m \, ns^{-1}}$, although a slight overcorrection is visible for panel
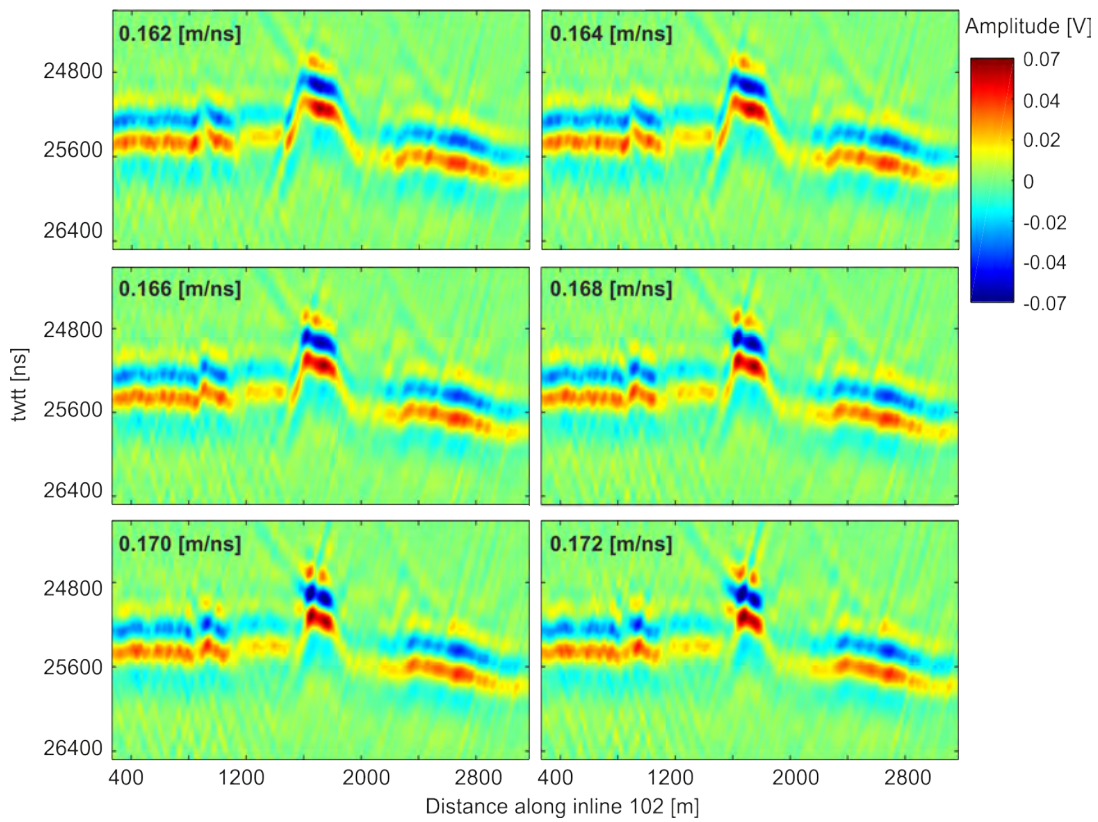
Figure 10.7: Data of inline 2 migrated using different RMS-velocities between 0.162–$0.172\,\mathrm{m\,ns^{-1}}$. The colourcode shows the amplitude of the samples, while the scale for the panels is constant.
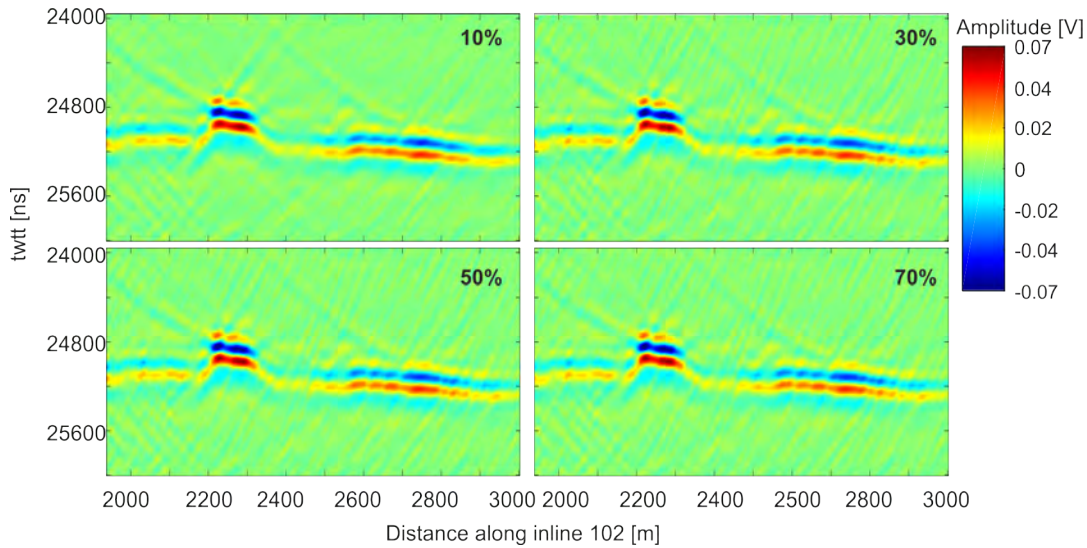
Figure 10.8: Data of inline 2 migrated using different percentages of maximum stretch mute between 1–70% with velocity of $0.168 \, \mathrm{m \, ns^{-1}}$. The colourcode shows the amplitude of the samples, while the scale for the panels is constant. The x- and y-axis shows the same range.

0.170–$0.172 \, \mathrm{m \, ns^{-1}}$. Therefore the the RMS-velocity with the optimum migration results according to the panels is around $0.168 \, \mathrm{m \, ns^{-1}}$, which is consistent with the theoretical calculations (Table 10.3).

10.3.2 Migration Aperture

Aside from the migration velocity, several other parameters can be adjusted during the migration. In the following, parameter tests performed using different limits of stretch mute, maximum image location and maximum dip limit are described. The migration velocity was chosen to be $0.168 \, \mathrm{m \, ns^{-1}}$.

10.3.2.1 Maximum Stretch Mute

Migration can caused stretched wavelets, which create artificially low frequencies within the data. This effect is also known as *normal moveout* (NMO) stretching during velocity picking. The so-called NMO stretching is a frequency distortion that occurs particularly at large offsets and for shallow events (Yilmaz, 2001). As a result, the period of a wave is stretched, resulting in lower frequency after NMO correction. To prevent stretched zones to have a negative effect on the migration, a maximum stretch mute is applied to the data.
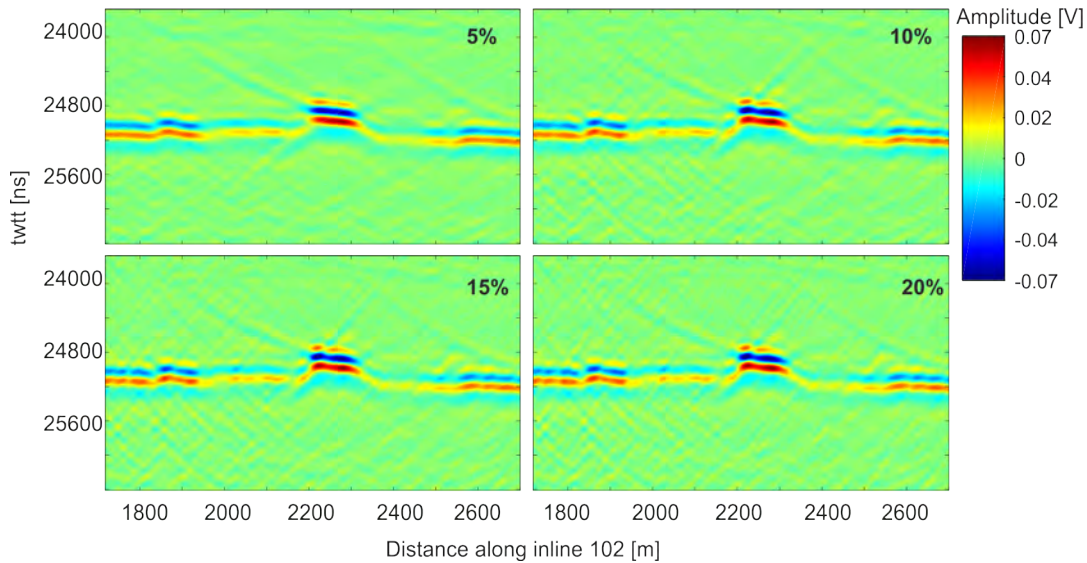
Figure 10.9: Data of inline 2 migrated using different percentages of maximum stretch mute between 5-20% with velocity of $0.168\,\mathrm{m\,ns^{-1}}$. The colourcode shows the amplitude of the samples, while the scale for the panels is constant. The x- and y-axis shows the same range, while x-axis represents trace number (trace spacing $2\,\mathrm{m}$), y-axis represents sample number (sample interval $4\,\mathrm{ns}$).

Figure 10.8 shows panels of migration results using varying stretch mute between 10 and 70%. Amplitudes of the bed reflection appear more spatially discontinuous when applying stretch mute >30%. Furthermore, data recorded prior to the bed reflection appears more noisy with higher stretch mute compared to lower. The amplitude of the reflection was analysed for 2 locations of the 4 panels, highest amplitudes can be found for the panel with 10% maximum stretch mute. Figure 10.9 shows panels of migration results using varying stretch mute between 5, 10, 15 and 20%. If a stretch mute smaller than 10% is applied the amplitude decreases, and therefore the reflector seems less continuous in places (see panel 5%). Due to the clarity of the reflection a maximum stretch mute of 15% is used for the whole dataset of grid 2.

10.3.2.2 Spatially Limiting the Aperture Width

The limitation of the width of the migration aperture is used to decrease computing time as well as costs, as a narrower aperture will include less data in one migration step. Two different delimiters for the aperture width are given here, the image location limit and the maximum migration dip (both limits are referred
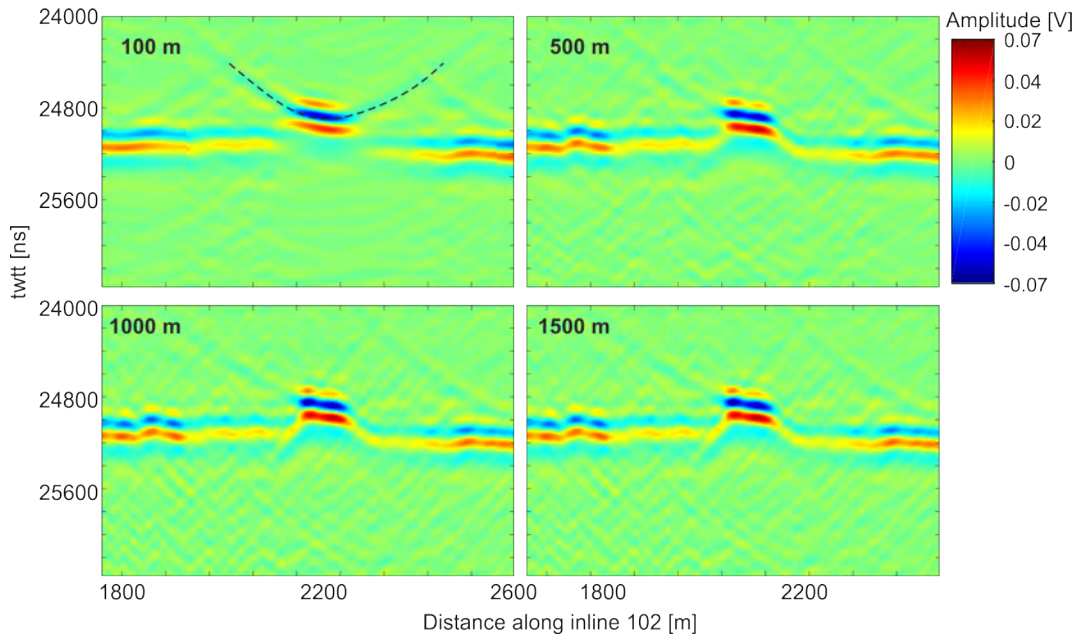
Figure 10.10: Data of inline 2 migrated using different image location distances between 100–1500 m with velocity of 0.168 m ns^{-1} and stretch mute of 15%. The colourcode shows the amplitude of the samples, while the scale for the panels is constant. The x- and y-axis shows the same range.

to the CMP position). The option to limit the migration direction does determine whether the migration is applied in 2D or 3D.

10.3.2.3 Maximum Image Location Limit

By defining a maximum image location distance only traces within the chosen radial distance are used for the migration. This is a non-time varying parameter, which has to be kept in mind when imaging layers in different depth (Figure 10.14). Since data presented here is focussed on the bed reflection, which is relatively smooth and flat, the first Fresnel zone (r$_{fresnel}$=228 m, see Section 3.3.2.2) at the ice-bed reflection can be chosen as the lower limit for this parameter.

Figure 10.10 shows inline 2 after migration with a stretch mute of 15%, as well as four different maximum image location distances (100–1500 m) applied. Using an image location distance of 100 m, the topography of the Bump, especially the flanks are not imaged properly. Furthermore, a migration smile (highlighted by the dashed line) appears above the Bump. A migration with an image location distance of 1500 m on the one hand, does remove the prominent migration smile but on the other hand the reflector is less continuous compared to data with
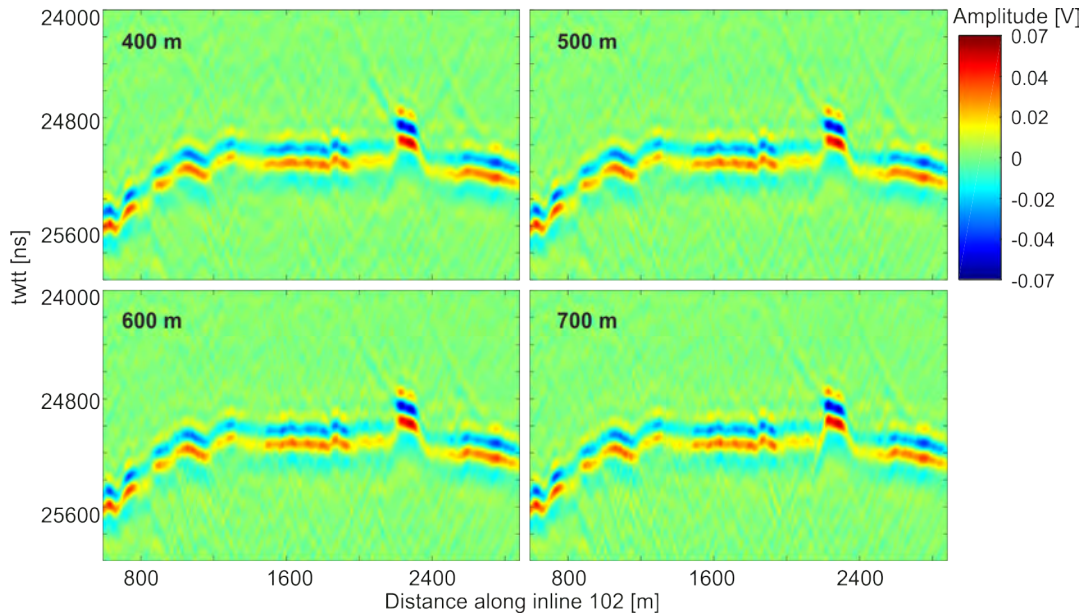
Figure 10.11: Data of inline 2 migrated using different image location distances between 400–700 m with velocity of $0.168\,\mathrm{m\,ns^{-1}}$ and stretch mute of 15%. The colourcode shows the amplitude of the samples, while the scale for the panels is constant. The x- and y-axis shows the same range, while x-axis represents trace number (trace spacing 2 m), y-axis represents sample number (sample interval 4 ns). Data have been bandpass-filtered, corrected for spherical divergence and a AGC-gain has been applied.

image location distance of 500 m (e.g.at distance 1050 m). The most continous bed reflection seems to result from migration using an image location of around 500 m. Figure 10.11 shows inline 2 migrated using image location distance between 400–700 m. Only little changes can be seen. Data in the upper left panel (maximum image location distance 400 m) seems more smooth and continuous along the bed reflection, when comparing to greater image location distances. Data migrated with images location distance above 500 m seems more scattered, especially when looking at the background noise around the bed reflection. Comparison of the amplitude of the reflection of the Bump shoes, highest values for image location distance of 400 m, decreasing towards greater image location distances, while a constant amplitude is achieved after 500 m.

10.3.2.4 Maximum Dip Limit

Unlike the maximum image location distance, the maximum dip limit does define a maximum dip of the wavefield that will be migrated. This parameter does

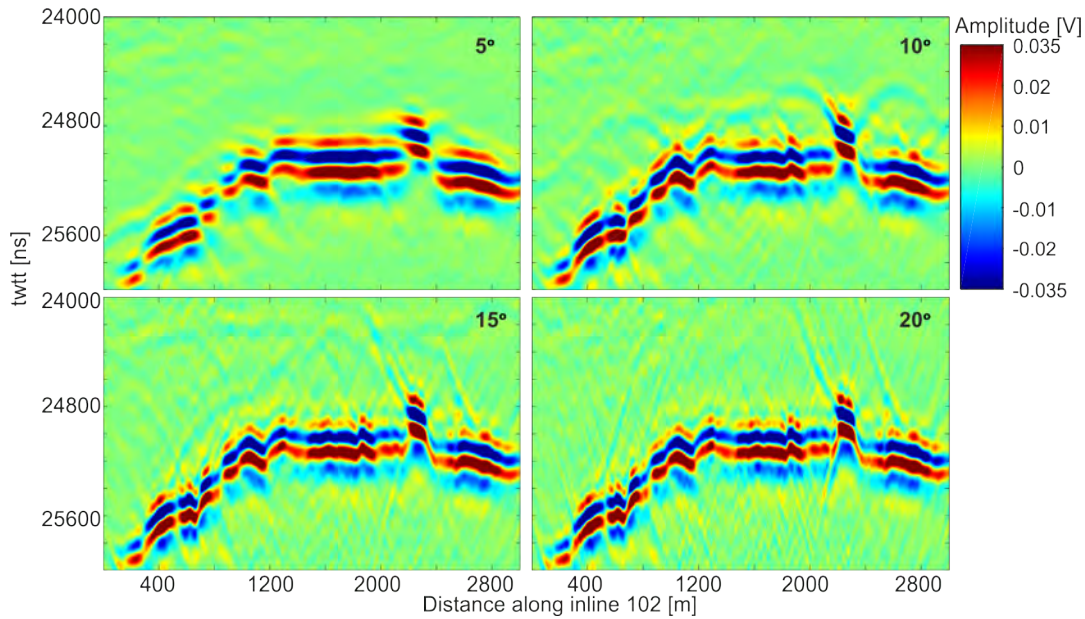Figure 10.12: Data of inline 2 migrated using different maximum dip between 5–20° with velocity of $0.168 \, \mathrm{m \, ns^{-1}}$ and stretch mute of 15%. The colourcode shows the amplitude, while the scale for the panels is constant. The x- and y-axis shows the same range.

determine the aperture width as well but, the effective width changes with depth (see yellow line in Figure 10.13).

Figure 10.12 shows the results of migration of inline 102, using stretch mute of 15% and maximum dip between 5–20°. Similar to the image location distance, a narrow aperture does not image the topography, e.g. the flanks of the Bump (1000–1250 m). Migration results using a maximum dip of 10° is lacking a clear continuous eastern flank of the Bump, furthermore a signal looking similar to a migration smile, is visible above the Bump reflection. Variations in amplitudes along the bed reflections seem smoothed out and smeared for dips <10°, while background noise around the bed reflection appears more prominent with increasing dip. If the maximum dip is chosen very big, high amplitude signals in the shape of hyperbola tails appear above the bed reflection (e.g. at distance 1100 m (> maximum dip 20°)). These signals have been identified as artefacts see Section 10.4. A maximum dip around 15° seem to minimize these artefacts, while imaging the topography properly. Considering the background noise, artefacts, migration effects like migration smiles, the maximum dip was chosen to be 15° for grid 2.
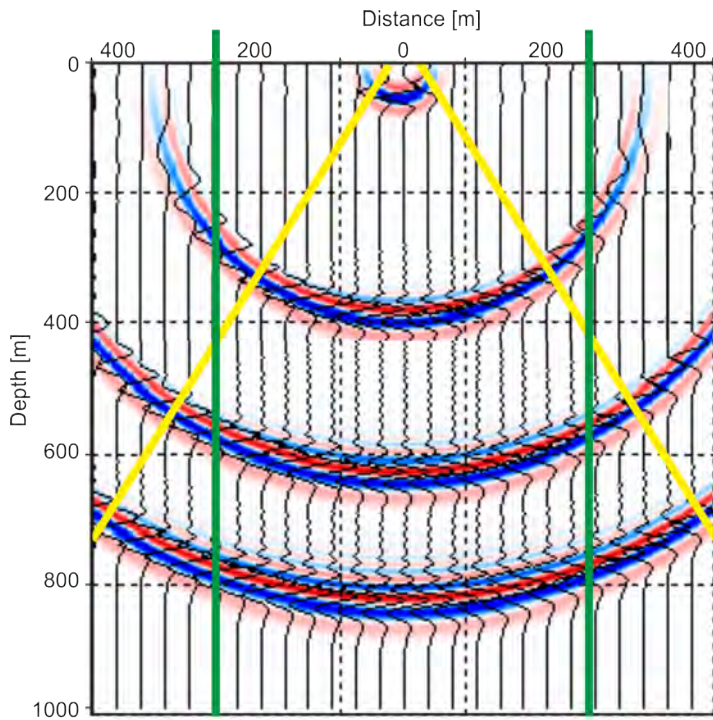
Figure 10.13: Exemplary impulse response function at four different times. The CMP in this example is situated at distance 0 m. The green line illustrated a image location distance of 300 m from CMP. The yellow line illustrate a maximum dip, in this case of 65°. Data outside the yellow and green line are located outside the migration aperture and will not be used for the migration.

10.3.2.5 Image Location Distance vs. Maximum Dip Limit

The main difference between the maximum dip (yellow lines, Fig. 10.13) and image location distance (green line) option is, that the image location is a twtt independent distance, while the effective distance using the maximum dip changes with depth. Figure 10.13 illustrates an example of an impulse response, the CMP is located at 0 m distance. The image location distance is chosen to be 300 m here, resulting in the incorporation of traces with maximum radial distance of 300 m (independent of the depth of the reflector) to the CMP (at distance 0 m). Traces located farther than 300 m from the CMP are not incorporated into the migration at this CMP. Using the definition of a maximum dip to limit the aperture, creates a fan-like aperture, whereas different numbers of traces are used for migration, depending on the depth.

Figure 10.14 shows post migration data, with a stretch mute of 15% applied for both panels. The aperture was limited using a maximum image location
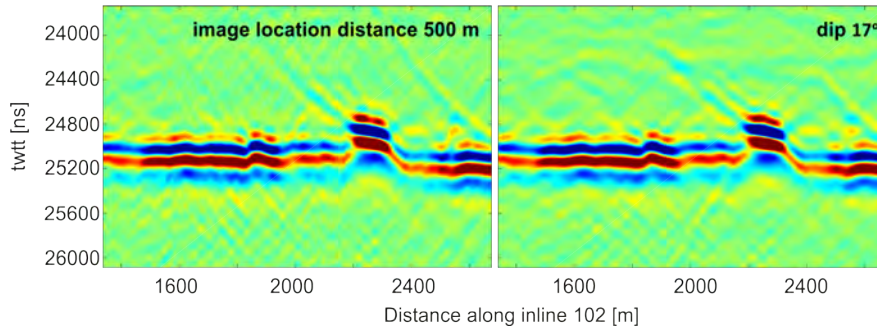
Figure 10.14: Data from inline 2 migrated using a maximum image location distance of $500\,\mathrm{m}$ (left panel) and a maximum dip of $17°$ (right panel) with velocity of $0.168\,\mathrm{m\,ns^{-1}}$ and stretch mute of 15%. The colourcode shows the amplitude of the samples, while the scale for the panels is constant.

distance of $500\,\mathrm{m}$ for the left panel and maximum dip of $17°$ for the right panel. The amplitude of the bed reflection is comparable in both images, while the right image seems to have smother amplitude variation along the reflection. The Bump shows the same topography in both images. The artefacts above the bed reflection in the right image appear more smooth and continuous, although the signals are visible in both panels. Due to the slight reduction of signal strength and signals above the bed reflection and the more continuous amplitudes for the bed reflection, the aperture was limited using the maximum dip for further processing. Furthermore, unless explicitly stated, data acquired in 2017/18 are 3D migrated.

10.4   Englacial Reflections or Artefacts?

Different signals within the ice column can be seen when looking at data of grid 2 migrated using a 15% stretch mute and a maximum dip of 17° (Figure 10.15 a). Two different classes of events can be seen: The first class marked by the green dashed line are upwards dipping events which seem to occur around bed bumps. The second class of events is highlighted in purple; these appear more horizontally, at different twtt. Both classes of events can be found throughout all inlines of grid 2 with varying amplitude. These internal reflectors might be interpreted as englacial sediment or excising anisotropy, therefore their origin is discussed in the following.

Area around bed bumps (green dashed line):   The events seen around bedrock bumps, e.g. distance 2200 m in Figure 10.15 a, appear to have a convex shape. At first glance one might interpret these signals as migration smiles (e.g. Figure 10.6 panel $0.20\,\mathrm{m\,ns^{-1}}$ around distance 2400 m), a sign for overcorrected data. However, migration smiles have a concave shape, opposed to the convex shape visible in Figure 10.15 a. Furthermore, these convex events change in shape and amplitude when limiting the migration aperture using the maximum image location distance (Figure 10.15 b). Data migrated in 2D do also include parts of these events, but with much weaker amplitude and a smaller spatial extent (Figure 10.15 c). Figure 10.16 shows results of 3D migration using different maximum dips (a–e) to limit the migration aperture and the unmigrated data (f) of inline 30. No clear continuous englacial reflection can be seen in the unmigrated section (f). Using a maximum dip of 5° (a), no convex events can be identified, limiting the dip to a maximum of 10° (b) the convex events are visible, however this reflector appears more flat, when compared to a maximum dip 17° (c). The section with maximum dip 30° (d) contains an upwards dipping reflector to the west at distance 2400 m, that appears longer compared to maximum dip 17° (c). At a maximum dip 45° the section looks indistinguishable from the section with maximum dip 30°; no change in length of the convex reflector can be seen.

Figure 10.17 shows a comparison of umigrated (left panel) and 3D migrated (right panel) data along inline 30 with different mutes applied to the data (prior to migration). Muting signals immediately below the bed reflection (c) creates a migration result (d), which contains the convex reflections. When applying a bottom mute including the bed reflection (e), no convex reflectors are visible
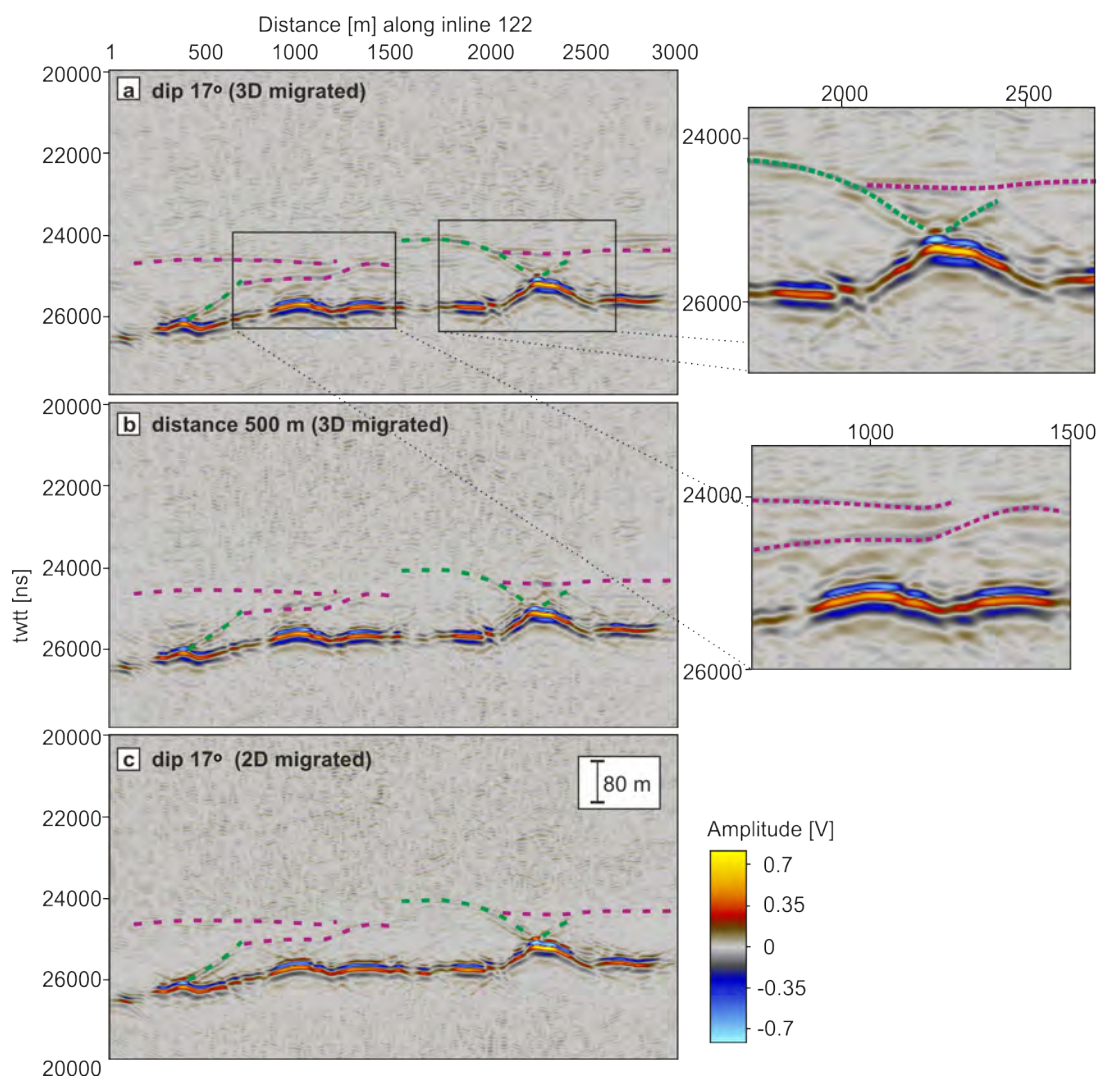
Figure 10.15: Inline 122 using a maximum stretch mute of 15% and a) 3D migration of whole dataset at maximum dip 17°, b) 3D migration of whole dataset using a maximum image location distance of 500 m, c) 2D migration of inline 122, using maximum dip 17°. Green line marks the position of convex shaped signals, purple lines mark the position of horizontal signals, as seen using a maximum dip 17° for comparison.
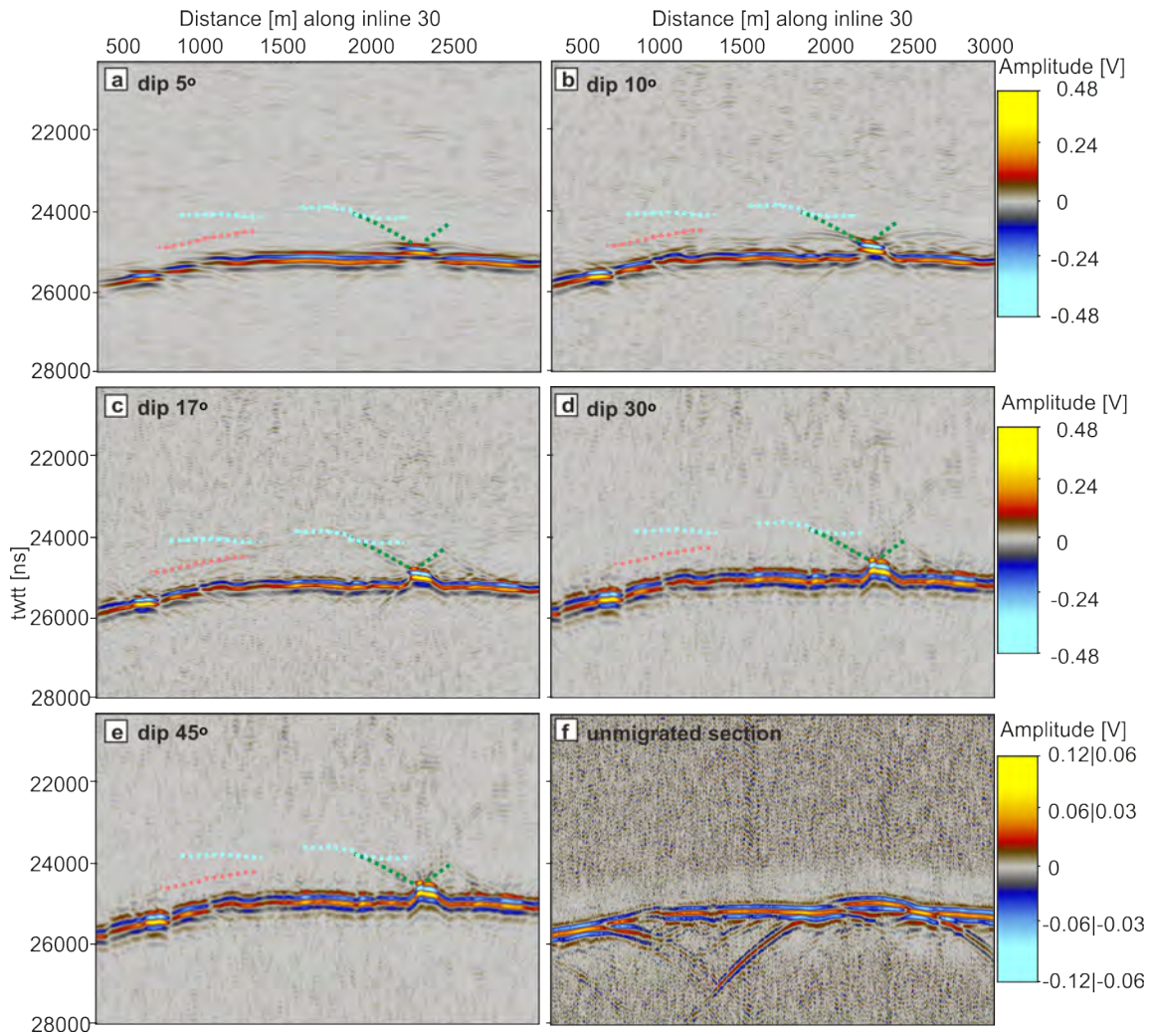
Figure 10.16: Results of inline 30: data were 3D migrated with a constant velocity of $0.168 \, \mathrm{m \, ns^{-1}}$, maximum stretch mute of 15% and with the following parameters: a) maximum dip 5°, b) maximum dip 10°, c) maximum dip 17°, d) maximum dip 30° and e) maximum dip 45°. Panel f shows unmigrated data for comparison. Panel a–e have the same colour scale. Panel f has a different colour coding to amplify possible englacial reflections. Green line marks the position of convex shaped signals, red and blue lines mark the position of horizontal signals, as seen using a maximum dip 17° for comparison.
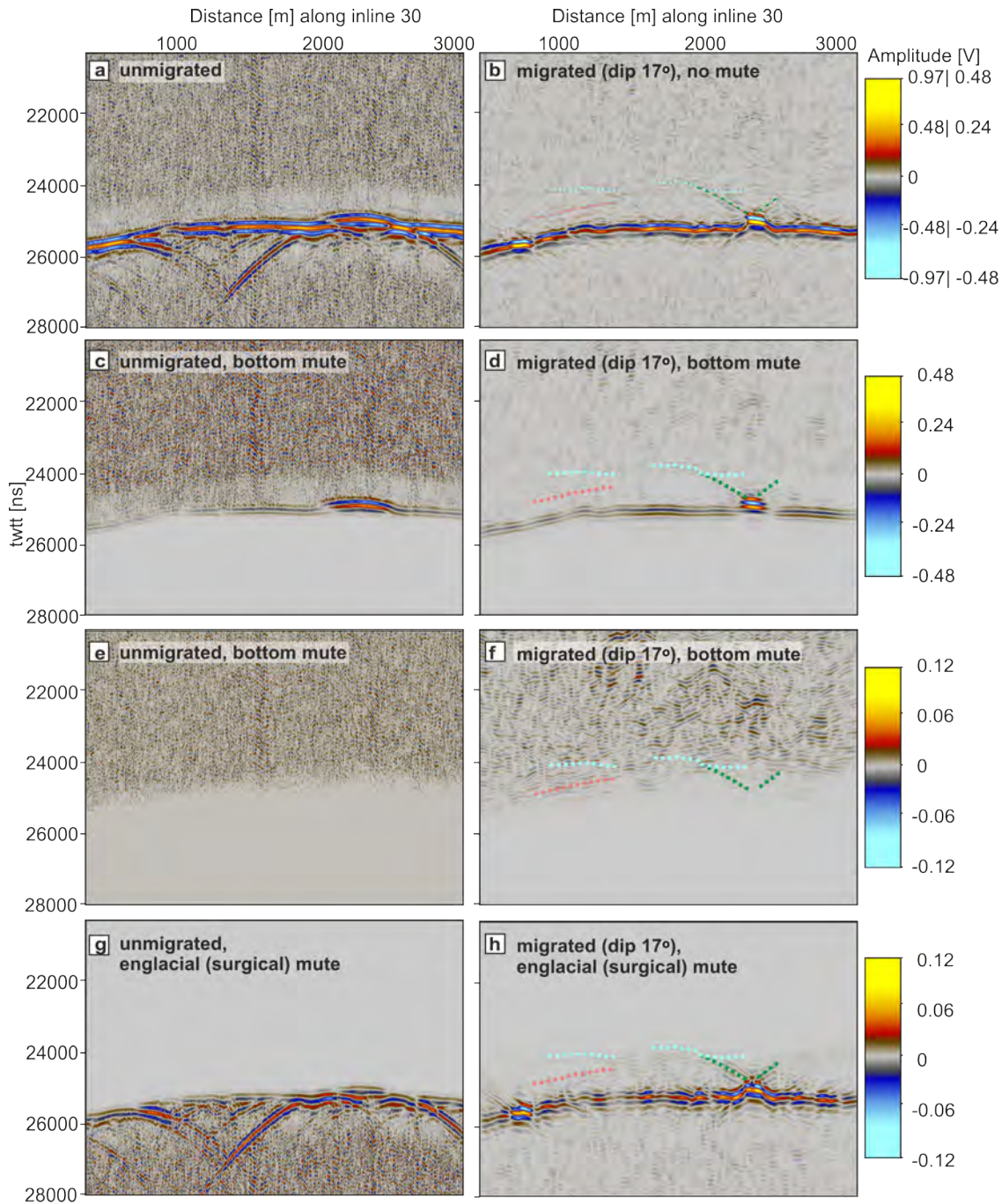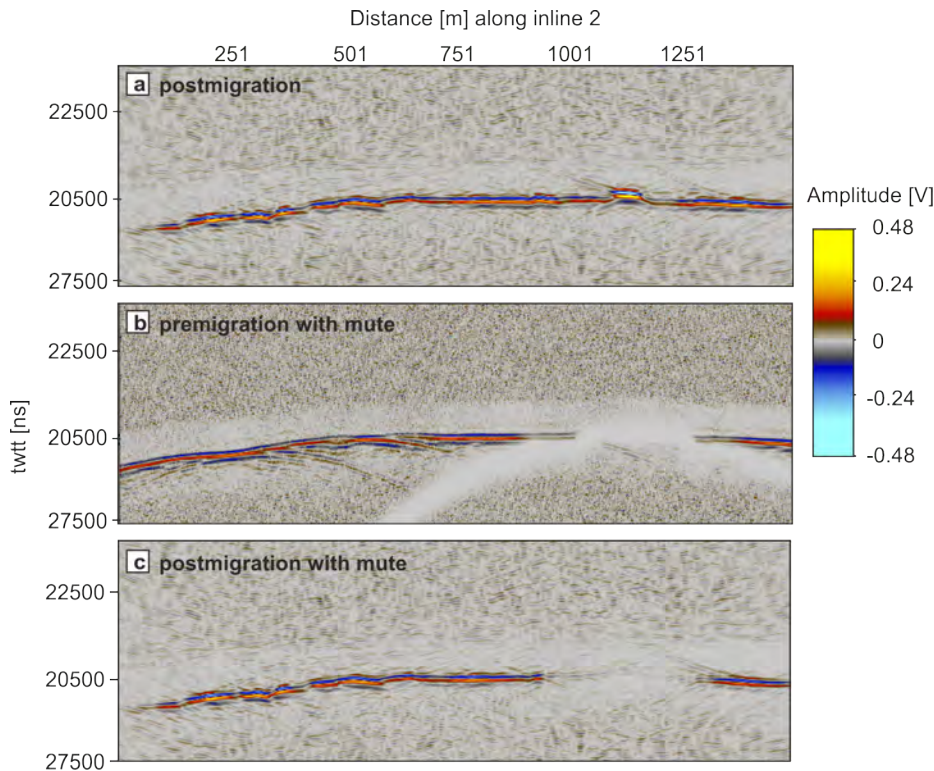
Figure 10.17: Results of inline 30, after applying 3D migration. The left column shows unmigrated data, right column shows migrated data with a migration velocity of $0.168\,\mathrm{m\,ns}^{-1}$, stretch mute of 15% and a maximum dip of 17°, with a mute applied prior to migration on sections as follows: a & b no mute, c & d bottom mute excluding the bed reflection, e & f bottom mute including the bed reflection, therefore energy reflected off the bed is assumed to be suppressed and g & h surgical mute to suppress any energy reflecting from above the bed. Images on the right have the same colour scale and images on the left have the same colour scale. Green line marks the position of convex shaped signals, red and blue lines mark the position of horizontal signals, as seen using a maximum dip 17° for comparison.

Figure 10.18: Results of inline 2, a) after 2D migration with maximum dip 17°
and maximum stretch mute of 15%, b) unmitigated data after applying a surgical
mute to suppress the signal of the Bump reflection, c) 2D migration of data with
surgical mute applied.

after 3D migration (f). If signals above the bed reflection are suppressed (g),
therefore (nadir) energy coming from englacial layers, the migrated section shows
the convex reflectors. Figure 10.18 shows data of inline 2, after migration (a),
prior to migration with a surgical mute applied to reflections origination of the
Bump (b) and data after the application of migration to data presented in (b).

For reasons of lacking convex reflectors when applying mutes that include the
bed reflection, as well as reasons stated above, these convex events are assumed
to be created by the migration of noise and do not represent the reflection of
energy at englacial layers.

Horizontal events (purple dashed lines): When applying the migration
with different maximum dips, the location of these horizontal events, as well as
the amplitude and continuity changes (Figure 10.16). The horizontal events are
most prominent in panel c (maximum dip 17°), furthermore, the position of these
events changes with varying aperture limits. This is most obvious comparing

panel c & d, where the aperture has been increase, the signal of horizontal events vanishes. Horizontal events are visible closer to the bed for a maximum dip of 10° and completely absent for a dip of 5°. As seen in Figure 10.17 the horizontal events are visible when applying a bottom mute excluding the bed reflection (c & d) but are not clearly visible when applying a bottom mute including the bed (e & f). Furthermore, when applying a surgical mute to suppress signal received above the bed reflection, therefore englacial signals, the horizontal structures still appear. The strength of the signals increase when applying 3D migration compared to 2D migration (Figure 10.15 a and c).

Considering the lack of horizontal events when muting the bed as well as the appearance of signal even though englacial energy is suppressed (e.g. Figure 10.17 h) favours the interpretation, that the horizontal reflectors are artefacts caused by migration of noise.

Noise causing the two different classes of artefacts, could be limited by using different apertures for different segments of lines. With increasing relief in flow direction, a greater dip is necessary to migrate the bed reflection properly. The variation of the migration aperture with distance is unfortunately not possible and represents a software limitation.

10.5 Additional Images Chapter 7

10.5.1 Comparison of Data With Different Processing and Line Spacing
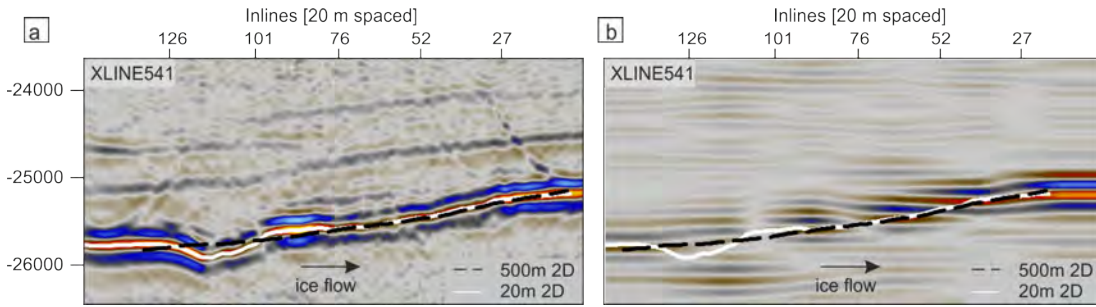

Figure 10.19: Radargram along crossline 599 (a) 20 m spaced data and (b) 500 m spaced data. Lines superimposing the amplitude of the bed reflection show twtt picks based on different datasets for comparison.
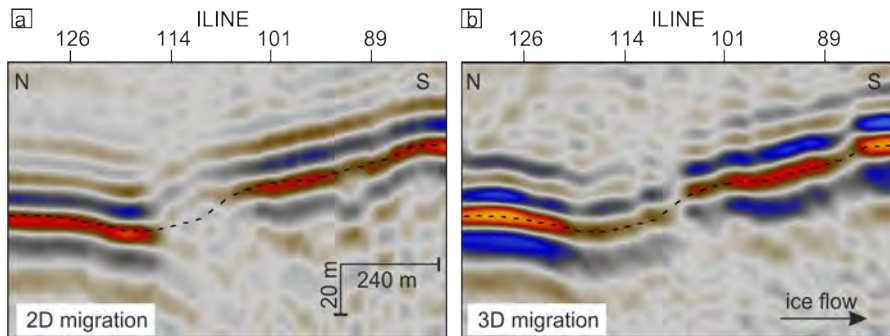

Figure 10.20: Radargram along crossline 589 of 20 m spaced data after (a) 2D and (b) 3D migration. The black dashed line superimposing the amplitude of the bed reflection show twtt picks based on 3D migrated data.

10.5.2 Attributes of Data Along In- and Crosslines

Figure 10.22 shows inline 76 of grid 1, as recorded amplitude. Signals in the upper 1000 ns originate from the arrival of the direct wave. Traceable englacial reflections are visible until a twtt of ~15000 ns. The area between 15000 ns and the bed reflection appears chaotic and no continuously traceable englacial reflections are visible. The bed reflection at ~25000 ns is visible due to its high amplitude (~0.2 V). No continuous or traceable signal can be seen beneath the
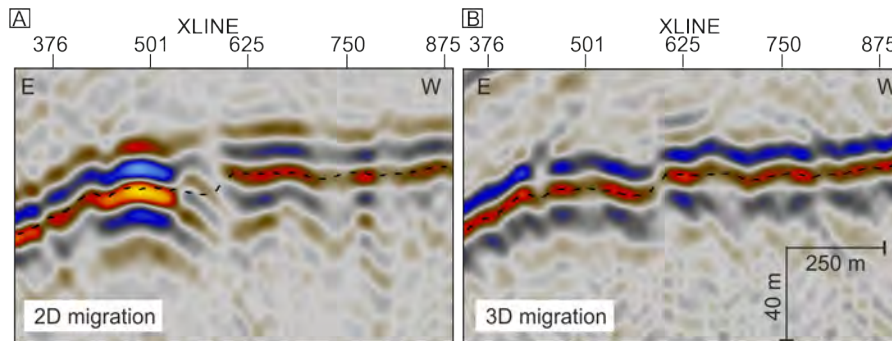
Figure 10.21: Radargram along inline 109 of 20 m spaced data after (a) 2D and (b) 3D migration. The black dashed line superimposing the amplitude of the bed reflection show twtt picks based on 3D migrated data.

bed reflection. The frequency content of the radargram (Figure 10.23) is between 0–15 MHz (as expected due to the application of a bandpass filter early on in the processing in Section 3.3.4.3). The signals of the direct wave contain frequencies of around 3 MHz. The traceable continuous englacial reflections often contain a frequency around 1 MHz (red), 4 MHz (yellow) or 8 MHz (green). The overall frequency content in the chaotic zone (15000–25000 ns) seem to be higher ($\sim$8 MHz) than in the shallow ice. The bed reflection contains frequencies of 1.5–4 MHz. The signal below the bed reflection show a generally higher frequency content ($\sim$8 MHz).

The COP of the bed reflection (Figure 10.24) shows a clear change from negative to positive and back to negative, all along the reflections. No inversions in polarity are visible. Furthermore, as described before (Section 7.1), using the COP when picking the bed reflection does partly improve the continuity of reflections. Horizontal signals at $\sim$20000 ns twtt, which originate from migration artefacts, show a high continuity in cosine of phase. Figure 10.25 does display the envelope of inline 76, with high values of envelope on the crest of some landforms, and other areas with very low envelope, like the flank of the Bump. The envelope of englacial signals (envelope <0.08 V) is much weaker than what has been calculated for the bed reflection (<0.25 V). The enhanced continuity of englacial reflections in the upper part of the radargram and the bed reflection, compared to the chaotic zone, is also displayed using the GLCM attribute (Figure 10.26). Furthermore, some structures at a twtt of $\sim$21000 and 24000 ns appear continuous using the GLCM attribute, which were not visible using other attributes. These structures are visible within several in- and crosslines, and seem to show
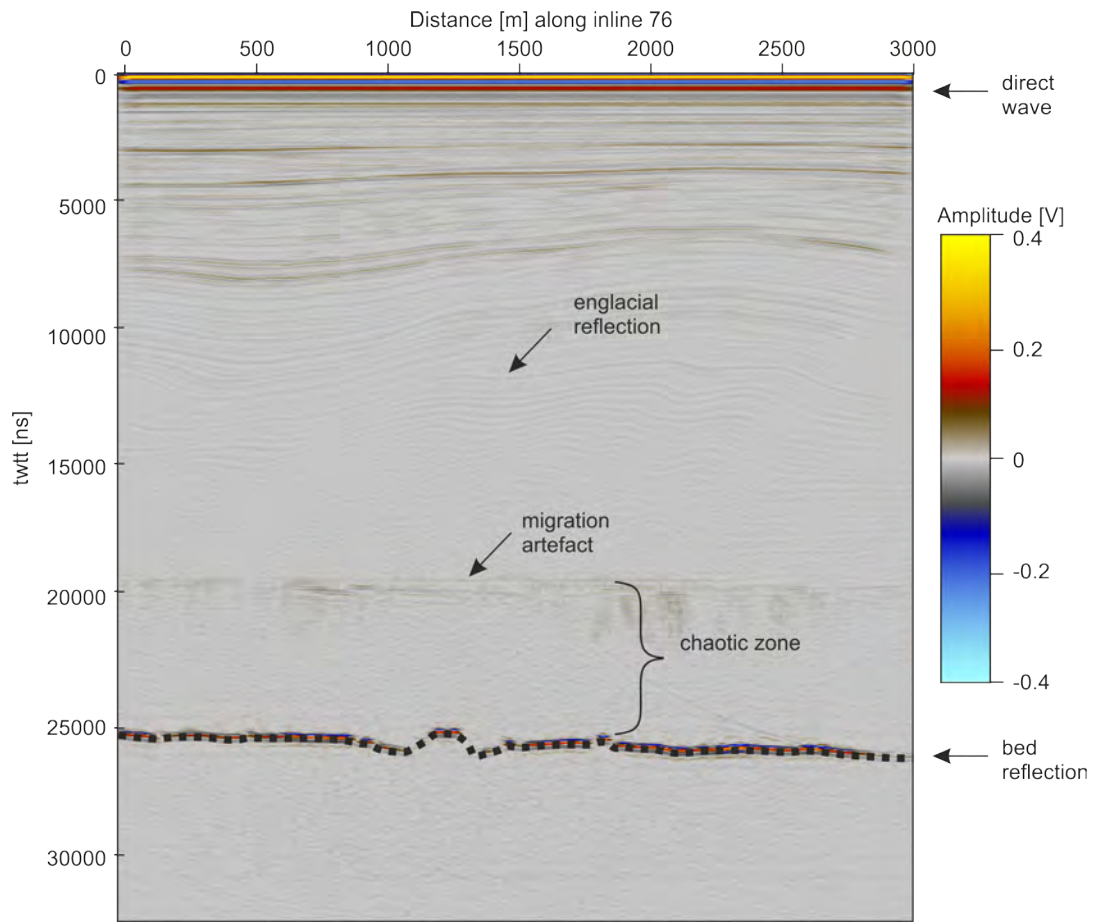
Figure 10.22: Inline 76 of grid 1 displaying the amplitude of the data. The signal of the arrival of the direct wave, englacial as well as the bed reflection (black dashed line) and artefacts are marked. Furthermore, an area referred to as chaotic zone is highlighted.
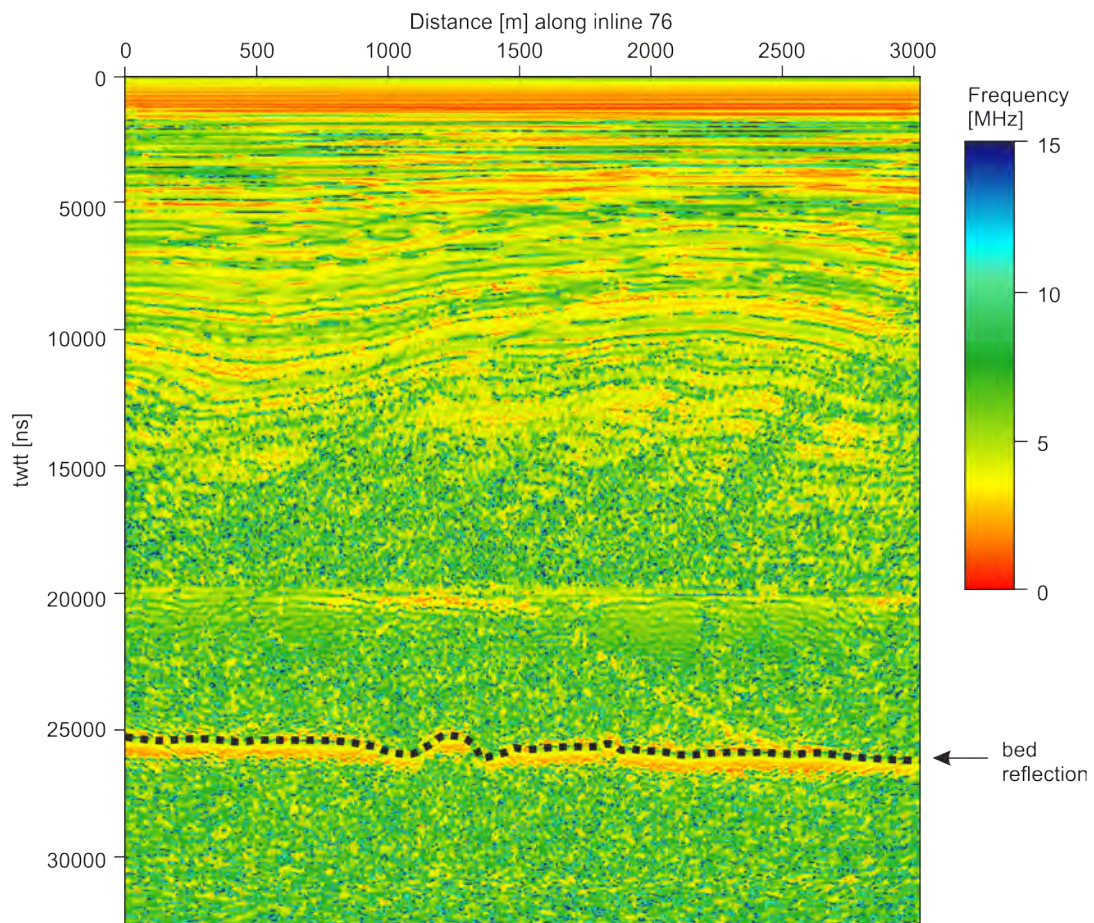
Figure 10.23: Inline 76 of grid 1 displaying the dominant frequency content. The rough location of the bed reflection is highlighted by the black line.
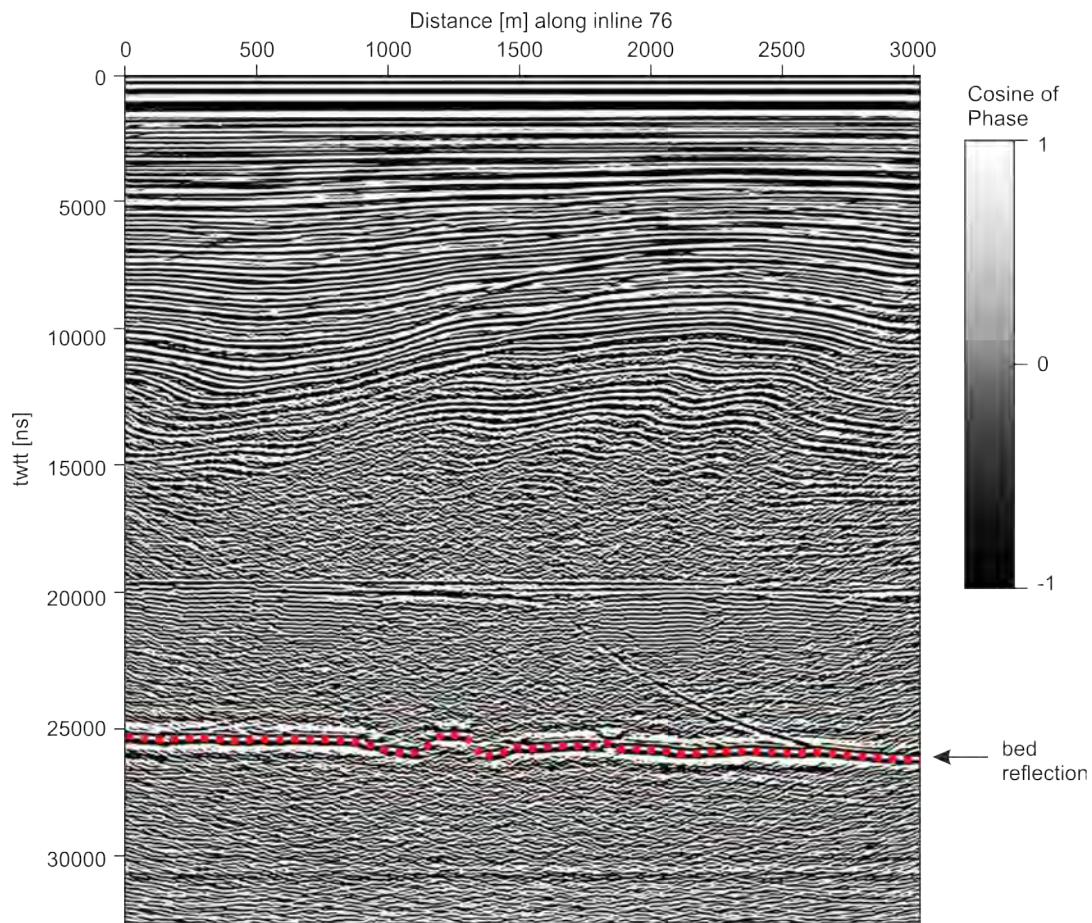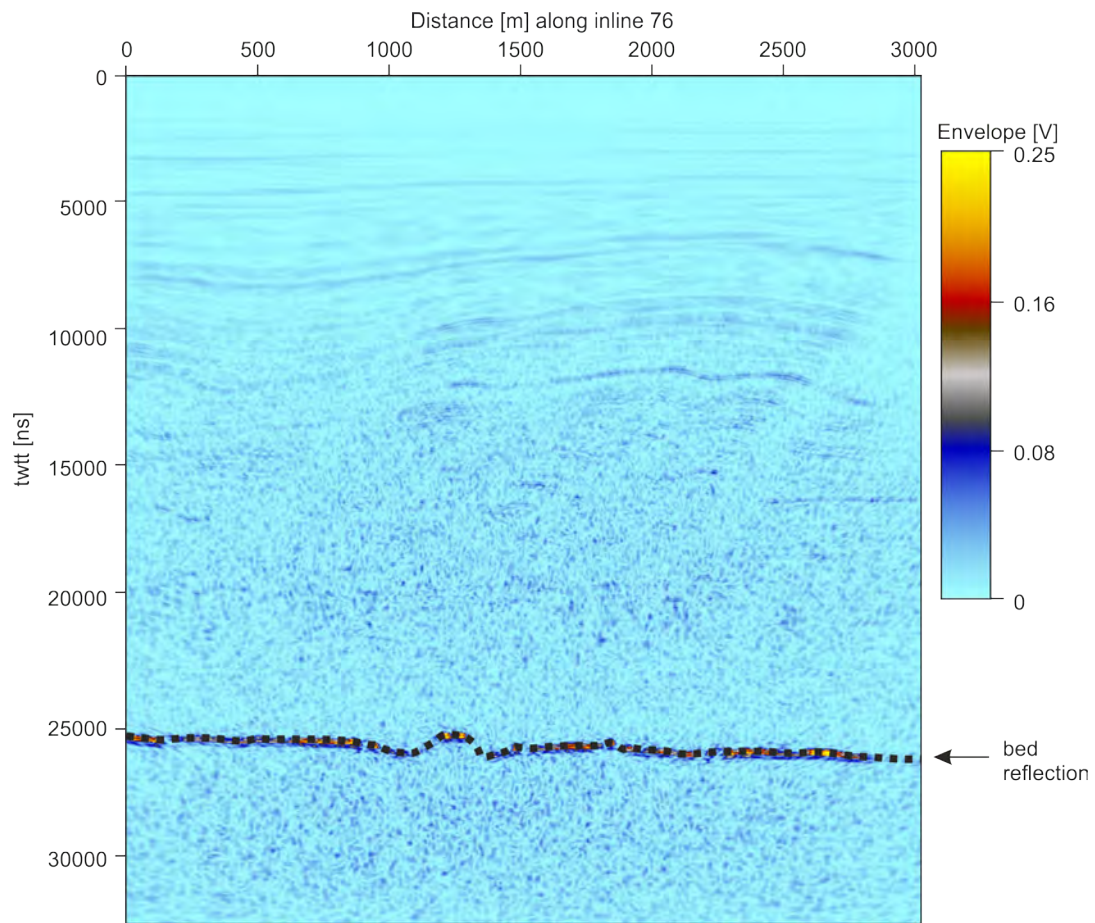
Figure 10.24: Inline 76 of grid 1 displaying the COP.

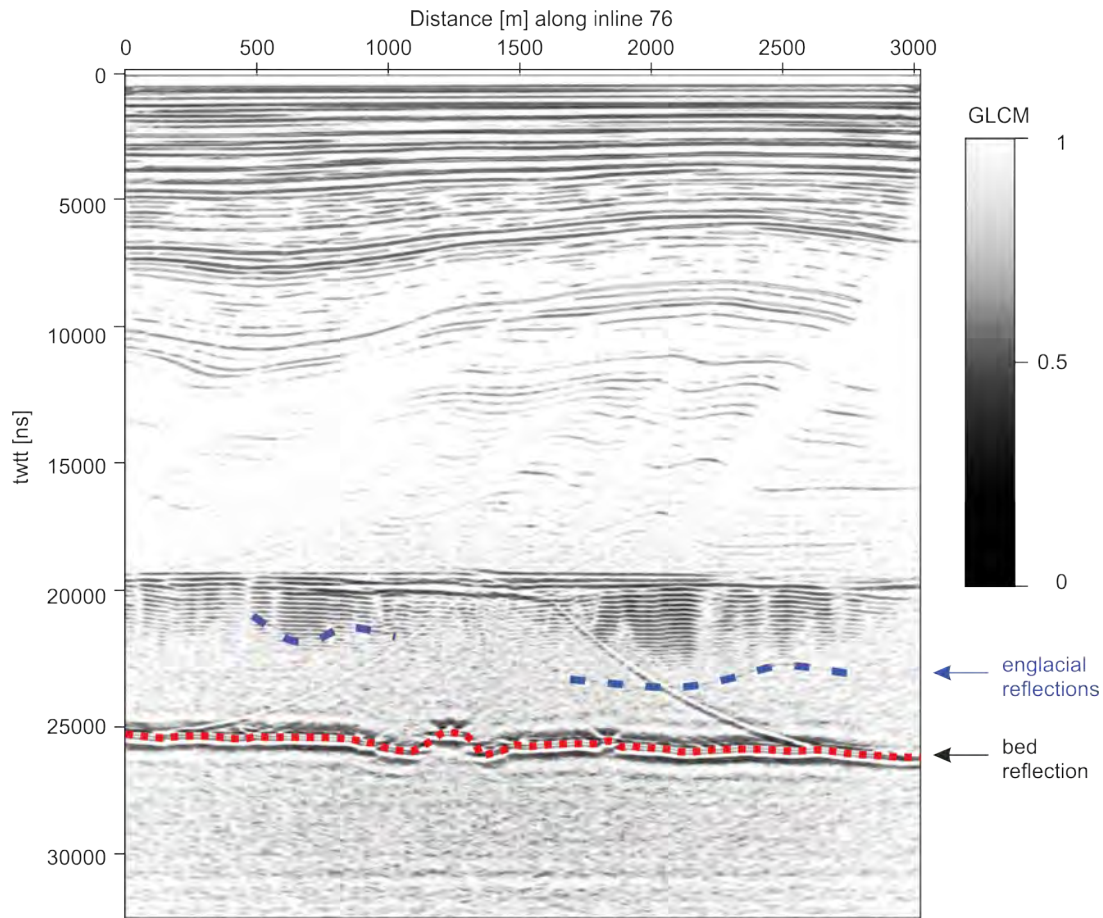Figure 10.25: Inline 76 of grid 1 displaying the envelope.

Figure 10.26: Inline 76 of grid 1 displaying the GLCM. The blue arrow highlights englaical reflections, only visible in the GLCM plot.

variations in shape and location comparable to englacial reflections in the upper ice column. No coherent signals received from beneath the bed reflection have been identified for grid 1 or grid 2.

10.5.2.1 Discussion

10.5.2.1.1 Englacial Properties Englacial reflections are visible within all attributes, however they are well pronounced using the GLCM (Figure 10.26) and COP (Figure 10.24), which shows the most (spatial) consistent signals. The chaotic zone identified in the lower part of the ice column (15000–25000 ns twtt) does not show any coherent reflections in any attribute except for the GLCM, where some continuous reflections within the chaotic zone are visible. Englacial reflections are caused by variations in density, conductivity (like acid concentration due to ash layers) and or crystal orientation fabric (Clough, 1977; Fujita &

Mae, 1994; Fujita *et al.*, 1999). Density variations are known to get smoothed out with increasing depth (Millar, 1981), therefore changes in crystal orientation fabric and conductivity are likely causes of deep englaical reflections. It is possible, that no changes in crystal orientation fabric or conductivity occur in the chaotic zone, however it is more likely, that weak englacial reflection in these areas are overprinted by noise e.g., the migration artefact at 20000 ns twtt which is visible over 2500 ns (Figure 10.26 and Figure 10.24). The strong continuity of the migration artefacts possibly impedes the identification of weak englacial reflections. The analysis of the dominant frequency within a certain time window over the whole radargram allows the interpretation of attenuation trends, which might be caused by spatial variations in temperature as described by MacGregor *et al.* (2015). No significant variation in frequency content can be seen in the ice column. The chaotic zone contains higher frequencies, which can be attributed to the lack of englacial reflections (with frequency content $<5\,\mathrm{MHz}$). Therefore, no clear attenuation trend is visible over depth, which highlights the homogeneity of the ice and makes spatial variations in temporal state less plausible. This is consistent with the spatial pattern of englacial envelope, where no area of significant high envelope has been identified.

10.5.2.1.2 Sub-bed Properties The calculation of different attributes did not reveal any coherent signals from beneath the bed reflection, which might imply that (1) there are no further boundaries representing dielectric contrasts within the remaining time recorded, (2) most of the energy transmitted got attenuated and reflections from boundaries are too weak to be visible within the background noise.

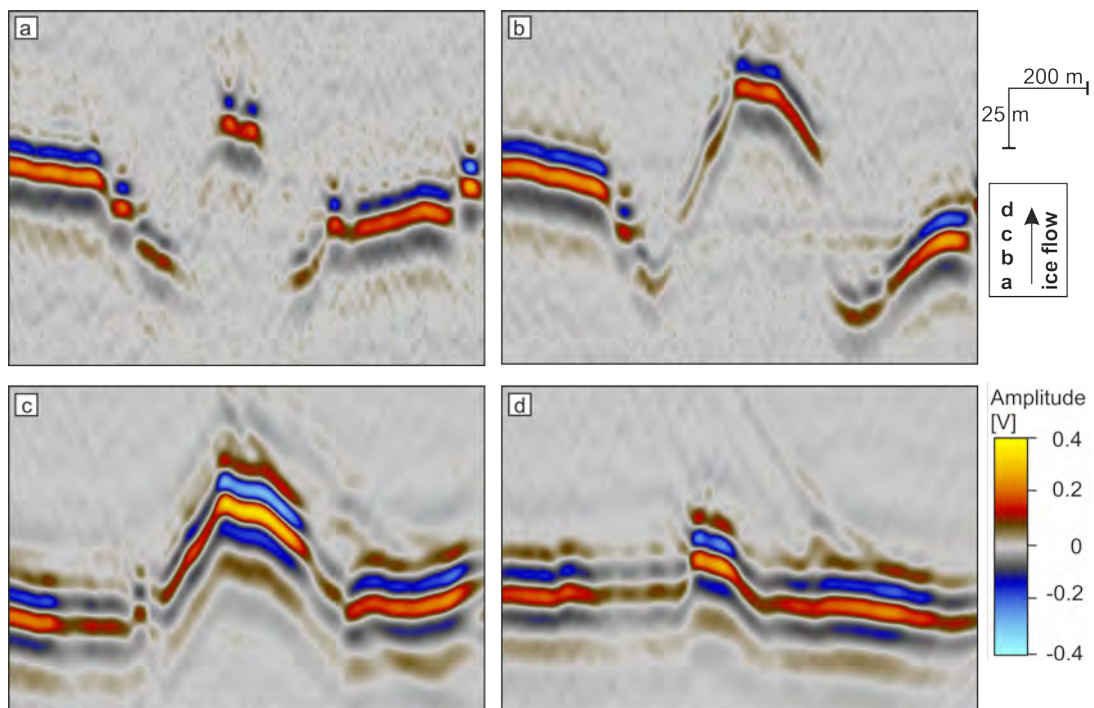### 10.5.3   Additional Images

Figure 10.27: Radargram of the Bump at four different locations: a) Inline 77, the upstream end of the Bump, b) Inline 5, the downstream end of grid 1 c) Inline 148, the downstream end of grid 2 and d) Inline 5, the downstream end of grid 2. Distance between a and b is 1.4 km, b and c 9.4 km and c and d 1.7 km.
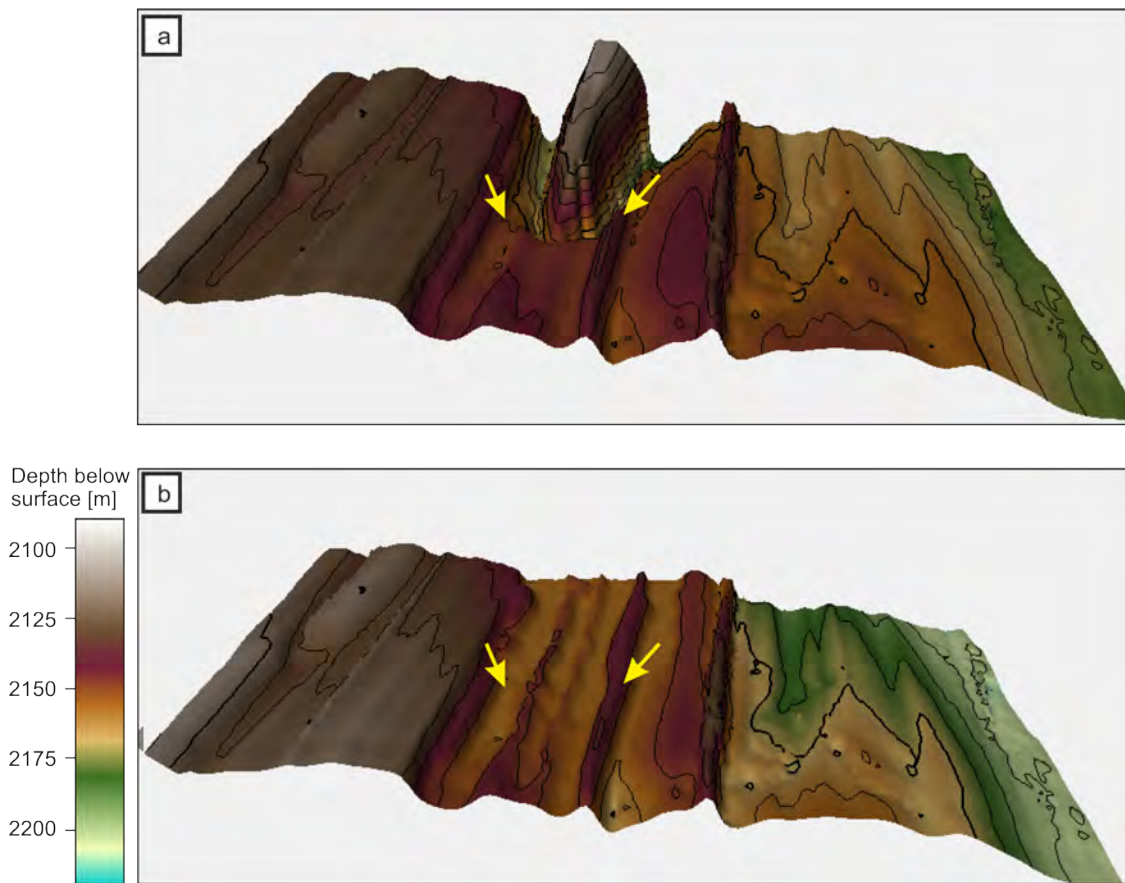
Figure 10.28: Comparison of current topography and interpretation of initial topography in grid 1. a) Current 3D bed topography. b) Interpretation of initial 3D topography . For the interpretation displayed using the curvature attribute see Figure 10.29 in the Appendix.
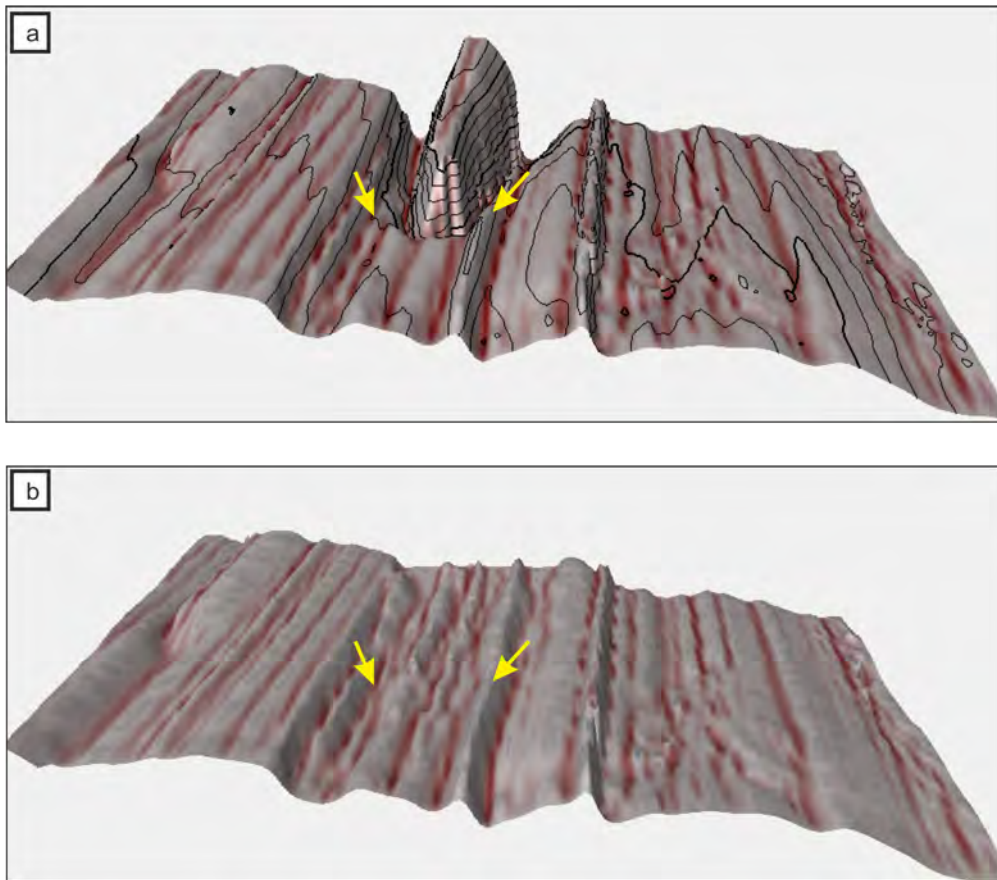
Figure 10.29: a) 3D bed topography in grid 1 showing the curvature. b) interpretation of initial 3D topography in grid 1 showing the curvature.
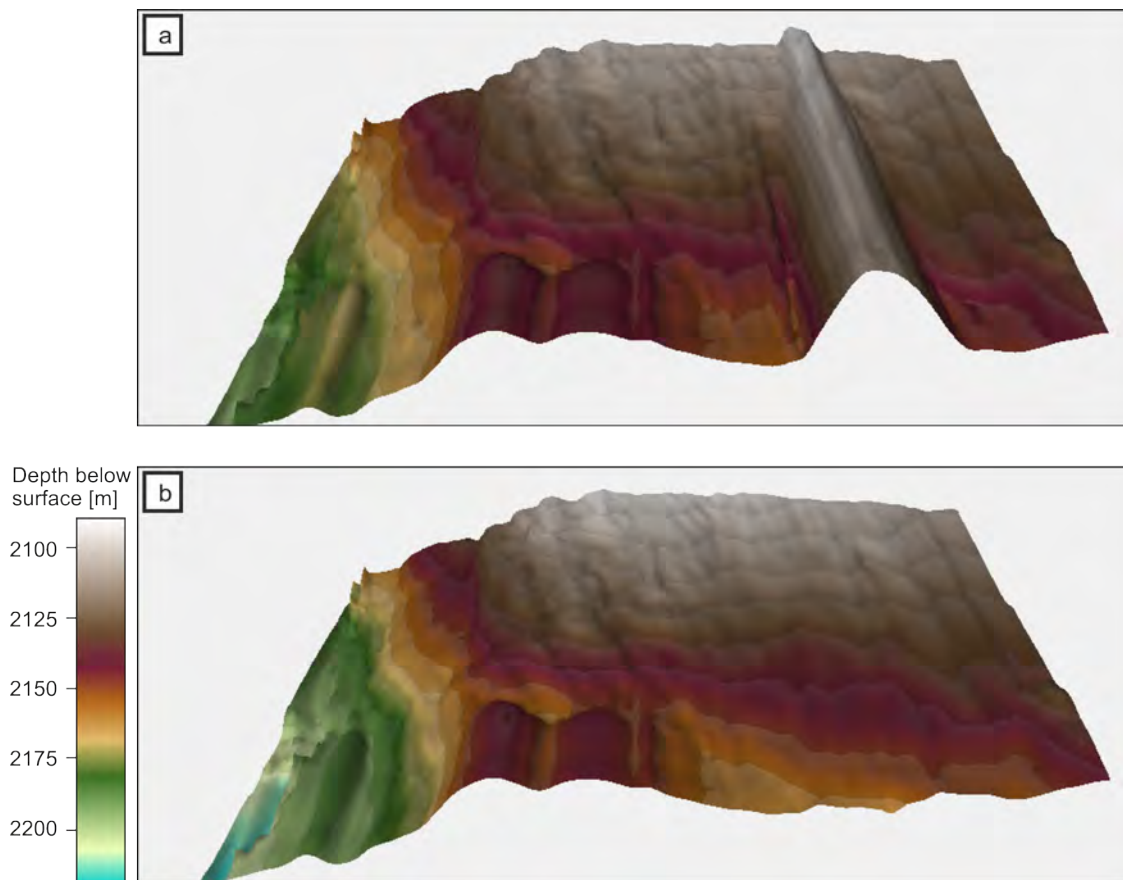
Figure 10.30: Comparison of current topography and interpretation of initial topography in grid 2. a) Current 3D bed topography. b) Interpretation of initial 3D topography in grid 2 showing the curvature. For the interpretation displayed using the curvature attribute see Figure 10.31 in the Appendix.
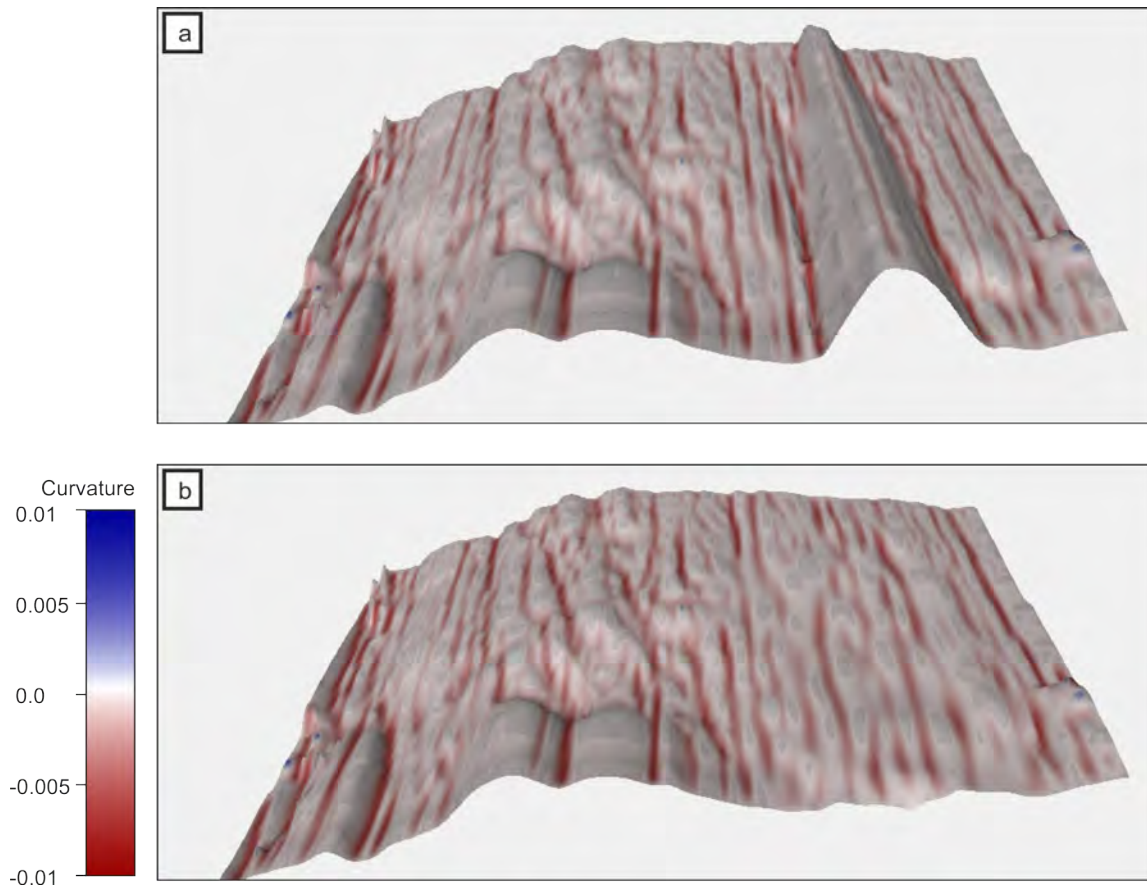
Figure 10.31: a) 3D bed topography in grid 2 showing the curvature. b) interpretation of initial 3D topography in grid 2 showing the curvature.
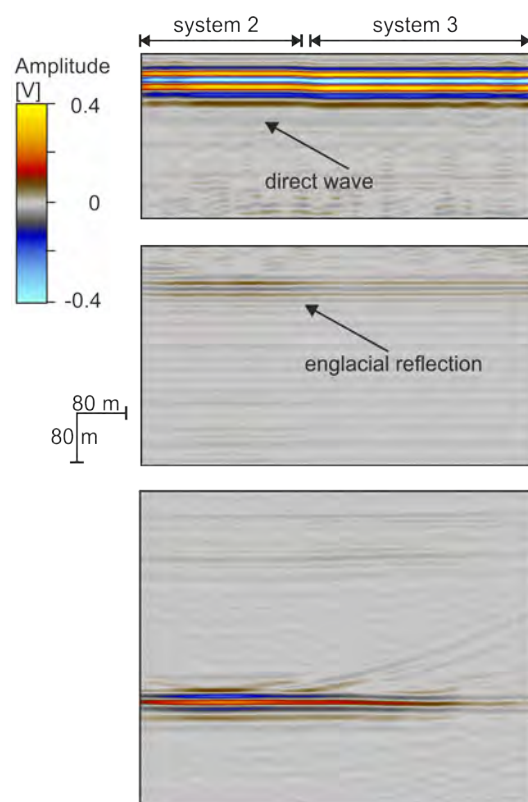
Figure 10.32: Arrival of the direct wave, englacial and bed reflection in crossline 146 of grid 2, colour code represents the amplitude.

10.5.4 Advice for Imaging Subglacial Topography

The survey design should always be linked to the main research aims. If the aim is to image 3D structures, like the up- or downstream end of landforms, then 3D processing should be applied to data (assuming data acquisition results in data compliant with 3D migration). By applying 3D migration, the true location and dip of topography can be calculated, especially when imaging cross-cutting features and complex geometries that are not aligned perpendicular to the acquisition direction.If the proposed main aim is to get an image that represents the overall topography, then the application of 2D migration should be sufficient. In this case the sampling interval is more important than the algorithm. Furthermore, if the bed topography is known to consist of 2D features (e.g., no significant topographic change along flow), theoretically no differences between 2D and 3D migration should be visible. 200 m spaced data does resolve the overall topography, although features of less than 200 m size are most likely missed and small scale features (e.g. cross-cutting features) are smoothed out. Decreasing the line spacing to ~60 m will provide the theoretical maximum resolution, therefore, another option for covering a big area is to have e.g. a 200 m spaced grid over a larger area and then a denser spaced (e.g. 60 m) grid around a target, e.g. lee of landforms. However, if only 2D migration is applied it has to be kept in mind, that sub-bed reflections are possibly caused by off-nadir reflections. Furthermore, features with an orientation not perpendicular to acquisition direction are possibly not imaged correctly and possibly appear with a false dip and azimuth.